Development and Processing Maps of High Entropy Alloys for High-Temperature Applications

Ph.D. Thesis

By

RELIANCE JAIN

DEPARTMENT OF METALLURGY ENGINEERING AND MATERIALS SCIENCE

INDIAN INSTITUTE OF TECHNOLOGY INDORE

MAY 2021

Development and Processing Maps of High Entropy Alloys for High-Temperature Applications

A THESIS

Submitted in partial fulfillment of the

requirements for the award of the degree

of

DOCTOR OF PHILOSOPHY

by

RELIANCE JAIN

DEPARTMENT OF METALLURGY ENGINEERING AND MATERIALS SCIENCE

INDIAN INSTITUTE OF TECHNOLOGY INDORE

MAY 2021

INDIAN INSTITUTE OF TECHNOLOGY INDORE

CANDIDATE'S DECLARATION

I hereby certify that the work which is being presented in the thesis entitled **"Development and Processing Maps of High Entropy Alloys for High-Temperature Applications"** in the partial fulfillment of the requirements for the award of the degree of **Doctor of Philosophy** and submitted in the **Department of Metallurgy Engineering and Materials Science, Indian Institute of Technology Indore**, is an authentic record of my own work carried out during the time period from **July 2017** to **April 2021** under the supervision of Dr Sumanta Samal, Assistant Professor at IIT Indore.

The matter presented in this thesis has not been submitted by me for the award of any other degree of this or any other institute.

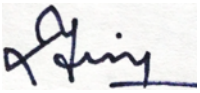

Signature of the student with date
(RELIANCE JAIN)

This is to certify that the above statement made by the candidate is correct to the best of my/our knowledge.

S. Samal

23/09/2021

Signature of Thesis Supervisor #1 with date

(DR SUMANTA SMAL)

RELIANCE JAIN has successfully given his Ph.D. Oral Examination held on **15/09/2021.**

S. Samal

23/09/2021

Signature of Thesis Supervisor #1 with date

(DR SUMANTA SMAL)

ACKNOWLEDGEMENTS

I am immensely obliged to many people for making a journey as a Doctoral student at IIT Indore exhilarating one. All of them deserve my devoted acknowledgment, and I proved my best to list all of them here. However, it may be possible that I might have dropped some of them; unwittingly, I beg for their forgiveness. It is because of my colleagues and friends in the Department of Metallurgy Engineering and Materials Science and the group members, I have been able to do research and complete my thesis in a relaxed environment. I would also like to give a special thanks to the government of India, MHRD, for providing me a scholarship to come here to IIT Indore for Doctoral studies.

First, I am indebted to my thesis supervisor **Dr. Sumanta Samal**, who provided me an opportunity to work here as a Doctoral student in the Department of Metallurgy Engineering and Materials Science and helped me throughout my stay both educationally and mentally. I am most obliged to him for his supervision, encouragement, constructive discussions, suggestions, patience, and invaluable support, which made this work possible. I am thankful to Dr. Vinod Kumar for his inspiration and helpful suggestions to achieve my goal during my Doctoral studies. I would like to thank my PSPC members, Dr. Santosh S Hosmani and Dr. Eswar Prasad Korimili, for their guidance and valuable suggestions during my thesis work.

I would also like to thank my collaborator Prof. Gandham Phanikumar (IIT Madras), Dr. Rahul M R (ISM DHANBAD), Dr. Ramakrushna Sabat (IIT Bhubaneshwar), and Dr. Poulami Chakraborty (BARC) for scientific discussions during all the collaborative projects. I would like to acknowledge IIT Indore for providing laboratory, computational facilities, and financial support during my doctoral work. I would convey my overwhelming thanks to the administration of our department. They always manage an excellent working environment and are ready to support. I extend my deep appreciation to my past and present group members (Sandeep, Piyush, Girish, Ashok, Avi, and Divik) at IIT Indore for their generous help and co-operation to make my doctoral work successful.

I would personally like to extend my admiration to all my friends during various times of my Ph.D. period, Sheetal, Vishesh, Digvijay, Aditya, Rameshwar, Siddhartha, Sangam, Achyut,

Mahesh, Narshima, Sushmita, Priyanka, Uma Shankar, Mukurala Nagaraju, who were always there to support and never let me down during these Ph.D. days.

I feel extremely grateful to acknowledge all my teachers who have taught me in some other ways since my childhood. I could never achieve anything without their guidance, blessings, and support. I would also like to thank my friends Pradeep, Roopendra, Rajneekant, Gaurav, Ankit, and Nitin.

Most importantly, none of this would have been possible without the support of my family. I do not have words to express my love and gratitude towards my lovable parents (**Mr. Vinay Kumar Jain** and **Mrs. Asha Jain**), wife (**Chandni Jain**), son (**Shreyas Jain**), and all other family members for their unconditional love, support, encouragement, and blessings during this journey of Ph.D.

I would like to thank every person, who has directly or indirectly contributed to making this journey successful, I wish I could thank them all, but time and space compel me to stop here. I thank you all for being a part of my life.

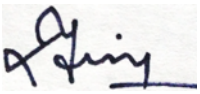

RELIANCE JAIN

DEDICATED TO

MY FAMILY

AND

ALL WELL-WISHERS

Abstract

Multicomponent high entropy alloys (HEAs) have been attracting attention worldwide and constitute an active, frontier area of research in the exploration of novel materials development. The current study focuses on design and development of a single-phase $Fe_{25}Co_{25}Ni_{25}Cr_{20}V_5$ FCC HEA, higher-order seven component $Fe_{35-x}Co_{10}Ni_{25}Cr_{15}Mn_5V_{10}Nbx$ (x =2.5, 5, 7.5, and 10 at. %) eutectic high entropy alloys (EHEAs), eight component $Fe_{32.5-x}Co_{10}Ni_{25}Cr_{15}Mn_5V_{10}Al_{2.5}Nbx$ (x= 5, 7.5, 10, and 12.5 at. %) EHEAs, Co-Fe-Mn-Ni-Ti quasi-peritectic HEAs (QHEAs), and Co-Cr-Fe-Ni-Zr QHEA by an integrated approach of combining thermodynamic simulation and experimental solidification techniques. Experimentally, it is found that the microstructure of studied EHEAs consists of FCC solid solution phase and Nb-rich $(Co, Fe)_2Nb$-type C14 Laves phase. Further, $Co_{25}Fe_{25}Mn_5Ni_{25}Ti_{20}$ QHEA consists of primary BCC(β) and eutectic mixture of FCC solid solution and $Ti_2(Ni, Co)$ Laves phase and $(CoCrFeNi)_{90}Zr_{10}$ QHEA shows bimodal eutectic microstructure having globular eutectic (FCC+ Ni_2Zr) and lamellar eutectic (FCC + Ni_7Zr_2). Based on structural and microstructural characterization, a new pseudo-quasi-peritectic four-phase reaction, i.e., L + BCC (β) $\longrightarrow$ FCC (α) + $Ti_2(Ni, Co)$ is established for $Co_{25}Fe_{25}Mn_5Ni_{25}Ti_{20}$ QHEA, and L + Ni_2Zr $\rightarrow$ FCC (α) + Ni_7Zr_2 is proposed for $(CoCrFeNi)_{90}Zr_{10}$ QHEA.

Further, the mechanical properties and hot deformation behavior (at different temperatures and strain rates) of developed HEAs are carried out. Also, the processing maps using multiple models are generated to identify the hot workability regimes, as well as the plausible deformation mechanism of HEAs, is understood. The optimum thermomechanical processing conditions of single-phase $Fe_{25}Co_{25}Ni_{25}Cr_{20}V_5$ FCC HEA lie in the temperature range 1165-1235K and strain rate range 10^{-3} s^{-1}-$10^{-1.65}$ s^{-1} as well as temperature range 1235-1373K and strain rate range 10^{-3} s^{-1}-$10^{-0.73}$ s^{-1}. The optimum hot workability conditions of $Co_{25}Fe_{25}Mn_5Ni_{25}Ti_{20}$ QHEA lie in temperature range 1073-1273 K and strain rate range 10^{-3} s^{-1}-$10^{-1.6}$ s^{-1} as well as temperature 1130-1225K and strain rate $10^{-0.5}$-1 s^{-1}, while for $(CoCrFeNi)_{90}Zr_{10}$ QHEA stable region lie in temperature range 1073-1323 K and strain rate range 10^{-3}-$10^{-1.3}$$s^{-1}$ as well as 1073-1125 K and 10^{-3}-$10^{-0.75}$ s^{-1}.

Furthermore, the neural network-based computational approach has been established for predicting the mechanical properties and flow behavior of studied alloys. The flow curve

prediction has been done by conventional models and artificial neural network (ANN) model at different hot working conditions. The performance of these models is evaluated by different parameters such as average absolute relative error (AARE), mean square error (MSE), and coefficient of correlation. Furthermore, FEM simulation predicts the effective plastic strain distribution and material flow behavior during thermomechanical processing of studied HEAs. Finally, it is observed that QHEA having peritectic and eutectic microstructure or two eutectics microstructure shows improved mechanical properties at elevated temperature.

LIST OF PUBLICATIONS

List of published papers from thesis work

1. **Reliance Jain**, Sandeep Jain, Rahul M R, Sumanta Samal, Vinod Kumar, "Phase evolution and mechanical behaviour of Co-Fe-Mn-Ni-Ti eutectic high entropy alloy", **Transaction of Indian Institute of Metals (2018),** 71, 2795-2799.
2. **Reliance Jain**, Rahul M R, Sumanta Samal, Vinod Kumar, Gandham Phanikumar, "Hot workability of Co-Fe-Mn-Ni-Ti eutectic high entropy alloy" **Journal of alloys and Compounds (2019),** 822, 153609.
3. **Reliance Jain,** Sheetal K. Dewangan, Sumanta Samal, Vinod Kumar, "Artificial neural network approach for microhardness prediction of eight component FeCoNiCrMnVAlNb eutectic high entropy alloys" **Material science and Engineering A (2020),** 797, 140059.
4. **Reliance Jain**, Avi Jain, Rahul M.R., Ashok Kumar, Mrigendra Dubey, Ramakrushna Sabat, Sumanta Samal, Gandham Phanikumar "Development of ultrahigh strength novel Fe-Co-Ni-Cr-Zr quasi-peritectic high entropy alloy by integrated approach using experiment and simulation". **Materialia (2020),** 14, 100896.
5. **Reliance Jain,** Sheetal K. Dewangan, Priyanka Umre, Vinod Kumar, Sumanta Samal, "Microstructure evolution and an ANN approach for microhardness prediction of suction cast FeCoNiCrMnVNb eutectic high entropy alloys" **Transaction of Indian Institute of Metals**, **(2021)**, **doi: 10.1007/s12666-021-02335-1.**
6. **Reliance Jain**, M.R. Rahul, Poulami Chakraborty, Rama Krushna Sabat, Sumanta Samal, Gandham Phanikumar, Raghvendra Tewari "Design and deformation characteristics of single-phase Co-Cr-Fe-Ni-V high entropy alloy", **Journal of alloys and Compounds (2021),** 888, 161589.

List of an ongoing manuscript from thesis work

7. **Reliance Jain**, M.R. Rahul, Poulami Chakraborty, Rama Krushna Sabat, Sumanta Samal, Gandham Phanikumar, Raghvendra Tewari "Hot deformation behaviour and

processing maps of single-phase Co-Cr-Fe-Ni-V high entropy alloy", 2021 **(Manuscript under communication)**.

8. **Reliance Jain**, Priyanka Umre, Ramakrushna Sabat, Vinod Kumar, Sumanta Samal, "Constitutive and artificial neural network modeling to predict high-temperature deformation behavior in CoFeMnNiTi eutectic high entropy alloy", 2021, **(Manuscript under communication)**.
9. **Reliance Jain,** Priyanka Umre, Divik Parte, Vinod Kumar, Sumanta Samal "Prediction of hot deformation behaviour in $AlCoCrFeNi_{2.1}$ eutectic high entropy alloy using a conventional and artificial neural network model", 2021 **(Manuscript under communication)**.

TABLE OF CONTENTS

LIST OF FIGURES

LIST OF TABLES

ACRONYMS

HEAs	High Entropy Alloys
EHEAs	Eutectic High Entropy Alloys
QHEAs	Quasi Peritectic High Entropy Alloys
XRD	X-Ray Diffraction
SEM	Scanning Electron Microscopy
TEM	Transmission Electron Microscopy
EBSD	Electron Back Scattered Diffraction
BSE	Back Scattered Electron
EDS	Energy Dispersive X-Ray Spectroscopy
ANN	Artificial Neural Network
DRV	Dynamic Recovery
DRX	Dynamic Recrystallization
CALPHAD	CALculation of PHAse Diagrams
MICRESS	Microstructure Evolution Simulation Software
FEM	Finite Element Method
DMM	Dynamics Materials Modeling

Chapter 1

Introduction

1.1 Introduction:

Recently, high entropy alloys (HEAs) have fascinated researchers due to their significant advantages over conventional alloys for possible structural and functional applications [1]. Eutectic-based HEAs have captivated special attention, with the possibility of obtaining improved mechanical properties and easy castability. The new alloy design concept of multicomponent HEAs was first christened by Yeh et al. [1] and subsequently explored by many research groups in the last few years [2][3][4], owing to their excellent properties. It is experimentally often observed that the multicomponent HEAs exhibit simple microstructure consisting of solid solutions of FCC and/or BCC phases, which are attributed to the effect of alloying multiple elements in equiatomic or near equiatomic ratio. The simple crystal structure in HEAs is the outcome of several core effects [5][6], such as high configurational entropy, severe lattice distortion, and sluggish diffusion [7], which acts as a barrier for the formation of complex phases and also slows down the kinetics of phase transformations.

Consequently, the design approach of EHEAs is adopted by developing *in-situ* composite microstructure of combining the benefits of both solid solution phase(s), which is considered as main product phase(s) of HEAs and intermetallics [8] to obtain balanced mechanical properties in terms of strength and ductility. It is reported in the literature [9][10] that EHEAs have the following advantages such as near-equilibrium microstructure, which is stable at high temperature, lowest energy in phase boundaries, high rupture strength, excellent creep resistance. The improved mechanical properties of EHEAs is attributed to Hall-Petch type mechanism, i.e., $\sigma_{ye} = \sigma_{fe} + K\,\lambda^{-1/2}$, where the σ_{ye} is the yield strength for eutectic alloy, σ_{fe} is the friction stress, K is Hall-Patch slope, and the λ is the inter-lamellar spacing of eutectics. Consequently, it is essential to reduce the interlamellar spacing (λ) in order to get high strength. The strength of the eutectic alloys can substantially be increased by reducing λ-value. It is important to develop higher-order multicomponent EHEAs so that the diffusion is expected to be sluggish, and hence EHEAs with nanoscale/ultrafine microstructure can probably be prepared in bulk form by

solidification processing techniques to obtain superior mechanical properties for large-scale applications. Therefore, the field of EHEAs is also expected to remain vibrant for researchers in the near future and raise hope of excellent properties for high-temperature applications that still emerge unexpectedly.

Although the design of EHEA is challenging; the researchers are coming up with different methods for the design of EHEAs such as the simple mixture method [11], CALculation of PHAse Diagrams (CALPHAD) aided approach [12], mixing enthalpy approach [13], use of thermo-physical parameters [14] [15], etc. The CALPHAD aided approach is even used for the design of higher-order EHEAs [16]. The stability of the EHEAs was studied by many researchers, and reports show good mechanical properties even after heat treatment processing at high-temperature [17]. The promising strength, castability, and ability to do cold working and modify the properties in EHEAs are reported in the literature [18][19]. The processing of metals and alloys are always accompanied by a different hot working process such as rolling, forging, and extrusion. Therefore, it is of great significance to investigate the hot deformation behavior of high entropy alloys under hot processing conditions.

An ANN is a computational model that learns from the available data and observes the patterns in the form input/output without any prior assumption. ANN approach offers unprecedented opportunities to solve complex problems such as the nonlinear system and unknown data prediction [20]. Sabokpa et al. [21] predicted the flow stress using the ANN approach at temperature range 250-400 and strain rate 0.0001 to 0.01 for AZ81 magnesium alloy. Singh et al.[22] predicted the flow behavior during hot deformation of phosphorus steel using the ANN method. Therefore, in materials engineering, ANN has recently emerged as a promising modeling approach to predict different parameters.

1.2 Objective:

In the backdrop of the above considerations to the exciting field of HEAs, the primary objectives of the present investigation are listed as follows:

(i) To design and develop CoCrFeNiV single-phase FCC HEA, seven component FeCoNiCrMnVNb EHEAs, eight component FeCoNiCrMnVAlNb EHEAs (mixture of FCC and intermetallic phases), CoFeMnNiTi QHEA (mixture of peritectic and eutectic

microstructure), and CoCrFeNiZr QHEA (mixture of two eutectics) by thermodynamics simulation and experimental approach.

(ii) To generate the processing maps using multiple models to identify hot workability regimes and understand the plausible deformation mechanism of studied HEAs.

(iii) To predict microhardness of EHEAs against the compositional variation using ANN approach.

(iv) To predict the flow curve at different temperatures and strain rates of HEAs using different models and ANN approach as well as to study the material flow behavior and strain distribution using finite element method (FEM) simulation during thermomechanical processing of HEAs.

1.3 Thesis Structure:

The thesis outline derived from the primary objectives is summarized in the following sections.

Chapter 1 is the introductory chapter, which describes the background, and goals of the current work.

Chapter 2 presents a comprehensive literature review on different aspects of HEAs and motivation, which led to the foundation of the current thesis.

Chapter 3 describes the experimental methodologies associated with the synthesis of alloys and characterization techniques used in the present work.

Chapter 4 deals with the design and development of single-phase CoCrFeNiV HEA using ICME approach.

Chapter 5 describes the design and development of seven component Fe-Co-Ni-Cr-Mn-V-Nb and eight component Fe-Co-Ni-Cr-Mn-V-Al-Nb EHEAs as well as artificial neural network (ANN) approach for microhardness prediction of EHEAs.

Chapter 6 demonstrates the flow curve prediction of EHEAs at different temperatures and strain rates using a phenomenological, physics-based model and ANN model.

Chapter 7 describes the phase evolution and hot workability of CoFeMnNiTi QHEA and prediction of hot deformation behavior using constitutive and ANN modeling.

Chapter 8 illustrates the development of ultrahigh strength novel CoCrFeNiZr QHEA by an integrated approach using experiment and simulation.

Chapter 9 contains the overall conclusions of the present thesis and the scope for future work.

Chapter 2

Literature Review

2.1 Introduction to high entropy alloys (HEAs):

The first-time multicomponent alloys or high entropy alloys (HEAs) were developed by cantor et al. and yeh et al. [1] in the year 2004. They focused on producing a single-phase alloy system by varying the concentration of elements (concentration of each component between 5-35 at. %). The development of HEAs is a breakthrough to alloy design in traditional physical metallurgy and opens up a new field for the exploration of new alloys with specific properties. HEAs exhibit unique properties which is dependent on developed microstructure and hence considered as an engineering material for structural applications (i.e. materials must have superior properties at elevated temperature) [23]. HEAs exhibit unique properties such as excellent ductility at high temperature [24][25], good corrosion and oxidation resistance [26][27], wear resistance [28][29], high hardness at elevated temperature [30][31][32][33], better thermal stability [34] and sluggish diffusion [35][7]. Therefore, HEAs have been seen as futuristic engineering material for high-temperature applications due to their high corrosion resistance, wear resistance, and good strength at high-temperature. Further, HEAs have unique properties than conventional alloys. However, researchers face some problems to obtain improved mechanical properties in terms of strength and ductility, which is necessary to be solved. It is reported in the literature [6][36] that the single-phase HEAs also show the problem with their balancing ductility and tensile strength. It is to be noted that single-phase FCC HEAs show better ductility due to FCC crystal structure but do not give enough strength to protect from the fracture under service [37][38]. Whereas BCC crystal structure-based single-phase HEAs shows better strength with brittleness [39].

Therefore, researchers are doing work in the direction of composite HEAs to solve the problem of mechanical properties. The researchers developed HEAs having composite microstructure consisting of both BCC and FCC phases to solve this problem. Hence, it is necessary to have proper understanding of phase equilibria and solidification behavior of HEAs [40]. Futher there are some other difficulties in processing of HEAs such as poor castability and chemical inhomogeneity which limit the use of HEAs for engineering applications [41][42]. Finally, the

researchers solve the above problem by developing the eutectic high entropy alloys (EHEAs) having microstructure consisting of mixture of FCC and BCC phases. It is observed that EHEAs exhibit good ductility and strength [9]. It is also reported [9][43] that EHEAs have some advantages, such as low energy phase boundary, high rupture strength, excellent high temperature creep resistance, controllable microstructure, stable defects structures, near equilibrium microstructures. The above poor cast-ability problem was also solved by using EHEAs and hence the EHEAs show improved mechanical properties in terms of strength and ductility.

2.2 Criteria for the formation of phases in HEAs

The phase stability of HEAs is predicted from the fundamental properties of alloying elements by many researchers as an initial stage in the development of HEAs. Here, we focus on understanding the properties of individual alloying elements and also the interactions with others. The idea here is to determine the rules governing the phase stability in HEAs by statistically analyzing the collective behavior of constituent elements in an extensive database of HEAs. It is to be noted that thermodynamics and Hume-Rothery parameters are taken into consideration to understand the phase formation and phase stability in HEAs. First time Zhang et al. [44] demonstrated the different phase stability parameters in HEAs such as enthalpy of mixing (ΔH_{mix}), entropy of mixing (ΔS_{mix}) and Gibbs free energy (ΔG_{mix}). All these parameters are described below.

1) **Gibbs free energy (ΔG_{mix}):**

Gibbs free energy (ΔG_{mix}) is the combined effect of two parameters such as enthalpy of mixing (ΔH_{mix}) and entropy of mixing (ΔS_{mix}), which measures the behavior of the process; either the process is spontaneous or not, at a given temperature and pressure. Mathematically, it can be expressed as [45]:

$$\Delta G_{mix} = \Delta H_{mix} - T_m \Delta S_{mix}$$

Where; ΔH_{mix} = mixing enthalpy, ΔS_{mix} = mixing entropy for alloy T_m = melting temperature.

2) **Enthalpy of Mixing (ΔH_{mix}):**

Enthalpy of mixing (ΔH_{mix}) can be defined as total heat content in the system, which is given by [45]:

$$\Delta H_{mix} = \sum_{i=1, i\neq j}^{n} \Omega_{ij} c_i c_j ; \left(\Omega_{ij} = 4\Delta H_{ij}^{mix}\right)$$

Where ΔH_{ij}^{mix} = enthalpy of mixing for binary liquid metals/alloys ij, and C_i = concentration of i^{th} element, Cj = concentration of j^{th} element.

3) Entropy of mixing (ΔS_{mix})

Entropy of mixing or configuration entropy (ΔS_{mix}) is related to arrangements of atoms in lattice sites in different ways [45], which is expressed as

$$\Delta S_{mix} = -R\sum_{i=1}^{n} (c_i \ln c_i)$$

The combined effect of ΔS_{mix} and ΔH_{mix} is taken into consideration and the new parameter Ω, is introduced to understand the phase formation which can be expressed as [45]:

$$\Omega = \frac{(T_m)\, \Delta S_{mix}}{\Delta H_{mix}}$$

Here, Vagard's mixture rule is used to calculate the T_m.

$$T_m = \sum_{n=1}^{n} (c_i\, (T_m)_i)$$

For solid solution phase formation, the value of Ω must be positive, and $\Omega = 1$ is taken as a critical value to form the solid solution. If $\Omega > 1$, the term T_m ΔSmix will exceed that of ΔHmix for solid-solution phase formation. If $\Omega \leq 1$, ΔHmix is the predominant factor, which leads to the formation of intermetallic compounds and segregations. Thus, the value of Ω is taken into consideration to estimate the solid solution phase formation in HEAs.

4) Atomic size difference (δ):

The size of alloying elements in the HEAs plays an essential role in the prediction of the phase formation. The atomic size difference (δ) is given by [45]:

$$\delta = \sqrt{\sum_{i=1}^{n} c_i \left(1 - \frac{r_i}{\bar{r}}\right)^2} \; ; \bar{r} = \sum_{i=1}^{n} c_i r_i$$

Where r_i is the radius of the i^{th} element and $\bar{r}$ is the mean radius.

C_i = concentration of each element

5) Valence electron concentration (VEC):

Valence electron concentration determines the structure of the solid solution phase formed in HEAs. Here VEC is calculated using the mixture rule [45]:

$$VEC = \sum_{i=1}^{n} c_i (VEC)_i$$

Where $(VEC)_i$ is the valence electron concentration of the i^{th} element.

If the value of VEC

(i) ≥ 8 (Possibility of formation of FCC solid solution phase only)

(ii) 6.87 ≤ VEC < 8 (Possibility of formation of mixture of phases i.e. FCC, BCC and Intermetallics)

(iii) < 6.87 (Possibility of formation of BCC phase only)

6) Electronegativity (Δχ):

The electronegativity difference is a Hume-Rothery factor that is generally used to determine intermetallic formation in the complex alloy system which plays an essential role in predicting the formation of intermetallics in the HEA [46].

$$\Delta_{\chi} = \sqrt{\sum_{i=1}^{n} c_i \left(\chi_i - \overline{\chi}\right)^2} ; \overline{\chi} = \sum_{i=1}^{n} c_i \chi_i$$

Where, $\bar{\chi}_I$ is the mean Pauling electronegativity, and

χ_i is the Pauling electronegativity for the i^{th} element, C_i is the concentration of i^{th} element.

7) Λ – Parameter

The parameter Λ is generally used to study the understanding of the collective behavior of entropy of mixing (ΔS_{mix}) and atomic size difference (δ). Atomic size difference and entropy of mixing play an essential role in predicting the formation of solid solution phase(s) in the HEAs. The parameter Λ is expressed as [47].

$$\Lambda = \frac{\Delta Smix}{\delta^2}$$

If the value of Λ – Parameter is greater than equal 2.3403, it leads to the formation of a single-phase formation in HEAs, and if the Λ – Parameter value lies between 0.3165 to 0.5425, the mixture of both solid solution phase and Laves phase formation is possible in HEAs. If Λ – Parameter value is less than equal to 0.2567, there is possibility of formation of the solid solution phase, Laves phase, and intermetallic.

2.3 Thermodynamics Simulation for predicting the phase formation in HEAs

The CALculation of PHAse Diagram (CALPHAD) approach is the foundation of materials design, and recognizing the full potential of HEAs needs such computational tools to optimize alloy parameters within the complication of the HEA composition space [48]. It is a robust tool to estimate the thermodynamic properties of the multicomponent system by extrapolating the existing lower order system with an efficient manner. Details of the algorithm in thermodynamic simulation are given below:

- Firstly, extrapolate the Gibbs free energy of the existing lower order system and then for a higher-order system by using a well-established model such as Muggianu's method [49], Kohler's method [50], Toop's method [51] etc.

- Secondly, the CALPHAD method considers the Gibbs free energy of all phases and reduces the total Gibbs free energy of the system. For a multicomponent system, total Gibbs free energy of a phase is given by the equation:

$G^{\Phi} = G^{S} + G^{ideal} + G^{E}$

Where the G^{S} is the standard Gibbs free energy of the mechanical mixing of constitute phases, G^{ideal} is the ideal Gibbs free energy of mixing, G^{E} is the excess free energy.

- Finally, the stable phases in the multicomponent system is obtained by the minimization of total Gibbs free energy of the system i.e. $G = \sum_{i=1}^{n}[n_i\ G^{\Phi}]$ [52] should be minimum, where the n_i is the amount of phases and G^{Φ} is Gibbs free energy.

Nowadays, well established CALPHAD based software packages such as ThermoCalc, FACTSAGE [53], Pandat [54] are available and extensively used for the study of HEAs [55].

The phase formation during the non-equilibrium solidification is generally understood by two classical solidification models, such as Lever rule and Gulliver-Scheil models [56]. The lever rule model of solidification assumes the complete mixing of solutes in liquid as well as solid, which predicts the equilibrium solidification pathways. The solute balance equation in the Lever rule model for equilibrium solidification can be expressed as $C_l = \frac{C_i}{1-(1-K)\,fs}$ [56]; While in the Gulliver-Scheil model, the redistribution of solute during the solidification is described by considering no diffusion in solid, complete diffusion in liquid, and the local equilibrium at the interface. Also, at the solid-liquid interface, the liquid concentration is expressed as $C_l = C_i(1-fs)^{K-1}$ [56]; where C_i is the initial liquid concentration, K is the equilibrium partition constant, and f_s is a solid fraction. Therefore, the Gulliver-Scheil model is considered as a suitable model for predicting phase evolution during non-equilibrium solidification because of the limited diffusion of solute in solid [57].

2.4 Fabrication of HEAs:

Fabrication of HEAs is divided into four categories which are (1) solid-state processing (SSP) [6][58], (2) liquid state processing (LSP) [31][59], (3) thin-film deposition (TFD) method, and

additive manufacturing process [58]. The different fabrication techniques of HEAs is represented in **Figure 2.1**.

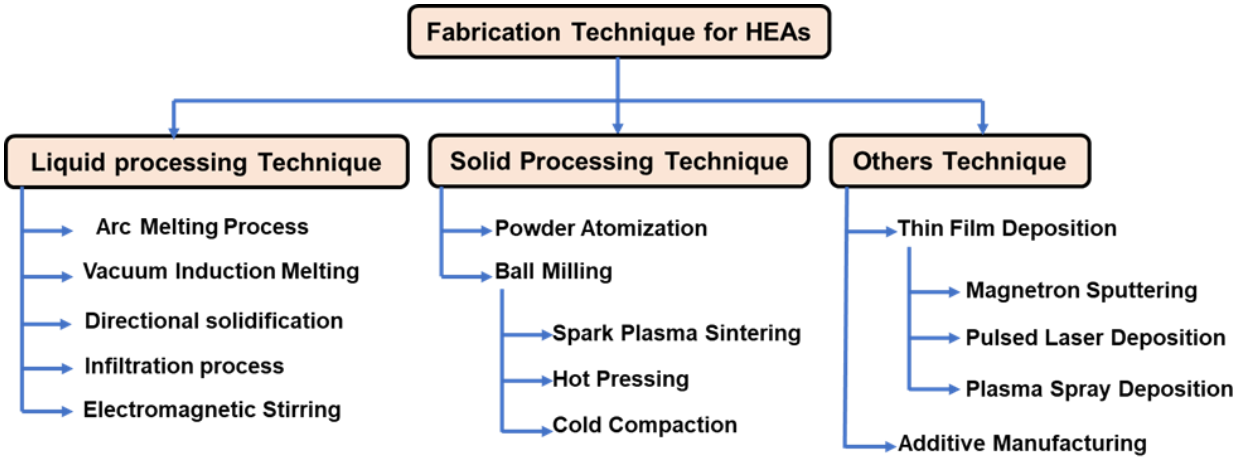

Figure 2.1 Various fabrication techniques for HEAs

(1) Solid-State Processing:

In general, most of the alloys are synthesized by solid-state processing (SSP). In this technique, different alloying elements mix at room temperature and further consolidated at high temperatures. Manufacturing of HEAs via the SSP route is schematically represented in **Figure 2.2**. SSP technique involves powder formation, mixing of powders through mechanical alloying using ball milling, spark plasma sintering, hot pressing, cold compaction, and other manufacturing processes such as rolling, extrusion, and machining [58]. It is reported that the sintered AlCoCrFeNi HEA shows the higher density (7.05 g/cm^3) than the values of the same HEA, prepared via vacuum arc melting and the hot isostatic pressing [60][61]. The microhardness of alloys is found to be 518 HV, which is also higher than the same HEAs, synthesized by arc melting route because of formation of FCC and BCC duplex structure [60]. Recently, Sheetal et al. also reported the AlCrFeMnNiW$_X$ (x = 0, 0.05, 0.1, 0.5) HEAs via vacuum arc melting as well as SPS route and compared the hardness and observed that hardness of alloys, prepared by SPS route varies from 600 to 925 HV, while the hardness varies from the 450 to 530 HV [62][63] for the HEAs, prepared by vacuum arc melting route. The hardness of SPSed HEAs is high due to the formation of hard and brittle sigma phase along with ordered B2, BCC phase, and minor FCC solid solution phase.

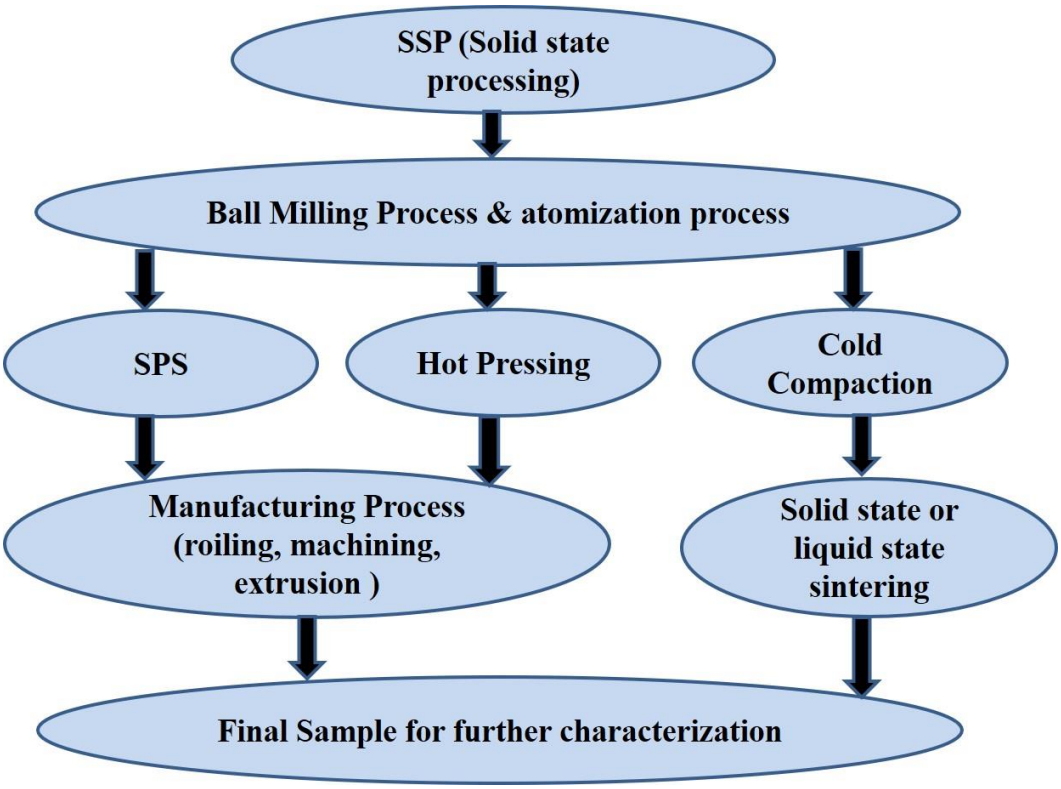

Figure 2.2 Solid state processing of HEAs

(2) Liquid State Processing:

Apart from the solid-state processing, HEAs are also manufactured by melting and casting routes such as vacuum arc melting, vacuum induction melting, mechanical stirring.

2.4.1 Vacuum arc melting:

The melting and casting route is widely used which can melt most of the metals used for making HEAs. It is also economical and feasible, thus attracting significant attention from both academia and the industrial field. HEAs can be synthesized by melting and casting, known as vacuum arc melting (VAM). The main advantages of that technique are given as; (1) low energy consumption, (2) time saving, (3) less porosity, (4) high vacuum to avoid oxidation, and (5) high melting temperature [58][64][65][66][67]. In the VAM process, the vacuum was created in the vacuum chamber to avoid any oxidation. The alloy ingots were put in a Cu-crucible and then melted using non-consumable tungsten electrode under the argon atmosphere. The alloy ingot is

melted 5-6 times to ensure chemical homogeneity and crucible is connected with the chiller unit for cooling purpose. The detailed study of VAM process is discussed in chapter 3.

2.4.2 Vacuum induction melting:

Vacuum induction melting utilizes the electrical current, called the eddy current, to melt the metal in a vacuum. The different materials with particular proportion put in the crucible furnace and is melted using electromagnetic induction energy source to produce alloy ingot. Further, the alloy ingot is remelted several times to get homogenous alloy ingot [68][69][58]. The schematic of vacuum induction melting is given in **Figure 2.3**.

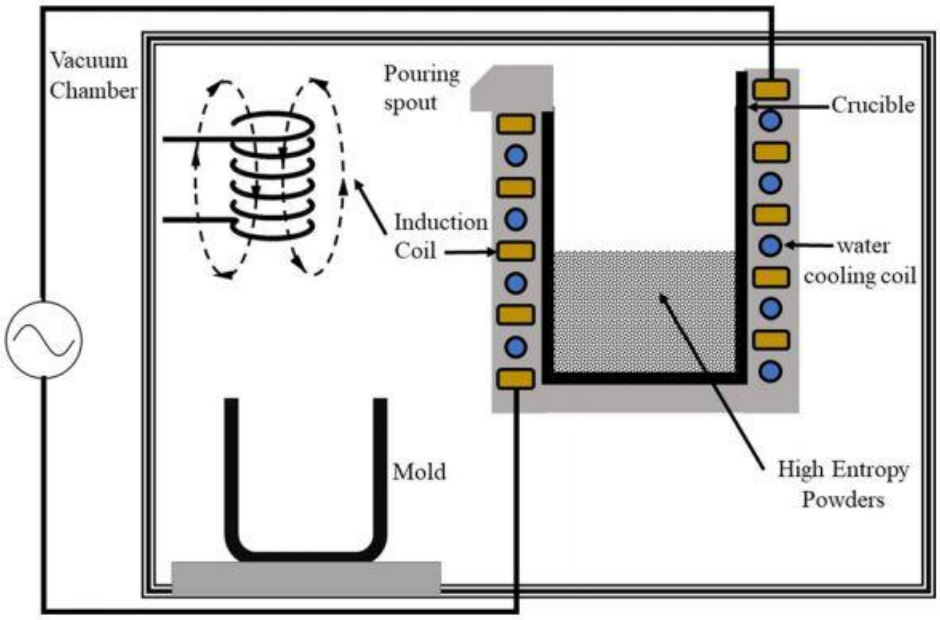

Figure 2.3 Schematic of vacuum induction melting technique [58]

2.3.3 Directional solidification process:

In the directional solidification process, homogenous microstructure, single grain boundaries, and columnar grains can be achieved [58]. It is to be noted here that both molten metal feeding and mould temperature are controllable, the schematic of the direction solidification technique is given in **Figure 2.4**.

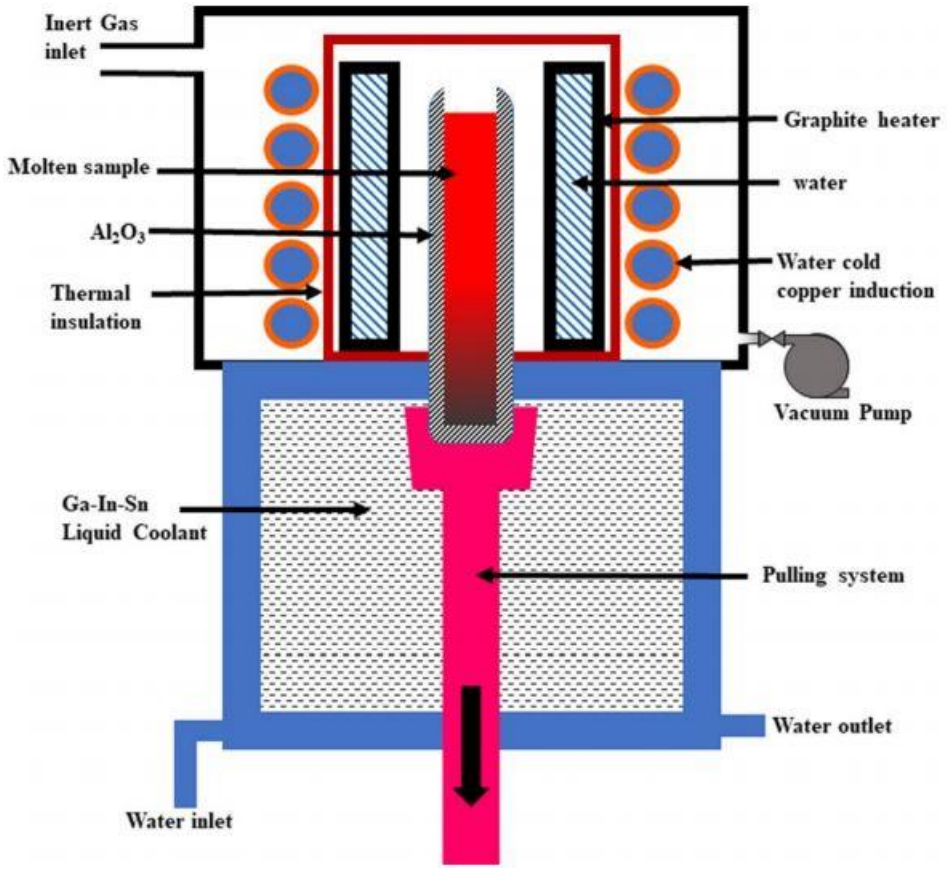

Figure 2.4 Schematic of the direction solidification technique [58]

2.5 Microstructure and mechanical properties of HEAs

It is reported [70] that FeCoNiCr alloy system having single-phase FCC solid solution phase exhibits good ductility but poor yield strength, while FeCoNiCrAl HEA sytem consisting of BCC solid solution phase possesses good yield strength but low ductility. The mechanical properties of EHEAs are attributed to the Hall-Petch mechanism. In multicomponent EHEAs, the characteristic length-scale is very small, and the strength is high due to the refinement of eutectic lamellae [71]. Hall-Patch equation for eutectic alloys is defined as $\sigma_{ye} = \sigma_{ie} + K \lambda_e^{-1/2}$, where the σ_{ye} is the yield strength of the material, σ_{ie} is the friction stress, λ_e is the interlamellar spacing of the eutectic microstructure and K is the hall patch slope [71].

2.5.1 Microstructure and mechanical properties of (FCC + Intermetallics) EHEAs

Mishra et al. [72] investigated $Co_{20}Cu_{20}Fe_{20}Ni_{20}Ti_{20}$ EHEA, exhibiting the eutectic microstructure between FCC Cu- rich solid solution phase (α_2) and Ti_2(Ni, Co) type Laves phase,

FCC Co-rich solid solution phase (α_1) and BCC Ti-rich solid solution phase (**β**) and reported that EHEA shows high yield strength (1000.4 MPa) and ultimate compressive strength (1897 MPa) and moderate plastic strain (15.1 %). Dong et al. [73] prepared the $AlCrFeMo_{0.2}Ni$ HEA via vacuum induction melting, and the microstructure consists of lamellar and rod-type eutectics having FeCr-rich solid solution phase and AlNi-rich intermetallic and the effect on mechanical properties with electromagnetic field intensity is observed. It is found that compressive fracture strength and fracture strain first increase and then decrease, while hardness increases with increasing the electromagnetic field intensity. The highest fracture strength of 2282.3 MPa, yield strength of 1160.5 MPa, and fracture strain of 0.29 are observed at 15 mT electromagnetic field.

Jiang et al. [74] reported $Co_2Mo_{0.8}Ni_2VW_{0.8}$ fully EHEA having FCC CoWMo-rich solid solution phase and Co_7Mo_6-type μ phase and the EHEA (FCC + Intermetallics) exhibits compressive strength and plastic strain of 2364 MPa and 14.4 %, respectively. He et al. [75] reported the $CoCrFeNiNb_{0.5}$ EHEA, revealing eutectic microstructure consisting of FCC CoCrFeNi-rich solid solution phase and CoCrNb-type intermetallic and the alloy system shows balanced mechanical properties i.e., the compressive fracture strength of 2300 MPa and fracture strain of 23.6 %. Huo et al. [76] reported the Zr-containing CoCrFeNiZrx (x=0.1, 0.2, 0.3, 0.4, and 0.5) EHEA consisting of FCC solid solution phase and C15 type Laves phase. It is found that $CoCrFeNiZr_{0.4}$ EHEA shows the highest strength of 667 MPa, while $CoCrFeNiZr_{0.1}$ EHEA shows highest 11 % ductility as compared to the other alloys system. In this study, it is observed that with increasing the amount of Zr, the volume fraction of the C15 Laves phase also increases and at x=0.5 fully eutectic microstructure is obtained (SEM images is given in **Figure 25a, 2.5b**). TEM images for x=0.5 (as given in **Figure 2.5c, 2.5d**) and selected area electron diffraction pattern (SAED) pattern of phase as marked as ‘A’ in the EHEA is shown in **Figure 2.5e**.

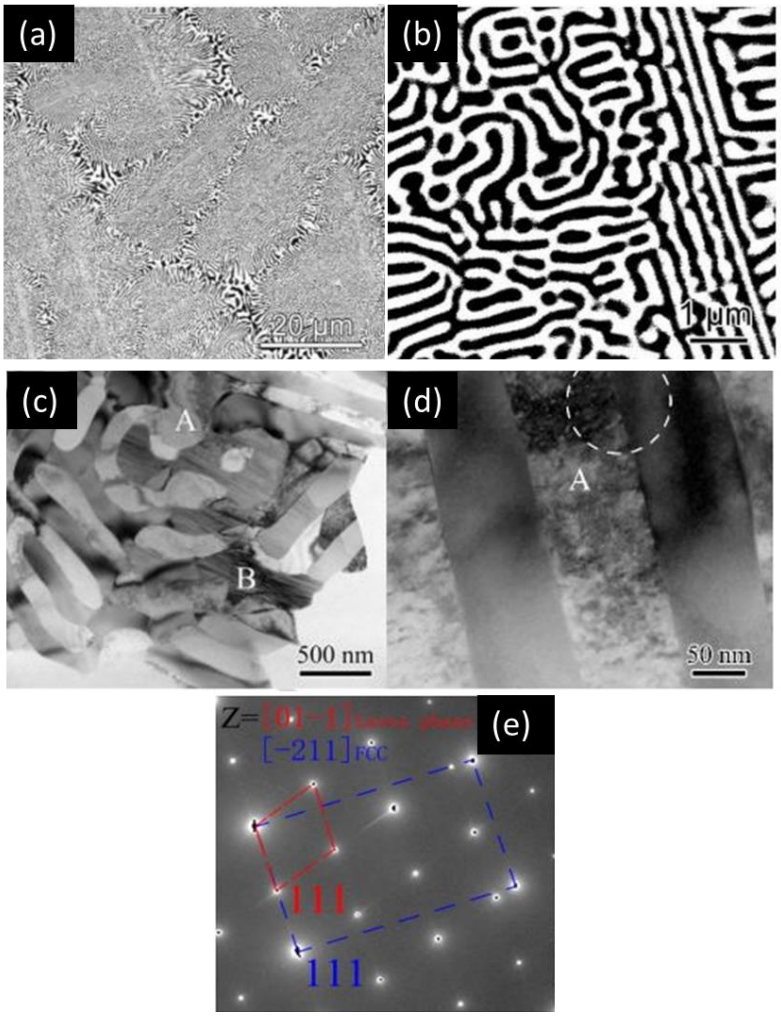

Figure 2.5 SEM and TEM morphology $CoCrFeNiZr_{0.5}$[76]

Jiang et al. [77] reported the CoCrFeNbxNi (x values in molar ratio, x = 0, 0.25, 0.45, 0.5, 0.75, 1.0 and 1.2) HEAs. It is observed that the alloy with x=0 shows the microstructure having FCC solid solution phase, while the alloy with x=0.25, 0.45, 0.5, 0.75, 1.0 and 1.2 exhibits eutectic microstructure between FCC solid solution phase and Laves phase. It is observed that the alloy reveals hypoeutectic microstructure at x=0.25, fully eutectic at x=0.45, and finally hyper eutectic microstructure for other value of x. It is to be noted that fully eutectic alloy system at x=0.45 shows the highest compressive fracture strength of 2558 MPa with fracture strain of about 27.9 %. The $CoFeNb_{0.75}$ $Ni_2V_{0.5}$ EHEA is reported by Jiang et al. [78], and they observed the fully lamellar microstructure with FeCoNi-rich (FCC) solid solution phase and Fe_2Nb-type Laves phase. The alloy shows the yield stress, compressive strength and plastic strain of 2073 MPa, 2232 MPa, and 3.4, respectively.

Zhang et al. [79] investigated CoCrFeNiNbx (x= 0.15, 0.3, and 0.45) hypoeutectic HEA and found that the minor addition of Nb increases the hardness from 297 HV to 500 HV and the yield strength from 300 MPa to 1115 MPa. Chanda et al. [80] reported the nano-eutectic $CoCrFeNiNb_{0.5}$ HEA consisting of FCC solid solution and Fe_2Nb-type Laves phase with 134 nm interlamellar spacing (SEM micrograph for $CoCrFeNiNb_{0.5}$ HEA is shown in **Figure 2.6**). The alloy exhibits a yield strength of 2060 MPa, compressive strength of 2200 MPa, and a plastic strain of 17 %. In this study, the prediction of phase evolution and their stability is also accessed by thermodynamic parameters, atomic size differences, valence electron concentration, and electronegativity. It is found that the atomic size difference and electronegativity are successfully used to predict the coexistence of dual-phase FCC (or BCC) and TCP phase. The DTA (differential thermal analyzer) curve of $CoCrFeNiNb_{0.5}$ HEA shows a single endothermic peak, (as shown in the inset of **Figure 2.6)**, confirming eutectic melting temperature. The liquidus temperature (T_l) and peak temperature (Tp) were measured to be 1277 and 1266 °C, respectively.

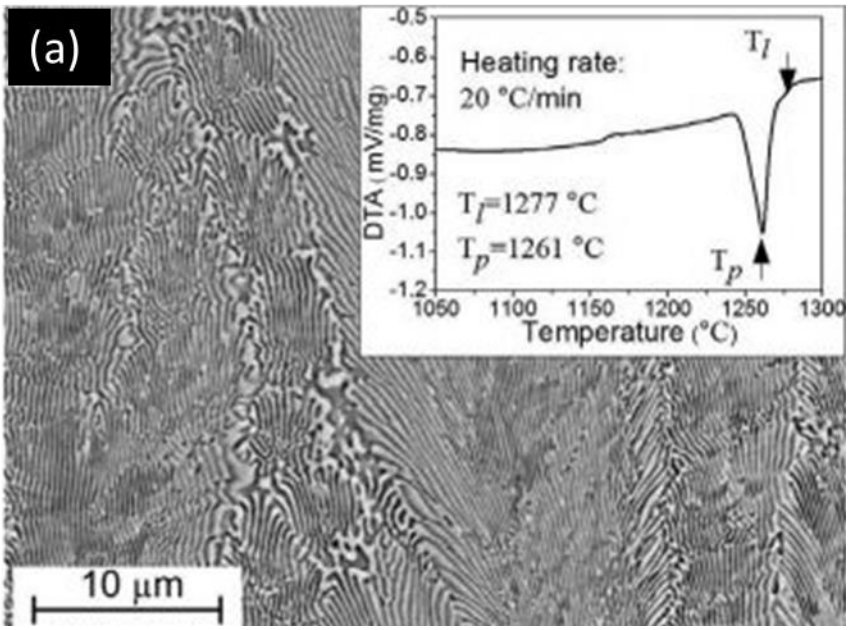

Figure 2.6 SEM micrograph and DTA for $CoCrFeNiNb_{0.5}$ HEA [80]

Guo et al. [10] reported the $CoCrFeMo_{0.8}Ni$ EHEA consisting of FCC solid solution phase and $Cr_9Mo_{21}Ni_{20}$-type intermetallic (as shown in **Figure 2.7a**). The alloy exhibits a compressive strength of 2200 MPa, plastic strain of 7.5 % and hardness of 610 HV. The fracture surface after

compression testing for EHEA reveals the quasi-cleavage type fracture (as shown in **Figure 2.7b**).

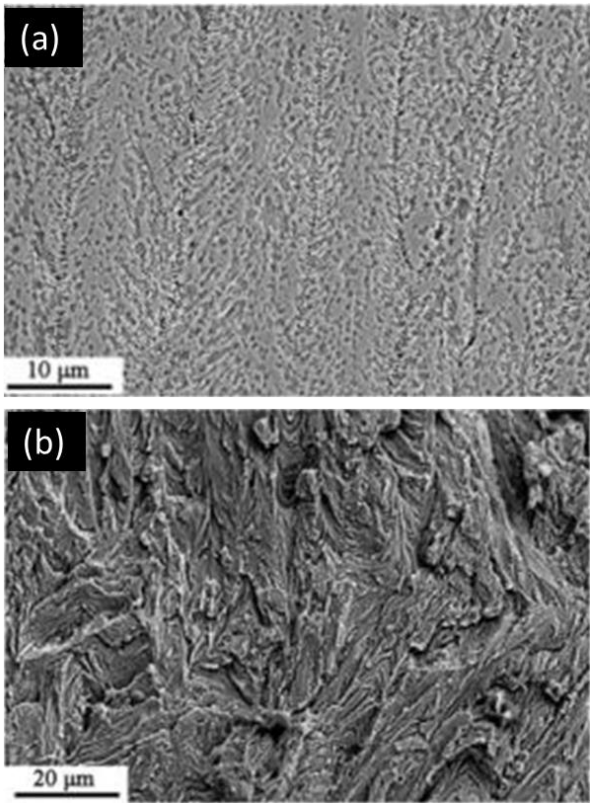

Figure 2.7 (a) SEM image of $CoCrFeMo_{0.8}Ni$ HEA as cast, (b) Fracture surface after Tensile testing [10]

Zhang et al. [81] developed the $Ni_{48.7}Co_{17.5}Cr_{10}Fe_{9.3}Al_{7.5}Ti_7$ and $Ni_{47.7}Co_{17.5}Cr_{10}Fe_{9.3}Al_{7.5}Ti_7Mo_1$ (at%) HEAs by combining the design concepts of HEAs and Ni-base superalloys. These HEAs consist of FCC solid solution phase and nano Ni_3(Al, Ti)-type intermetallics. The mechanical properties of $Ni_{47.7}Co_{17.5}Cr_{10}Fe_{9.3}Al_{7.5}Ti_7Mo_1$ HEA show a good combination of strength and ductility. It is found that the alloy exhibits a yield strength of 899 MPa, an ultimate tensile strength of 1064 MPa and a plastic strain of 14.3 %. Jiang et al. [82] investigated $CoCrFeNiTa_{0.4}$ EHEA and reported that the microstructure of EHEA reveals the presence of FCC solid solution phase and Co_2Ta-type Laves phases. It is found that the alloy system shows excellent fracture strength of 2293 MPa and plasticity of 22.6 % due to uniform lamellae structure.

Huo et al. [83] reported the $CoCrFeNiTa_x$ (x=0.1, 0.2, 0.3, 0.395, 0.4, 0.5, x value in molar ratio) EHEA consisting of CrFe-rich FCC solid solution phase and Ta-rich Laves phase. EHEA with

x=0.395 shows the good mechanical properties (i.e. yield strength of 1.4 GPa) which is due to the formation of dual-phase microstructure (SEM images of EHEA at x=0.395 is given in **Figure 2.8a** at low magnification, **Figure 2.8b** at higher magnification).

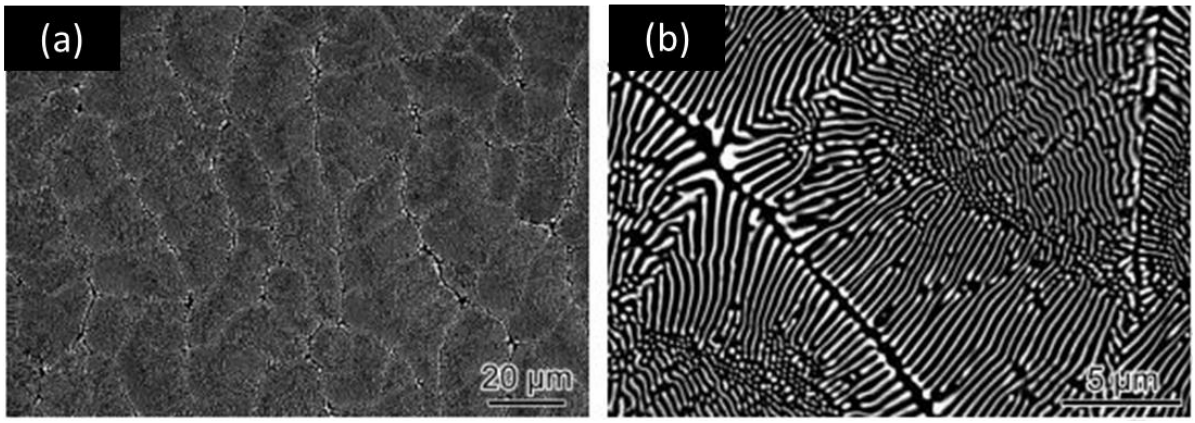

Figure 2.8 SEM images of EHEA at x=0.395 (a) low magnification (b) higher magnification [83]

Recently, Han et al. [84] reported a novel equiaxed EHEA consisting of FCC solid solution phase and C14 Laves phase and found the high strength as well as good ductility at a temperature up to 800°C, i.e. yield strength of ~800 MPa and tensile ductility of ~16%. It is observed that improved mechanical properties are largely due to the strengthening of the highly stable nano-scaled L12 precipitate and the ductility is attributed to the fine equiaxed Laves phase. **Figure 2.9a** shows X-ray diffraction (XRD) patterns of the gas-atomized powder, the as-extruded and different annealed EHEA samples, while **Figure 2.9b** shows the morphology of the gas-atomized powder and the particle size distribution (as shown in inset), **Figure 2.9c** show a cross-section view of the gas atomized powder, **Figure 2.9d, 2.9e** shows the microstructure of the as-heated and as-extruded EHEA. **Figure 2.10** shows the engineering stress-strain curves for the as-extruded and subsequently annealed EHEA alloy, tested at 800°C. It is to be noted that the strain-softening is not observed for all the samples.

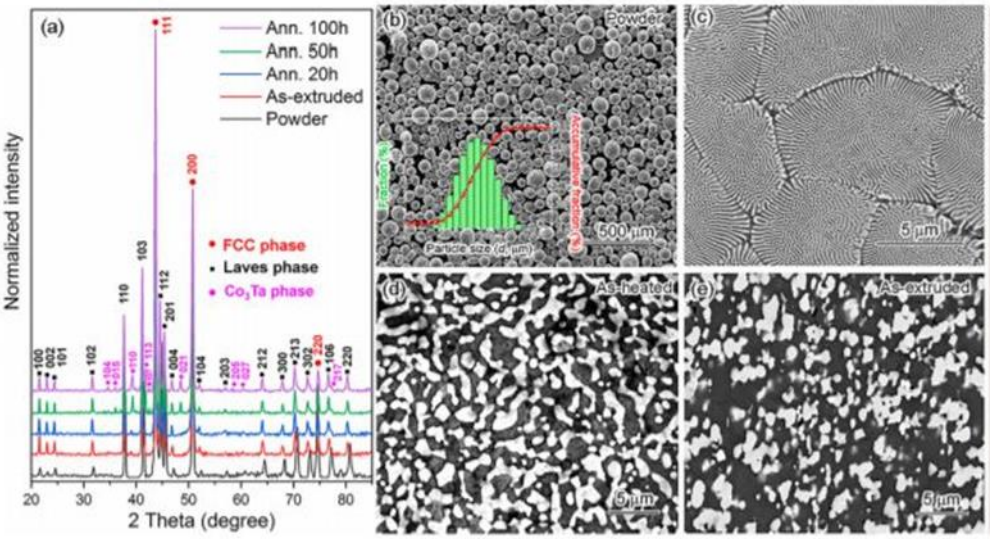

Figure 2.9 (a) show X-ray diffraction (XRD) patterns of the gas-atomized powder, the as-extruded and different annealed EHEA samples, (b) Morphology of the gas-atomized powder and the particle size distribution (inset), (c) Cross-section view of the gas atomized powder, (d) microstructure of the as-heated EHEA, and (e) as-extruded [84]

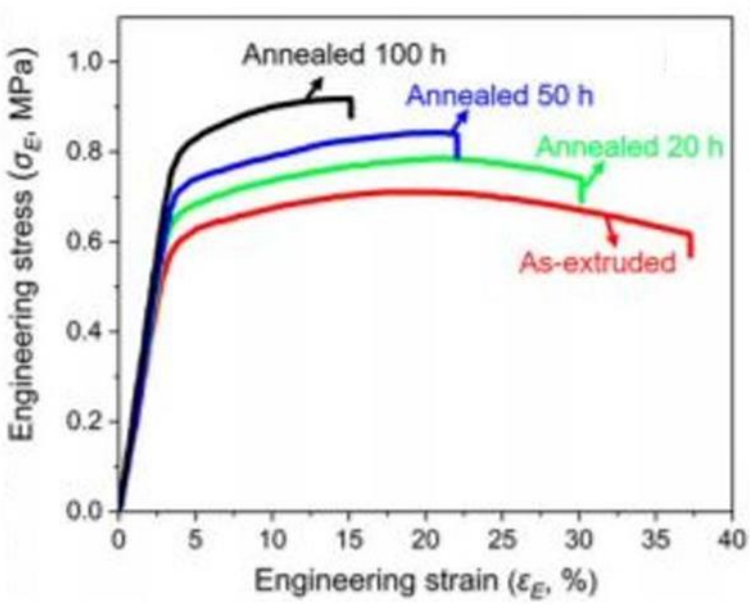

Figure 2.10 Engineering stress-strain curves for the as-extruded and subsequently annealed EHEA alloy tested at 800°C [84]

2.5.2 Microstructure and mechanical properties of (BCC + Intermetallics) EHEAs

Ma et al. [85] studied the AlCoCrFeNbx EHEAs which reveals the microstructure varying from hypoeutectic to hypereutectic, consisting of BCC solid solution phase, and (CoCr)Nb type Laves phase,. It is found that with the addition of Nb, the yield strength increases from 1373 MPa to 2473 MPa, whereas plastic strain decreases from 24.5 % to 4.1 %. The $AlCoCrFeNb_{0.25}$ EHEA shows 1959 MPa and 3008 MPa yield strength and ultimate strength, respectively, and fracture strain of 10.5 %. Samal et al. [86] developed the equiatomic CoCuFeNiTi EHEA, consisting of BCC (β) and FCC (α_1) solid solution phases as well as eutectic between FCC (α_2) and Ti_2(Ni, Co)-type Laves phase. It is found that the optimum hot workability conditions is identified in the temperature range T = 930°C – 990°C (1203 K-1263 K) and strain rate in the range of 10^{-3} s^{-1} – 10^{-1} s-1.

2.5.3 Microstructure and mechanical properties of (BCC + FCC) EHEAs

Yong et al. [87] studied the $AlCrFeMo_{0.2}Ni$ EHEA, consisting of FeCr-rich BCC solid solution phase, and AlNi intermetallic compound and EHEA exhibits 1487 MPa, 3222 MPa yield strength, and fracture strength, respectively. Lu et al. [9] reported the $AlCoCrFeNi_{2.1}$ EHEA having two alternating FCC and BCC lamella and observed good fracture strength and plastic strain at room temperature as well as elevated temperature. It is found that $AlCoCrFeNi_{2.1}$ EHEA shows good fracture strength (944 MPa) and plastic strain (25.6 %) under tension at room temperature. Further, the yield stress, fracture strength, and elongation are found to be 95 MPa, 806 MPa, 33.7% at 600 °C and 108 MPa, 538 MPa, and 22.9% at 700 °C, respectively. It is also reported that $AlCoCrFeNi_{2.1}$ EHEA shows better strength as compared to the NiAl-based eutectic alloys atleast up to 700 °C. The $AlCoCrFeNi_{2.1}$ EHEA shows a lower density (7.38 g/cm^3) over Ni-based superalloys (8.0 g/cm^3). Therefore, low density EHEA can be considered as potential candidates for high-temperature applications.

Li et al. [88] studied the AlTiCrxFeCoNiCu (x: molar ratio, x = 1.0) EHEAs, fabricated by vacuum arc melting technique and reported that HEAs consist of three phases, i.e., two FCC and BCC solid solution phases. EHEA consists of FCC (Ni, Al, Ti, Co) -rich (α) solid solution phase and BCC (Cr, Fe)-rich (β) solid solution phase, showing the compressive strength of 1.42 GPa, and elongation of 5.68 %. Rahul et al. [89] investigated the hot deformation behavior of

$AlCoCrFeNi_{2.1}$ EHEA having FCC (CoCrFe-rich) solid solution phase and BCC (NiAl-rich) solid solution phase. The XRD plot and electron microscopy (SEM and TEM) micrographs of as-cast alloy is presented in **Figure** 2.**11**. The hot deformation behavior of that alloy at a temperature range of 800-1100 °C and the strain rate range 10^{-3}-10 s^{-1} is represented in **Figure 2.12**.

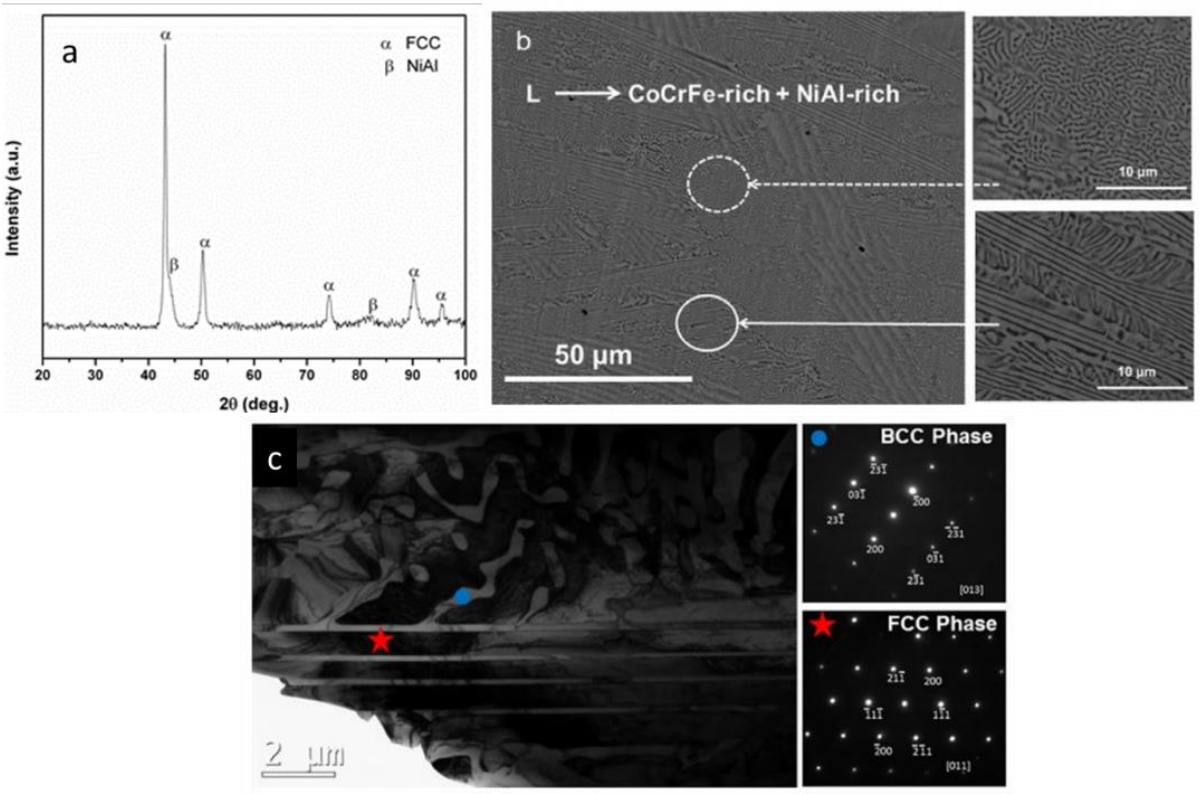

Figure 2.11 (a) XRD plot (b) BSE-SEM micrographs (c) TEM analysis of $AlCoCrFeNi_{2.1}$ EHEA [89]

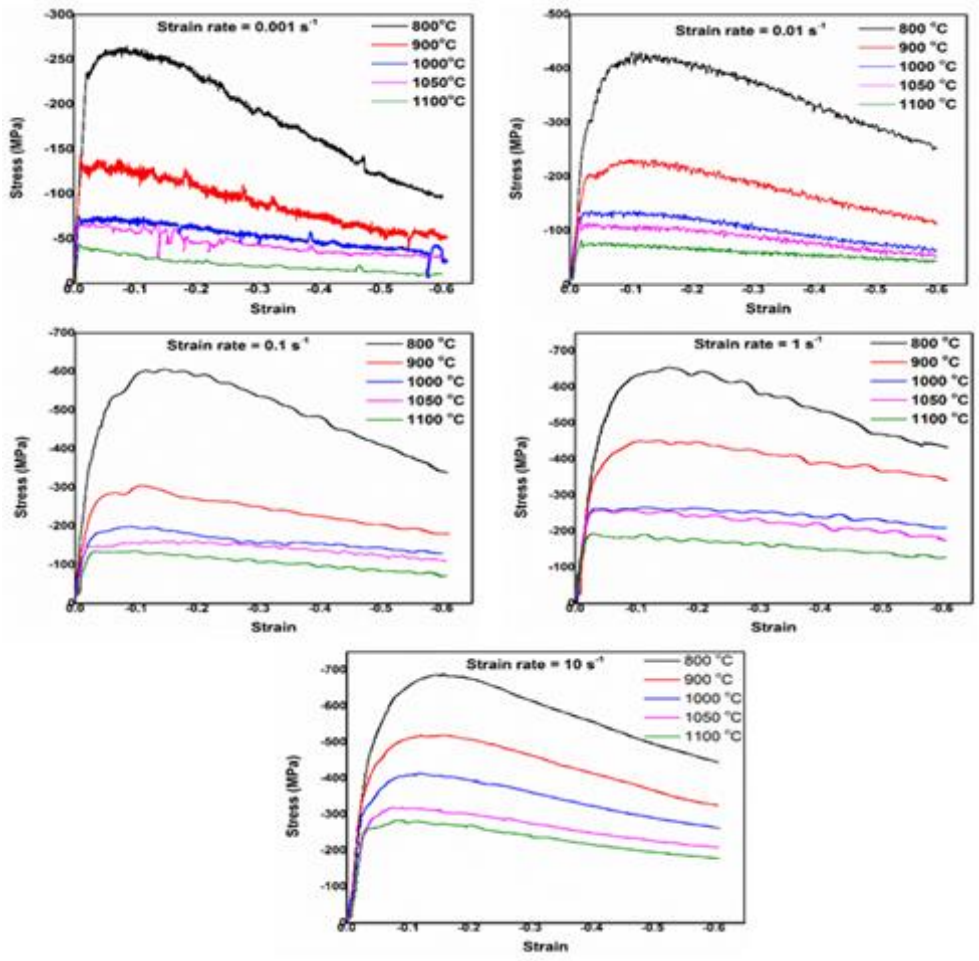

Figure 2.12 Flow curve (true stress-true strain plot) at different hot working conditions for $AlCoCrFeNi_{2.1}$ EHEA [89]

Tang et al. [61] studied the AlCoCrFeNi HEA using two processes such as (i) as-cast, and (ii) hot isostatic pressing (at pressure 207 MPa and temperature 1100°C) for 1 hour and annealed at 1150 °C for 50 hours. The studied alloy consists of nano-lamellar morphology between the BCC ordered and disordered phases. Co-free $AlCrFe_2Ni_2$ EHEA is reported by Dong et al. [90], showing the FCC (FeCr-rich) solid solution phase with noodle-like structure and BCC (NiAl-rich) solid solution phase with spinodal microstructure. The yield strength, ultimate strength, and plastic strain of EHEA at room temperature is found to be 796 MPa, 1437 MPa, and 15.7 %, respectively.

Wani et al. [91] reported the $AlCoCrFeNi_{2.1}$ EHEA in as-cast conditions as well as at different thermomechanical processing conditions and observed that there is tremendous gain in mechanical properties in the different thermomechanical conditions. It is found that EHEA

exhibits 620 MPa yield strength, 1050 ultimate strength and plastic strain 17 % at as-cast state respectively, while after 90 % cold-rolled condition, the yield strength and ultimate tensile strength of thermomechanical processed EHEA is found to be 625 MPa and 1800 MPa respectively with plastic strain 6 %. Lee et al. [92] reported the $Al_{0.5}CoCrFe_{0.5}NiTi_{0.5}$ EHEA having FCC solid solution phase and BCC solid solution phase with ordered and ordered phases and the alloy shows the yield strength of 1659 MPa, compressive strength of 2240 MPa, and failure strain of 11 %. Ma et al. [93] reported the $AlCrCuFeNi_2$ EHEA having the eutectic microstructure consisting of FCC FeCr-rich solid solution phase and BCC AlNi-rich ordered phase. It is observed that EHEA shows the yield strength of 855 MPa, the fracture strength of 2123 MPa, and failure strain of 30 % at a strain rate of 1×10^{-3} s^{-1}. Shukla et al. [94] studied the fatigue behavior of $AlCoCrFeNi_{2.1}$ EHEA and observed that fatigue stress increases from 390 MPa (as-cast condition) to 500 MPa (rolled specimen with 50 % of the initial thickness and heat-treated at 700 °C for 12 hours) up to 10^7 cycles. Wang et al. [95] studied the friction stir processed $AlCoCrFeNi_{2.1}$EHEA and observed the refinement of the grains after processing and also the coarse lamellar eutectic structure in the as-cast condition is transformed into the ultrafine-grained structure. After processing, the mechanical properties of studied alloys are also improved i.e., the ultimate tensile strength increases from 1000 MPa to 1360 MPa and plastic strain from 6.5 % to 10 %.

Hu et al. [96] performed the ceramic rolling (Al_2O_3 granules act as pressure transmission medium during the cold rolling up to 23.06 % reduction in thickness) and annealing (400 °C and 800 °C) on $AlCoCrFeNi_{2.1}$EHEA. After cold rolling, the yield strength, the compressive strength increases from 557.09 MPa to 1611 MPa, 1747.66 MPa to 2212.99 MPa respectively, while plastic strain decreases from 34 % to 28.6 %. It is observed that the EHEA with cold rolling and annealing at 400 °C shows the yield strength, compressive strength, and plastic strain 1330.12 MPa, 2055.46 MPa, and 33.72 % respectively. Furthermore, EHEA with cold-rolling and annealling at 800 °C shows the yield strength of 102840 MPa, compressive strength of 1900.73 MPa, and plastic strain 38.54 % respectively. It is concluded that the strength of EHEA is improved due to the formation of multiple shear bands and uniform distribution of residual stress during the secondary processing.

Furthermore, Y lu et. al. [97] reported large scale eutectic and near-eutectic AlCoCrFeNix (x = 2.0, 2.1 and 2.2) EHEAs having L12 FCC and BCC B2 phases. The tensile test of EHEAs shows good combination of ductility and strength at different compositional and temperature ranges. The excellent ductility is attributed to dislocation motion in the soft FCC phase, while good strength is due to a pile-up of dislocation in FCC/B2 phase boundaries.

2.5.4 Microstructure and mechanical properties of others type EHEAs

Rogal et al. [98] developed equiatomic $Nb_{25}Sc_{25}Ti_{25}Zr_{25}$ EHEA consisting of the nano-scale lamellar eutectic between α(Sc, Zr) HCP plates and β-NbZrTi with BCC phase. The balanced mechanical properties in terms of strength and ductility is observed due to dual-phase formation. The value of hardness, yield strength, compressive strength and plasticity are found to be 418 HV, 1020 MPa,1250 MPa and 8.2 %, respectively.

Rogal et al. [99] reported the Sc-Ti-Zr-Hf-Re dual-phase HEA having HCP and BCC phase with ω nanoprecipitates and alloy, showing the high compressive strength and good ductility of 1910 MPa and 8%, respectively. Tiwary et al. [100] reported the possibility of development of high-strength structural engineering materials using EHEAs based upon the yield strength vs. ductility plot of the available alloys of EHEAs (given in **Figure 2.13**).

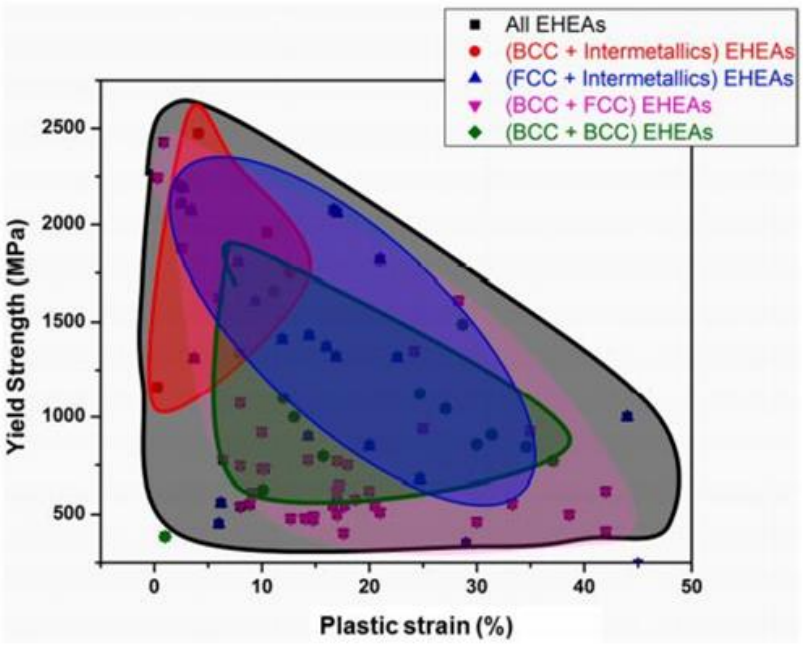

Figure 2.13 Yield strength vs. plastic strain plot for different HEA [100]

Chanda et al. [101] summarized the mechanical properties (yield strength and plastic strain) of stainless steel, bulk metallic glass, and other conventional alloys and also compared with eutectic alloys (as shown in **Figure 2.14**). It is reported that the mechanical properties of nano or ultrafine eutectic depend on the length scale of eutectic colony and heterogenous crystalline phases.

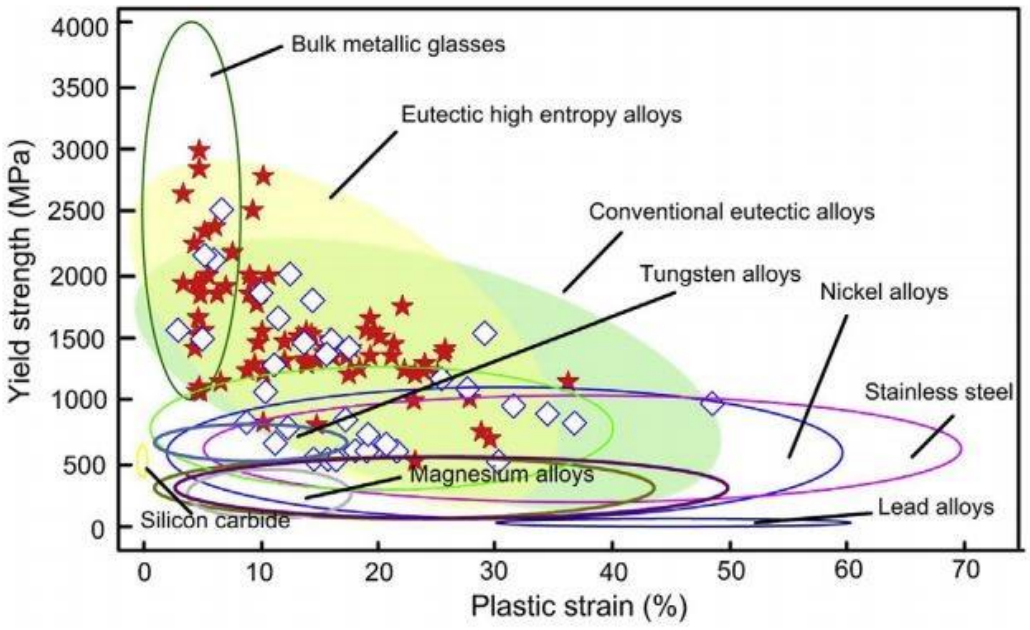

Figure 2.14 Mechanical properties (yield strength and plastic strain) of conventional alloys and eutectic alloys [101].

2.6 Materials modeling for hot deformation study:

Manufacturing processes like rolling, extrusion, forging, and other bulk deformation processes are conducted at a temperature of more than 0.6-0.7 T_m (T_m= Melting Point of material), which are associated with large strain and high strain rate during the thermomechanical processing, and microstructural changes. So, the flow instability during the hot deformation of materials is important to understand to get defect-free microstructure (micro or macro defect) of the final product. Therefore, different material modelling techniques are helpful to study the hot deformation behavior of materials to predict the following: (1) microstructural evolution during the processing of materials, (2) optimum process parameters, and (3) manufacturing environment effect on the materials. The different modeling techniques are available for analysis of the deformation mechanism available such as (1) kinetic model, (2) atomistic model, and (3)

dynamic materials modeling (DMM) and others [102][103]. A brief discussion of the above models is given below.

(1) Kinetic model:

Steady-state flow stress (σ) is a function of temperature (T), strain (ε) and strain rate ($\dot{\varepsilon}$) for the particular material through constitutive relation, which can be written in the functional form as $\sigma = f(T, \varepsilon, \dot{\varepsilon})$. The activation energy (Q) and stress exponent (n) parameters are derived by using experimental data [89][104].

The activation energy (Q) is a strain rate and a temperature-dependent physical parameter that is typically used to understand the thermomechanical process such as rolling, extrusion, forming, and forging for any type of materials [105][106][107]. It also provides important information about dislocation movement, dynamic recovery (DRV), dynamic recrystallization (DRX), movement of the grain boundary, and deformation mechanism, which is associated with the microstructural evolution during the hot forming process [108][109]. Zener-Holloman parameter (Z), which is also known as temperature compensated-strain rate [20] and constitute equation for activation energy (Q), can be written as:

$$Z = A \times [\sinh(\alpha\sigma)]^n = \dot{\varepsilon} \times \exp\left(\frac{Q}{RT}\right) \quad (2.1)$$

$$\dot{\varepsilon} = A \times [\sinh(\alpha\sigma)]^n \times \exp\left(-\frac{Q}{RT}\right) \quad (2.2)$$

Where $\dot{\varepsilon}$ is strain rate (s^{-1}), Q is the hot deformation activation energy (J/mol), R is the universal gas constant 8.314 J/mol-K, T is the temperature in K, σ is flow stress (MPa), and A, α, and n are materials constant.

Therefore, it is of great significance to investigate the hot deformation behavior of HEAs under hot processing conditions. The activation energy (Q) is used mainly to find the predominant mechanism during hot deformation [105][109][110]. Hence, several reports have been devoted for calculating activation energy for the hot deformation of different alloys. Because activation energy depends on the resistance to plastic deformation, which is estimated by using different flow equations involving the response of flow stress,

deformation temperature, and strain rate [109]. It is reported in the literature [109] that the addition of minor elements such as Nb, V and Ti etc. in the commercial alloys increases the activation energy. In the present study, the non-equiatomic HEAs is designed to contain some minor element(s) and the increase in the activation energy of the system is perhaps expected and hence can be used for thermomechanical processing of materials at high temperature. Reyes-Calderón et al. [111] also found that the activation energy of the different multicomponent alloy systems is controlled by the mechanism of dynamic recovery (DRV) and dynamic recrystallisation (DRX). This model is valid over a narrow range of temperature and strain rate. The kinetic model cannot give detailed information about microstructural changes during the hot deformation processing of materials for a wide range of temperature and strain rate.

(2) Atomistic model (Raj maps):

Atomistic model is proposed by Raj et al. [112], which describes the microstructural changes during the hot processing of materials and also represents limiting conditions of temperature and strain rate for the safe processing of materials without microstructural damage during the hot working of materials. Four different criteria are highlighted in Raj maps: (1) at lower temperature and higher strain rate, void formation occurs at hard particles, (2) at a higher temperature and lower strain rate, wedge cracking is observed at grain boundary triple junction, (3) at very high strain rate, adiabatic shear band formation is observed, and (4) at higher temperature, dynamic recrystallization occurs. Out of the four conditions mentioned above, only the fourth criterion is considered as the safe processing condition for hot working of material. This map does not provide the optimum processing conditions in large domain domains.

(3) Dynamic materials model (DMM):

Prasad et al. [113] first developed the DMM model, and the model is based on the continuum mechanics of large plastic flow, physical system modeling, thermodynamics for the irreversible system. The DMM model describes the dynamic behavior of materials and microstructural evolution during the hot processing of materials. In this model, the workpiece has the following different characteristics, such as (1) Dissipative (dissipate the energy

during the hot working of process and does not store energy), (2) Dynamic (at given temperature, change in the strain rate and small extent of strain), (3) Non-linear (flow stress is non-linear due to change of temperature, strain rate and strain), (4) Away from the equilibrium (at high-temperature, large plastic flow takes place) and (5) Irreversible (microstructure of workpiece changes due to the large plastic flow at high temperature).

(4) Activation processing maps:

In this model, the activation energy is a function of temperature and strain rate. In general, activation energy maps are combined with stability maps. Those maps having different criteria, based on the Lyapounov functions are given below [114]:

(1) 0<m<1: Material will be no more dissipator of the energy. The increasing value 'm' implies the reduction of the flow localization and also leads to superplasticity.
(2) $\dot{m} < 1$: This parameter is defined as the change of strain rate sensitivity with respect to strain rate. a catastrophic fracture occurs if the value of $\dot{m}$ is positive.
(3) $S>1$: For an irreversible process, entropy production should always be positive. According to that criterion, high-temperature dependence flow stress has flow stability, while low-temperature dependence flow stress has flow instability.
(4) $\dot{S} < 1$: Stable flow occurs if temperature dependence flow stress decreases with increasing the strain rate. This criterion also defines the flow localization due to adiabatic heating.

The processing map provides information about optimum deformation conditions for identifying the hot working domains [102]. The dynamic material model (DMM) methodology has been utilized to develop the processing map of the investigated multicomponent HEAs during the thermomechanical processing [102][113], which helps to understand the hot deformation flow behavior. Results obtained through generating the processing maps are correlated with a microstructure of deformed samples. It is important to note that the processing map predicts the flow instability and regimes for safe processing. In general, the hot working processing of materials falls in the temperature range of 0.6-0.8 T/T_m and strain rate range of 0.001- 100 s^{-1}. Safe and unsafe zones during the hot working processing of materials are dependent on several atomistic mechanisms. The high-temperature processing of materials is mainly associated with the following mechanisms: (1) dynamic recrystallization, (2) superplastic deformation, (3)

adiabatic shear band formation, flow localization, (4) wedge cracking, and (5) crystalline cracking. From the above mechanism of hot deformation, dynamic recrystallization is a safe process, superplastic deformation under controlled conditions is also safe, while all the remaining processes are considered as unsafe and hence should be avoided for developing the good product.

During the thermomechanical processing of materials, defects have been observed under certain processing conditions. These defects make the material thermodynamically unstable. But during the high-temperature deformation of materials, these defects needs to be removed which is related to thermodynamically activated process [115]. By recovery phenomena, the microstructure is restored to some extent. If recovery is taken place by annealing, this is known as static recovery, while if recovery is taken place by deformation, then this is known as dynamic recovery. Store energy within the materials is the driving force for recrystallization. Recrystallization is a process in which the new grains form due to the lattice strain and crystalline imperfection during the deformation. Similar to the recovery process, there are two types of recrystallization: static and another is dynamic. The factor influencing the DRX are stacking fault energy, initial grain size, thermo-mechanical processing parameters (deformation temperature and strain rate), and second phase particle. It is to be noted that the hot deformation behavior of HEAs at different temperatures and strain rates are investigated, so it is helpful to understand how the thermomechanical processing parameters affect the DRX. In general, if the processing temperature is high and the strain rate is low, multiple peaks are observed in the flow curve (stress-strain curve), while in the opposite case (low temperature and high strain rate) single peak in flow curve is observed. Apart from that, strain hardening and softening processes occur during the hot deformation of alloys. The strain hardening is observed due to the increase in dislocation density because of the external load and dislocation interaction (dislocation pile-up). The softening was observed in the alloys due to a decrease in the dislocation density and redistribution of the dislocation (vacancy climb, formation of nuclei, and nuclei growth by migration of large-angle grain boundary) [116][117][118]. Microstructural evolution during the dynamic recovery and dynamic recrystallization is represented in **Figure 2.15** [119].

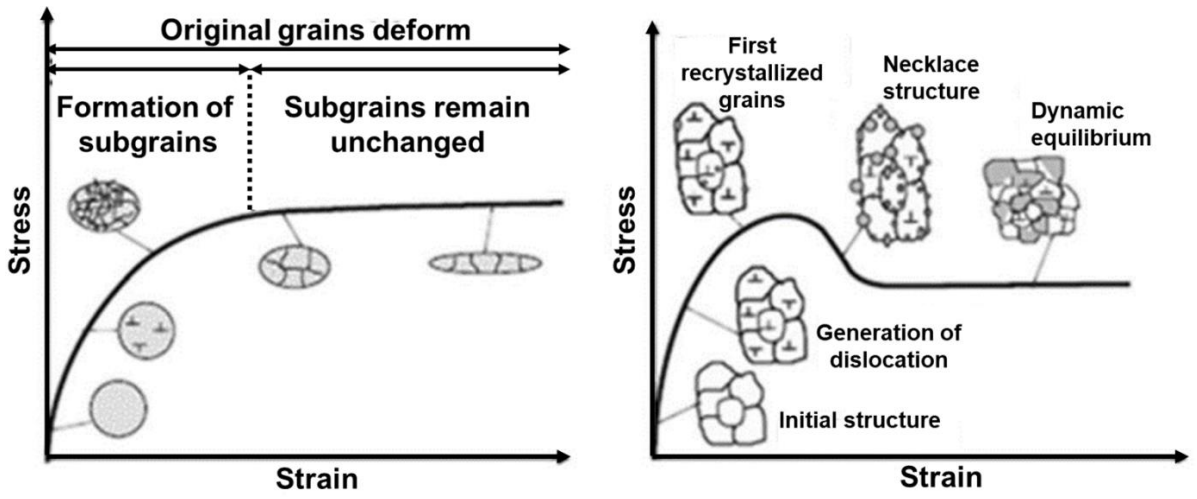

Figure 2.15 Microstructural evolution during the dynamic recovery and dynamic recrystallization [119]

Conventionally, DR process is associated with copper and nickel due to their low stacking fault energy (SFE) during hot deformation. These metals show flow softening behavior after reaching the critical strain. At large strain, the flow curve reaches a steady-state, while oscillation in the flow curve is observed at lower strain rates. DR process is also understood by the nucleation and growth model, proposed by Luton and Sellars [120], and that model considers both hardening (due to dislocation formation) and softening (due to grain boundary motion) effect. The microstructure observation of different models may not be the same as an actual dynamic condition due to the post deformation recrystallization during colling. The existing DR domain may be different from those conditions where the microstructures are being observed. To design the bulk material working process, modeling the constitutive behavior of materials and optimum processing conditions for the different mechanisms are useful. Here, the optimization of hot working parameters and control of microstructure during processing are the main aspects during thermomechanical processing of materials. The constitutive modeling of materials is very sensitive to the initial conditions such as alloy composition, initial microstructure, and thermomechanical processing conditions [102]. In the literature, it is found that the DR is an essential mechanism for bulk metalworking. All aspects of this mechanism help in studying the hot deformation, including optimum conditions under which it occurs, strain dependence on DR, and microstructural changes during DR [116][115]. The range of strain rate and temperature explain either the flow of materials is stable or unstable during the processing. At higher strain rates, the processing is done under the non-isothermal condition, and in this situation, the contact

between the workpiece and die is very small. On the other hand, isothermal processing is required if the temperature range is narrow for DR or the strain rate is slow, and the material has a large domain of instability [121]. Rahul et al. [89] generating the processing maps using the DMM model for $AlCoCrFeNi_{2.1}$ EHEA with different modeling parameters to understand the hot workability of material at different thermomechanical conditions. The processing maps for EHEA at different modeling parameters is represented in **Figure** 2.**16**. It is concluded that the EHEA exhibits stable plastic flow in the range 1073-1150 K and 10^{-3}-$10^{-2.2}$ s^{-1} as well as 1338-1373 K and 10^{-3}-$10^{-1.2}$ s^{-1}.

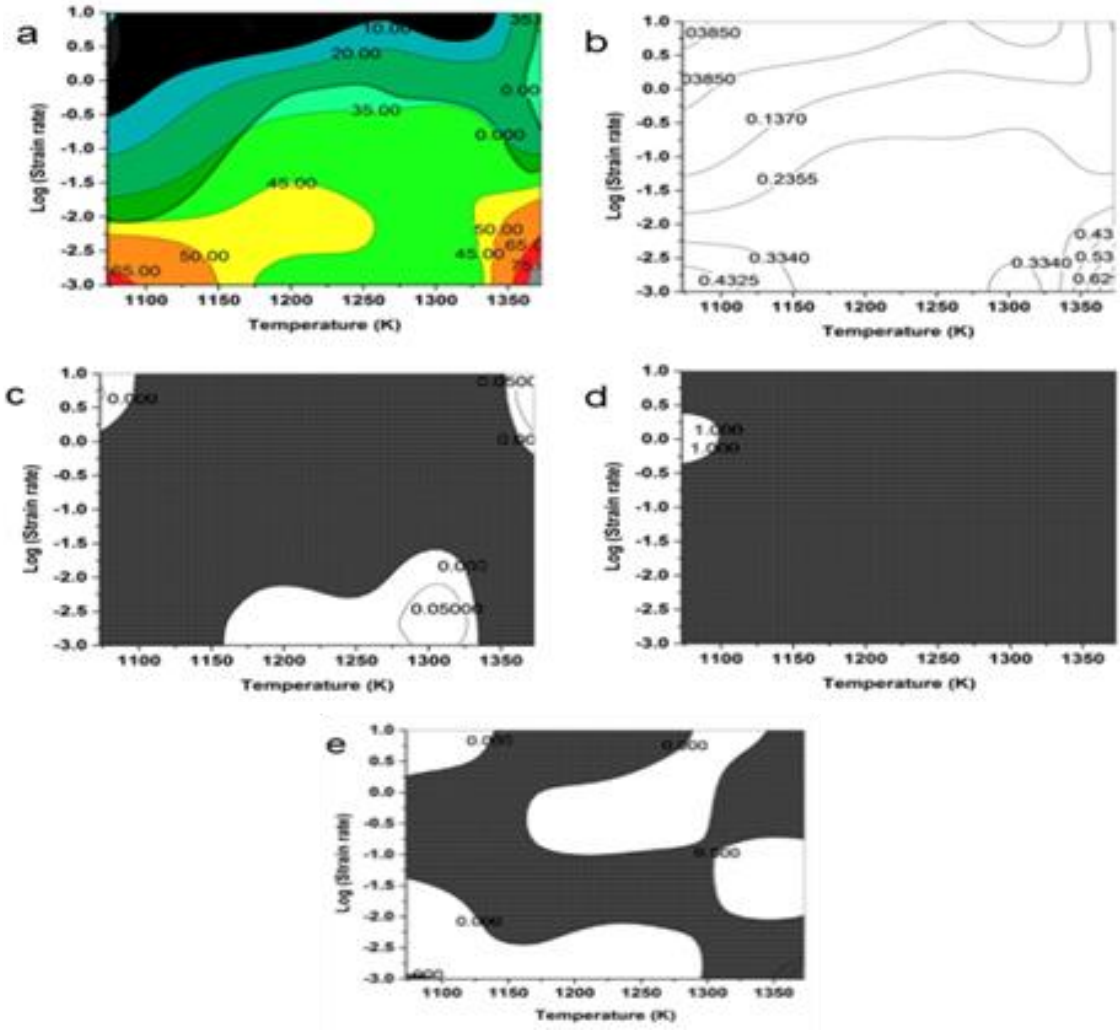

Figure 2.16 Processing maps of $AlCoCrFeNi_{2.1}$ EHEA at strain 0.65 [89]

2.7 Artificial Neural Network simulation approaches for prediction of the mechanical properties for HEAs

An ANN is a computational approach that collects the information by adaptive learning from the external source and is available for use to predict the properties of materials. A neural network consists of an interconnected layer, and that layers contain a small unit known as neurons with a parallel weighted connection [122]. The network has three kinds of layers such as input layers, hidden layers, and output layers. ANN is a non-linear statistical method to use for the simulation of systems that are difficult to be explained by a conventional model [123]. In the ANN technique, finding out the optimum network structure is one of the challenging tasks. Usually, this step can be completed by trial and error method by several iterations of datasets. The prediction of phases, as well as properties, is crucial for the development of HEAs. Few prediction approaches such as ab-initio, Molecular dynamics (MD) simulation, (density functional theory (DFT), and Calculation of Phase Diagram (CALPHAD) are very known. Machine learning is a computational approach that collects information by adaptive learning from an external source and is useful to predict the properties of materials. Machine learning algorithms are the program that can learn the hidden pattern from the input data, and predict the output and hence enhances the predictability from experiences on their own. The machine learning algorithm can be classified into three basic categories 1) supervised learning algorithm includes regression, decision tree, random forecast and classifier (KNN, Tress, Logistic regression, Navie-Bayes, SVM), 2) unsupervised learning includes clustering (SVD, PCA and K-means), association analysis, and 3) reinforcement learning algorithm. Apart from that, the artificial neural network (ANN) algorithm is also used for prediction [123].

Activation functions play an essential role in the ANN technique to obtain the exact output by applying some extra effort in input data. Some activation functions are given below; (1) Linear activation function, (2) Sigmoid activation function.

One of the most popular algorithms in the field of a neural network to solve the problem is back propagation (BP) neural network and the schematic is given in **Figure 2.17** which shows the arrangements of a layer of a BP neural network with one input layer, one hidden layer, and one output layer. The input layer first provides each nodes input pattern, then the signal is converted in each node and transferred to the hidden layer. Further, in the output layer, output

signals are generated, and output values are compared with the set values. If output values do not match the set values, then connection weights are adjusted to minimise the error. Each node in a hidden layer and output layer acts as a summing junction that combines and altered the earlier layers inputs. The summation from each node to the output of the node is transferred by suitable sigmoid function [124][125][126].

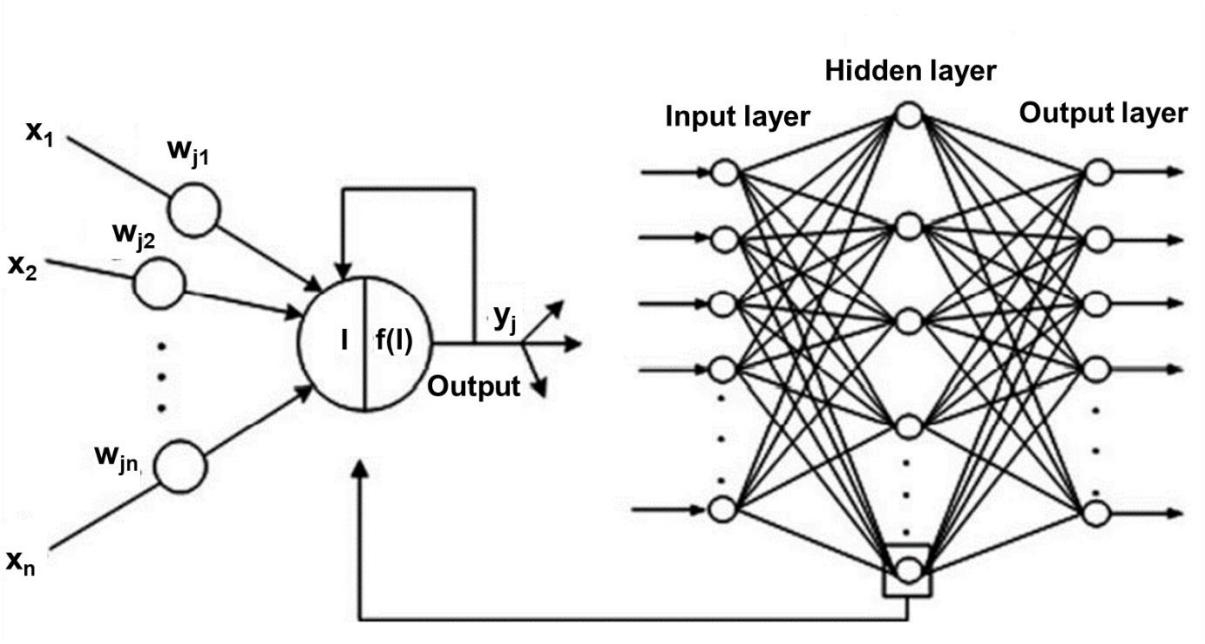

Figure 2.17 Model processing and structure of the neural network [126]

$$y_i = \sum_j x_j w_{ij} + b_i \qquad (2.3)$$

$$z_i = \frac{1}{1+exp(-y_i)} \qquad (2.4)$$

Where $y_i$the total input of the ith node in the layer, $w_{ij}$is the weight from the jth to ith neurons, $b_i$is the threshold of the ith neuron, $x_j$is the inputs of the ith neuron and z_i is the output of the jth neuron. Hagan et al. [127] modified the equation by updating the weight in momentum learning is given as:

$$w_{ij}(n+1) = w_{ij}(n) + \eta\delta_i x_j + \alpha\Delta w_{ij}(n) \qquad (2.5)$$

Where w_{ij} is the weight between nodes i and j at iteration n is discrete-time, η is the learning rate, $\delta_i$difference between the actual and predicted values, and α is momentum value between 0.1 to 0.9. The network error after the activities of all the output node has been calculated, which is described by

$$error = \frac{1}{2}\sum_j [x_j - t_j]^2 \qquad (2.6)$$

Where $x_j$is the activity level of all the jth units in the last layer, $t_j$is the desired target output of the j[th] unit.

Huang et al. [128] used a machine learning approach for predicting the formation of a solid solution and intermetallics in HEAs with an accuracy of 70 %. Agrawal et al. [129] predicted the FCC and BCC solid solution phase in HEAs based on elemental composition and thermodynamics parameters. Nusrat et al. [130] predicted the applicability of ANN for phase prediction in multi-principal element alloys with an average predictive accuracy of ~80% with 118 compositions as a data set. Recently, Dixit et al. [131] used ANN approach to predict the phases in HEAs based on the elemental composition, processing route and thermodynamic parameters with an accuracy of 87 %. In this model, the accuracy is calculated using the Hammering score, known as label-based accuracy hammering accuracy which is calculated by using following equation.

$$A = \left[1 - \frac{1}{|N|.|L|}\sum_{i=1}^{|N|}\sum_{j=1}^{|L|} XOR(y_{i,j}, z_{i,j})\right] \times 100 \qquad (2.7)$$

Where A= Accuracy, N= Number of examples, L= Number of levels, y= actual levels, z= predicted levels.

But the scope of all independent reported research works is limited to predict the phases with good accuracy and mechanical properties of HEAs at room and elevated temperature. From the literature, the following challenges remain to fully utilize that approach for practical applications such as optimization of the neural network, data shortage problem should be taken into account when using the ANN approach, in which input parameters largely contribute to the decision of the given model. It is to be noted that multiple machine learning algorithms are useful for

predicting phases and mechanical properties at room and high temperatures. The performance of machine learning algorithms is verified with the experimental and another prediction methods.

Ji et al. reported [20] that the hot deformation behavior of aermet 100 steel is predicted using the ANN model in the temperature from 800°C -1200°C and the strain rate from 0.01 s^{-1} to 50 s^{-1}. Raj et al. [132] reported the prediction of compressive properties (plateau stress, Young's modulus and energy absorption capacity) of closed-cell aluminum foam using the ANN approach using the input variables such as relative density, average pore diameter and cell anisotropy ratio, and found that predicted results are in good agreement with experimental data. Paliwal et al. [133] reviewed the comparative studies on ANN and conventional statistical approaches for prediction and classification in the several fields of applications and pointed out that it is possible to handle any non-linear mathematical problems using ANN approach over the statistical method. Furthermore, the ANN modeling technique has been widely used for prediction of mechanical properties in different alloy systems [134][135] such as titanium alloys [136], cast iron [137], PTFE based fiber-reinforced composites [138]. Hence, the ANN-based model can effectively simulate various input-output databases and anticipate the complex materials science problem.

2.8 FEM simulation

The finite element method (FEM) is a mathematical tool that is widely used for engineering applications in the field of solid mechanics, fluid mechanics, and heat transfer etc. FEM is used to solve the physical problem in engineering analysis and design, which involves the structural component subjected to an external force. FEM provides the approximation solution to a mathematical model because the idealization of physical to a mathematical model requires a certain assumption. While the FEM is the numerical method, it is necessary to assess the solution's accuracy. If the solution accuracy is not met with the desired accuracy, further modification is required. For better accuracy, the numerical solution has to be repeated with the variation of the solution parameter. The FEM simulation can be used to identify the bulk deformation characteristics by identifying the strain, stress and strain rate fields in the material. By utilizing this capability, the more sensitive zones in material flow regions with complex geometries can be identified in actual industrial production conditions. The FEM simulation is useful for better understanding the hot deformation behavior, plastic strain field distribution,

material flow behavior during thermomechanical processing of the material. The macroscale simulation will help to identify the stress concentration points in complex geometries in actual forging conditions. Rahul et al. [89] investigated the hot deformation simulation study of $AlCoCrFeNi_{2.1}$ EHEA using the FEM analysis to understand the plastic strain distribution and material flow behavior.

2.9 Current and potential applications of HEAs

It is worthy to mention that HEAs are used as structural and functional materials, and their potential applications are given below:

(i) HEAs are used as filler materials for welding of different materials such as pure titanium and chromium-nickel-titanium stainless steel, cemented carbide and steel, respectively [6].

(ii) Due to the good irradiation and corrosion resistance of HEAs, HEAs are considered as a potential candidate for the cladding materials in nuclear fuels and high-pressure vessels [139].

(iii) HEAs are used as coating materials due to their excellent heat resistance or wear resistance properties. It is also observed that HEAs coatings are more uniform and well cohesive with substrate material [140].

(iv) Carbides and nitrides of HEAs are used as biomedical coatings and usable as diffusion barriers and hard coatings tool cutting steel. HEAs are also useful in the electronics industry due to constant resistivity [141][142].

(v) **Gas storage and sensing:** Kao et al. [143] reported the CoFeMnTiVZr HEA having the C14 Laves phase, absorbs and desorbs 1.6 wt% of H_2 at room temperature. The high entropy effect promotes the formation of the single Laves phase, and observed that the H_2 storage capacity is closely correlated with the enthalpy formation of H_2 and HEA. For practical applications, sensing of H_2 is also important due to the problem of H_2 gas leakage. Shalberg et al. [144] reported the TiVZrNbHf HEA and observed that material absorbs a large amount of H_2 with a H/M ratio of 2.5. The H/M ratio for that alloy system is similar to that of rare-earth alloy.

(vi) **HEAs as thermocatalysis**: Yao et al. [145] reported the PtPdRhRuCe HEA nanoparticles, prepared by carbothermal shock (CTS) synthesis and applied in ammonia oxidation.

(vii) **HEAs as shape memory alloys (SMAs)**: To improve plastic deformation ability of conventional alloys, alloys should have characteristics of shape memory feature. Stress-induced martensitic transformation (SIMT) and mechanical twinning are the effective way to improve the plastic deformation ability. Lee et al. [146] reported the non-equiatomic CrMnFeCoNi HEA with shape memory feature at elevated temperature. That alloy system shows heat and stress-induced martensitic transformation between FCC and HCP solid solution phases. It is also found that the shape memory recovery temperature of that alloy system is 698 K, which is better than conventional SMAs. Piorunek et al. [147] reported that the maximum shape memory strain is about 15 % for NiCuPdTiZrHf high entropy SMA (HE-SMA). The above result shows that the HEAs can be considered as one of the possible materials for high-temperature actuator.

2.11 Motivation of thesis:

A critical analysis of the available literature on developing novel HEAs for high-temperature applications indicates that the microstructure in HEAs consisting of quasi-peritectic having peritectic and eutectic mixture, and quasi-peritectic with two eutectics have not been explored. The design of these alloys with a combination of hard and soft phases will be promising for high-temperature applications. While developing any alloy, it is necessary to identify the hot workable region and high-temperature properties. Furthermore, higher-order eight component EHEAs have not been reported in the open literature, and artificial neural network (ANN) analysis for predicting mechanical properties of EHEAs has not been investigated so far. Furthermore, study related to the prediction of hot deformation behaviour using the different models (phenomenological, physics-based, and ANN-based model) for HEAs is also limited. It is to be noted that limited study has been reported on the deformation mechanism during the hot deformation of different class of HEAs.

Chapter 3

Experimental Details and Methodology

This chapter deals with experimental methodologies which is associated with the preparation of high entropy alloys (HEAs). Also, the experimental strategy to design and develop the HEAs and get the desire goals are summarized in the flow chart.

3.1 Materials

High purity elemental Al, Co, Cr, Fe, Mn, Nb, Ni, Ti, V, and Zr (purity level ≥ 99.7) were used as starting material.

3.2 Fabrication of HEAs:

The different HEAs were prepared by vacuum arc melting (VAM) cum suction casting technique in our project. The alloys were melted at least five times to get chemical homogeneity. The VAM unit consists of mainly (i) vacuum unit, (ii) welding unit, and (iii) chiller unit.

Vacuum unit

In a vacuum chamber, the vacuum is generated with a turbo-molecular and roughing pump to obtain a pressure of about 10^{-6} Torr. The switches used in it are pneumatic control, powered by the compressor of 2HP. The vacuum chamber consists of the water-cooled copper-hearth plate in which metals get melted with a tungsten electrode. In the presence of an argon atmosphere, a direct current is used to generate the arc. The distance between the electrode tip and die is known as arc length. It is to be noted that the distance between the electrode tip and die should be kept constant during melting, and the electric arc is maintained by a DC power supply, connected to the electrode and the die.

Welding unit

A standard Tungsten Inert Gas (TIG) welding unit is used as a power source (maximum voltage is 30V and current is 400 Amp). The melting is accomplished using a non-consumable tungsten electrode.

Chiller unit

The circulation of water from the chiller cools both the copper hearth and the electrodes which helps in the fast cooling of the die and electrode.

Fig. 3.1 shows the experimental setup of the vacuum arc melting cum suction casting unit. The arc melted button is suction cast to a 6 mm diameter rod and subsequently, sectioned with an aspect ratio of 1.5:1 using an EDM wire cut machine for isothermal hot compression test.

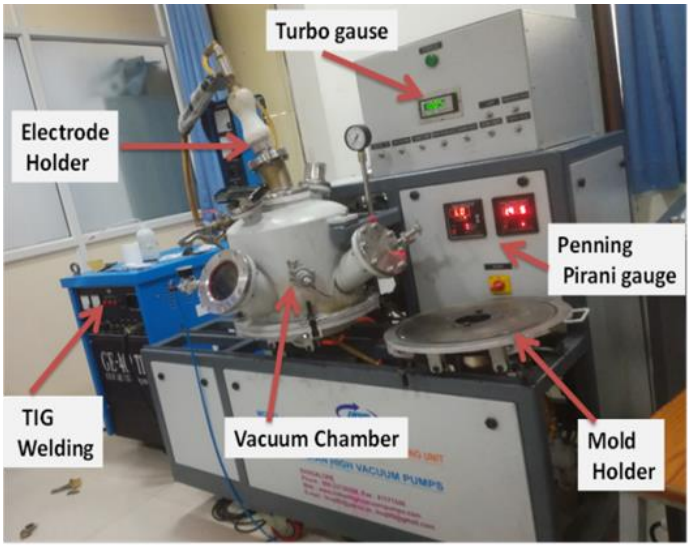

Figure 3.1 Experimental setup of the vacuum arc melting cum suction casting unit

3.3 Structural and microstructural analyses of HEAs

3.3.1 X-ray diffraction technique (XRD)

The X-ray Diffraction (XRD) was performed on a specimen to investigate phase characterization via BRUKER D2 PHASER (with Cu radiation target, λ=0.154056 nm) instrument, operating at 45 kV and 30 mA having 2θ ranging from 20-90º (with a step size of 2θ = 0.017 deg.). X-pert PRO software was used to analyze the obtained diffraction pattern.

3.3.2 Scanning Electron Microscopy (SEM):

For microstructural studies, the as-cast and deformed sample were hot mounted using bakelite powder. Such mounted specimens were ground and polished by different abrasive paper (SiC – 120 to 1200 grit size). For the mirror finish of the specimen, a velvet cloth was used along with

alumina slurry (particle size up to 0.25μm) and dispersive oil. In this study, the microstructural characterization of as-cast and deformed specimens of HEAs were carried out using field emission-scanning electron microscopy (FE-SEM, Make: JEOL JSM-7610F-Plus and NOVA, NANOSEM 450), coupled with a back Scattered electron detector. SEM micrographs of studied HEAs were collected at 20 kV accelerating voltage. The compositional analysis was carried out using energy dispersive spectroscopy (EDS) at 20 kV accelerating voltage.

The texture analysis of hot deformed samples at different temperatures and strain rates was characterized by electron back scattered diffraction (EBSD). For EBSD analysis, the hot deformed samples were first cut vertically through the center along the compression axis. Electropolishing (at -5°C using a constant voltage of 15V applied for 15s) was performed over the deformed samples after mechanical polishing.

3.3.3 Transmission Electron Microscopy (TEM):

The fine-scale microstructural feature of studied HEAs was carried out using TEM. The constituent phases in the microstructure were identified using selected area electron diffraction (SAED) patterns and EDS measurements. In this study, TEM FEI G$^{2®}$ with high-resolution capabilities model, operated at 200 kV was used.

3.4 Mechanical Experiments

3.4.1 Vickers hardness Test

Vickers hardness was calculated by applying the load on the test material using a square base pyramid-shaped diamond. The hardness measurement was carried out using a Vickers microhardness tester under the load of 200 gf for 10 seconds. For the present study, Vickers hardness measurements were performed by UHL VMHT (Walteruhl GmBH, Germany).

3.4.2 Hot Deformation Test

Isothermal hot compression tests of HEAs at different temperatures and strain rates were carried out using Gleeble 3800® thermo-mechanical simulator with hydrawedge module. The cylindrical specimen with diameter (Ø) = 6 mm and aspect ratio = 1.5:1 was used. The cylindrical specimen was deformed to approximately 50% reduction in height.

3.5 Simulation details

The thermodynamic simulation was carried out in the studied HEAs for the analysis of phase formation during the solidification by the thermodynamic simulation approach with the help of ThermoCalc® software (thermo-Calc Software, Salona, Sweden) using TCHEA2® database. The microscale simulation was done using the phase-field simulation approach. The multiphase field approach available in MICRESS software was used to simulate the solidification of the FCC phase from the liquid. Here the real-time coupling with the thermodynamic database (Thermo-Calc) was realized by using the T.Q. interface, and diffusion values for each component were optimized to get the stable simulation.

The Artificial Neural Network (ANN) model with the back-propagation (L-M training algorithm) predicts microhardness against varying the composition and flow curves at different hot working conditions. MATLAB 9.6 (R2019a) version was utilized as a simulation tool for ANN analysis. Macroscale simulation was done using SIMUFACT® FEM software by assuming hydraulic type press. The material property data required for the simulation were taken from the experimental data and the other required properties for the simulation was determined by using rule of mixture. The overall experimental strategy of the current thesis is summarised in **Fig. 3.2**.

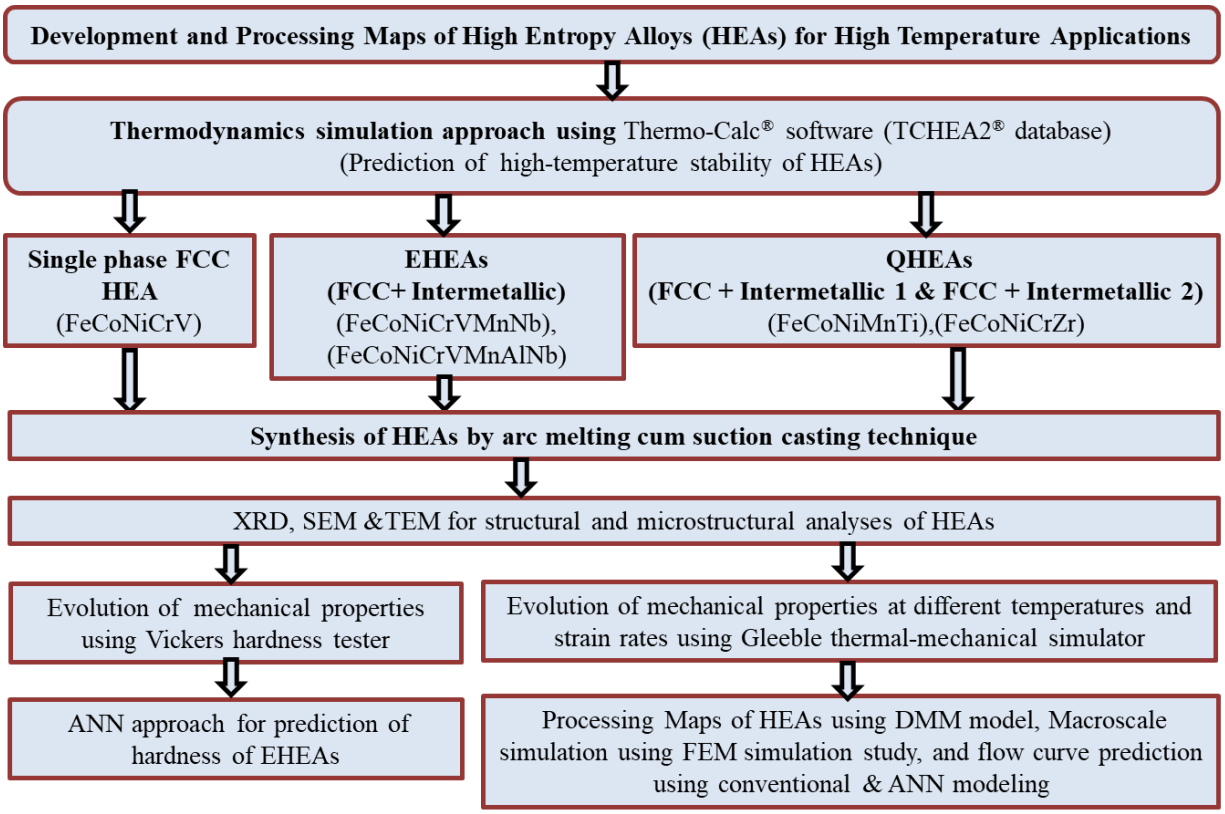

Figure 3.2 Experimental Strategy of the current thesis

Chapter 4

Design and development of single-phase CoCrFeNiV HEA

4.1 Introduction:

The present study explores the development of $Fe_{25}Co_{25}Ni_{25}Cr_{20}V_5$ single-phase FCC high entropy alloy (HEA) using ICME approach. The simulation guided composition was arc melted and verified using microstructure characterization. The alloy was subjected to high-temperature deformation in the as-cast condition to predict its optimum processing domain for industrial application. The high-temperature flow stress behavior was correlated with microstructure evolution. The inhomogeneity in the deformed sample was correlated with the strain field distribution in the deformed sample by an integrated approach using FEM modeling and EBSD results. The current study realizes the ICME approach to develop a new single-phase FCC HEA. A schematic representation of the detailed study of FCC HEA is given in ***Figure 4.1****.*

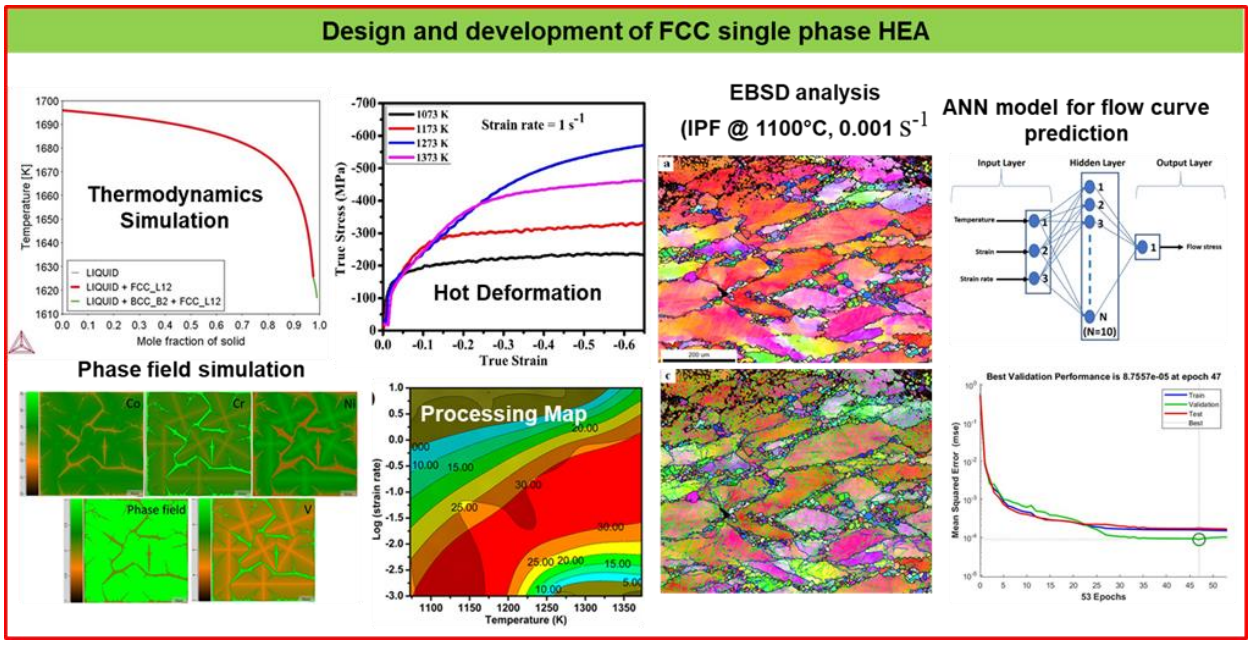

Figure 4.1 Schematic representation of the detailed study of FCC HEA

4.2 Objective:

The primary objectives of the present investigation are listed as follows:

(i) To design and development of a $Fe_{25}Co_{25}Ni_{25}Cr_{20}V_5$ single-phase FCC HEA by integrated approach of combining simulation and experimental methods.

(ii) The processing map is generated and correlated with EBSD maps of the deformed sample. The microstructure inhomogeneity in the sample is correlated with macroscale finite element method (FEM) simulation.

4.3 Experimental and simulation details

Pure elements of the required composition were arc melted using a non-consumable vacuum arc meting system. The melted buttons were flipped and remelted five times to ensure the homogeneity of the samples. The arc melted buttons were suction cast to 6 mm diameter rods and sectioned with an aspect ratio of 1.5:1 using an EDM wire cut machine. The nominal composition of the suction cast samples was given as $Co_{25}Cr_{20}Fe_{25}Ni_{25}V_5$ (in at. %). The cylindrical samples were used for hot deformation studies with varying temperatures and strain rates. The deformed samples were sectioned along the axis of deformation and polished using the standard metallographic techniques. The as-cast and deformed samples were characterized using SEM and SEM coupled with EBSD. The structural characterization was carried out using XRD measurements. The simulation was carried out in microscale and macroscale. The microscale simulation was done using the phase-field method and macroscale simulation using FEM. The multiphase field approach available in MICRESS software is used to simulate the solidification of the FCC phase from the liquid. Here the real-time coupling with the thermodynamic database (Thermo-Calc) was realized by using the T.Q. interface, and diffusion values for each component were optimized to get the stable simulation. FEM simulation was carried out to understand the strain field distribution inside the sample during isothermal compression. The simulation was done using Simufact forming software and assumed the press is of hydraulic type. The material

property data required for the simulation were taken from the experiments and rule of mixture. The sample is maintained at the isothermal condition, and the strain rate is controlled by controlling the stroke velocity and time. The friction between the anvil and the sample was taken as moderate (average friction factor: 0.5). The strain field distribution obtained was compared with the inhomogeneity in the deformed sample microstructure.

4.4 Results and discussion:

4.4.1 Thermodynamics and phase-field simulation:

The phase formation was predicted by using Thermo-Calc with the TCHEA2 database. It shows that the alloy consists of a large FCC stable domain comparable to the reported single-phase alloy (**Figure 4.2a**). Scheil's solidification pathway suggests that the primary phase will be of FCC type and the BCC phase formation for the last solidifying liquid (**Figure 4.2b**).

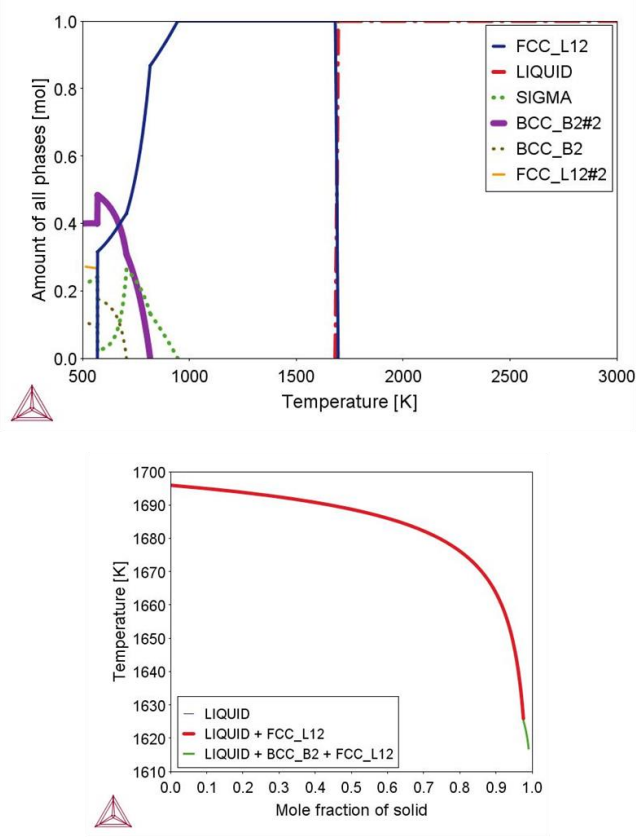

Figure 4.2 (a) Phase fraction Vs. temperature plot, (b) Scheil's solidification plot.

The phase-field simulation of the FCC phase from the liquid shows that the elemental segregation can be expected in the alloy while solidifying (**Figure 4.3a**). The multiple dendrite simulation shows the segregation of Cr and V at the interdendritic region but limited. The coring effect during solidification was visible in each dendrite. The elemental segregation amount suggests that the sample will be homogeneous during the suction casting process due to the high cooling rate. The multiple dendrite simulations show segregation of Cr and V at the interdendritic region (**Figure 4.3b**). Diffusion values used for the current simulation are listed in **Table 4.1**.

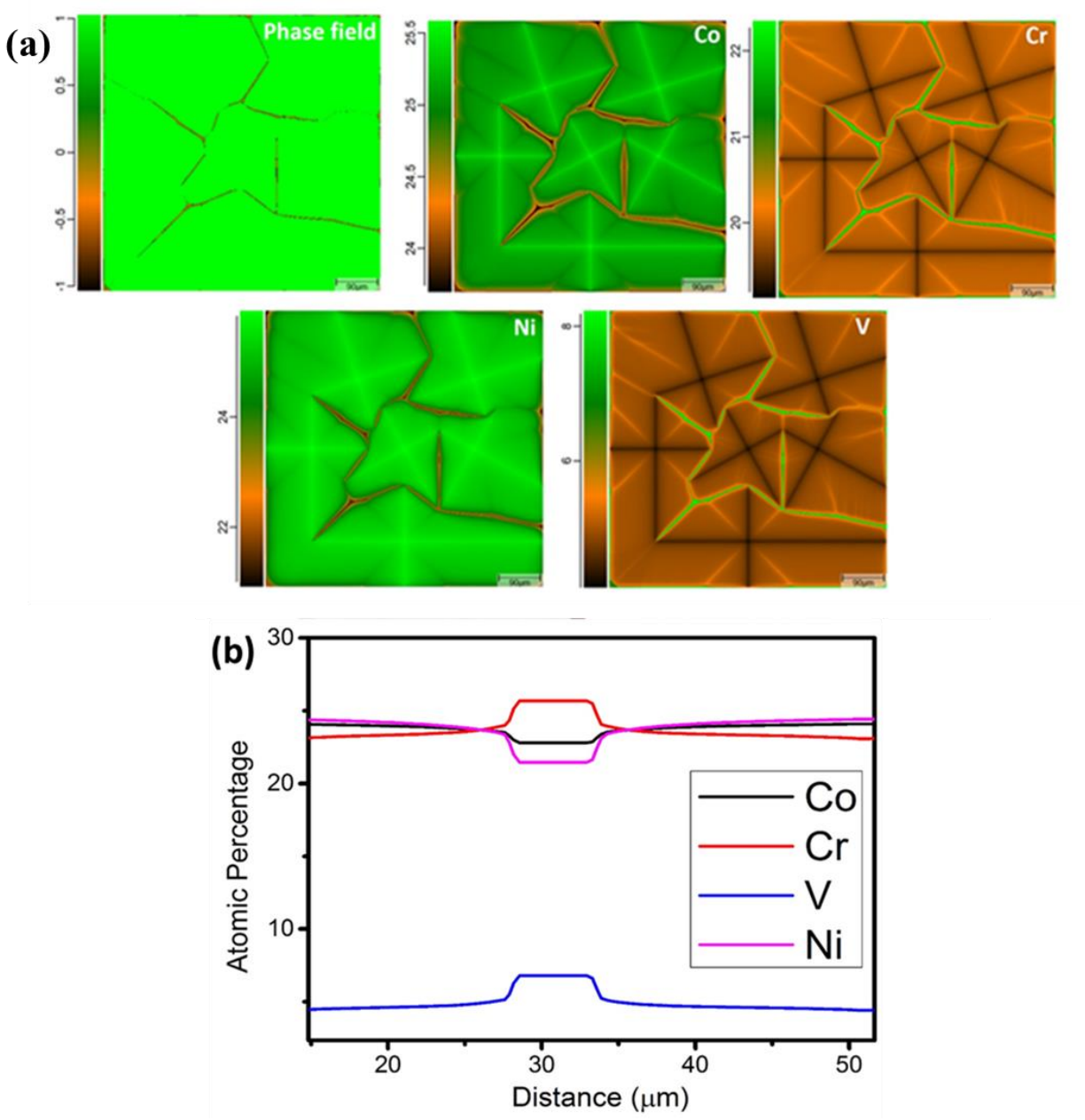

Figure 4.3 (a) Phase field simulation plots and segregation profiles of as-cast CoCrFeNiV HEA showing formation of dendrites and chemical segregation (time: 0.8 s), (b) The virtual EDS line scan data, obtained through phase-field simulation of CoCrFeNiV HEA (line starts from one dendrite to another including interdendritic region) and Interdendrtic region shows the segregation of Cr and V.

Table 4.1 Parameters used for phase field simulation of CoCrFeNiV FCC HEA

Parameter	Value and Unit
Diffusion constant of Co in the melt	5.4 x 10^{-5} cm^2/sec
Diffusion constant of Co in the dendrite	5.4 x 10^{-10} cm^2/sec
Diffusion constant of Cr in the melt	2.24 x 10^{-5} cm^2/sec
Diffusion constant of Cr in the dendrite	2.24 x 10^{-10} cm^2/sec
Diffusion constant of V in the melt	2.2 x 10^{-5} cm^2/sec
Diffusion constant of V in the dendrite	2.2 x 10^{-10} cm^2/sec
Diffusion constant of Ni in the melt	6.0x 10^{-5} cm^2/sec
Diffusion constant of Ni in the dendrite	6.01 x 10^{-10} cm^2/sec
Domain size and grid size (μm)	600 x 600 and 0.3
Kinetic coefficient between solid and liquid phase	30.0 x 10^{-04} cm^4/Js

4.4.2 Structural and Microstructural characterization

The as-cast sample shows the elements are distributed uniformly on the sample in the SEM level of characterization, and the XRD results confirm that the sample is of FCC type (**Figure 4.4**).

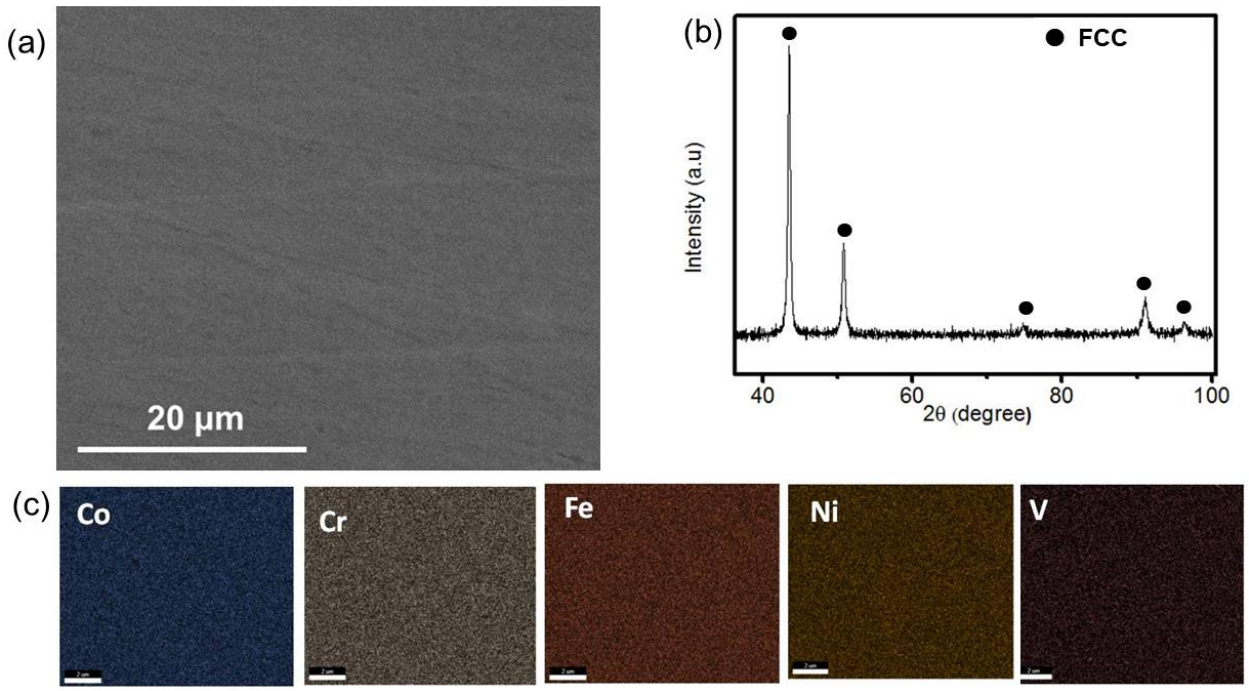

Figure 4.4 (a) BSE SEM image of as-cast alloy, (b) XRD of as-cast alloy and (c) EDS mapping of as-cast alloy.

4.4.3 Flow stress behaviour of $Fe_{25}Co_{25}Ni_{25}Cr_{20}V_5$ FCC HEA

The flow behaviour of FeCoNiCrV HEA obtained by room temperature compression test is shown in the **Figure 4.5.** Initially, the engineering stress is found to be increased rapidly due to work hardening caused by the increase of dislocation density.

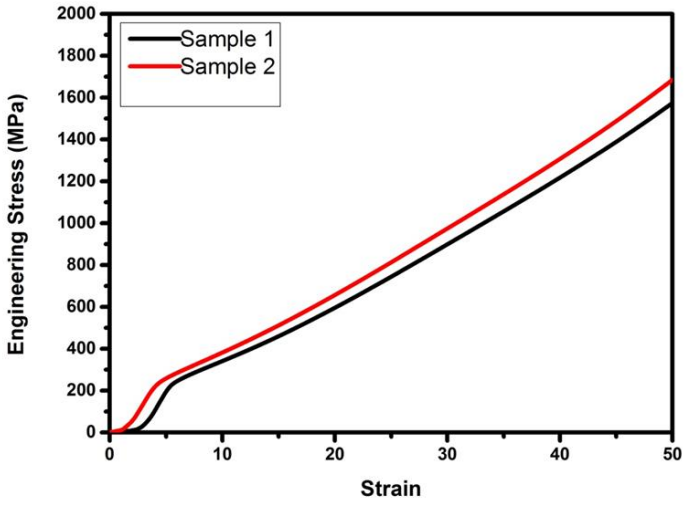

Figure 4.5 Room temperature compression curve of as-cast alloy.

The true stress vs. strain curves of all the samples deformed in the temperature range of 1073 – 1373 K are shown in **Figure 4.6.**

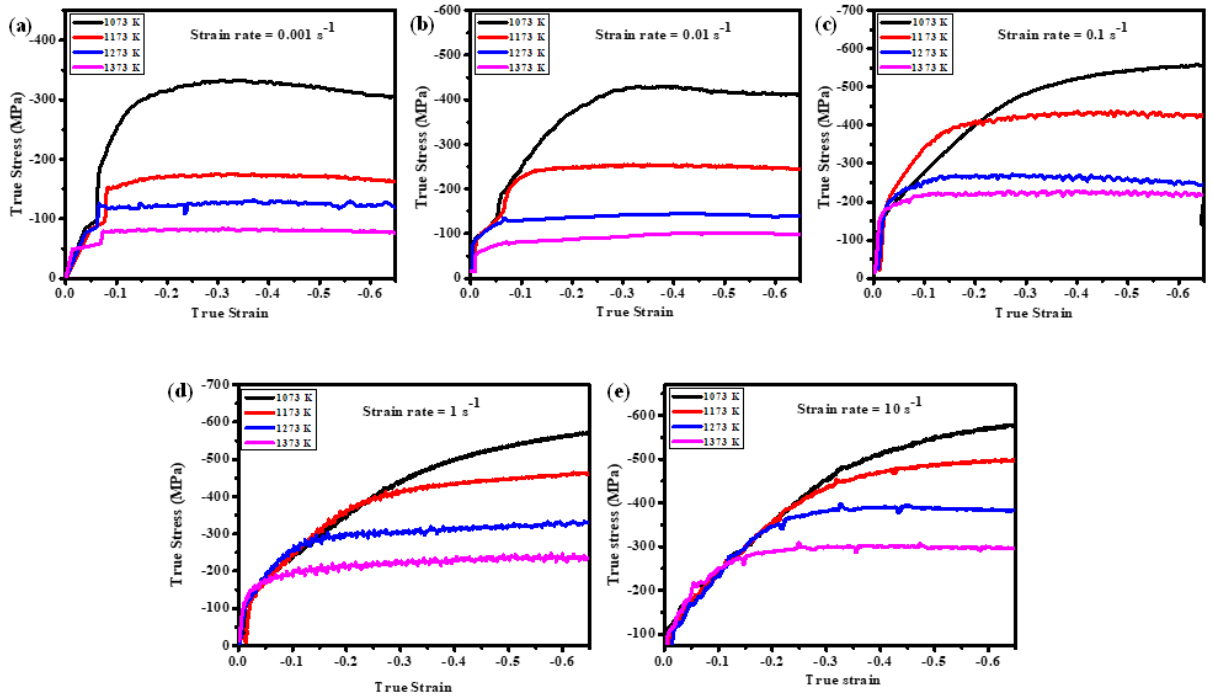

Figure 4.6 True stress Vs. true strain plot of as-cast multicomponent HEA.; at (a) $\dot{\varepsilon}$ = 0.001 s^{-1}, (b) $\dot{\varepsilon}$ = 0.01 s^{-1}, (c) $\dot{\varepsilon}$ = 0.1 s^{-1}, (d) $\dot{\varepsilon}$ = 1 s^{-1} and (e) $\dot{\varepsilon}$ = 10 s^{-1}

All the stress strain curves show a peak value in strength followed by constant value of the strength with increase in deformation the samples deformed at strain rates of 0.001s^{-1}, 0.01s^{-1} and

$0.1s^{-1}$ except at 1073 K. However, a continuous increase in stress value with deformation is observed for the samples deformed at strain rates of $1s^{-1}$ and $10s^{-1}$. The above observation indicates that the microstructure evolution is different for the samples deformed at lower strain rates and higher strain rates. It is well known that microstructure evolution is related to the dislocation content and its interaction during the deformation in the material. Hence, to capture the dislocation evolution, hardening curves for all the samples are plotted in the **Figure 4.7**.

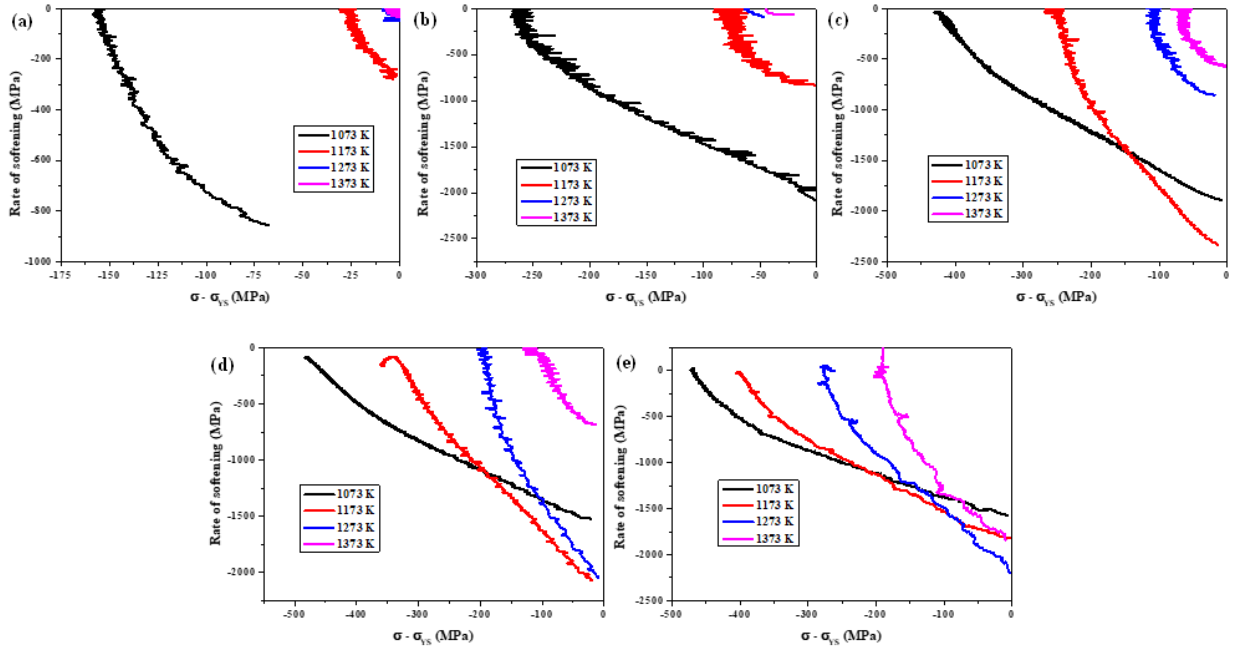

Figure 4.7 Rate of softening vs. strength plot

All the samples show stage III hardening behavior. The negative and positive values represent the softening and hardening behavior during deformation. It is observed that all the samples show softening behavior during deformation and the rate of softening increases with increase in the amount of deformation. However, for the sample deformed at $0.1s^{-1}$ at 1273 K and 1373 K, hardening is observed during the later stage of deformation. The hardening and softening behavior depends on the grain orientation during deformation. Since, all the materials are cast sample having different initial orientation, it is difficult to develop the correlation between the initial softening rate to later stage of softening rate with respect to amount of deformation at all operating temperatures. The hardening rates of all the samples are documented in **Table 4.2**.

Table 4.2 Hardening rates at different hot working conditions

Strain rate (s^{-1})	Temperature (^{o}C)	θ_1	θ_2	θ_2 / θ_1
0.001	800	-4.74	-14.22	
	900	-6.72	-11.19	
	1000	-2.21		
	1100	-2.21		
0.01	800	-6.0		
	900	-3.99	-4.41	
	1000	-5.55		
	1100	-5.02	-5.63	
0.1	800	-3.75	-8.08	
	900	-7.63	-17.34	
	1000	-5.74	1.76	
	1100	-5.77	1.77	
1	800	-2.6	-3.99	
	900	-5.67	-7.92	
	1000	-7.77	-19.69	
	1100	-4.05	-9.54	
10	800	-2.51	-5.25	
	900	-4.04	-7.15	
	1000	-7.09	-9.64	
	1100	-5.19	-12.75	

The hardening occurs in the samples deformed at $0.1s^{-1}$ at 1273 K and 1373 K may be attributed to the presence of deformation twinning formed during deformation because formation of deformation twinning acts as a hindrance to the movement of dislocation in the parent grain because of the boundary which is present between the parent grain and twins. Further, twinning

changes the orientation of the twinned grain which is different from the parent grain. Hence, the dislocations which are present in the twinned grain may or may not be glissile depending on the orientation with respect to the compression axis resulting in the hardening behavior during later stage of deformation at a certain combination of strain and strain rate. The above hardening phenomenon is not observed in all the samples which can be attributed to the difference in initial orientation of all the samples. The strength of the sample is related to mean free path of the dislocations which is shown in **Figure 4.8.**

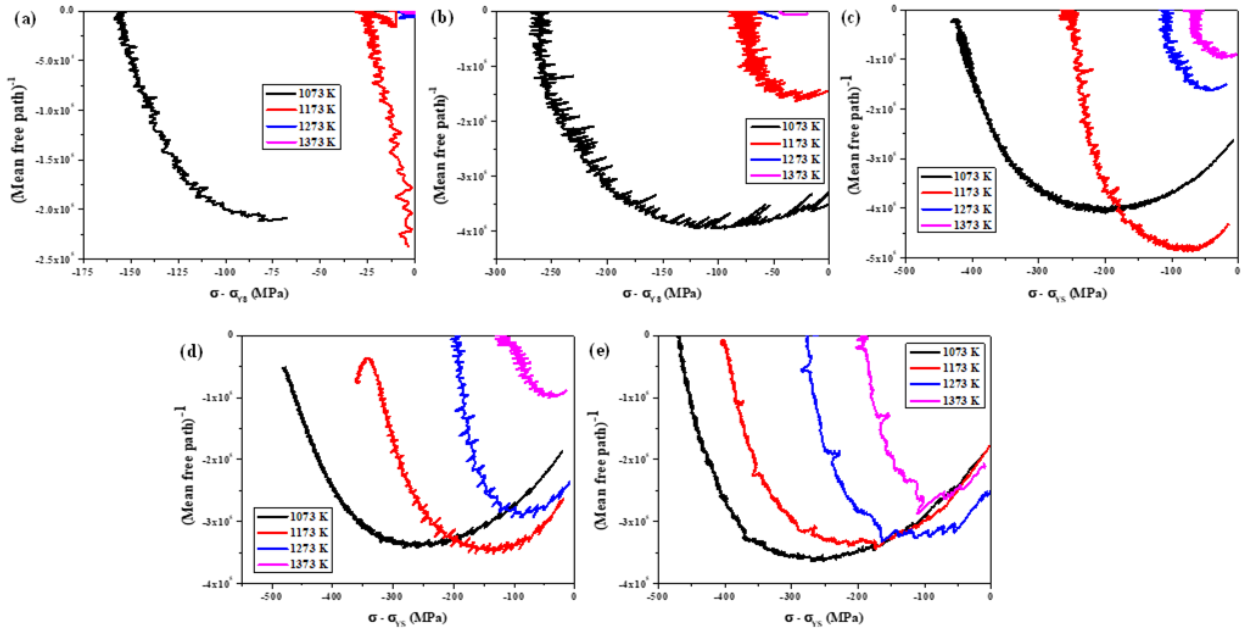

Figure 4.8 Mean free path of dislocation vs. strength

It is observed that mean free path of dislocations initially decreased and later on it is increased because of the dynamic recovery. The lowest value of mean free path of dislocation indicates the transition point from the dislocation-dislocation or dislocation-solute interaction to dynamic recovery. During dynamic recovery, the climb and cross slip of dislocations increase the mean free path of dislocations. These transition points are marked in **Figure 4.7,** where dynamic recovery onsets during deformation.

4.4.4 Flow curve prediction using conventional and ANN model

The experimental flow stress data were used for modeling purposes at different hot deformation conditions (at temperature range 800-1100°C and strain rate range 0.001-10 s^{-1}). In this study, we

used the phenomenological, physical, and ANN models to predict the flow behavior of HEA. We used modified Johnson-Cook (JC), modified Zerilli–Armstrong (ZA), and Arrhenius-type constitutive equations to predict the flow stress for the present studied single-phase HEA. The accuracy or performance of models is evaluated by the coefficient of correlation (R) and average absolute relative error (AARE).

4.4.4.1 Modified Johnson-Cook model for flow stress prediction:

J-C model is a very known phenomenological model for flow stress prediction. In this model, flow stress dependent on the temperature, strain, and strain rate. That model used for different types of materials and a more comprehensive range of temperature and strain rate due to the simplicity and easy availability of model parameters. In the modified JC model, the relationship between the deformation temperature, flow stress, strain rate, and strain can be expressed as [148][149]:

$$\sigma = (A_1 + B_2\varepsilon + B_2\varepsilon^2)(1 + C_1 \ln(\dot{\varepsilon}^*) \exp\left[(\lambda_1 + \lambda_2 \ln(\dot{\varepsilon}^*)\, T^*\right] \qquad (4.1)$$

Where, the σ is flow stress, A_1, B_2, B_2, C_1, λ_1, and λ_2 are constant. $\dot{\varepsilon}^*$ dimensionless coefficient (ratio of strain rate $\dot{\varepsilon}$ and $\dot{\varepsilon}_r$ reference strain rate) and T^* is homologous temperature. T^* can be expressed as:

$$T^* = T - T_r \qquad (4.2)$$

Where the T is the hot working temperature, and T_r is reference temperature. The 1100 °C of temperature and 1 s^{-1} of strain rate during hot working consider as a reference value. The calculation of different material constant for that model represent in **Figure 4.9**. Using a plot between stress and strain after second-order polynomial fitting at the reference condition, we get A_1, B_2, B_2given **Figure 4.9a**. C1 is calculated with the help of a plot between $\sigma/(A_1 + B_2\varepsilon + B_2\varepsilon^2)$ and $\ln\dot{\varepsilon}$ given in **Figure 4.9b**. Here, one new term λ introduced for the calculation of λ_1, and $\lambda_2$and it can be written as

$$\lambda = \lambda_1 + \ln \dot{\varepsilon}\, \lambda_2 \qquad (4.3)$$

The value of λ can be calculated by slope of plot between $\ln\{\sigma/(A_1 + B_2\varepsilon + B_2\varepsilon^2)(1 + C_1\ln(\dot{\varepsilon}^*)\}$ and T^*. In this study, we have 5 different strain rates to get 5 different values of λ can

get as slope after linear fitting (for strain rate 1 given in **Figure 4.9c**. Finally, λ_1, and λ_2 get from the intercept and slope of plot between λ and ln $\dot{\varepsilon}$ (**Figure 4.9d**).

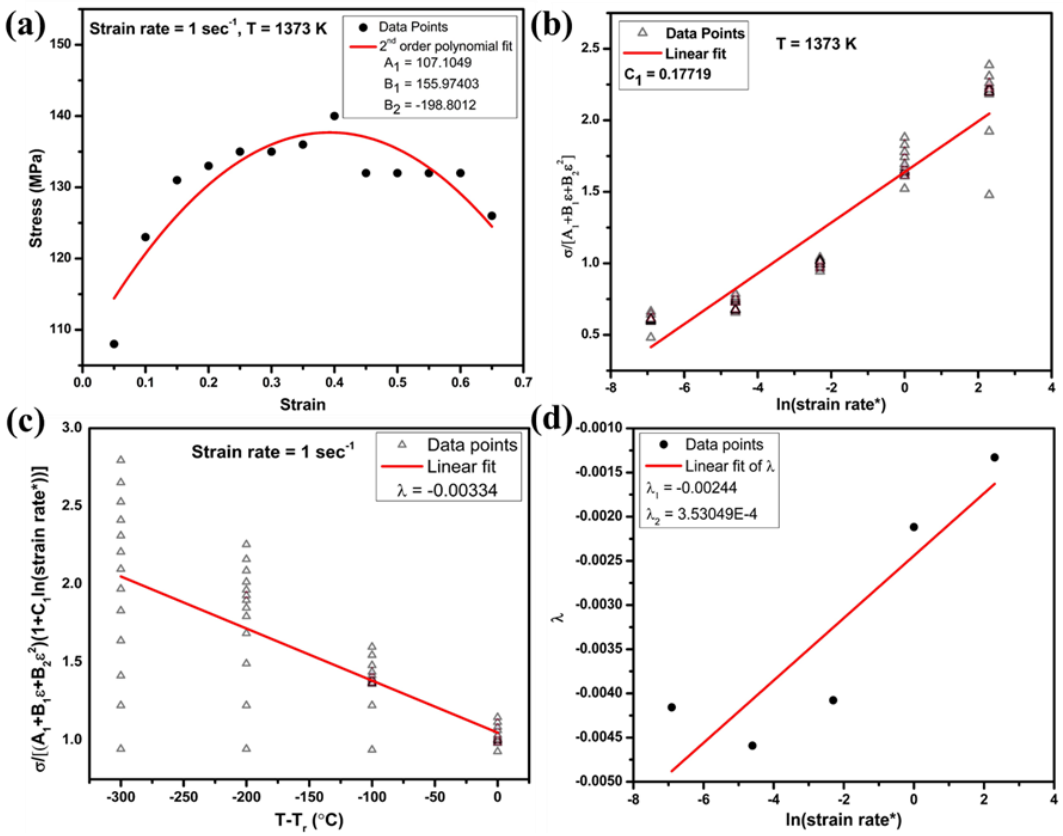

Figure 4.9 Material constant calculation for modified JC model

4.4.4.2 Modified Zerilli-Armestrong (ZA) model:

Based on the dislocation mechanism that the model introduced, the constitutive equation for that model gives the effect of strain hardening, thermal softening, and strain on flow stress [149]. In modified ZA model flow stress (σ) can be expressed as [148][149]:

$$\sigma = (C_1 + C_2\varepsilon^n)\exp\{-(C_3 + C_4\varepsilon)T^* + (C_5 + C_6T^*)\ln\dot{\varepsilon}^*\} \qquad (4.4)$$

$$T^* = T - T_r \qquad (4.5)$$

$$\dot{\varepsilon}^* = \frac{\dot{\varepsilon}}{\dot{\varepsilon}_r} \qquad (4.6)$$

Where n, C_2, C_3, C_4, C_5 and C_6 are the material constants. Where T and T_r is the processing temperature and reference temperature, respectively. The term $\dot{\varepsilon}^*$ the dimensionless coefficient is the ratio of strain rate $\dot{\varepsilon}$ and $\dot{\varepsilon}_r$ reference strain rate. The calculation of different material constant which are associated with equation can be calculated step by step. The value of C_1 is yield stress (at reference temperature and strain rate). The calculation of C_2 and n at reference strain rate 1 determined by using equation:

$$\sigma = (C_1 + C_2\varepsilon^n)\exp\{-(C_3 + C_4\varepsilon)T^* \quad (4.7)$$

Taking the natural logarithm of equation 7, we get equation:

$$\ln\sigma = \ln(C_1 + C_2\varepsilon^n) - (C_3 + C_4\varepsilon)T^* \quad (4.8)$$

In equation 8, term $\ln(C_1 + C_2\varepsilon^n)$ is written as I_1, and the term $(C_3 + C_4\varepsilon)T^*$ is written as S_1. The slope and intercept value (at strain 0.5) of linear plot between $\ln\sigma$ and T^* give the value S_1 and I_1 respectively given in **Figure 4.10a**. Similarly, calculation of S_1 and I_1 for all strain value calculated and then the value of C_2 and n finally get by linear plot between $\ln(\exp(I_1) + C_1)$ and $ln\varepsilon$ represent in **Figure 4.10b**. Similarly, the value of C_3 and C_4 determined with the help of a linear plot between S_1 and ε represent in **Figure 4.10c**. To calculate others constant C_5 and C_6 taking the natural logarithm of equation 4 and then written as:

$$ln\sigma = \ln(C_1 + C_2\varepsilon^n) - (C_3 + C_4\varepsilon)T^* + (C_5 + C_6T^*)\ln\dot{\varepsilon}^*\} \quad (4.9)$$

The term S_2 introduces to calculate the constant C_5 and C_6 and can be written as:

$$S_2 = (C_5 + C_6T^*) \quad (4.10)$$

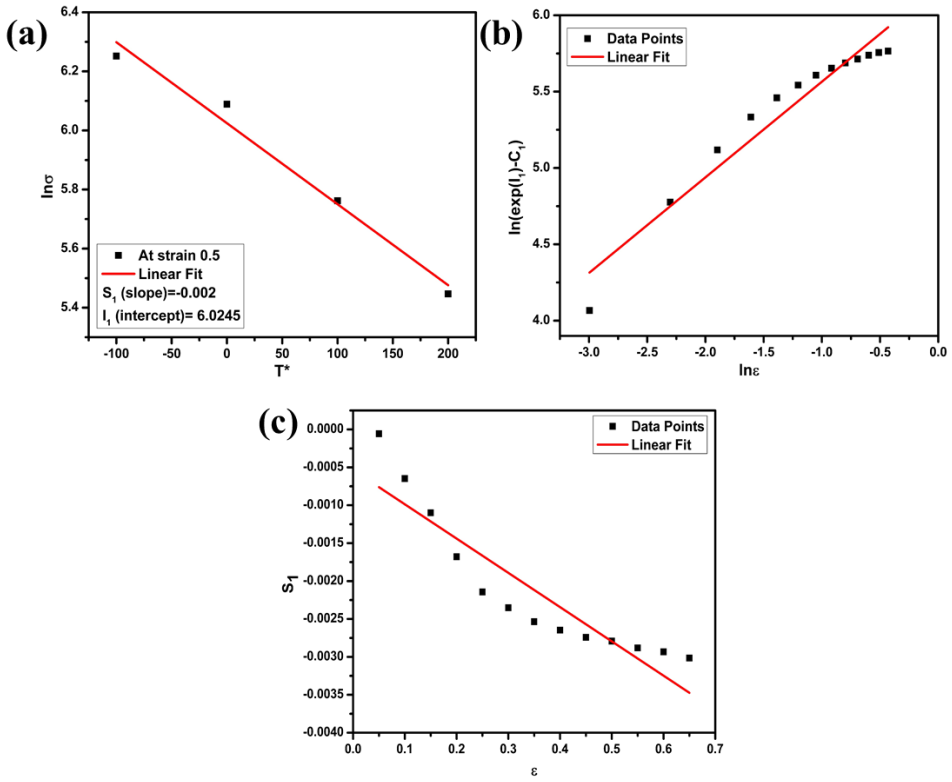

Figure 4.10 Material constant calculation for modified ZA model

The linear fitted plot between the $ln\sigma$ and $\ln\dot{\varepsilon}^*$ at different deformation, temperatures give the value of S_2 as a slope of fitted curve given in **Figure 4.11a**. Then value of S_2 at different strains with an interval of 0.25 was calculated. Finally, obtained C_5 and C_6 by plotting the curve between S_2 and T^*represent in **Figure 4.11b**. The slope and intercept of the plot gives the value of C_5 and C_6 respectively.

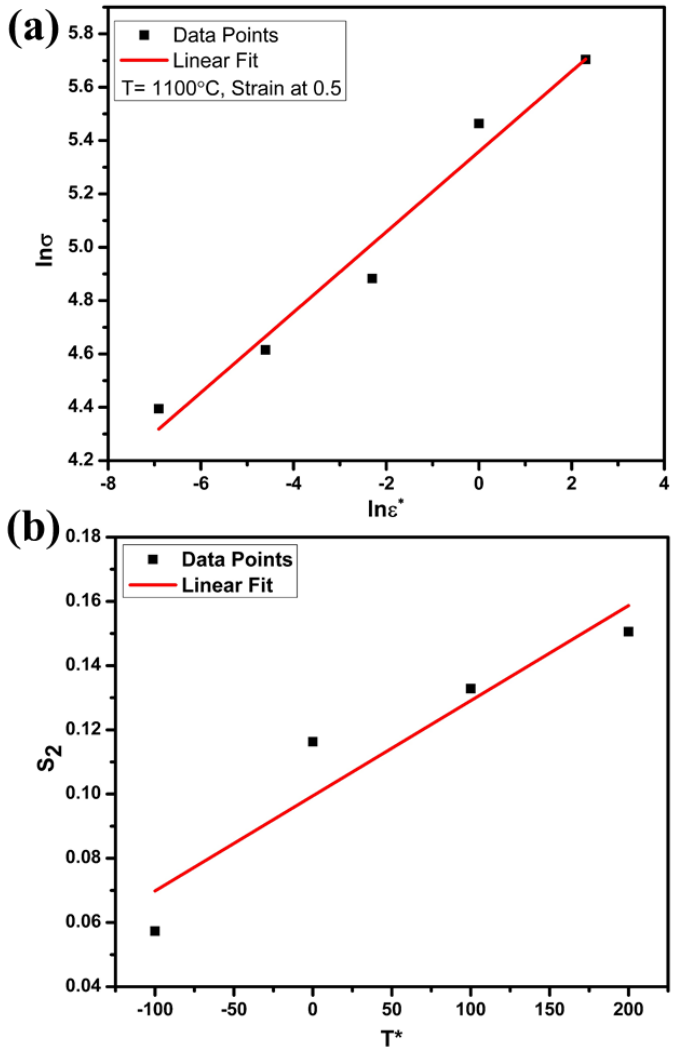

Figure 4.11 Material constant calculation for modified ZA model

4.4.4.3 Flow stress prediction using constitution model:

The constitutive equation based on the hyperbolic sinusoidal Arrhenius-type model is currently used by many researchers for estimation of the flow stress behavior during hot deformation [150], but accuracy usually is limited. Further, the improvement in the model by considering the Zener-Holloman parameter (Z) [151], which is also known as temperature compensated-strain rate. The respective governing equation can be expressed as

$$Z = A \times [\sinh(\alpha\sigma)]^n = \dot{\varepsilon} \times \exp\left(\frac{Q}{RT}\right) \quad (4.11)$$

$$\dot{\varepsilon} = A \times [\sinh(\alpha\sigma)]^n \times \dot{\varepsilon} \times \exp\left(-\frac{Q}{RT}\right) \quad (4.12)$$

Where $\dot{\varepsilon}$ is strain rate (s^{-1}), Q is the hot deformation activation energy (J/mol), R is the universal gas constant 8.314 J/mol-K, T is temperature in K, σ is flow stress (MPa), and A, α, and n are materials constant. Value of α calculated by the ratio of β/N, where β and N are the slopes of the lnσ vs. ln$\dot{\varepsilon}$ and σ vs. ln$\dot{\varepsilon}$ plot with a linear fit. The value of n is the slope of ln$\dot{\varepsilon}$ vs. ln[sinh(ασ)] plot with a linear fit. The value of Q is expressed in equation 13. In equation 13, the value of s is the slope of the linear fit of 10,000/T vs. ln[sinh(ασ)]. **Figure 4.12a**, **4.12b**, **4.12c**, and **4.12d** show the plots for calculation of constant β, N, n, and s, respectively. The value of A can be calculated by taking the logarithm; both sides of equation 11 can be given in equation 14 [151].

$$Q = 10{,}000 \times R \times (n)_T \times (s)_{\dot{\varepsilon}} \qquad (4.13)$$

$$lnZ = lnA + n \times [\sinh(\alpha\sigma)] \qquad (4.14)$$

The intercept of the linear plot between the ln[sinh(ασ)] vs. lnZ gives the value of lnA shows in **Figure 4.12e**. Finally, the flow stress in terms of Z expressed as

$$\sigma = \frac{1}{\alpha} \times \ln\left\{\left(\frac{Z}{A}\right)^{\frac{1}{n}} + \left[\left(\frac{Z}{A}\right)^{\frac{2}{n}} + 1\right]^{\frac{1}{2}}\right\} \qquad (4.15)$$

The n is calculated as a mean of the slopes of $\{(\partial ln\dot{\varepsilon})/\partial ln[sinh\,(\alpha\sigma)\,]\}$ at different temperatures because the n is dependent on temperature and strain rate. Thus, the value of Q is calculated by putting the value of R, n, and s in equation 3 at strain 0.5 (at strain 0.65 value of β=0.02679, α=0.004007, N=7.25, n=5, and s=0.82) is approximately 340381 KJ/mol.

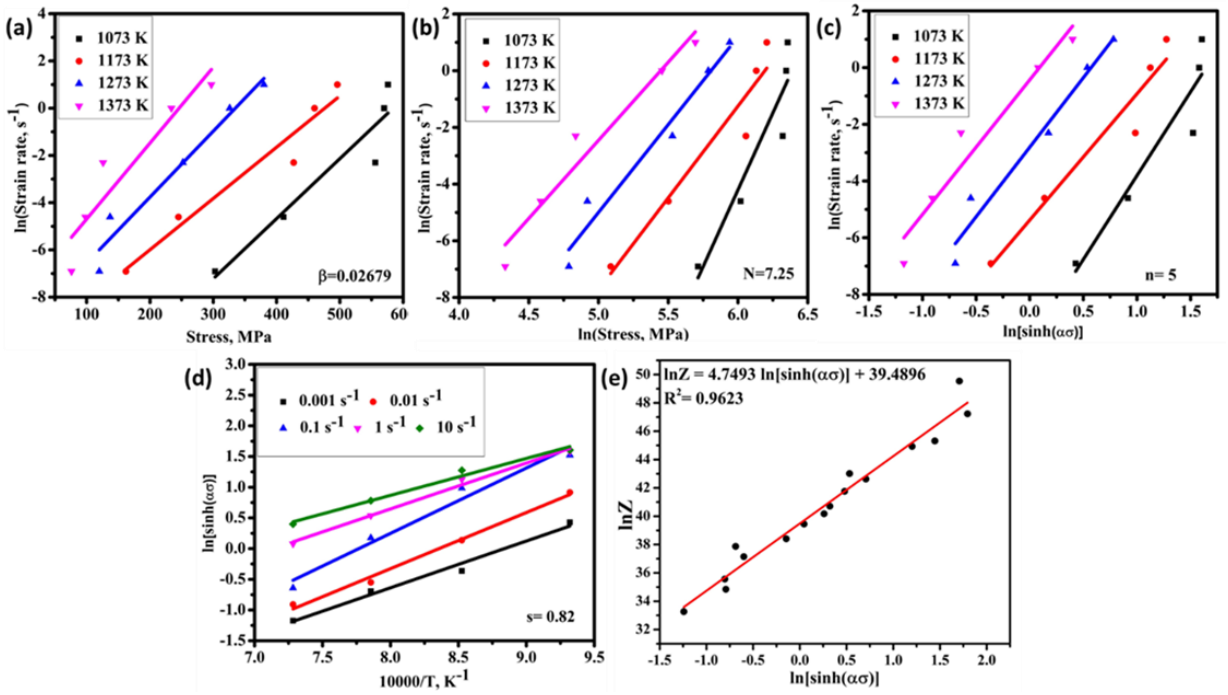

Figure 4.12 Calculation for (a) β, (b) N, (c) n, (d) s, and (e) lnA

For all other strains, the value of α, Q, n, and A are evaluated given in **Figure 4.13**. The parameter Z, $\dot{\varepsilon}$ and σ at strain 0.65 can be expressed as the following equation:

$$Z_{0.65} = \dot{\varepsilon}.\exp\left(\frac{340381}{RT}\right) \qquad (4.16)$$

$$\dot{\varepsilon} = 1.40 \times 10^{17} \times [\sinh(0.004007.\sigma_{0.65})]^5 \times \dot{\varepsilon}.\exp\left(\frac{340381}{RT}\right) \qquad (4.17)$$

$$\sigma_{0.65} = \frac{1}{0.004007} \times \ln\left\{\left(\frac{Z_{0.65}}{1.40\times10^{17}}\right)^{\frac{1}{5}} + \left[\left(\frac{Z_{0.65}}{1.40\times10^{17}}\right)^{\frac{2}{5}} + 1\right]^{\frac{1}{2}}\right\} \qquad (4.18)$$

Figure 4.13 shows the strain effect on material constant (α, Q, n, and A). The material constant (α, Q, n, and A) calculated by the polynomial fitting and is fitted by sixth order was found good correlation with strain for calculating the flow stress at different strain.

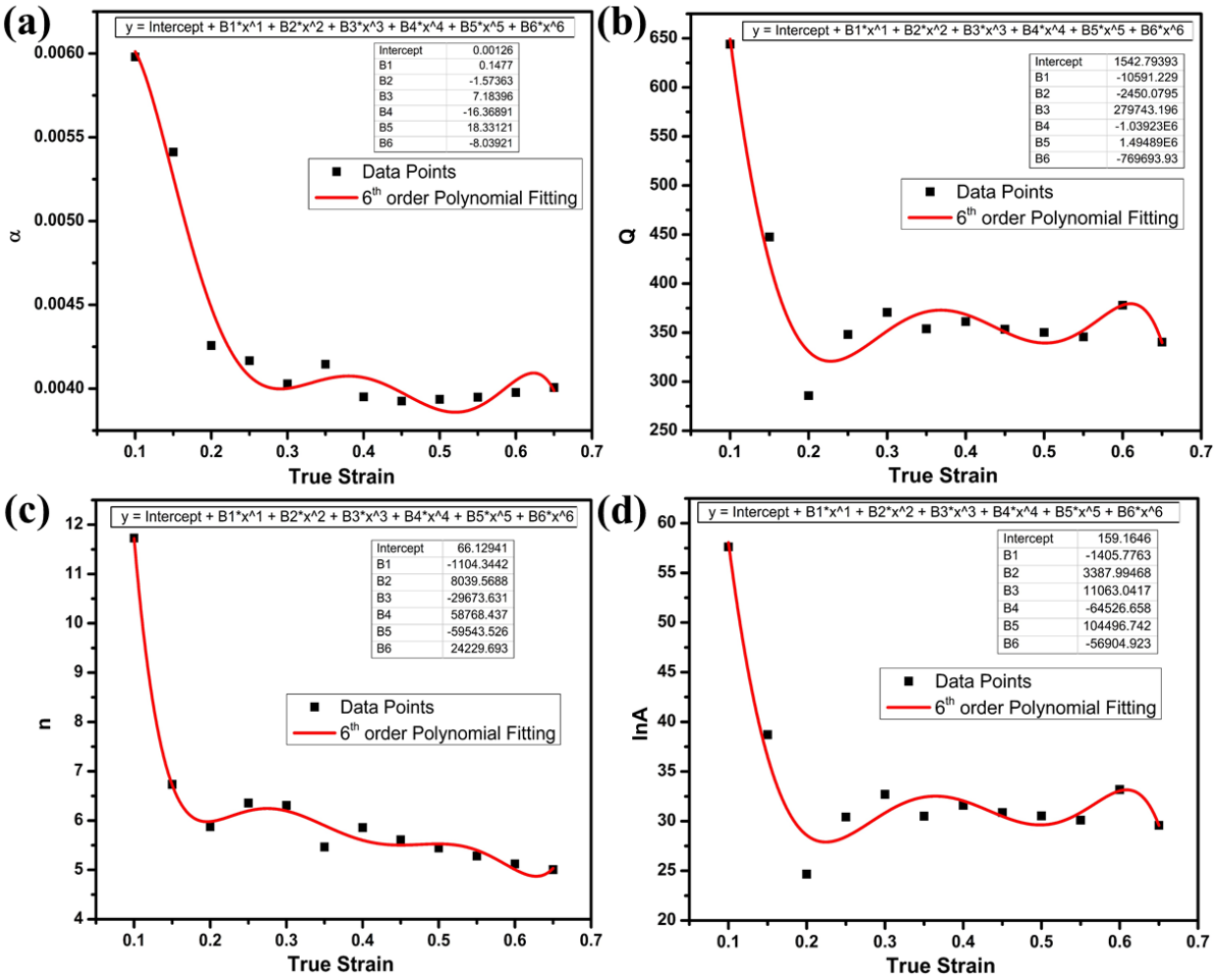

Figure 4.13 Effect of strain on material constant (a) α, (c) Q, (c) n, and (d) lnA

4.4.4.4 Modelling with an artificial neural network:

An artificial neural network is a computational model to deal with complex problems such as non-linear systems, optimization problems, and unknown data predictions. ANN model has found various applications in materials engineering, including the prediction of flow stress during the hot deformation, hot working processing maps, and prediction of different mechanical properties. ANN approach is useful and efficient to predict the flow behaviour of materials at different hot deformation working condition. The ANN model learns from an input-output database and identifies the pattern without any prior assumption about their behaviour and interaction. The neural network mainly consists of an input layer, hidden layer and output layer. Neurons in the input layer represent the independent variable and that layer receives the input

data for processing and then transfers it to the hidden layer. Neurons in that layer used for the computational purpose, and in hidden layer performed the data calculation and sent to the outer layer as a response. Finally, the output layer gives the final output. Ji et al. [20] used the ANN model to predict the hot deformation behavior of Aermet 100 steel in the temperature from 800°C -1200°C and the strain rate from 0.01 s^{-1} to 50 s^{-1}. Jain et al.[152] predict the microhardness of eight component FeCoNiCrMnVAlNb eutectic high entropy alloys as a function of alloying elements using the ANN approach. In the current study, the hot deformation behaviour of CoCrFeNiV single phase HEA has been carried out in the temperature range 1073K-1323K and strain rate of 0.001, 0.1, 1, 10 s^{-1}.

To predict the flow behaviour during the hot deformation feed-forward backpropagation ANN model with the L-M algorithm has been used. The BP algorithm adjusted each neuron's weight and minimized the mean squares error between experimental output and targeted output during the training of the network. In this study, temperature, strain rate, and strain are taken as input data and flow stress as output data. The representation of the optimal network for present study is given in **Figure 4.14**. A total of 260 experimental input-output datasets were used to develop the ANN model, and the model containing the 3 neurons in the input layer, 10 neurons in the hidden layers, and 1 neuron in the output layers. Before trained, the model data points should be scaled to get a good prediction. We scaled the data (temperature, strain rate, strain, and flow stress) by two approaches designated as ANN model 1 and ANN model 2 (details given in **Table 4.3**).

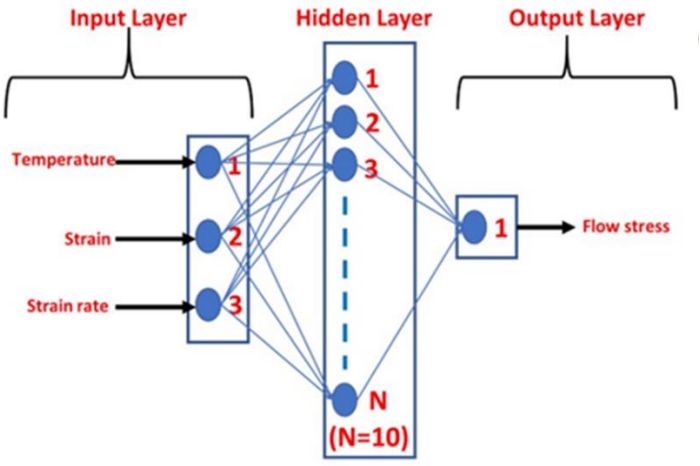

Figure 4.14 Schematic representation of the ANN model for flow stress prediction

Table 4.3 ANN models used to scale the data

Model	Scaling of data for training
ANN model 1	$X_{nor.} = 0.1 + 0.8 \times \frac{(X - X_{min})}{(X_{max} - X_{min})}$ Normalization of Stress (σ), Temperature (T), and Strain rate ($\dot{\varepsilon}$)
ANN model 2	$\dot{\varepsilon}_{nor.} = 0.1 + 0.8 \times \frac{(\log\dot{\varepsilon} - \log\dot{\varepsilon}_{min})}{(\log\dot{\varepsilon}_{max} - \log\dot{\varepsilon}_{min})}$ Normalization of Strain rate ($\dot{\varepsilon}$), while Stress (σ) and Temperature (T) normalized by as per the ANN model 1

For ANN model 1, the correlation between experiment and predicted value during different modeling stages such as training, validation, and testing is given in **Figure 4.15**. **Figure 4.16** represents the mean square error plot for ANN model 1, and the best validation performance is 0.0011521 at epoch 55. **Figure 4.17** presents the correlation coefficient after ANN modeling during the training, testing, validation, and overall data for ANN model 2.

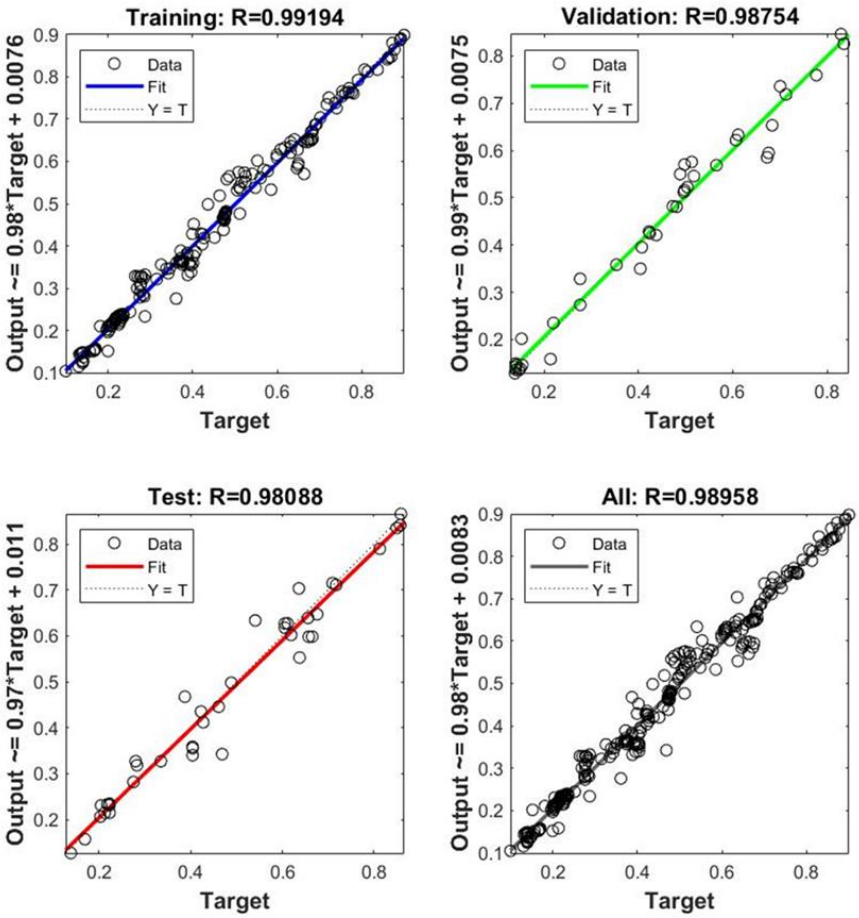

Figure 4.15 Correlation coefficient for ANN model 1

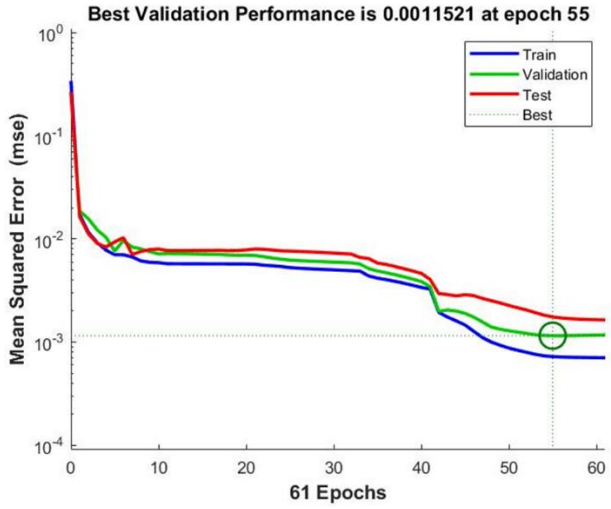

Figure 4.16 MSE (mean square error) for ANN model 1

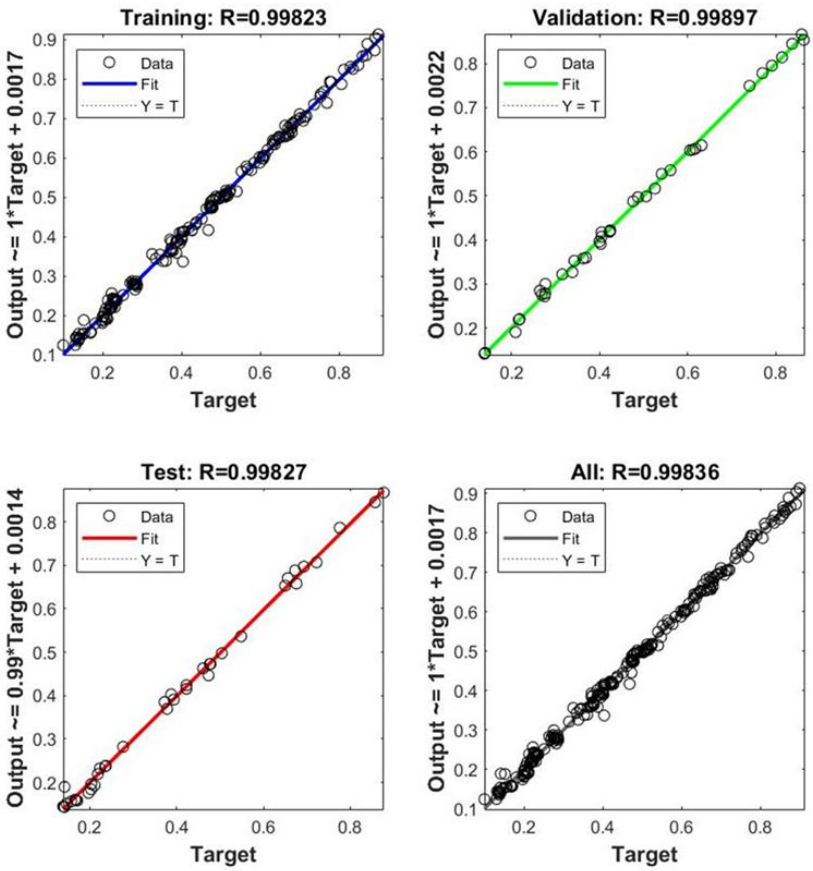

Figure 4.17 Correlation coefficient for ANN model 2

Figure 4.18 indicates the mean square error convergence plot, which indicates that the best validation performance is observed 8.7557×10^{-5} at epoch 47 for ANN model 2. The variation of the experimental and predicted value of flow stress for different temperatures (800°C -1050°C) and strain rate (0.001 s^{-1} to 1 s^{-1}) shown in **Figure 4.19** for ANN model 2.

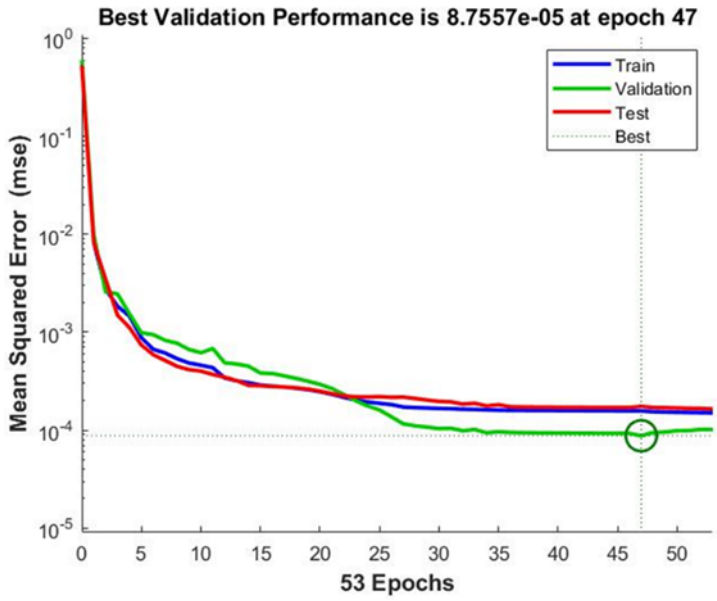

Figure 4.18 MSE (mean square error) for ANN model 2

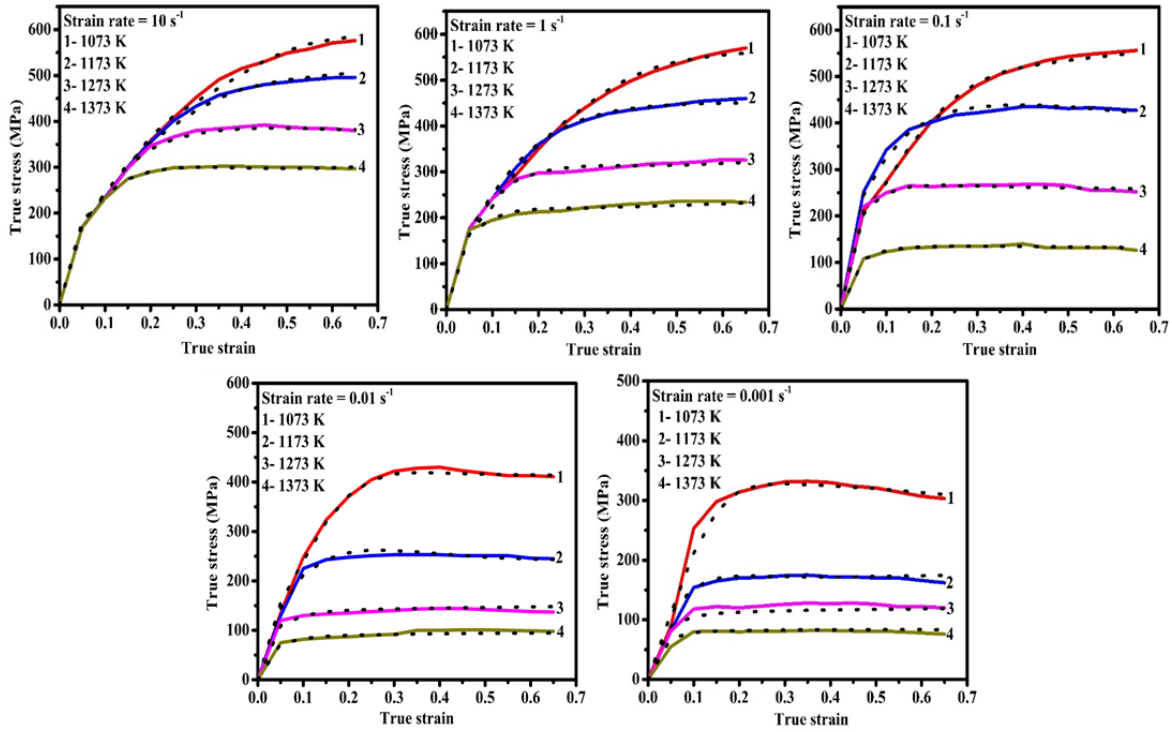

Figure 4.19 Comparisons between the experimental (solid lines) and predicted (dotted lines) flow curve using the ANN model 2 at various temperatures for strain rates.

4.4.4.5 Performance of model:

Predictability of all studied model is evaluated by the coefficient of correlation (R), and absolute average relative error (AARE) are given as:

$$R = \frac{\sum_{i=1}^{N}\left(\sigma_{ef}^{i}-\overline{\sigma_f}\right)\times\left(\sigma_{pf}^{i}-\overline{\sigma_f}\right)}{\sqrt{\sum_{i=1}^{N}\left(\sigma_{ef}^{i}-\overline{\sigma_f}\right)^{2}\times\sum_{i=1}^{N}\left(\sigma_{pf}^{i}-\overline{\sigma_f}\right)^{2}}} \quad (4.19)$$

$$AARE(\%) = \frac{1}{N}\times\sum_{i=1}^{N}\left|\frac{\sigma_{ef}^{i}-\sigma_{pf}^{i}}{\sigma_{ef}^{i}}\right|\times 100 \quad (4.20)$$

Where σ_{ef} and σ_{pf} are an experimental and predicted value of flow stress, respectively, N total number of datasets. In this study, the calculated value of R and AARE for different models was calculated and given in **Figure 4.20**. It is observed that the prediction of flow stress by both the ANN models are accurate as compared to other phenomenological (modified JC model and Arrhenius model) and physics-based model (modified ZA model).

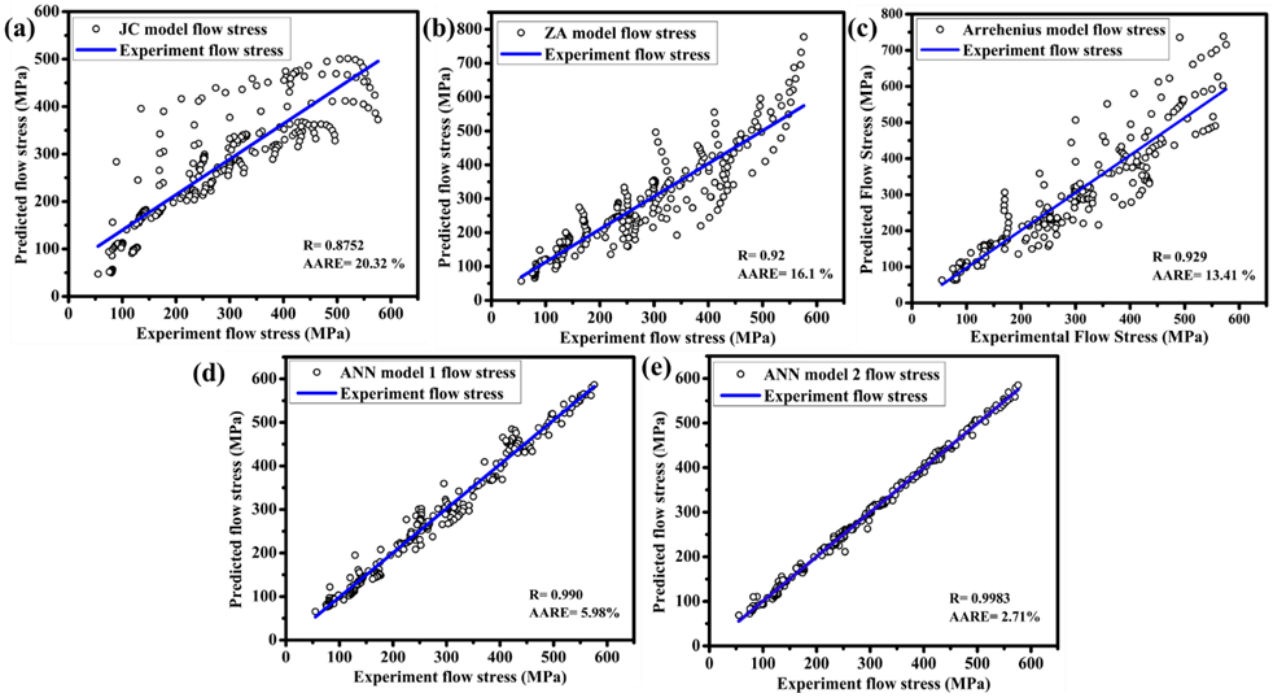

Figure 4.20 Performance (a) JC model, (b) ZA model, (c) Arrhenius type model, (d) ANN model 1, and (e) ANN model 2

4.4.5 Microstructure correlation with processing map

Processing map based on DMM (dynamic material model) has been established to describe the hot workability of materials to provide the reference for the formulation of hot deformation processing parameters [20] [153].

In DMM model, the total instantaneous power (P) of the system is given by the product of flow stress and strain rate. Also, the power dissipation during the thermomechanical processing at different hot working condition can be divided into two parts first one is $E_{.P.,}$ and another one is the $E_{.M.}$ can be written as:

$$P = \sigma \dot{\varepsilon} = \int_0^{\varepsilon} \sigma d\dot{\varepsilon} + \int_0^{\sigma} \dot{\varepsilon}\, d\sigma = E_p + E_M \qquad (4.21)$$

Where $E_{.P.}$ is the power dissipated through plastic deformation and $E_{.M.}$ is power dissipation during metallurgical processing of materials such as DRV, DRX and superplasticity [102][113]. Deformation mechanism can be defined by important factor strain rate sensitivity (m) and m also affect the hot workability of materials. The value of m can be estimated by partial derivative of $\left[\frac{\partial \log \sigma}{\partial \log \dot{\varepsilon}}\right]_{T,\varepsilon}$ at constant absolute temperature (T) and strain (ε) or partial derivative of $E_{.M.}$ w.r.t. E_p. Furthermore, a different parameter used in DMM model such as power dissipation efficiency (η), instability parameter $\xi(\dot{\varepsilon})$, partial derivative of strain rate sensitivity w.r.t. strain rate (ṁ) and temperature sensitivity (s) and partial derivative of temperature sensitivity w.r.t. strain rate ($\dot{S}$) can be expressed as the following equations:

$$\eta = \frac{E_M}{E_M max} = \frac{2m}{m+1} \qquad (4.22)$$

$$\xi(\dot{\varepsilon}) = [\partial \ln (\frac{m}{m+1})/\partial ln\dot{\varepsilon}] + m < 0 \qquad (4.23)$$

$$\dot{m} = \frac{\delta m}{\delta log \dot{\varepsilon}} \qquad (4.24)$$

$$s = \frac{\delta ln \sigma}{\delta(\frac{1}{T})} \qquad (4.25)$$

$$\dot{s} = \frac{\delta s}{\delta log \dot{\varepsilon}} \qquad (4.26)$$

Based on DMM model criteria for homogenous or stable plastic deformation at different hot working condition can be defined as below:

$$0 < m < 1 \quad (4.27)$$

$$\dot{m} < 0 \quad (4.28)$$

$$S \geq 1 \quad (4.29)$$

$$\dot{S} \leq 0 \quad (4.30)$$

The processing maps constructed with change of the third parameter in z-axis at a different range of temperature and strain rate are shown in **Figure 4.21**. Processing maps with different parameters gives the estimation of stable plastic flow and unstable plastic flow, which correlates with the microstructure of the hot deformed samples. Further, it is found that microcrack free microstructure observed under the stable plastic flow while microcracks and porosity observed during unstable plastic flow condition.

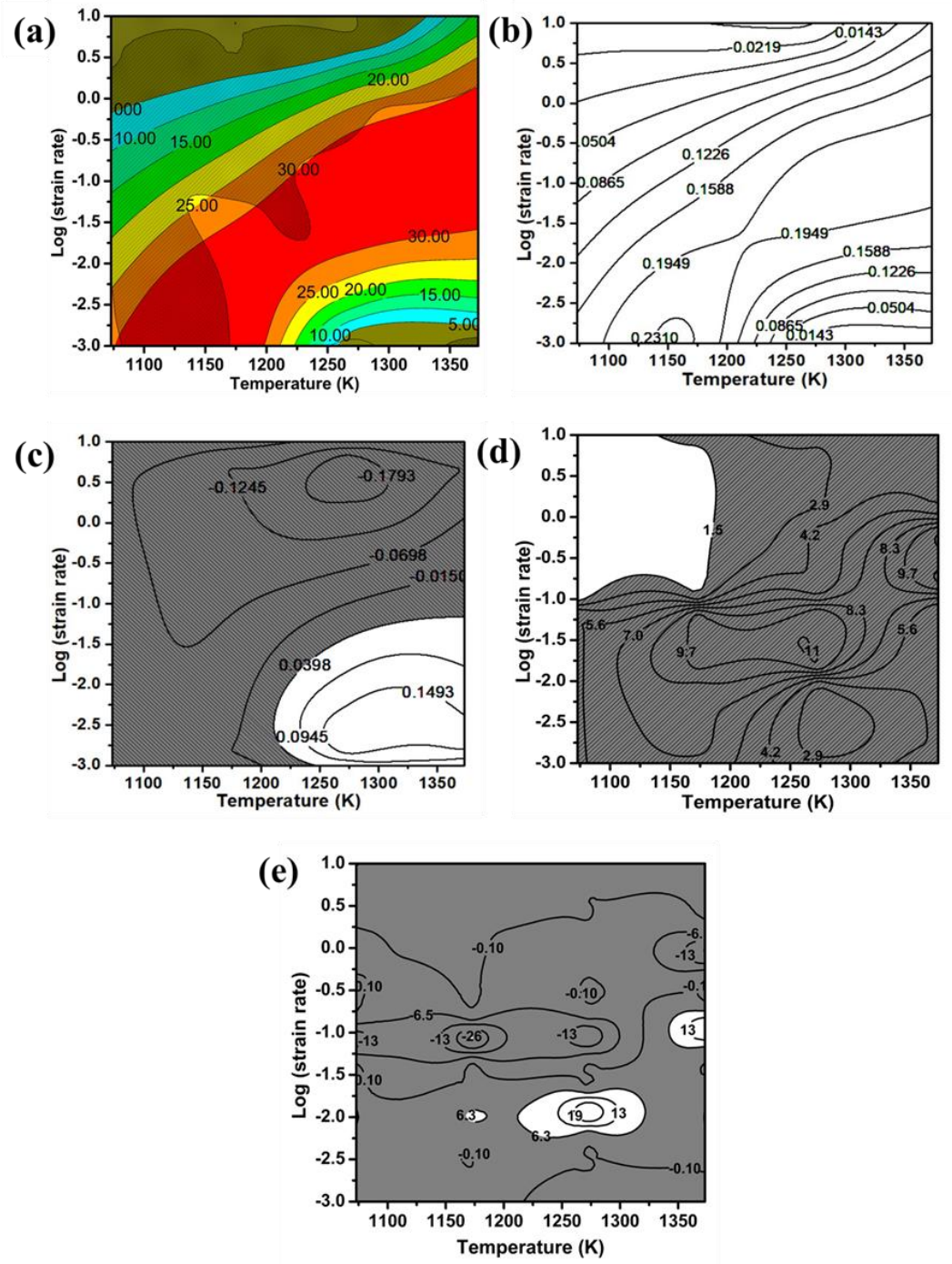

Figure 4.21 (a) Processing map at 0.69 strain, (b) m, (c) $\dot{\mathbf{m}}$, (d) s and (e) $\dot{\mathbf{s}}$.

The instability region in the processing maps is generally characterized by the identification of localized plastic flow or cracks in the hot deformed samples [106][154]. It is noted that DMM modelling fails to predict some microstructural geometry-related instability parameters; for example, during compressive loading, excessive bulging was observed in the deformed samples

under different thermomechanical conditions. For predicting geometry-based instabilities Semiatin and Jonas proposed the criteria of flow localization [155][156]. Processing map at strain 0.69 is obtained by superimposing the iso-efficiency contour plot over the instability parameter and observed unstable region with hatched line while other parts represent the stable region. The contour plot for strain rate sensitivity (m) investigated and observed no instability region found for the entire range of temperature with the strain rate regime. Furthermore, contour plots for other parameters $\dot{m}$, s and $\dot{s}$ shows the unstable zone marked as white, while stable zone marked as dark and hatched region. The stable and unstable regions with different parameters using the DMM model are given in **Table 4.4**.

Table 4.4 Stable and unstable regions with different parameters using DMM model.

DMM Parameters	Stable region	Unstable region
m	All	No
η	T=1165-1235K, 1235-1373K $\dot{\varepsilon}=10^{-3}$-$10^{-1.65}$ S^{-1}, 10^{-3}-$10^{-0.73}$ S^{-1}	T=1073-1133K, 1133-1373K $\dot{\varepsilon}=10^{-3}$-$10^{0.75}$ S^{-1}, $10^{-0.25}$-$10^{0.75}$ S^{-1}
$\xi(\dot{\varepsilon}) \leq 0$	T=1073-1133K, 1133-1373K $\dot{\varepsilon}=10^{-3}$-$10^{0.75}$ S^{-1}, $10^{-0.25}$-$10^{0.75}$ S^{-1}	T=1165-1235K, 1235-1373K $\dot{\varepsilon}=10^{-3}$-$10^{-1.65}$ S^{-1}, 10^{-3}-$10^{-0.73}$ S^{-1}
$\dot{m} < 0$	All stable (except T=1215-1373K $\dot{\varepsilon}=10^{-3}$-$10^{-1.25}$ S^{-1})	T=1215-1373K $\dot{\varepsilon}=10^{-3}$-$10^{-1.25}$ S^{-1}
$S \geq 0$	All stable (except T= 1073-1175 K $\dot{\varepsilon}=10^{-0.75}$-10 S^{-1})	T= 1073-1175 K $\dot{\varepsilon}=10^{-0.75}$-10 S^{-1}
$\dot{S} \leq 0$	T=1073-1340K, 1073-1373K,1340-1373K,1325-1373K,1073-1210K $\dot{\varepsilon}=10^{-1.65}$-10 S^{-1}, $10^{-0.25}$-10^{-3} S^{-1}, 10^{-3}-$10^{-1.20}$ S^{-1}, $10^{-0.75}$-10 S^{-1}, $10^{-2.25}$-$10^{-1.65}$ S^{-1}	T=1340-1373K, 1210-1325K $\dot{\varepsilon}=10^{-1.20}$-$10^{-0.75}$ S^{-1}, $10^{-2.25}$-$10^{-1.65}$ S^{-1}

The microstructural feature of the hot deformed samples identified the stable or unstable zone at different strain rates and temperatures, and these micrographs correlated with the processing maps. **Figure 4.22** shows the microstructure of the deformed sample at unstable (T=1000°C & SR=1 s^{-1}) domain. Furthermore, the unstable zone is characterized by localized plastic flow,

pores, and adiabatic shear banding. The microstructural features, efficiency, temperature range, and strain rate range are highlighted in **Table 4.5** with stable and unstable regimes.

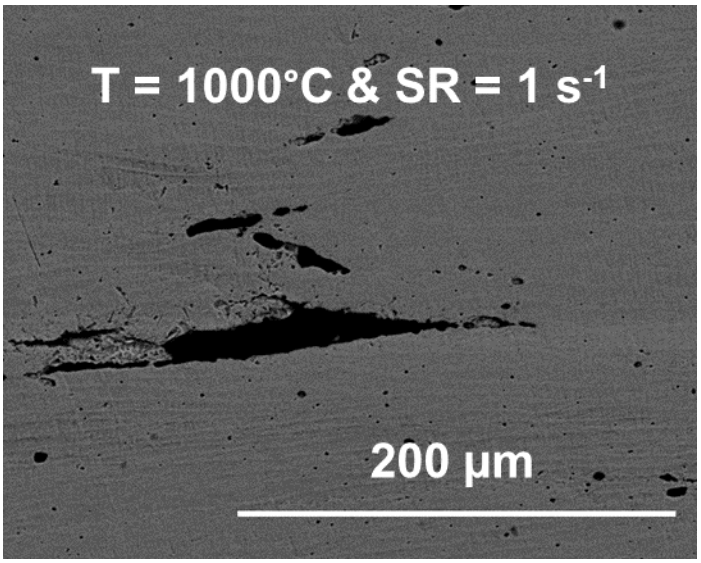

Figure 4.22 Microstructure characterization of deformed sample at unstable domain (T=1000°C, SR=1 s^{-1})

Table 4.5 Microstructural features at different strain rates and temperatures.

Domain	$\dot{\varepsilon}$ (s^{-1})	Temperature (K)	η (%)	Microstructural feature
Stable regimes	Stable (except $10^{-0.55}$-10^{1}, 10^{-3}-$10^{-2.55}$)	Stable (except 1073-1273, 1200-1373)	>20	Uniform distribution of phases in microstructure
Unstable regimes	$10^{-0.55}$-10^{1}, 10^{-3}-$10^{-2.55}$	1073-1273, 1200-1373	<10	Cracks and pores in the deformed microstructure

4.4.6 Deformation mechanism of single-phase $Fe_{25}Co_{25}Ni_{25}Cr_{20}V_5$ FCC HEA

The microstructure shows the presence of deformation bands in the grains at low temperature i.e. at 800° C, 0.1 s^{-1}. The deformation band is observed for both the orientations i.e. [001] and [111] which are parallel to the compression axis of the sample (**Figure 4.23a**). It is also observed the strain accumulation for both the above orientations are similar which can be seen from the grain orientation spread (GOS) value (**Figure 4.23d**). With the increase in the strain rate to 10 s^{-1} at 800° C, the deformation band is observed only in the large grains and most of the grains show the presence of annealing twins (**Figure 4.23b**). The presence of annealing twin reduces the local strain accumulation to a greater extent compared to the grains which do not contain annealing twins (**Figure 4.23c**). Nearly 13% of annealing twins is observed at 800° C, 10 s^{-1}. The annealing twin volume fraction is more in [001] oriented grains compared to that of [111] oriented grains resulting in the lower GOS value in the former one compared to the later (**Figure 4.23e**).

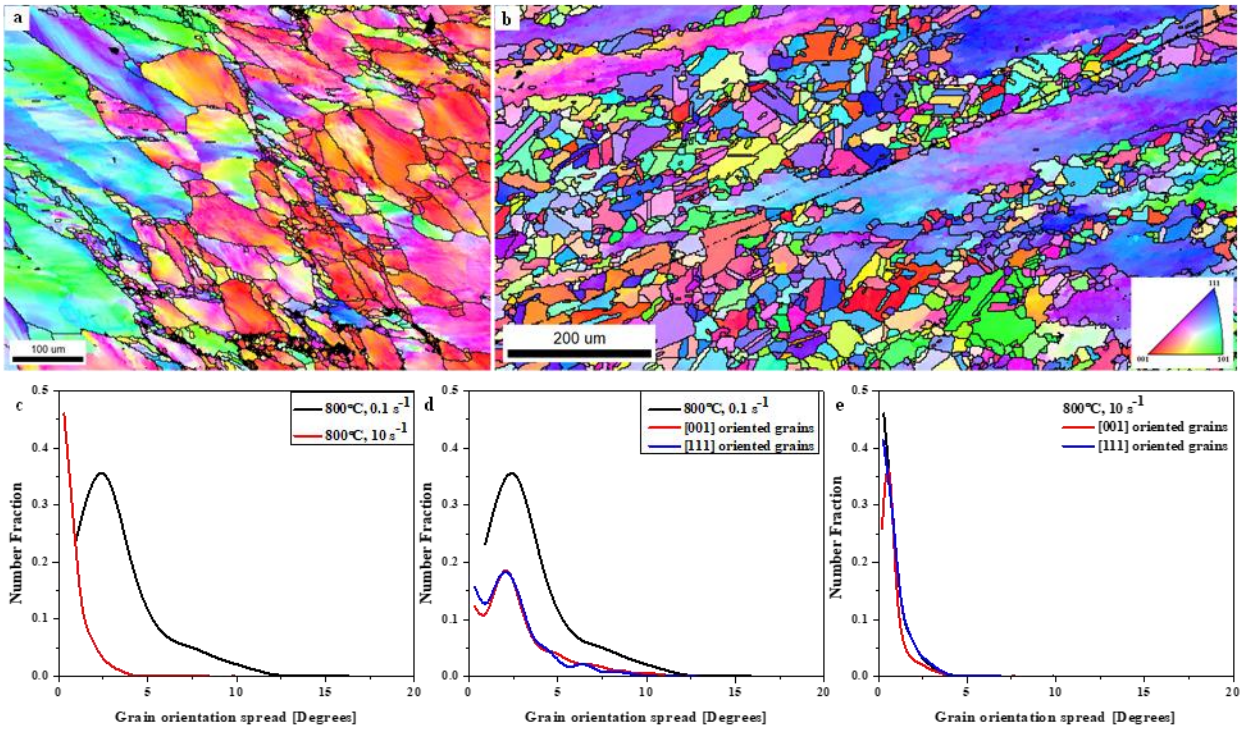

Figure 4.23 Inverse pole figure (IPF) map of the sample deformed at (a) 800° C, 0.1 s^{-1}, (b) 800° C, 10 s^{-1}, (c) comparison of local strain distribution in the form of GOS plot at two different strain rates, (d) comparison of local strain distribution of [001] and [111] orientations with respect to the overall GOS value of the sample deformed at 800° C, 0.1 s^{-1} and (e) comparison of local strain distribution of [001] and [111] orientations with respect to the overall GOS value of the sample deformed at 800° C, 10 s^{-1}.

However, the presence of deformation band is observed in the samples deformed at 1000° C only in [001] oriented grains (**Figure 4.24**). The [111] oriented grains present as small grains in the boundary of [001] oriented grains (see **Figure 4.24b**) which indicates that at high temperature, [001] orientation is stable compared to other grains. The magnified image of small grains present at the boundary (see **Figure 4.24d**) indicates that the small grains of similar orientation to that of parent grain are formed through gradual transformation of very low angle grain boundaries in the range of 2-5° (VLAGBs) to low angle grain boundaries in the range of 5-15° (LAGBs) and finally high angle grain boundaries (HAGBs). The gradual transformation from VLAGBs to LAGBs indicate that the dynamic recovery is the dominant grain refinement mechanism in the above alloy. Further, no annealing twins are observed in the grains deformed at 1000° C resulting in the higher GOS value at high strain rate compared to low strain rate of deformation (**Figure 4.24e**).

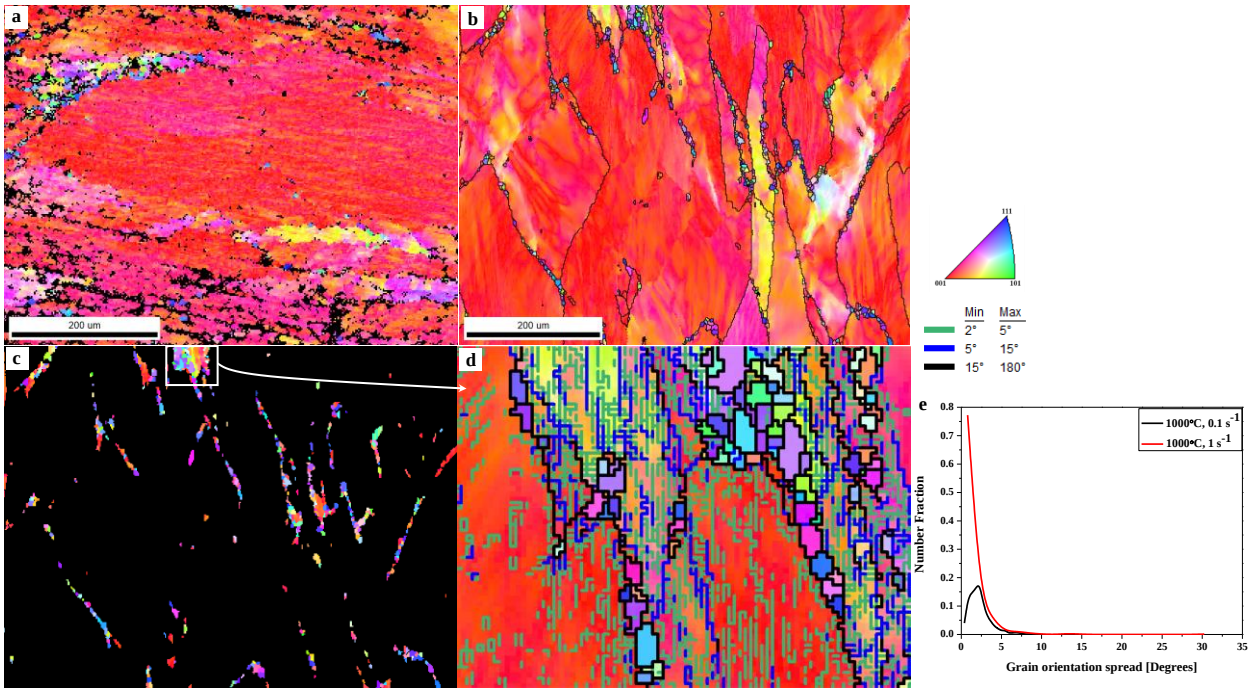

Figure 4.24 Inverse pole figure (IPF) map of the sample deformed at (a) 1000° C, 0.1 s^{-1}, (b) 1000° C, 1 s^{-1}, (c) partitioned microstructure containing small grains for the sample deformed at 1000° C, 1 s^{-1}, (d) magnified image of the rectangular section in the Fig. (c), (e) comparison of local strain distribution in the form of GOS plot at two different strain rates.

Similarly, at high temperature and low strain rate i.e 1100° C, 0.001 s^{-1}, deformation bands are observed in the large grains (**Figure 4.25a, 4.25b**). The small grains of similar orientation to that of parent grain or different orientation to that of parent grain (**Figure 4.25c, 4.25d)** are decorating the grain boundaries of large grain. With increase in the strain rate to 0.1 s^{-1} at 1100° C, the presence of annealing twins are observed in the microstructure (**Figure 4.25d**). Consistent with the observation at 800° C and 10 s^{-1}, the presence of annealing twins reduces the strain accumulation in the grains compared to the microstructure which do not show the formation of annealing twins during deformation (**Figure 4.25e**).

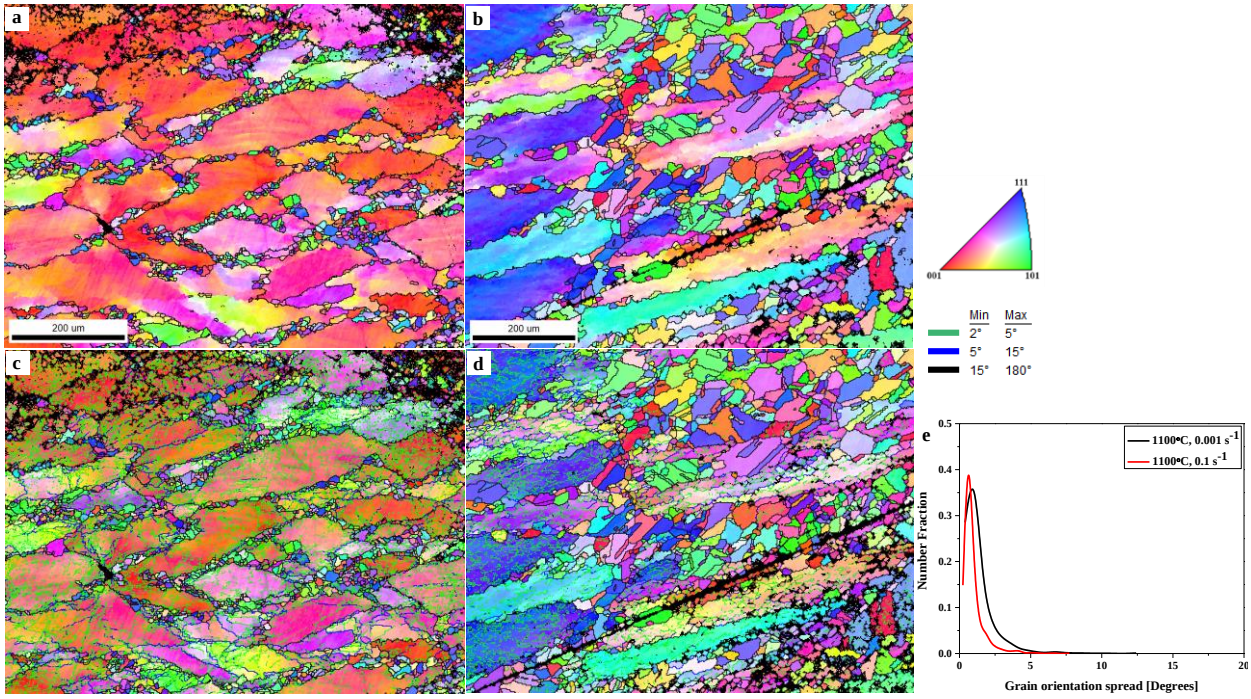

Figure 4.25 Inverse pole figure (IPF) map of the sample deformed at (a) 1100° C, 0.001 s^{-1}, (b) 1100° C, 0.1 s^{-1}, (c) microstructure superimposed with different types of grain boundaries for the sample deformed at 1100° C, 0.001 s^{-1}, (d) microstructure superimposed with different types of grain boundaries for the sample deformed at 1100° C, 0.1 s^{-1}, (e) comparison of local strain distribution in the form of GOS plot at two different strain rates.

The microstructure reveals the gradual transformation of VLAGBs to LAGBs and finally to HAGBS, indicating that the dynamic recovery is the dominant mechanism of grain refinement during high-temperature deformation. It is concluded that the deformation band forms during low strain rate deformation and annealing twins formed during high strain rate deformation. The strain accumulation is also less in the microstructure containing annealing twins compared to the microstructure which do not show the presence of annealing twins. The possible deformation mechanism of CoCrFeNiV single-phase FCC HEA is schematically shown in **Figure 4.26**. Figure 4.26a and Figure 4.26b show the Thompson tetrahedra for high and low stacking fault energy of the material, respectively. It is known that the material having low and high SFE favors the planar slip and cross slip of dislocations. The HEA which contains the maximum solubility of solute atoms favors the planar slip by decreasing the SFE of the material resulting in difficulty in cross-slip of the dislocations (Figure 4.26(b)). Further, the planar dislocations interacted with solute atoms during the intermediate stage of deformation (Figure 4.26(d)) and making it hard for further movement of dislocations. As the applied load increases during further

deformation, saturation of planar slip in the slip planes leads to the formation of deformation bands (shown by red color bands in Figure 4.26(e)). The probability of formation of deformation band decreases with increase in the deformation temperature because at high temperature, the dislocation can easily break away from the solute atmosphere and enhancing the dislocation-dislocation interactions. The dislocation-dislocation interaction facilitates the annihilation of dislocations at high temperature resulting in no saturation of planar slip during deformation. Further high temperature deformation enhances the migration of grain boundaries resulting in the formation of annealing twins (shown by blue color bands in Figure 4.26(f)). The low stacking fault energy (SFE) of HEA favors the planar slip (**Figure 4.26b**) whereas the cross-slip is favored by the materials with high SFE (**Figure 4.26a).** The dislocations interacted with solute atoms during the intermediate stage of deformation **(Figure 4.26d).** As in HEA, planar slip favors during initial stage of deformation and on further deformation, saturation of planar slip in the slip planes leads to the formation of deformation bands (shown by red color bands in **Figure 4.26e**). The probability of formation of deformation band decreases with increase in the deformation temperature. Further high temperature deformation enhances the migration of grain boundaries resulting in the formation of annealing twins (shown by blue color bands in **Figure 4.26f**).

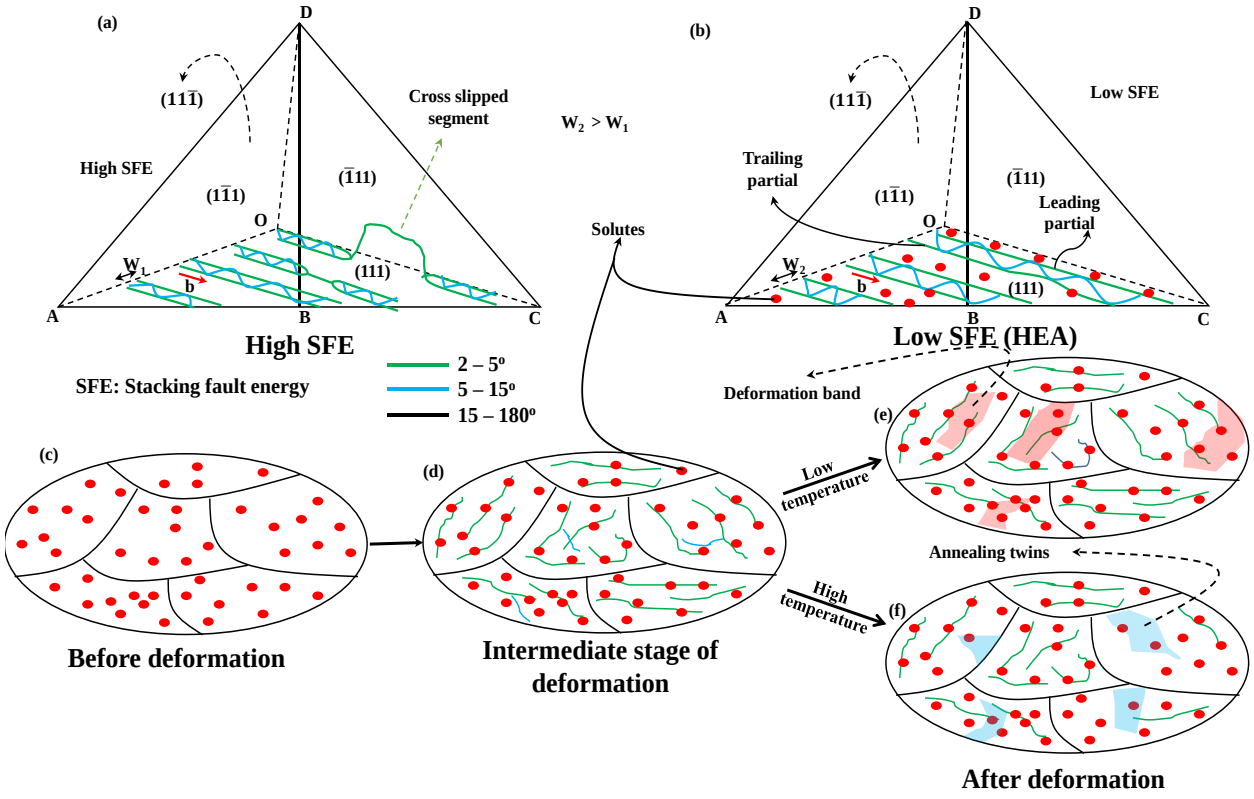

Figure 4.26 Plausible deformation mechanism of CoCrFeNiV single-phase FCC HEA.

4.4.7 FEM simulation

Figure 4.27 shows the effective strain field distribution inside sample after the compression isothermal compression of 50 %. From the FEM simulation, it is clear that the distribution of strain field will change according to the strain rate and temperature. It is to be noted that all cases the high strained region is observed at the center of the sample and it is greater than the average strain experienced by the bulk sample. This stain field distribution will cause inhomogeneous microstructure evolution within the sample and will be prominent if a large gradient in strain field distribution. The macroscale simulation will help to identify the stress concentration points in complex geometries in actual forging conditions.

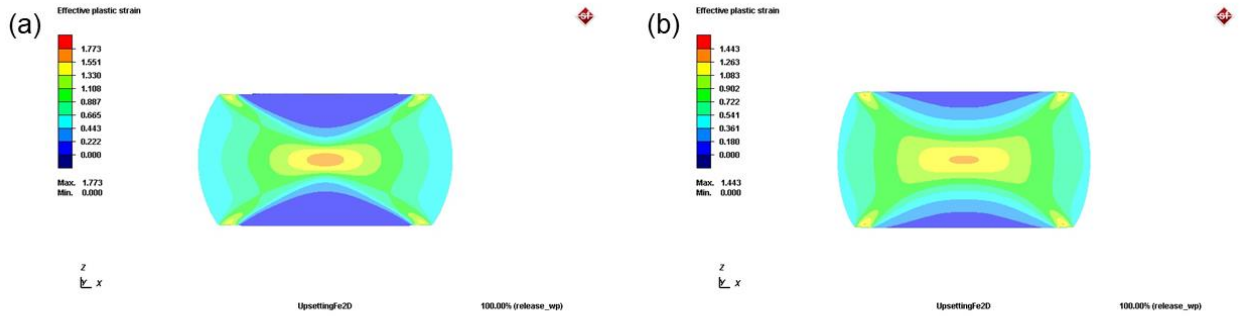

Figure 4.27 Strain field distribution simulated by FEM studies (a) T = 900 ^{o}C and strain rate = 0.001 s^{-1} and (b) T = 900 ^{o}C and strain rate = 10 s^{-1}.

4.4.8 ICME framework for HEA design

The current work implements the ICME workflow for alloy design and development. **Figure 4.28** shows the workflow adopted for the current study and it confirms that the current study will accelerate the alloy development. Here based on the property requirement the elements will be selected and then thermodynamic simulation for prediction of possible phase formation. This Thermo-Calc study will be carried out to screen the possible composition. The approximate microstructure for the selected alloy will be predicted by phase-field simulation and one can avoid some compositions with detrimental phase formation at this stage. Then the alloy can be prepared and characterized, the current study will provide the direction to reduce the number of experimental trials and also accelerate the material development.

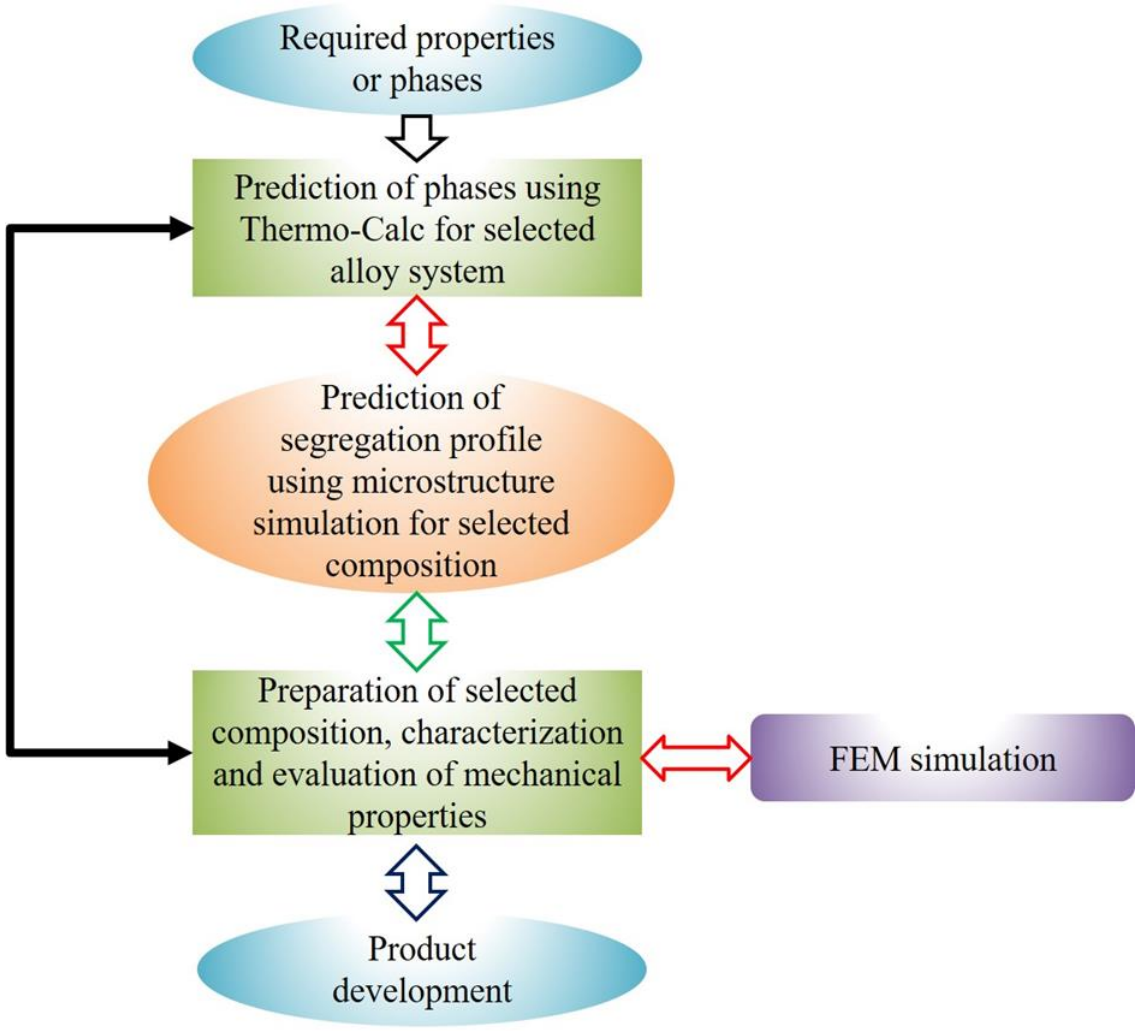

Figure 4.28 Workflow adopted in the current study

4.5 Summary

- Using phase-field simulation, a refractory metal based single-phase CoCrNiFeV HEA was identified and prepared by arc melting route.
- Scheil's solidification pathway analysis showed that during solidification limited segregation of Cr and V at the interdendritic region was possible. Using suction casting under fast cooling rates, such segregations were suppressed.

- EBSD examination of deformed samples showed the formation of the deformation bands in the lower temperature range 1073-1173K and annealing twins at high temperature range 1273-1373K.
- The presence of deformation bands and annealing twins causes hardening and softening during deformation respectively. The annealing twins formed at high temperature because of the higher mobility of the grain boundaries at high temperature compared to lower temperature of deformation. Based on the evolution of the microstructures during the deformation process, the spread of GOS and softening could be explained.

Chapter 5

Design and development of higher order EHEAs

5.1 Introduction:

The present work explores the design and development of seven component $Fe_{35-x}Co_{10}Ni_{25}Cr_{15}Mn_5V_{10}Nbx$ *(x =2.5, 5, 7.5, and 10 at. %) and higher-order eight component* $Fe_{32.5-x}Co_{10}Ni_{25}Cr_{15}Mn_5V_{10}Al_{2.5}Nbx$ *(x= 5, 7.5, 10, and 12.5 at. %) eutectic high entropy alloys (EHEAs) using a combination of thermodynamic simulation and experimental approach. The studied seven-component EHEAs consist of primary Fe-Ni-Cr rich FCC solid solution phase and eutectic mixture between FCC solid solution phase and Nb-rich* $(Co, Fe)_2Nb$*-type C14 Laves phase. The studied* $Fe_{32.5-x}Co_{10}Ni_{25}Cr_{15}Mn_5V_{10}Al_{2.5}Nbx$ *(x= 5, 7.5, 10, and 12.5 at. %) consist of FeCoNiCr-rich FCC solid solution phase and eutectics mixture between FCC solid solution phase and the* Co_2Nb*-type Laves phase. The microstructural feature of studied EHEAs varies from hypoeutectic to fully eutectic with an increase of Nb concentration, and the microhardness increases with increasing Nb concentration. Furthermore, the hardness values of reported HEAs along with the studied EHEAs as a function of alloying elements are taken into consideration to establish an artificial neural network (ANN) model to predict the microhardness of EHEAs.*

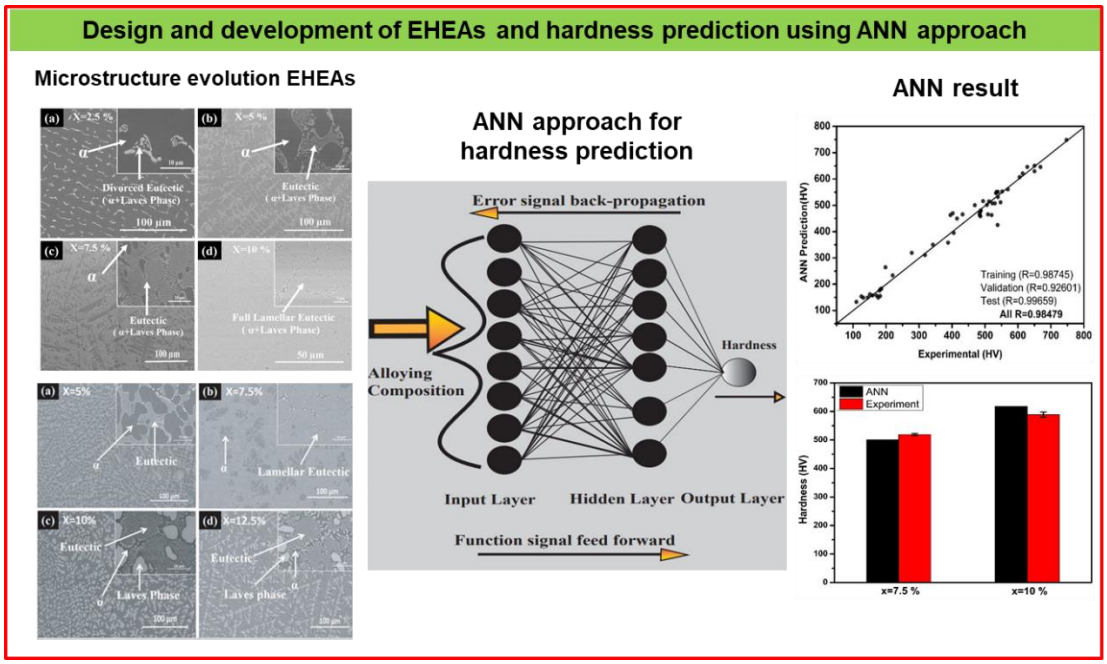

Figure 5.1 Schematic representation of the detailed study of EHEAs

5.2 Objective:

To the best of the author's knowledge, higher-order eight component EHEAs have not been reported in the open literature and the artificial neural network (ANN) analysis of EHEAs has not been investigated so far. Therefore, the primary objective of the current study are highlighted as follows:

(i) Single-phase FCC $Fe_{32.5}Co_{10}Ni_{25}Cr_{15}Mn_5V_{10}Al_{2.5}$ HEA, seven component $Fe_{35-x}Co_{10}Ni_{25}Cr_{15}Mn_5V_{10}Nbx$ (x =2.5, 5, 7.5, and 10 at. %) and higher-order eight-component $Fe_{32.5-x}Co_{10}Ni_{25}Cr_{15}Mn_5V_{10}Al_{2.5}Nbx$ (x=5 at. % and x=12.5 at. %) EHEAs have been designed based on thermodynamic simulation, followed by preparation of HEAs by vacuum arc melting technique. Subsequently, the microstructural evolution of studied HEAs is studied.

(ii) **Seven component $Fe_{35-x}Co_{10}Ni_{25}Cr_{15}Mn_5V_{10}Nbx$ (x=2.5, 5, 7.5, and 10 at. %)**: The different thermodynamics parameters are calculated to understand the phase stability and phase formation criteria in studied EHEAs. Furthermore, a simple ANN approach used a back-propagation (B-P) training algorithm is developed by considering mechanical properties data of 53 HEAs, including present studied $Fe_{35-x}Co_{10}Ni_{25}Cr_{15}Mn_5V_{10}Nbx$

(x=2.5, 5, 7.5, and 10 at. %) EHEAs, and the performance of the developed ANN model is assessed through the R and AARE for the prediction of microhardness of HEAs.

(iii) **Higher-order eight-component $Fe_{32.5-x}Co_{10}Ni_{25}Cr_{15}Mn_5V_{10}Al_{2.5}Nbx$ (x= 5, 7.5, 10, and 12.5 at. %)**: An ANN model with a back-propagation (B-P) training algorithm was established based upon the microhardness database of 51-HEAs, including the current studied two EHEAs x=5 at. % and x=12.5 at. %. The microhardness of two other designed EHEAs with x=7.5 at. % and x=10 at. % is predicted using the ANN model and correlated with the observed experimental value.

5.3 Experimental and simulation details

High purity elements Al, Co, Cr, Fe, Mn, Nb, Ni, Nb, and V (purity level ≥ 99.7) were used as preliminary material. The $Fe_{35-X}Co_{10}Ni_{25}Cr_{15}Mn_5V_{10}Nbx$ (x =2.5, 5, 7.5, and 10 at. %) and $Fe_{32.5-x}Co_{10}Ni_{25}Cr_{15}Mn_5V_{10}Al_{2.5}Nbx$ (x= 5, 7.5, 10, and 12.5 at. %) alloy ingots were prepared by vacuum arc melting under ultra-high purity argon gas in the water-cooled copper hearth plate using non-consumable tungsten electrode. The alloy ingot was melted five times to achieve good homogeneity. The phase identification of the as-cast alloy was carried out using X-ray diffraction (Panalytical X-pert pro instrument) with Cu K_α (λ = 0.154056 nm) radiation, operating at 45 kV and 30 mA, with a step size of 2θ=0.017 deg. The microstructural characterization and the composition analysis of constituent phases of the investigated alloys were examined using the scanning electron microscope (model NOVA NANOSEM 450) equipped with a Bruker SDD-EDS detector. The hardness measurement was carried out using Vickers microhardness tester under the load of 200 gf for 10 seconds. It is to be noted that ten measurements were made on each studied EHEAs to get the averaged experimental microhardness.

5.3.1 ANN model for seven component EHEAs:

It is important to note that ANN modelling includes generating desired data, selecting the algorithm for modelling, dividing the datasets for training, testing, and validation, followed by training of data. In this study, the alloying element considers as input data and experimentally obtained microhardness as output data. For ANN simulation, a total of 53 datasets are used (given in **Appendix 1)**. Among these datasets, 70 % dataset is used in training, 15% dataset is used for validation, and 15% dataset is used in testing. For efficient training, it is necessary to scale the input and output dataset together in the range of 0 to 1 using the following equation.

$$X_{nor.} = 0.1 + 0.8 \times \left(\frac{X - X_{min.}}{X_{max.} - X_{min.}}\right) \qquad (5.1)$$

; where Xnor. is the normalized value, X is the original value, $X_{min.}$, and $X_{max.}$ are the minimum and maximum value of datasets, respectively.

5.3.2 ANN model for eight component EHEAs:

An artificial neural network (ANN) based computational model, has been established to predict the microhardness of HEAs, along with studied EHEAs as a function of alloying elements. A data set of the 49 previously reported different multicomponent HEAs compositions with their microhardness and 2 datasets of present work has been taken into consideration for performing the modeling work in the present studied HEAs. Initially, the data set could be reduced to the value between 0 - 1 before applying for the training. The purpose of the reduction is to maintain the steadiness of the input data that could be achieved by the feature scaling. The equation of feature scaling can be presented as equation 5.2:

$$x_{fscale} = \frac{x_i - mean(x_i)}{std(x_i)} \qquad (5.2)$$

Where x_i is the composition of ith element in the alloy and i ∈ 1, 2, 3……n and x_{fscale} is scaled value.

The back-propagation (BP) neural network, which alters the network weights to minimize the mean square error (MSE) was used. The model was tested, validated, and found that the excellent performance of the model was achieved. The Artificial Neural Network (ANN) model with the back-propagation 8-8-1 model (8, 8, and 1 are neurons in the input layer, hidden layer, and in the output layer, respectively) is used for predicting microhardness. MATLAB 9.6 (R2019a) version is utilized as a simulation tool. A HEAs database with different compositions for the ANN model is given in **Appendix 2**.

5.3.3 Performance of ANN model:

The predictability of the model is expressed in the form of mean square error (MSE) and correlation coefficient (R), and absolute average relative error (AARE). The correlation coefficient (R) and the average absolute relative error of the model calculated using equations 5.3 and 5.4, respectively.

$$R = \frac{\sum_{i=1}^{N}(H_e^i - \overline{H}_e) \times (H_p^i - \overline{H}_p)}{\sqrt{\sum_{i=1}^{N}(H_e^i - \overline{H}_e)^2 \times \sum_{i=1}^{N}(H_p^i - \overline{H}_p)^2}} \qquad (5.3)$$

$$AARE(\%) = \frac{1}{N} \times \sum_{i=1}^{N} \left| \frac{H_e^i - H_p^i}{H_e^i} \right| \times 100 \qquad (5.4)$$

Where $H_e^i$and H_p^i are predicted and experimental microhardness, respectively; $\overline{H}_e$and $\overline{H}_p$are the mean value of H_e^i and H_p^i, respectively; N is the total number of the dataset used for the model.

5.4 Results and discussion:

5.4.1 Thermo-physical properties calculation:

Thermo-physical properties for $Fe_{35-X}Co_{10}Ni_{25}Cr_{15}Mn_5V_{10}Nbx$ (x=2.5, 5, 7.5, 10 at. %) EHEAs:

It is worthy of mentioning that the theoretical thermo-physical properties such as mixing of entropy (ΔS_{mix}), mixing of enthalpy (ΔH_{mix}), atomic size difference (δ), valence electron concentration (VEC), theoretical melting point (T_m), and electronegativity difference are calculated for the investigated EHEAs [45][36][157][14]. The mathematical expressions for all thermo-physical properties are given in the chapter 2 in section 2.2.

Atomic size difference (δ), valence electron concentration (VEC), and electronegativity of alloying elements are taken from the open literature. All physicochemical and thermodynamic parameter provides the guideline for the prediction of phases in the designed HEAs. It is important to note here that all parameters (Thermodynamics and Hum-Rothery parameters) for $Fe_{35-X}Co_{10}Ni_{25}Cr_{15}Mn_5V_{10}Nbx$ (X=2.5, 5, 7.5 and 10 at. %) EHEAs are calculated by formula as mentioned above, and the value of different parameters was given in **Table 5.1.** ΔH_{mix} and ΔS_{mix} value are calculated for all phases present in the HEAs system. All other parameters such as VEC, δ, and $\Delta\chi$ are also calculated for only nominal composition. Chanda et al. [14] reported that the formation of the eutectic phase in HEAs is possible when (ΔH_{mix}) lies between -18 to -6 J/mol, and VEC ranges from 6 to 8.5. Therefore, in the present studied HEAs system, the value of (ΔH_{mix}) and VEC lie in the range -6.88 kJ/mol to -12.72 kJ/mol and 7.67 to 7.87 respectively, which indicates the possibility of formation of eutectic microstructure. It is noticed that the entropy of mixing increases with Nb concentration and the calculated mixing of entropy for different phases (primary FCC phase, and eutectic phase) varies with Nb-concentration, as given in **Table 5.1**. The ΔS_{mix} for primary FCC phase and eutectic phase increases with increasing of Nb concentration. **Figure 5.2a** shows that ΔH_{mix} of EHEAs decreases with increasing the Nb concentration as well as the δ parameter increases with increasing Nb concentration. It is to be noted that a higher negative value of enthalpy of mixing promotes the formation of intermetallic

compounds. In contrast, higher positive values of ΔHmix indicate the separation of phases. Hence, a higher negative value of ΔH_{mix} may lead to the formation of a dual-phase mixture by destabilizing the single solid solution phase in studied HEAs [14]. Moreover, the large value of δ parameter enhances the formation of different compounds or intermediate phase due to lattice distortion, which destabilizes the single phase. In the current study, the formation of both FCC solid solution phase and C14 Laves phase is possible by destabilizing the single-FCC solid solution phase due to the addition of Nb. It is found that the atomic radius (r) of Nb is 1.429 Å, which is larger than other alloying element (r_{Co}= 1.251Å, r_{Fe} =1.241Å, r_{Ni} =1.246 Å, r_{Cr}=1.249 Å, r_{Mn}=1.350 Å, r_V = 1.316Å) in the studied HEAs, which may favorable situation for the formation of secondary phase(s).

Furthermore, Guo et al. reported that single phase FCC HEAs are stable at VEC ≥ 8, BCC HEAs are stable at VEC < 6.87 [36] and both BCC and FCC phase are stable for VEC value in the range 6.87–8. The valence electron concentration (VEC) value for x= 0 at. % is near to 8 showing the formation of a single FCC solid solution. The calculated VEC values in the present studied HEAs are 7.87, 7.80, 7.72, and 7.65 for x=2.5 at. %, 5 at. %, 7.5 at. % and 10 at. % respectively. It is to be noted that the VEC value of Nb is lower than the average VEC value of the studied HEAs and observed that VEC value decreases with Nb concentration, as shown in **Figure 5.2b**. It is observed that the increase in Nb concentration leads to an increase in the Δχ, revealing the formation of intermetallics. It is reported that the parameter Δχ does not influence much in the formation of a solid solution phase in HEAs. For the formation of the solid solution phase in HEAs, the mixing of enthalpy (ΔH_{mix}) is considered an important factor and the rest of thermophysical parameters such as δ electronegativity difference, and VEC fails to predict the formation of solid solution phase effectively [36].

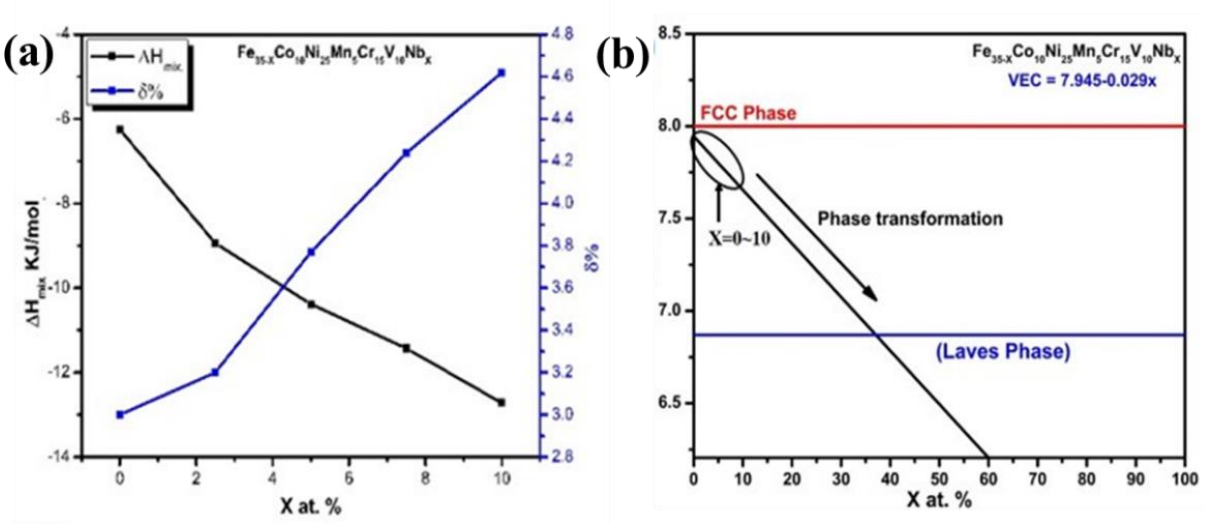

Figure 5.2 (a) Phase transformation with VEC w.r.t. Nb at. % (b) Mixing of Enthalpy ($\Delta H_{mix.}$) and atomic radius percent (δ%)

Yang et al. [46] and Guo et al. [157] introduced a new factor for the estimation of solid solution phase formation in HEAs, which is known as scald ratio (Ω). The scald ratio shows the collective effect of ΔH_{mix} and ΔS_{mix} (mathematical equations are given in the chapter 2 in section 2.2).

As in the case of x = 0 at. %; Ω is large, i.e., and the mixing entropy is predominant over enthalpy; thus, there is a formation of a single solid solution phase. It is noticed that the Ω decreases with increasing the Nb content, revealing that the effect of mixing of enthalpy is dominant over the entropy of mixing, thus showing an increase in the formation of intermetallic compounds in the studied EHEAs. Apart from the above parameter, Singh et al. [47] developed a new geometrical factor Λ, which consider the effect of ΔS_{mix} and δ simultaneously (mathematical equations are given in the chapter 2 in section 2.2).

The Λ parameter is used to predict the formation of phases and its volume fraction. Value of Λ for the formation single-phase (value of $\Lambda > 0.96$), dual-phase ($0.24 < \Lambda < 0.96$), and solid solution with compounds ($\Lambda < 0.24$). For the present study, The value of Λ for x= 0 at. %, x=2.5 at. % and x= 5 at. % are large, revealing that mixing entropy (ΔS_{mix}) is predominant over atomic size difference (δ) factor. Thus, there is an evolution of the single solid solution phase and increasing the Nb concentration, the value of Λ decreases, causing the formation of the dual-phase eutectic structure, comprising the solid solution phase and intermetallics. The value of Λ for studied EHEAs is also given in **Table 5.1**. The electron concentration factor (e/a)

significantly influences the phase evolution when the constituent size factor for an alloy is favourable. The stability of the phase can be described in terms of the brillouin zone and Fermi surface interaction. For the stability of a particular phase, spherical Fermi surface must touch the brillouin zone of the concerned phase. The calculated value of the average itinerant electrons per atom ($\overline{e/a}$) was found to increase from 0.89 to 1.59 as shown in **Table 5.1**. The parameter (e/a) ratio can be expressed as:

$$e/a = \sum_{i=1}^{n} c_i (e/a)_i$$

Thermo-physical properties for $Fe_{32.5-x}Co_{10}Ni_{25}Cr_{15}Mn_5V_{10}Al_{2.5}Nbx$ (x= 5, 7.5, 10, and 12.5 at. %) EHEAs:

All the calculation of thermo-physical properties for $Fe_{32.5-x}Co_{10}Ni_{25}Cr_{15}Mn_5V_{10}Al_{2.5}Nbx$ (x= 5, 7.5, 10, and 12.5 at. %) EHEAs given in **Table 5.2**.

Table 5.1 Thermo-physical properties ΔS_{mix}, ΔH_{mix}, VEC, δ%, $\Delta\chi$, Ω and ʌ for $Fe_{32.5-x}Co_{10}Ni_{25}Cr_{15}Mn_5V_{10}\ Al_{2.5}Nbx$ (X=5, 7.5, 10, 12.5)

Alloys compositions	**Phases**	**ΔH_{mix} (KJ/mol)**	**ΔS_{mix} (J/k-mol)**	**VEC**	**δ%**	**$\Delta\chi$**	**Ω**	**Λ**	**e/a**
x = 2.5%	FCC(α)	-6.88	1.61R	7.89	3.39	0.2267	3.89	1.16	1.03
	Eutectic	-11.64	1.71R	7.73	3.42	0.2356	2.35	1.05	1.04
	Nominal	-8.94	1.70R	7.87	3.20	0.2215	2.55	1.38	1.59
x = 5%	FCC(α)	-7.60	1.71R	7.83	3.81	0.2719	2.67	0.97	0.98
	Eutectic	-9.48	1.71R	7.65	3.84	0.2752	2.49	0.96	1.01
	Nominal	-10.38	1.75R	7.80	3.77	0.2680	2.30	1.02	1.42
x = 7.5%	FCC(α)	-7.82	1.79R	7.76	4.43	0.3195	2.43	0.75	0.91
	Eutectic	-11.77	1.79R	7.62	4.48	0.3274	2.02	0.76	0.97
	Nominal	-11.43	1.79R	7.72	4.24	0.3177	2.16	0.83	1.29
x = 10%	Eutectic	-11.90	1.82R	7.59	4.79	0.3093	2.16	0.65	0.89
	Nominal	-12.72	1.80R	7.65	4.62	0.3015	1.98	0.70	1.15

Table 5.2 Thermo-physical properties ΔS_{mix}, ΔH_{mix}, VEC, δ%, Δχ, Ω and ʌ for $Fe_{32.5-x}Co_{10}Ni_{25}Cr_{15}Mn_5V_{10}$ $Al_{2.5}Nbx$ (X=5, 7.5, 10, 12.5)

Alloys compositions	ΔH_{mix} (KJ/mol)	ΔS_{mix} (J/k-mol)	VEC	δ%	Δχ	Ω	ʌ
X= 5 at. %	-10.38	1.838R	7.7	4.20	0.123	2.78	0.866
X= 7.5 at. %	11.61	1.874R	7.5	4.64	0.126	2.56	0.723
X= 10 at. %	12.77	1.90R	7.3	4.96	0.129	2.39	0.642
X= 12.5 at. %	13.90	1.915R	7.25	5.23	0.131	2.24	0.582

5.4.2 Thermodynamics simulation:

It is worthy of mentioning that the novel HEAs are designed by a thermodynamic simulation approach to optimize alloy parameters within the complication of the HEA composition space [48][158]. The thermodynamic simulation is carried out in the studied EHEAs for the analysis of phase formation during the solidification by the thermodynamic simulation approach with the help of ThermoCalc® software (thermo-Calc Software, Salona, Sweden) using TCHEA2® database. The phase formation during the non-equilibrium solidification technique is generally defined by Gulliver-Scheil model in which the liquid concentration at the solid-liquid interface can be formulated as $C_l = C_i(1 - fs)^{K-1}$ [71]; where Ci is the initial liquid concentration, fs is a solid fraction, and K is the equilibrium partition constant. It is to be noted that the phase formation during solidification may deviate from solidification model due to the following factors: (a) diffusion in the solid phase is not always negligible due to the back diffusion, (b) diffusion in the liquid is not sufficiently high because of higher cooling rate, (c) phase(s) having high nucleation barrier may not able to form during solidification [159].

Thermodynamics simulation of seven component EHEAs:

Figure 5.3a and **Figure 5.3b** shows the mole fraction of phases *Vs.* temperature plot and Scheil solidification pathways plot of HEA with x= 5 at. %, respectively. It is observed that the formation of FCC_L12 primary phase, followed by the formation of a dual-phase mixture of FCC_L12 and C14_Laves phases from the remaining liquid and finally the last liquid solidifies into a three-phase mix of BCC_B2, C14_Laves, and FCC_L12 phases. It is also to be noted that

C14_Laves, FCC_L12, BCC_B2, SIGMA, NI3TA_DOA, and SIGMA#2 phases are evolved during the solid-state phase transformation. **Figure 5.3c** and **Figure 5.3d** shows the mole fraction of phases *Vs.* temperature plot and solidification pathway plot respectively for HEA with x=10 at. %, which indicates that first C14_Laves phase is formed from the liquid, then the remaining liquid undergoes phase transformation to form dual-phase mixture between FCC_L12 and C14_Laves phase form, then the evolution of three-phase mixture (BCC_B2+ C14_Laves + FCC_L12) and four-phase mixture (BCC_B2+ C14_Laves + FCC_L12 + SIGMA). The C14_Laves, FCC_L12, BCC_B2, SIGMA, NI3TA_DOA, and SIGMA#2 phases are formed during solid-state transformation.

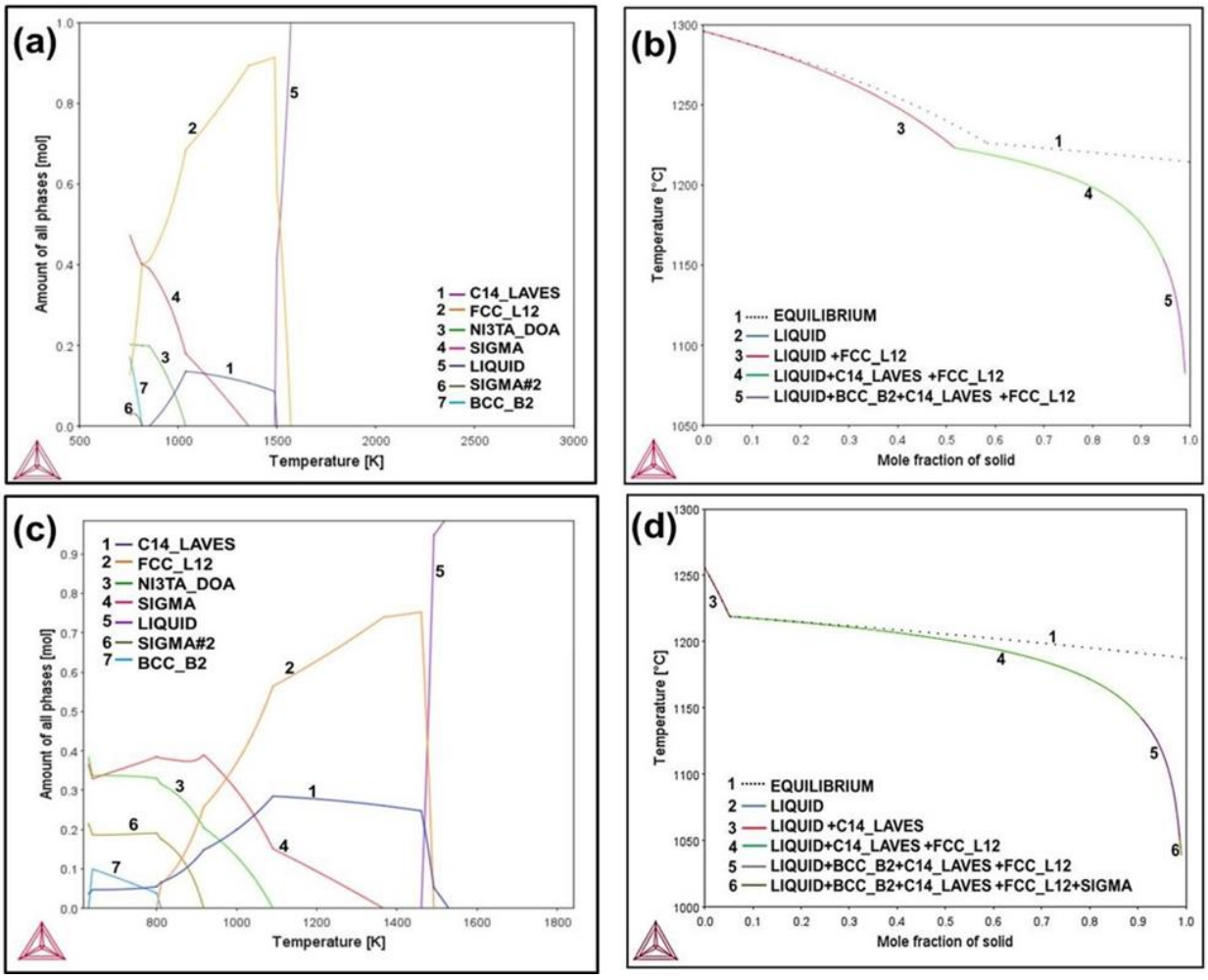

Figure 5.3 (a) Mole fraction of phases with temperature plot for alloy x=5%, (b) Scheil's solidification pathway for x=5%, (c) Mole fraction of phases with temperature plot for alloy x=10%, and (d) Scheil's solidification pathway for x=10%.

Thermodynamics simulation of eight component EHEAs:

Figure 5.4a shows the amount of phases with temperature plot for $Fe_{32.5}Co_{10}Ni_{25}Cr_{15}Mn_5V_{10}Al_{2.5}$ HEA, which indicates that the single-phase composition range is very large and also the alloy is stable at high temperature. **Figure 5.4b** shows the Scheil's solidification pathways for the $Fe_{32.5}Co_{10}Ni_{25}Cr_{15}Mn_5V_{10}Al_{2.5}$, which indicates the formation of the FCC solid solution phase from the liquid and last liquid solidifies to form a dual-phase mixture having FCC and BCC phase.

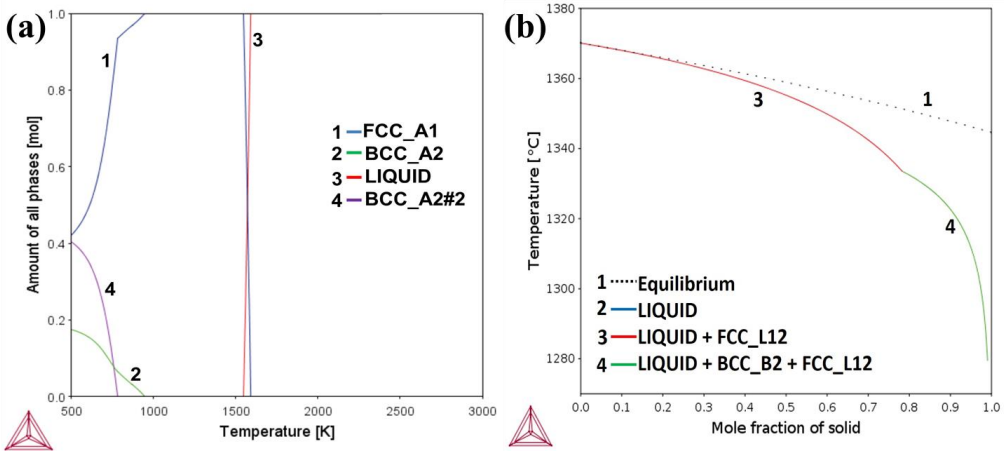

Figure 5.4 (a) Amount of phase with temperature plot, (b) Scheil's solidification pathway

Figure 5.5a and **Figure 5.5b** shows the amount of phase with temperature plot and Scheil's solidification pathways for x= 5 at. %, respectively. For x=5 at. %, it is observed that the formation of primary FCC solid solution phase from the liquid, followed by the evolution of dual-phase mixture containing FCC solid solution phase and C14 Laves phase from the remaining liquid and then the last liquid solidifies to form a three-phase mixture having BCC B2, FCC and C14 Laves phases. While SIGMA and Ni_3Ti_DOA phases are formed during solid-state transformation.

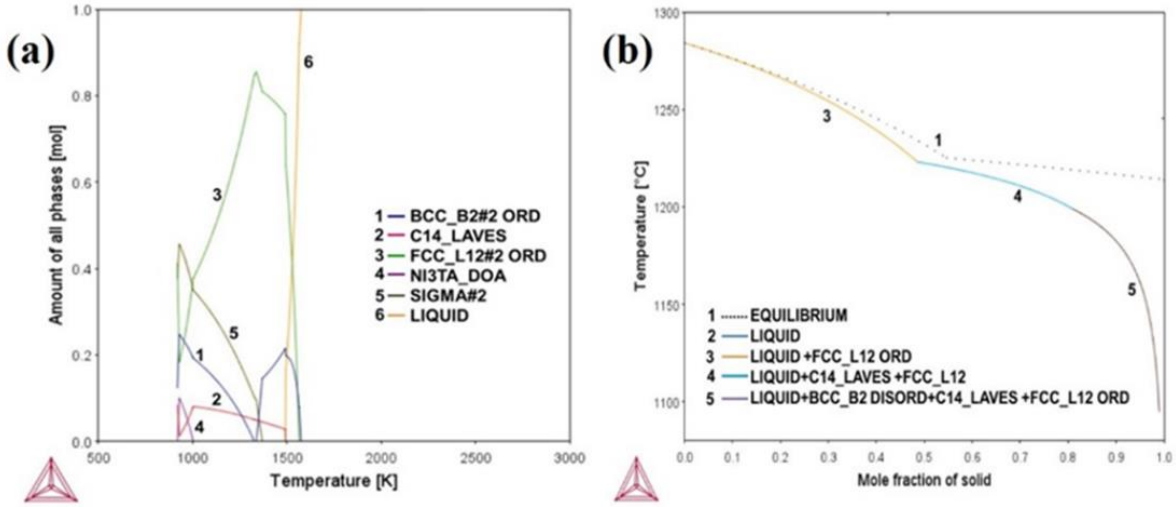

Figure 5.5 Amount of phase with temperature plot for X=5 at. %, (b) Scheil's solidification pathway for x=5 at. %

5.4.3 Design strategy for higher-order multicomponent EHEAs:

It is important to note that the novel seven component FCC single solid solution phase and then eight components EHEAs based upon the FCC single solid solution phase are designed by an integrated approach of combining both experimental and thermodynamic simulation techniques. **Figure 5.4a** shows the amount of phases *Vs.* temperature, and **Figure 5.4b** shows the solidification pathway using Scheil's assumption for $Fe_{32.5}Co_{10}Ni_{25}Cr_{15}Mn_5V_{10}Al_{2.5}$ HEA, respectively. Phase fraction with temperature plot indicates that alloy is stable in a large compositional range of temperature. Therefore, the development of single-phase HEA is expected by adopting a non-equilibrium solidification technique. Furthermore, the elements such as Nb and Al having a higher mixing of enthalpy with Co, Cr, Fe, and Ni are also expected to form the Laves phase [160]. Hence, it is possible to develop a dual-phase mixture in the designed single-phase HEAs. It is evident that Laves phases formation in multicomponent HEAs is considered as a strengthening agent for structural materials because of their excellent strength and excellent oxidation properties at high temperature [161][162]. In the present study, after the successful design of seven component FCC single-phase alloy having a maximum Fe concentration limit in HEAs by combining experimental and computational techniques, higher-order EHEAs are designed by incorporating Nb in the designed single-phase HEA, which leads to the formation of Laves phase by destabilizing the single-phase and forms the dual-phase HEAs. It is well known that the entropy stabilization in HEAs is increased by increasing the

number of elements, and also the addition of substitutional solid solution forming elements hinder the diffusion as well as reduce the subsequent eutectic growth in the higher-order multicomponent HEA systems, favoring the formation of ultrafine/nanoscale eutectics. The classical solidification model, proposed by Jackson-Hunt (J-H) gives the relation between the interlamellar spacing (λ) and eutectic solidification front velocity (V), which is given as $V^{1/2}\lambda=A$ [163][57]. According to the J-H model, λ is dependent on many factors such as liquidus slope, coefficient of diffusion, compositional range of eutectic, and contact angle between the solid phase and liquid at the triple point. It is also evident that for a given value of solidification velocity (V), a low value of the coefficient of diffusion decreases the constant A-factor (i.e., A-factor is directly proportional to diffusion coefficient (D)) and hence reduces interlamellar spacing (λ) value. The addition of more elements in the designed higher-order EHEAs will also favor the formation of ultrafine/nanoscale eutectic due to sluggish diffusion. It is worth mentioning that an integrated approach of combining both thermodynamics simulation and non-equilibrium solidification processing techniques helps in the development of novel higher-order multicomponent single-phase FCC as well as eight components EHEAs.

5.4.4 Structural and Microstructural characterization

5.4.4.1 XRD analysis

XRD analysis of seven component EHEAs:

The XRD pattern of the $Fe_{35-X}Co_{10}Ni_{25}Cr_{15}Mn_5V_{10}Nbx$ (X= 0, 2.5, 5, 7.5, and 10 at. %) EHEAs with different Nb content are shown in **Figure 5.6**. It is found that the XRD pattern reveals the FCC solid solution phase and $(Co, Fe)_2Nb$-type C14 Laves phase present in the studied alloys. It is found that the intensity of the Laves phase increases with an increase in the Nb-content, signifying the volume fraction of the Laves phase increases with an increase in Nb-concentration in studied EHEAs.

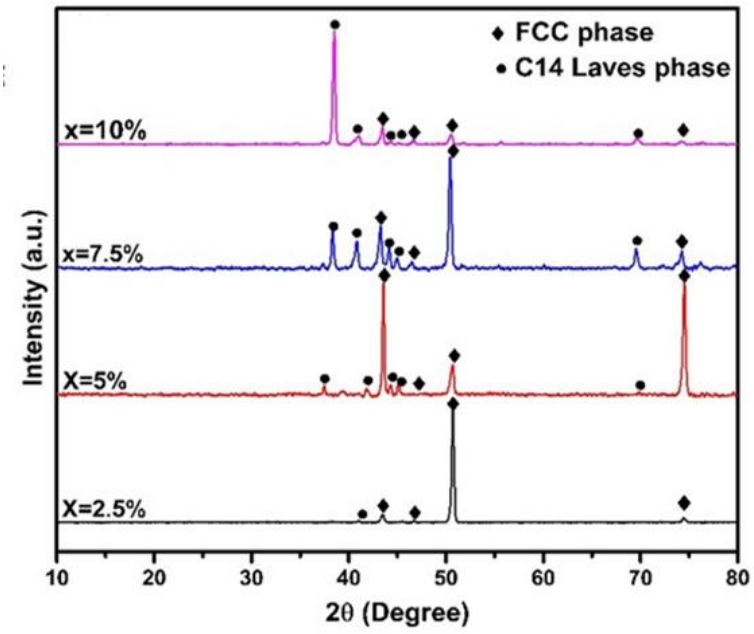

Figure 5.6 XRD pattern for $Fe_{35-x}Co_{10}Ni_{25}Cr_{15}Mn_5V_{10}Nbx$ (X=2.5, 5, 7.5 and 10 at. %) EHEAs.

XRD analysis of seven component single-phase and eight component EHEAs:

Figure 5.7a shows the XRD pattern of $Fe_{32.5}Co_{10}Ni_{25}Cr_{15}Mn_5V_{10}Al_{2.5}$ HEA that confirms the formation of the FCC solid solution phase**. Figure 5.7b** shows the XRD patterns for studied EHEAs that confirm the FCC phase and Co_2Nb-type Laves phase present in all alloy systems.

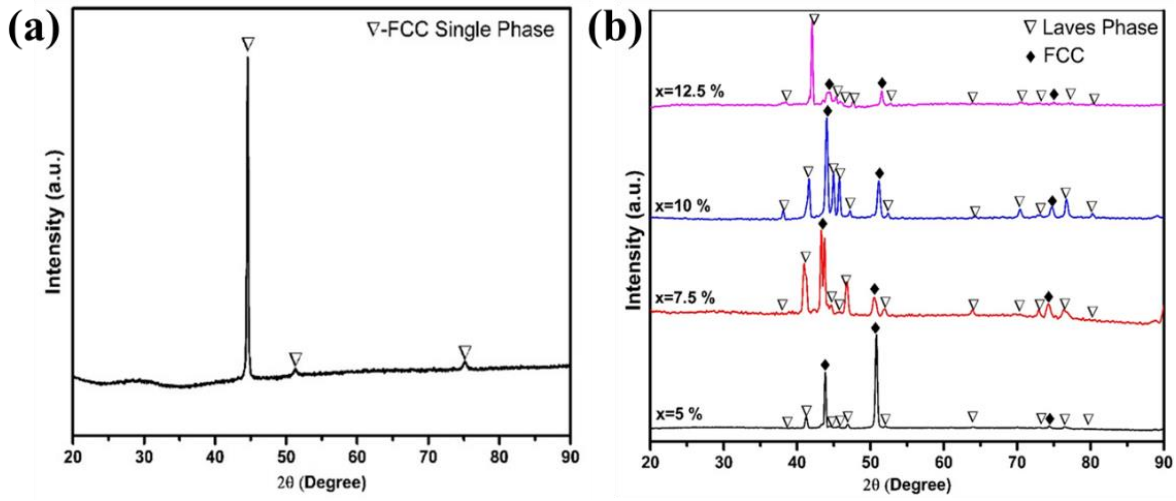

Figure 5.7 (a) XRD plot for $Fe_{32.5}Co_{10}Ni_{25}Cr_{15}Mn_5V_{10}Al_{2.5}$ HEA, (b) XRD plot for $Fe_{32.5-x}Co_{10}Ni_{25}Cr_{15}Mn_5V_{10}Al_{2.5}Nbx$ (x= 5, 7.5, 10, and 12.5 at. %) EHEAs

5.4.4.2 Scanning electron microscopy (SEM) results

SEM results of seven component EHEAs:

The detailed microstructural characterization of studied $Fe_{35-x}Co_{10}Ni_{25}Cr_{15}Mn_5V_{10}Nbx$ (x=2.5, 5, 7.5 and 10 at. %) EHEAs are carried out using backscattered electron (BSE) FESEM imaging mode to distinguish various phases in the microstructure, and the representative micrographs are shown in **Figure 5.8**. The SEM micrograph exhibits the presence of FCC primary solid solution phase (marked as α). The eutectic microstructure consists of FCC solid solution phase (α) and Laves phase for all studied EHEAs. The chemical composition of phases obtained using the EDS measurement are given in **Table 5.3**. EHEA with x=2.5 at. % show the eutectic type morphology has FCC primary solid solution (dark contrast), and a slight amount of Nb-rich Laves phase (bright contrast). In the case of x= 5 at. % and x= 7.5 at. %, the primary solid solution α phase and the lamellar eutectic mixture consist of FCC solid solution and Laves phase. A fully lamellar eutectic microstructure consists of the FCC solid solution phase, and the Laves phase has been observed for x= 10 at. %.

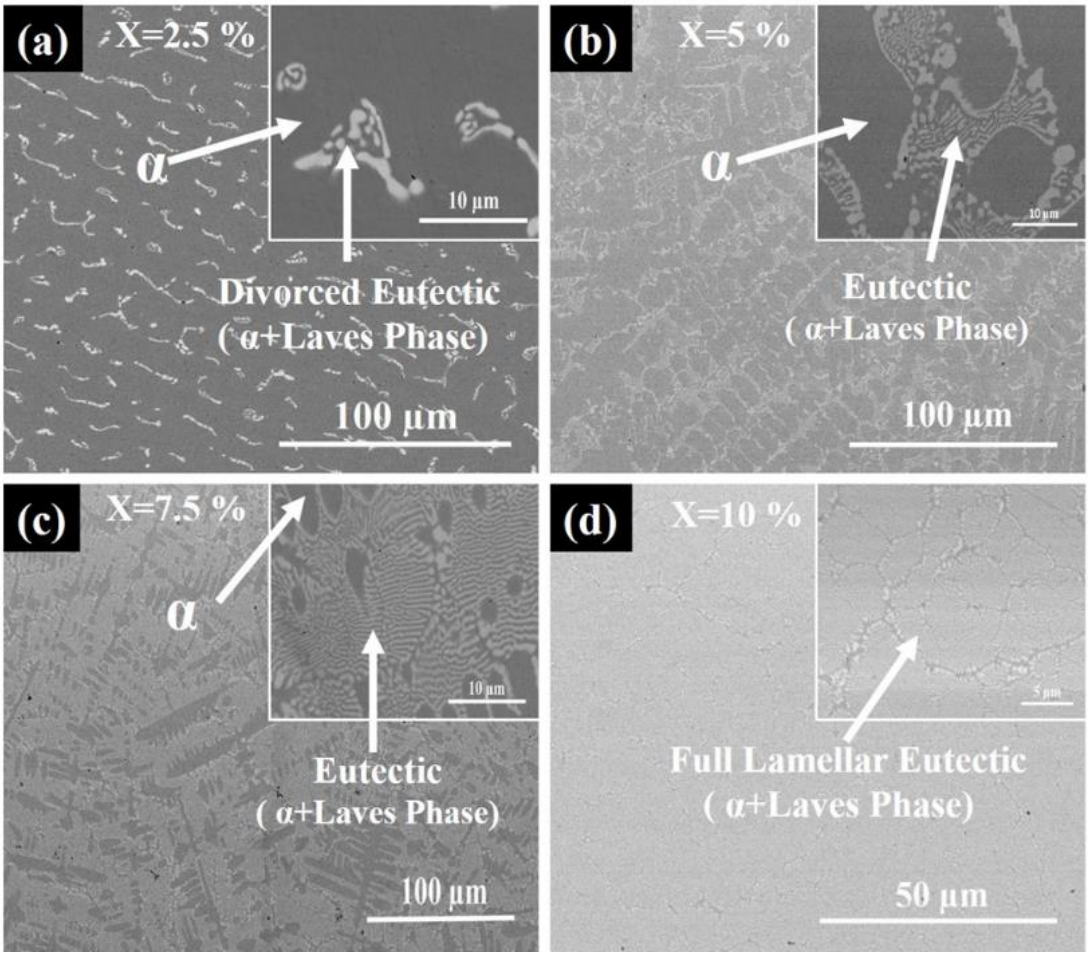

Figure 5.8 FESEM-BSE image of (a) x=2.5%, (b) x=5%, (c) x=7.5%, and (d) x=10%

Table 5.3 EDS Composition of nominal and individual phases in $Fe_{35-x}Co_{10}Ni_{25}Cr_{15}Mn_5V_{10}Nbx$ (X=2.5, 5, 7.5, 10 at. %)

Sample	Phases	Fe	Co	Ni	Cr	Mn	V	Nb
	Phase (α)	34.21	12.01	24.82	14.58	4.43	9.94	-
	Eutectic	32.36	10.20	23.90	14.66	4.56	11.43	2.90
x = 2.5%	Laves	27.3	10.23	22.29	13.56	4.94	9.35	12.33
	Nominal	32.5	10	25	15	5	10	2.5
	Phase (α)	32.63	10.09	25.49	15.06	3.55	8.15	5.02
	Eutectic	32.24	9.85	25.78	15.26	3.72	7.88	5.28
x = 5%	Laves	22.22	9.38	16.54	12.74	4.33	11.11	23.67
	Nominal	30	10	25	15	5	10	5
	Phase (α)	27.25	10.37	24.41	14.69	4.78	10.27	8.22
	Eutectic	28.43	9.50	24.42	14.43	4.89	10.05	8.28
x = 7.5%	Laves	27.61	9.98	22.80	14.42	4.70	9.07	11.43
	Nominal	27.5	10	25	15	5	10	7.5
x = 10%	Eutectic	16.64	12.04	28.58	17.46	5.07	11.58	8.63
	Nominal	25	10	25	15	5	10	10

SEM results of seven component single-phase and eight component EHEAs:

The SEM micrograph of as-cast $Fe_{32.5}Co_{10}Ni_{25}Cr_{15}Mn_5V_{10}Al_{2.5}$ HEA shows the Fe-Co-Ni-Cr-rich solid solution phase in **Figure 5.9a**. The microstructural features of studied EHEAs (**Figure 5.9b, 5.9c, 5.9d, 5.9e**) show the presence of FeCoNiCr-rich solid solution (marked as α) and lamellar eutectic morphology between FCC solid solution (α) and Co_2Nb-type Laves phase. It is observed that HEA with x= 7.5 at. % reveals the presence of more volume fraction of lamellar eutectic morphology.

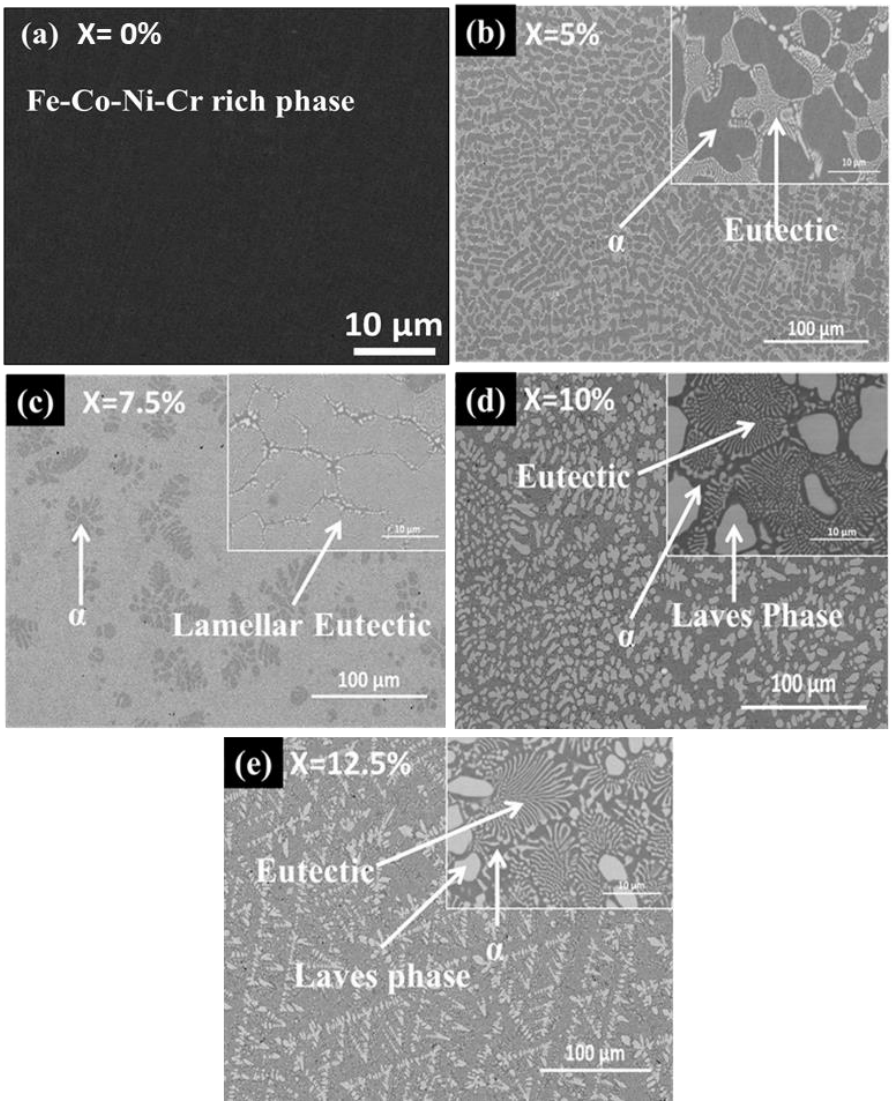

Figure 5.9 FESEM-BSE images for alloy (a) x=0 at. %, (b) x=5 at. %, (c) x=7.5 at. %, (d) x=10 at. %, and (e) x=12.5 at. %

The chemical compositions of the different phases in studied EHEAs are given in **Table 5.4**. EDS results of studied HEAs show that the Laves phase is enriched with Nb content. Since the Nb element has a large atomic radius in the developed EHEA system and also having a higher negative enthalpy of mixing with other alloying elements (Fe, Co, Ni, Cr), these factors favor the formation of Nb-rich Co_2Nb-type Laves phase. Finally, the microstructures of HEAs with x=10 at. % and x=12.5 at. % consists of a primary FCC solid solution (α) phase and the eutectic mixture of FCC solid solution (α) and Co_2Nb-type Laves phase. It is evident that the microstructure transforms from hypo-eutectic with primary FCC solid solution (α) phase to hyper-eutectic with primary Co_2Nb-type Laves phase with a variation of Nb-concentration.

5.4.5 ANN results:

Microhardness measurement and ANN result for seven component EHEAs:

Figure 5.10a shows the Vickers microhardness of $Fe_{35-X}Co_{10}Ni_{25}Cr_{15}Mn_5V_{10}Nbx$ (X=2.5, 5, 7.5, and 10at. %) EHEAs. The average experimentally observed Vickers microhardness for EHEA with x= 2.5 at. %, x= 5 at. %, x= 7.5 at. %, and x=10 at. % with standard deviations of 277±3.52 HV, 315±8.98 HV, 449±3.28 HV, and 607±4.40 HV, respectively. It is observed that the 8-7-1 neuron system was found to be the optimal structure for the ANN model after several iterations during the training of the model. The number 7 shows the neurons in the hidden layer, as shown in **Figure 5.10b**.

Table 5.4 EDS Composition of nominal and individual phases in $Fe_{32.5-X}Co_{10}Ni_{25}Cr_{15}Mn_5V_{10}Al_{2.5}Nbx$ (X=5, 7.5, 10, 12.5) EHEAs (all in atomic %)

Sample	Phases	Fe	Co	Ni	Cr	V	Mn	Al	Nb
x=5%	FCC (α)	30.53	10.28	25.03	15.96	9.78	4.42	2.37	1.63
	Eutectic	25.87	10.20	23.65	14.74	9.86	4.74	2.16	8.79
	Nominal	27.5	10	25	15	10	5	2.5	5
x=7.5%	FCC (α)	29.38	9.73	18.94	21.76	13.18	3.12	2.53	1.36
	Eutectic	25.22	10.73	26.08	14.78	9.60	3.53	2.07	8
	Nominal	25	10	25	15	10	5	2.5	7.5
x=10%	FCC (α)	25.22	10.24	28.76	16.82	12.19	1.80	2.85	2.12
	Eutectic	23.09	10.22	26.33	15.93	11.27	1.98	2.50	8.69
	Laves	23.18	11.24	18.72	14.58	6.56	1.26	1.35	23.11
	Nominal	22.5	10	25	15	10	5	2.5	10
x=12.5%	FCC (α)	19.98	9.58	31.09	15.96	13.76	4.68	3.04	2.0
	Eutectic	21.41	10.05	27.96	16.01	11.87	4.27	2.46	5.98
	Laves	20.41	11.30	20.36	15.06	7.13	3	1.29	21.45
	Nominal	20	10	25	15	10	5	2.5	12.5

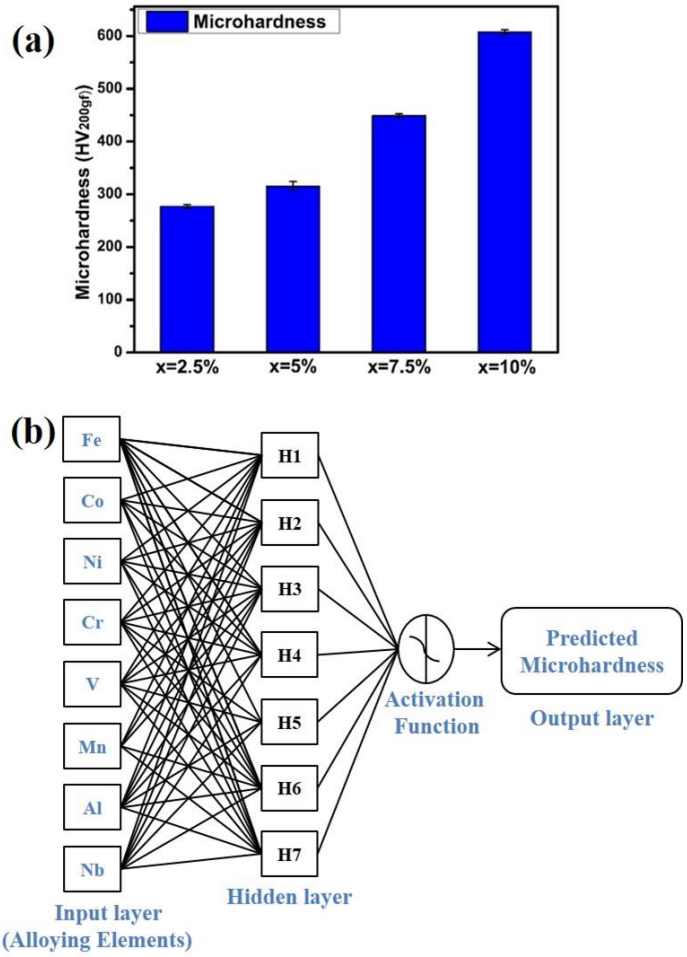

Figure 5.10 (a) Experimental microhardness for $Fe_{35-X}Co_{10}Ni_{25}Cr_{15}Mn_5V_{10}Nbx$ (X=2.5, 5, 7.5, and 10 at. %) EHEAs, and (b) Optimal ANN model for microhardness prediction.

It was observed that a network with 7 neurons in the hidden layer gives the optimal configuration for the present study with minimum MSE and coefficient of correlation. MSE convergence during the training of the ANN model 8-7-1 for microhardness is shown in **Figure 5.11a,** where the convergence to mean square error 6.7224 $x10^{-4}$ is saturated at epoch 22. The ANN model prediction and experimental value of microhardness are shown in **Figure 5.11b.**

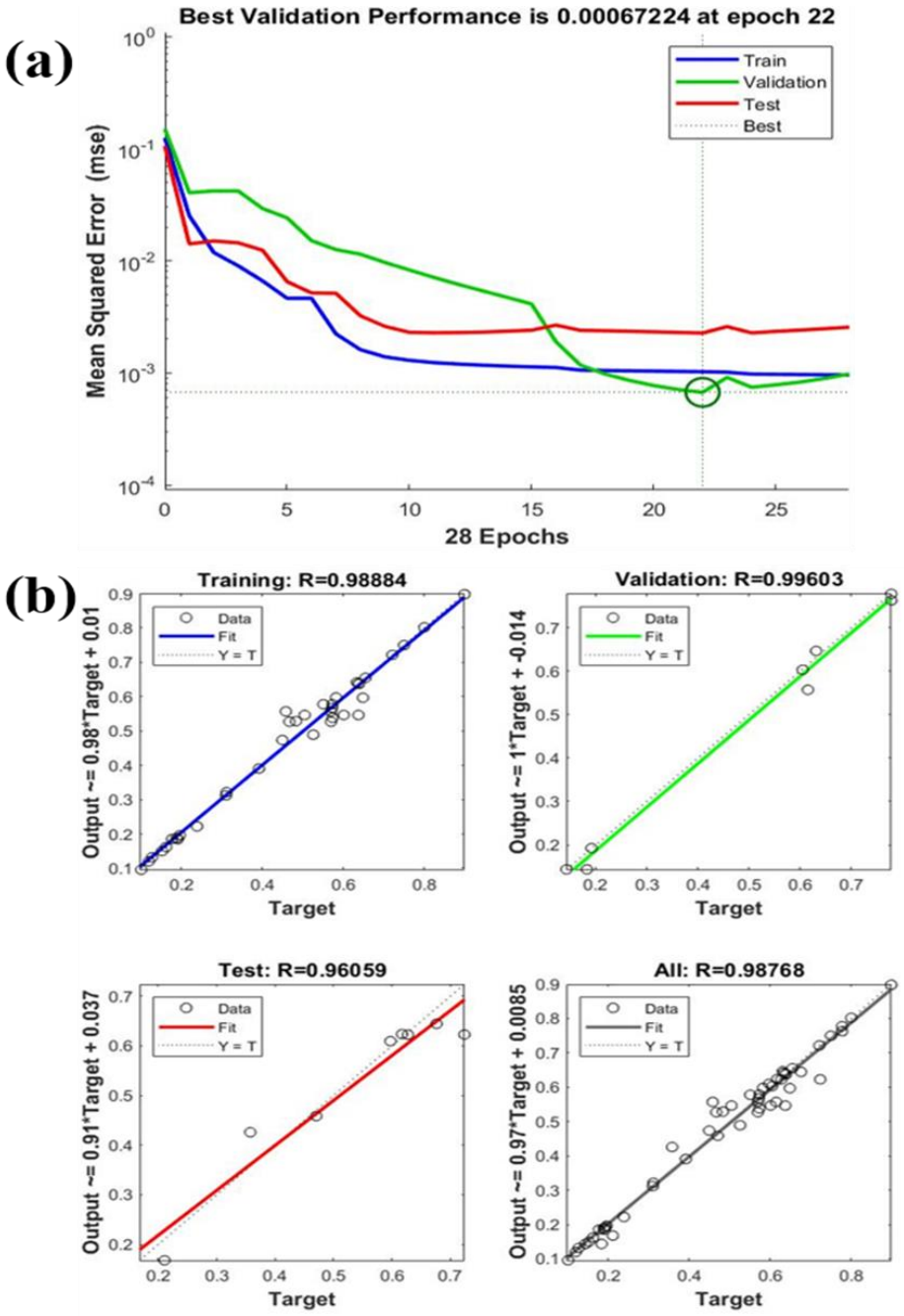

Figure 5.11 (a) MSE convergence during the training of the ANN model for Micro-hardness, and (b) Comparison of the ANN model simulation results with the experimental values for Micro-hardness.

The overall correlation coefficient (R) is observed 0.98768, while during training, validation, and testing, the observed correlation coefficient (R) is 0.98884, 0.99603, and 0.96059, respectively. It is important to mention here that the proposed ANN model effectively predicts the microhardness, and the ANN model performance is shown in **Figure 5.12**. The predicted and

experimental microhardness for HEAs and studied EHEAs are evaluated with an average absolute relative error of 4.82 % (as given in **Appendix 1**). The predicted microhardness of studied EHEAs with the percentage of error is given in **Table 5.5.** Therefore, the ANN modelling approach is useful for predicting HEAs mechanical properties with different alloying elements. The current study will encourage new opportunities in the HEAs research field to predict material properties with optimal composition for a specific application.

Table 5.5 Predicted and experimental microhardness for studied EHEAs

Alloys Compositions $Fe_{35-x}Co_{10}Ni_{25}Cr_{15}Mn_5V_{10}Nb_x$	**Experimental Hardness (HV)**	**Predicted Hardness (HV)**	**% Error**
x = 2.5%	277±3.52	276	0.45
x = 5 %	315±8.98	239	4.42
x = 7.5%	449±3.28	420	6.40
x = 10%	607±4.40	552	9.08
		Average error %	**5.08**

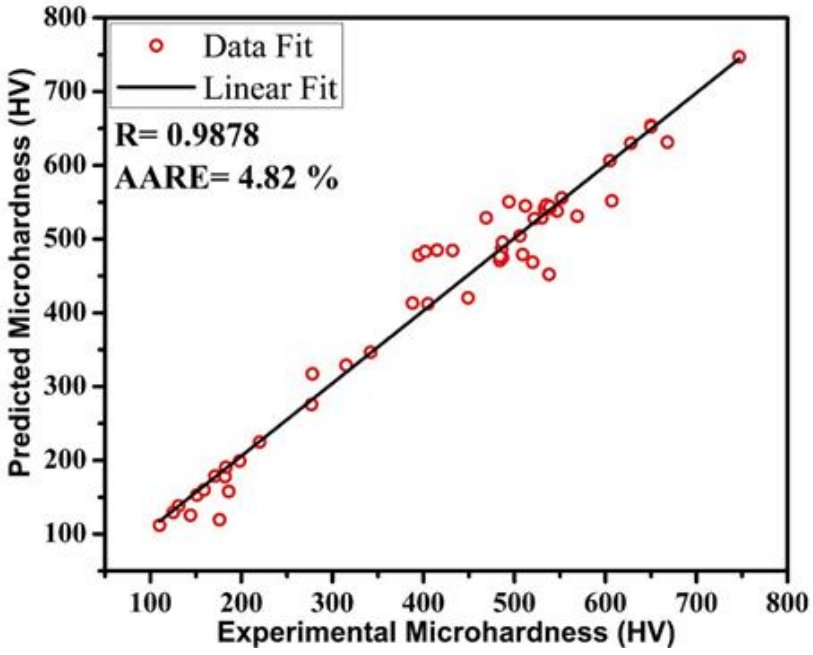

Figure 5.12 Performance of ANN model

For eight component EHEAs:

It is worthy of mentioning that the hardness prediction of developed EHEAs has been made using ANN modeling. In order to determine the finest architecture, the process of training, testing, and validation have been iterated several times by changing the hidden layers. Thus, an appropriate back-propagation ANN model has been developed based on several trails for the numbers of neurons. The optimum structure of the ANN model with back-propagation is found to be 8-8-1 (8, 8, and 1 are neurons in the input layer, hidden layer, and the output layer, respectively). The performance ability of individual network has been evaluated based on the coefficient of correlation (R) between the experimental output and model output. The optimal structure of the ANN model for the prediction of microhardness is shown in **Figure 5.13a.** Thus, the ANN model with a single hidden layer with 8 input parameters and 459 datapoints has been established for prediction of the microhardness of the designed and developed EHEAs. Further, the output results of the model have been compared with the actual values of microhardness. The absolute value has been calculated by the difference between the predicted value and the exact value. The predictability of the ANN model is quantified in the form of relative error and correlation coefficient. During the training, the best validation performance has been evaluated based on mean square error (MSE) (as shown in **Figure 5.13b**), where convergence to MSE with a saturation value of 0.062789 is achieved in 9th epoch.

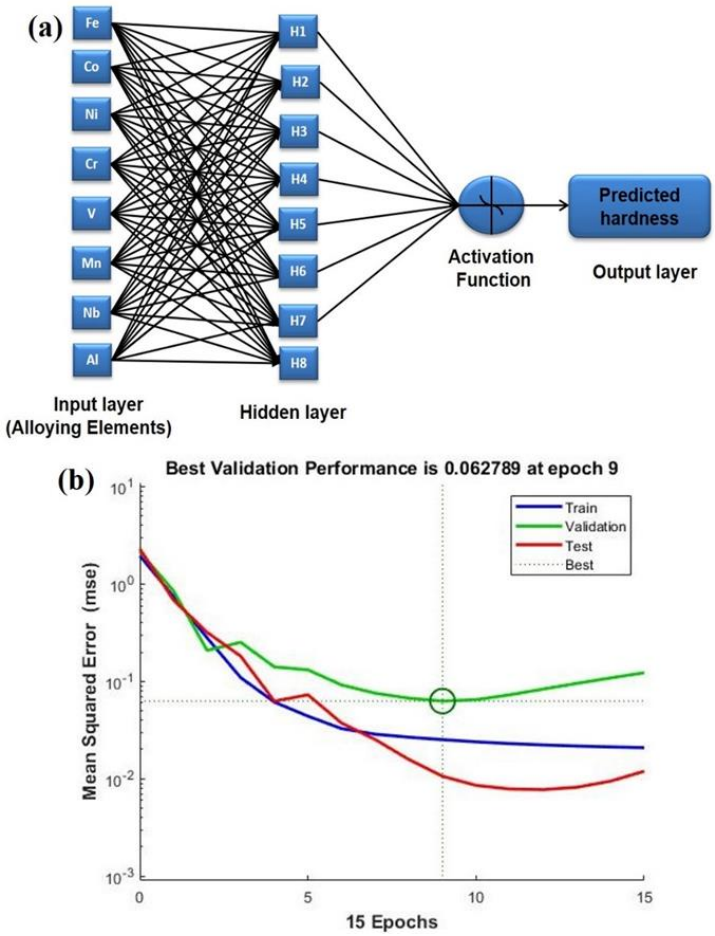

Figure 5.13 (a) The optimal structure of ANN model, (b) MSE convergence during the training of the ANN model 8-8-1for the hardness.

Among the 53 different alloys data, 60 % of data was used for training, 20 % for validation, while 20 % for the testing to observe the least mean square error (MSE) in predicting microhardness. The correlation coefficient (R) during training, validation, and testing observed 0.98745, 0.92601, and 0.99659 are shown in **Figure 5.14a, 5.14b, 5.14c,** respectively. The final simulated model shows the overall R=0.98479, which is the best correlation after several iterations (as shown in **Figure 5.14d**). The comparison of the expected microhardness drawn from the ANN model and experimental microhardness for EHEAs is given in **Appendix 2** [16][164][165][62]**.** Based on the established ANN model, the microhardness of EHEAs with x=7.5 at. % and x=10 at. % is predicted and compared with observed experimental microhardness (as shown in **Figure 5.14e**). The predicted microhardness using the ANN model is found to be 501 HV with an error of 3.47 % and 618 HV with an error of 4.92 % for EHEAs with x=7.5 at. % and x=10 at. %, respectively.

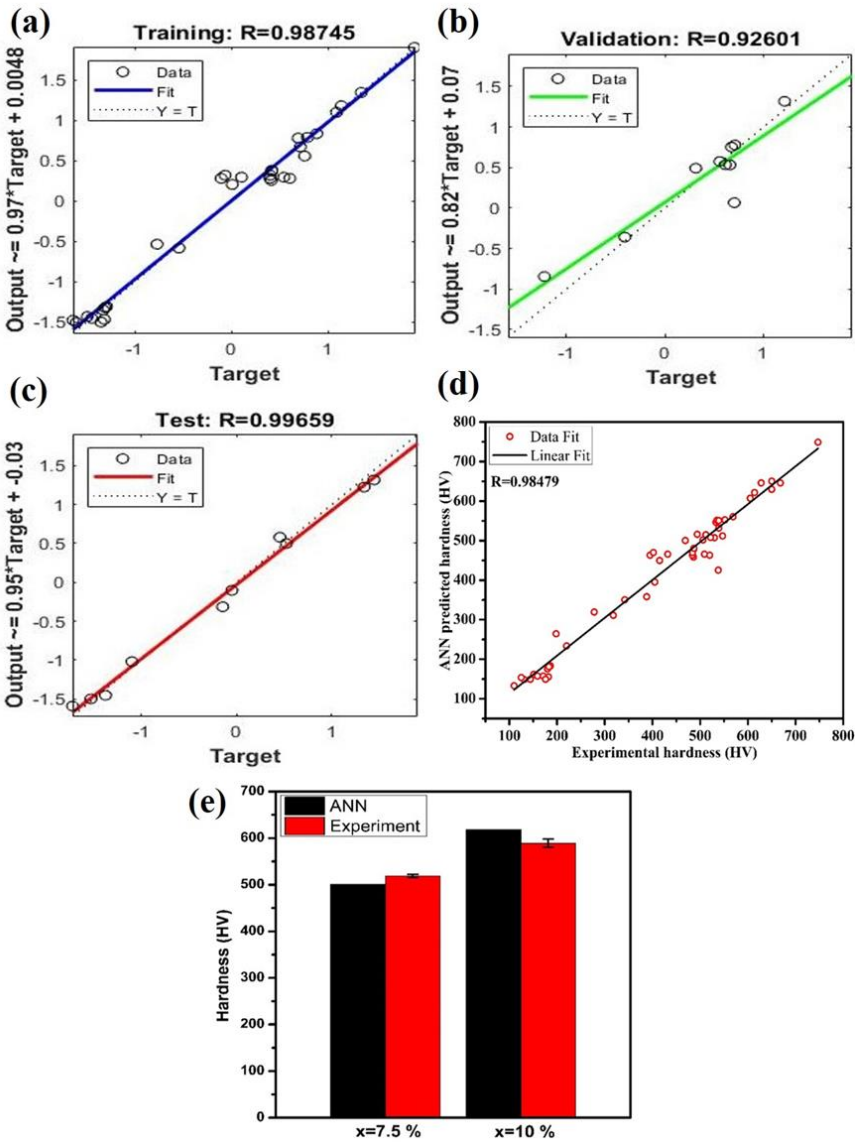

Figure 5.14 Comparison of the ANN model simulation results with experimental values for hardness (a) Training of dataset, (b) Validation of dataset, (c) Testing of dataset, (d) Overall dataset, and (e) Prediction of the hardness of alloy x=7.5 at .% and x=10 at. % by proposed ANN model.

5.5 Summary:

The following important conclusions emerge from this work for seven component $Fe_{35-x}Co_{10}Ni_{25}Cr_{15}Mn_5V_{10}Nbx$ (x = 2.5, 5, 7.5, and 10 at. %) EHEAs:

(i) An integrated thermodynamics simulation and experimental approach have been employed to develop $Fe_{35-x}Co_{10}Ni_{25}Cr_{15}Mn_5V_{10}Nbx$ (x = 2.5, 5, 7.5, and 10 at. %) EHEAs.

(ii) The quantitative measure of the microhardness of studied EHEAs increases with Nb concentration due to the formation of the (Co, Fe)$_2$Nb-type C14 Laves phase in the matrix.

(iii) The optimal structure of the developed ANN model is 8-7-1 with an average absolute relative error of 4.82 % with a back-propagation algorithm that enables predicting the microhardness of HEAs as a function of alloying elements. For alloy x = 2.5 at. %, the predicted microhardness value of 276 HV is observed with an error of only 0.45 %.

The following important conclusions for eight $Fe_{32.5-x}Co_{10}Ni_{25}Cr_{15}Mn_5V_{10}Al_{2.5}Nbx$ (x= 5, 7.5, 10 and 12.5 at. %) component EHEAs are:

(i) $Fe_{32.5-x}Co_{10}Ni_{25}Cr_{15}Mn_5V_{10}Al_{2.5}Nbx$ (x= 5, 7.5, 10 and 12.5 at. %) eight component EHEAs have been designed and developed by the addition of Nb in seven component FCC solid solution phase HEA by integrating both thermodynamics simulation and experimental approaches.

(ii) Experimentally it is found that the eutectic microstructure in studied EHEAs consists of Co_2Nb-type Laves phases and FeCoNiCr-rich FCC solid solution phase.

(iii) It is found that the developed EHEAs shows the experimentally observed microhardness ranging from 318±3.5 HV to 614±4.4 HV. The microhardness of EHEAs increases with the increase of Nb-concentration. The enhancement of property is attributed to the solid solution phase(s), the volume fraction of the Co_2Nb-type Laves phase, and the length scale of eutectics.

(iv) A back-propagation ANN model is established, which successfully predicts the microhardness of designed EHEAs with an error of 0.062 at 9 iterations. It is found that the predicted microhardness of studied EHEAs using the ANN model matches well with the experimentally observed microhardness with less than 5 % error.

Chapter 6

Hot deformation behaviour of AlCoCrFeNi EHEA

6.1 Introduction:

In the present work, we report here the flow curve prediction of $AlCoCrFeNi_{2.1}$ eutectic high entropy alloy (EHEA) at different temperatures and strain rates using different modeling techniques such as physics-based (modified Zerilli–Armstrong (ZA) model), phenomenological (modified Johnson-Cook (JC) model, Arrhenius model), and artificial neural network (ANN) modeling. Finally, the performance of all conventional (i.e., physics-based and phenomenological) and ANN modelling was evaluated by coefficient correlation (R) and average absolute relative error (AARE) parameters. It is found that the flow curve prediction by phenomenological modelling (i.e. modified JC model (R=0.9646, AARE=19.41 %) and Arrhenius model (R=0.9696, AARE=14.62 %) is better as compared to physics based modified ZA model (R= 0.9321, AARE=21.42 %). A comparative evaluation of obtained simulated results indicates that the prediction of hot deformation behaviour of studied EHEA using ANN modeling (where R = 0.9985, and AARE = 4.57 %) is matching excellently with experimental flow curve results as compared to conventional modelling approaches.

6.2 Objective:

The different modeling techniques, including physics-based modeling, phenomenological modeling, and artificial neural network (ANN), prove to be a useful tool in the analysis of materials flow behavior. In the current study, the conventional models and the ANN model are used to predict the hot deformation flow curve of studied EHEA. The conventional models have specific limitations to predict the flow behavior, such as JC model has not considered the thermal softening effect for flow stress prediction. While physics based ZA model considers the strain hardening, thermal softening, and other physical effects for flow stress prediction, but uses some parameters which are estimated using precision equipment. The main objective is to develop the different modeling approaches that predicts the hot deformation behavior of the studied EHEA at different hot working conditions with great accuracy.

6.3 Simulation details for flow stress prediction:

The experimental flow curve data were collected from previously studied EHEA at different hot deformation conditions (at temperature range 900-1100°C and strain rate range 0.001-10 s^{-1}). In this study, three different types of models such as the physics based, phenomenological, and ANN models were used to predict the flow behavior of EHEA. It is to be noted here that modified Zerilli–Armstrong (ZA) model, modified Johnson-Cook (JC) model, Arrhenius-type constitutive equations and ANN model ANN model with backpropagation training algorithm were used for prediction the flow stress. It is observed that in modified JC-model, the prediction of flow stress at lower strain rate is deviated from the experimental results while strain compensated Arrhenius model predictability is better for all deformation conditions, which shows the excellent ability of the strain-compensated Arrhenius-type constitutive model to predict the flow stress throughout the entire temperature and strain rate range [166]. Furthermore, the activation energy of alloys derived from this model is usually used as indicator of the degree of difficulty of the hot deformation process and can give the details to optimize the hot working process. Apart from physical model, ANN is the mathematical model and do not involve the physical nature of hot deformation process and the successful application of the ANN model needs extensive and accurate experimental data. The different models' accuracy or performance was evaluated by the following parameters such as coefficient of correlation (R) and average absolute relative error (AARE).

6.4 Result and discussion:

6.4.1 Flow curve prediction using Modified Zerilli-Armestrong (ZA) model:

The simple ZA model is based on dislocation mechanisms which primarily is the cause of inelastic behavior under different load conditions [149]. The effects of strain hardening, strain rate hardening, and thermal softening on flow stress are considered. But the simple ZA model considers only the coupling effect of temperature and strain rate. While the modified ZA model assumes the coupling effects of both temperature and strain rate as well as temperature and strain. The modified ZA model is represented by the following equation [149][148]:

$$\sigma = (C_1 + C_2\varepsilon^n)\exp\{-(C_3 + C_4\varepsilon)T^* + (C_5 + C_6T^*)\ln\dot{\varepsilon}^*\} \qquad (6.1)$$

Where C_1, C_2, C_3, C_4, C_5, C_6, n are material constants and $T^* = T\text{-}T_r$, T_r being the reference temperature, is taken as 900°C and $\dot{\varepsilon}^*$ (ratio of strain rate to reference strain rate) which is taken as 1 sec^{-1}. The following procedure has been employed to determine all the material constants:

(i) First, C_1 is to be determined from flow curves at reference conditions. Actually, C_1 is the yield stress at reference strain rate and temperature conditions, i.e., at 900°C and 1 sec^{-1}. C_1 was found to be 298.77 MPa.

(ii) C_2 and n are to be determined at reference strain rate using the following equation:

$$\sigma = (C_1 + C_2\varepsilon^n)\exp[-(C_3 + C_4\varepsilon)T^*] \qquad (6.2)$$

Taking natural logarithm and introducing two parameters I_1 and S_1 such that,

$$I_1 = \ln(C_1 + C_2\varepsilon^n) \qquad (6.3)$$

$$S_1 = -(C_3 + C_4\varepsilon) \qquad (6.4)$$

We get:

$$\ln\sigma = I_1 + S_1T^* \qquad (6.5)$$

By substituting the associated flow stress-strain data at reference strain rate 1 sec^{-1}, the values of S_1 and I_1 can be determined from slope and intercept of $\ln\sigma$ vs. T^* at every discrete strain and is given in **Figure** 6.**1a**. Now, to find C_2 and n, the following equation is used:

$$\ln(\exp(I_1) - C_1) = \ln C_2 + n\ln\varepsilon \qquad (6.6)$$

$\ln C_2$ and n are the intercept and slope of $\ln(\exp(I_1) - C_1)$ vs. $\ln\varepsilon$ linear fit curve (given in **Figure 6.1b**). C_2 and n are found to be 63.213005 and -0.14001898, respectively.

(iii) Now to find C_3 and C_4, the expression of S_1 is used:

$$S_1 = -(C_3 + C_4\varepsilon) \qquad (6.7)$$

For every strain, S_1 is obtained. In the S_1 vs. ε linear fit curve (given in **Figure 6.1c**), the slope is $-C_3$, and intercept is $-C_4$. Thus, C_3 and C_4 are found to be 0.00379014 and 0.00117786, respectively.

(iv) C_5 and C_6 can be found by taking natural logarithm of equation 6.1 and introducing a new parameter S_2 such that:

$$\ln\sigma = \ln(C_1 + C_2\varepsilon^n) - (C_3 + C_4\varepsilon)T^* + S_2\ln\dot{\varepsilon}^* \qquad (6.8)$$

$$S_2 = C_5 + C_6T^* \qquad (6.9)$$

For all the temperatures and discrete strains, S_2 is to be found by the slope of the $\ln\sigma$ vs. $\ln\dot{\varepsilon}^*$ linear fit curve. Then, C_5 and C_6 are found from the slope and intercept of S_2 vs. T* linear fits at every discrete strain (given in **Figure 6.1d**). The final C_5 and C_6 are the average of all C_5 and C_6 at each strain. Thus, C_5 and C_6 are found to be 0.164199 and 0.00039463, respectively. Now finally, the obtained modified ZA equation is expressed:

$$\sigma = (298.77 + 63.213005\varepsilon^{-0.14001898})\exp\{-(0.00379014 + 0.00117786\varepsilon)(T(°C) - 900) + (0.164199 + 0.00039463(T(°C) - 900))\ln\frac{\dot{\varepsilon}}{1}\} \qquad (6.10)$$

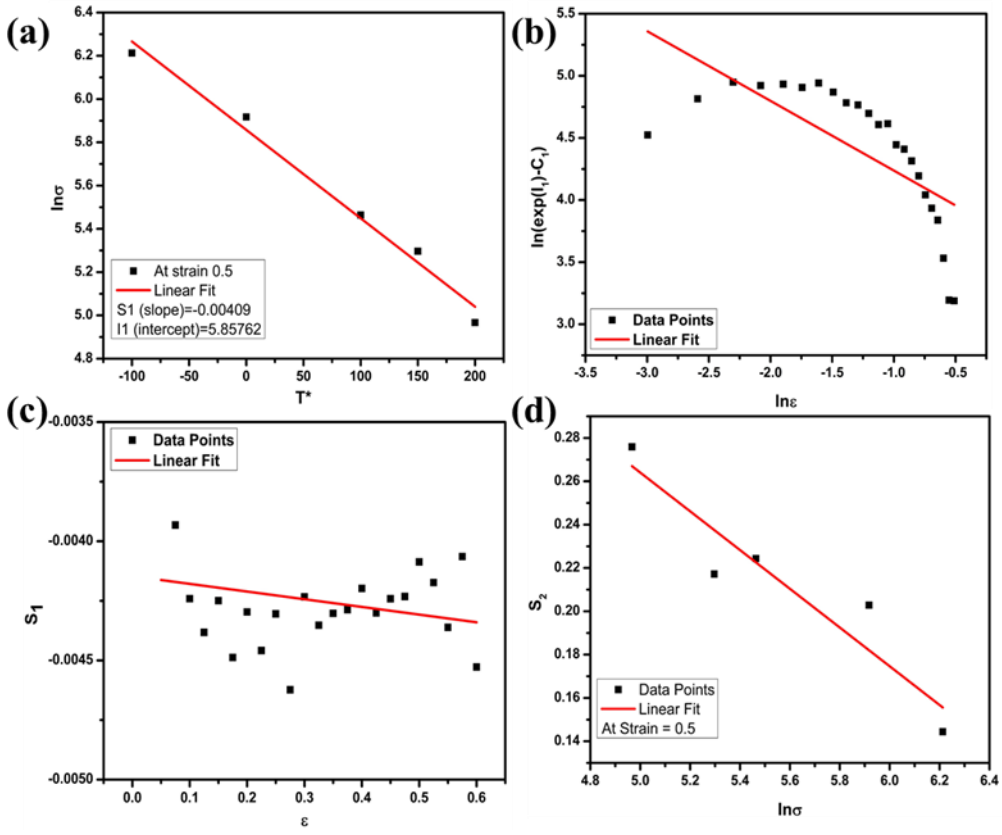

Figure 6.1 Calculation of material constant for modified ZA model

The predicted and experimental flow stress at different hot working conditions using modified ZA model is given in **Figure 6.2**.

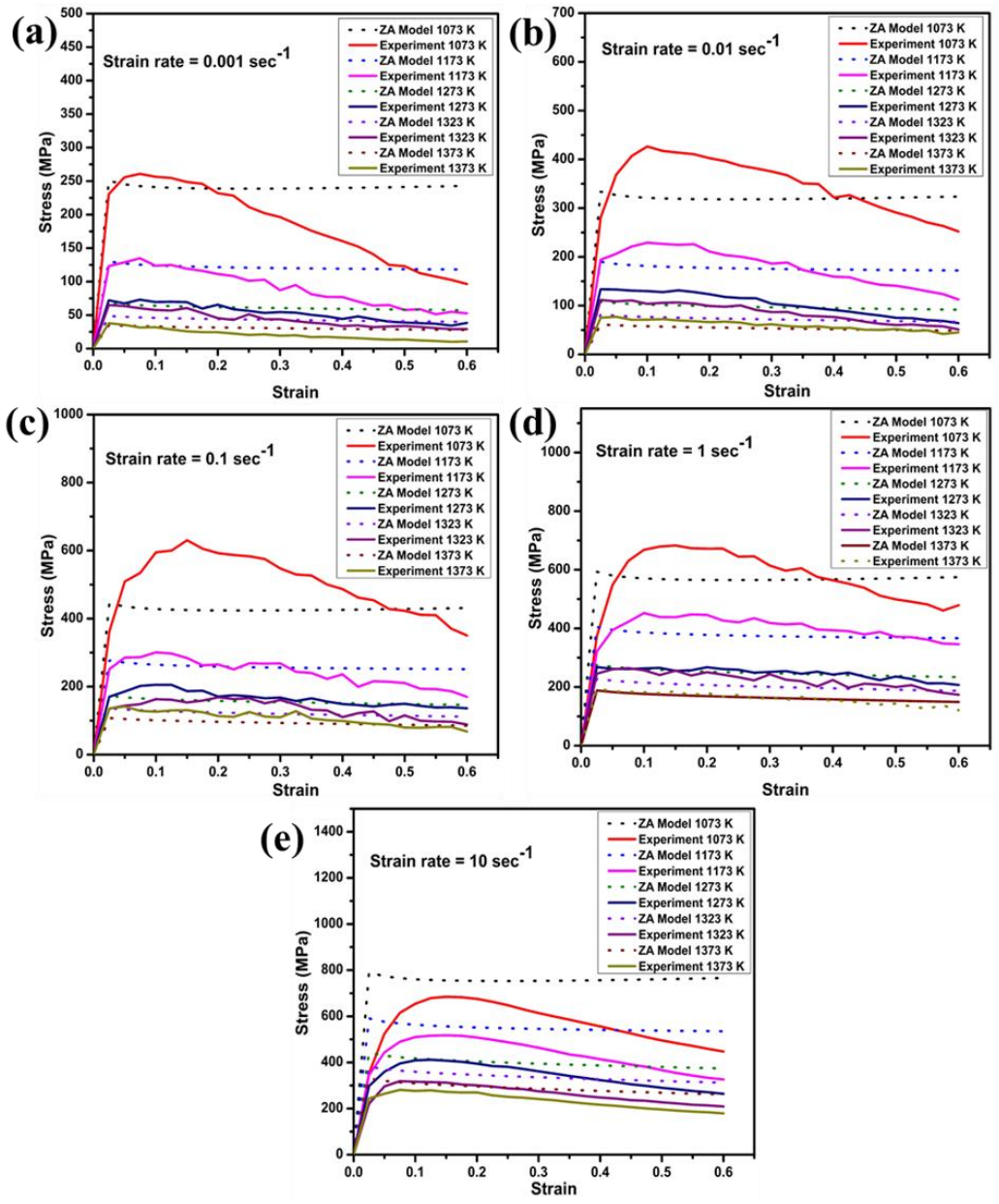

Figure 6.2 Predicted and experimental flow stress at different hot working conditions using modified ZA model

6.4.2 Flow curve prediction using Modified Johnson-Cook model for flow stress prediction:

In J-C model, flow stress is dependent on the temperature, strain, and strain rate which is used for different types of materials and a more comprehensive range of temperature and strain rate due to the simplicity and easy availability of model parameters. In simple JC model, the

relationship between the deformation temperature, flow stress, strain rate, and strain can be expressed as [148] [167]:

$$\sigma = (\sigma_y + A\varepsilon^n)(1 + B\ln(\dot{\varepsilon}^*))(1 - T^{*m}) \quad (6.11)$$

Where, the σ is flow stress, σ_y is the yield stress at the reference temperature and strain, A is strain hardening coefficient, n is strain hardening exponent, B is coefficient of strain rate hardening, m is the thermal softening coefficient, $\dot{\varepsilon}^*$ dimensionless coefficient (ratio of strain rate $\dot{\varepsilon}$ and $\dot{\varepsilon}_r$ reference strain rate) and T^* is homologous temperature. T^* can be expressed as:

$$T^* = \frac{T - T_r}{T_m - T_r} \quad (6.12)$$

Where the T is the hot working temperature, T_m is melting temperature, and T_r is reference temperature. The minimum value of temperature and strain rate during hot working is assumed to be the reference value. But it is observed that the temperature and strain rate do not have independent effects on flow stress. This leads to a new modified Johnson cook model, which identifies the coupling effects of temperature and strain rates [168]. The modified Johnson cook (JC) model can be expressed as:

$$\sigma = (A_1 + B_1\varepsilon + B_2\varepsilon^2)(1 + C_1\ln\dot{\varepsilon}^*)\exp[(\lambda_1 + \lambda_2\ln\dot{\varepsilon}^*)(T - T_r)] \quad (6.13)$$

Where A_1, B_1, B_2, C_1, λ_1, λ_2 are materials constants. The meanings of the rest of the variables are same as those in simple JC model.

The following procedure is employed to determine these material constants:

(a) First, to determine A_1, B_1, and B_2, a two-degree polynomial fitting is done at reference temperature 1100°C (not taken minimum in modified JC model) and reference strain rate of 1 sec^{-1} (given in **Figure 6.3a**). The stress would now be evaluated in the reference conditions by the following expression:

$$\sigma = (A_1 + B_1\varepsilon + B_2\varepsilon^2) \quad (6.14)$$

On performing a two-degree linear fit for all chosen discrete strains (0.025 to 0.6) at reference conditions, we get A_1, B_1, B_2 as 191.5067, -71.93108, -64.23083, respectively, from the coefficient of fitted polynomial equation.

(b) Now for determining C_1, only reference temperature (1100°C) is used. In this condition, we get the following equation:

$$\frac{\sigma}{(A_1+B_1\varepsilon+B_2\varepsilon^2)} = 1 + C_1 \ln\dot{\varepsilon}^* \qquad (6.15)$$

Thus, from the given expression, C_1 is the slope of $\frac{\sigma}{(A_1+B_1\varepsilon+B_2\varepsilon^2)}$ *Vs.* $\ln\dot{\varepsilon}^*$ (given in **Figure 6.3b**). This needs to be done for all discrete strains and strain rates in a single graph. C_1 is determined as 0.1424.

(c) Next to determine λ_1, λ_2, the following expression is used, which is resulted from rearranging the modified JC equation and taking its logarithm, we get

$$\ln\frac{\sigma}{(A_1+B_1\varepsilon+B_2\varepsilon^2)(1+C_1\ln\dot{\varepsilon}^*)} = (\lambda_1 + \lambda_2 \ln\dot{\varepsilon}^*)(T - T_r) \qquad (6.16)$$

In order to simplify this equation, a parameter λ is introduced such that:

$$\lambda = \lambda_1 + \lambda_2 \ln\dot{\varepsilon}^* \qquad (6.17)$$

λ can be easily determined as it is the slope of the $\ln\frac{\sigma}{(A_1+B_1\varepsilon+B_2\varepsilon^2)(1+C_1\ln\dot{\varepsilon}^*)}$ vs. $(T - T_r)$ given in **Figure 6.3c**. Similarly, a different λ for every strain rate is obtained. Hence, λ_1, λ_2 can be easily found from the intercept and slope of λ *Vs.* $\ln\dot{\varepsilon}^*$ plot, which is presented in **Figure 6.3d**. λ_1 and λ_2 are found to be -0.00401 and 0.000395208, respectively. Thus, the final modified JC equation can be expressed as following:

$$\sigma = (191.5067 + -71.93108\varepsilon - 64.23083\varepsilon^2)(1 + 0.1424\ln\frac{\dot{\varepsilon}}{1})\exp[(-0.00401 + 0.000395208\ln\frac{\dot{\varepsilon}}{1})(T(°C) - 1100)] \qquad (6.18)$$

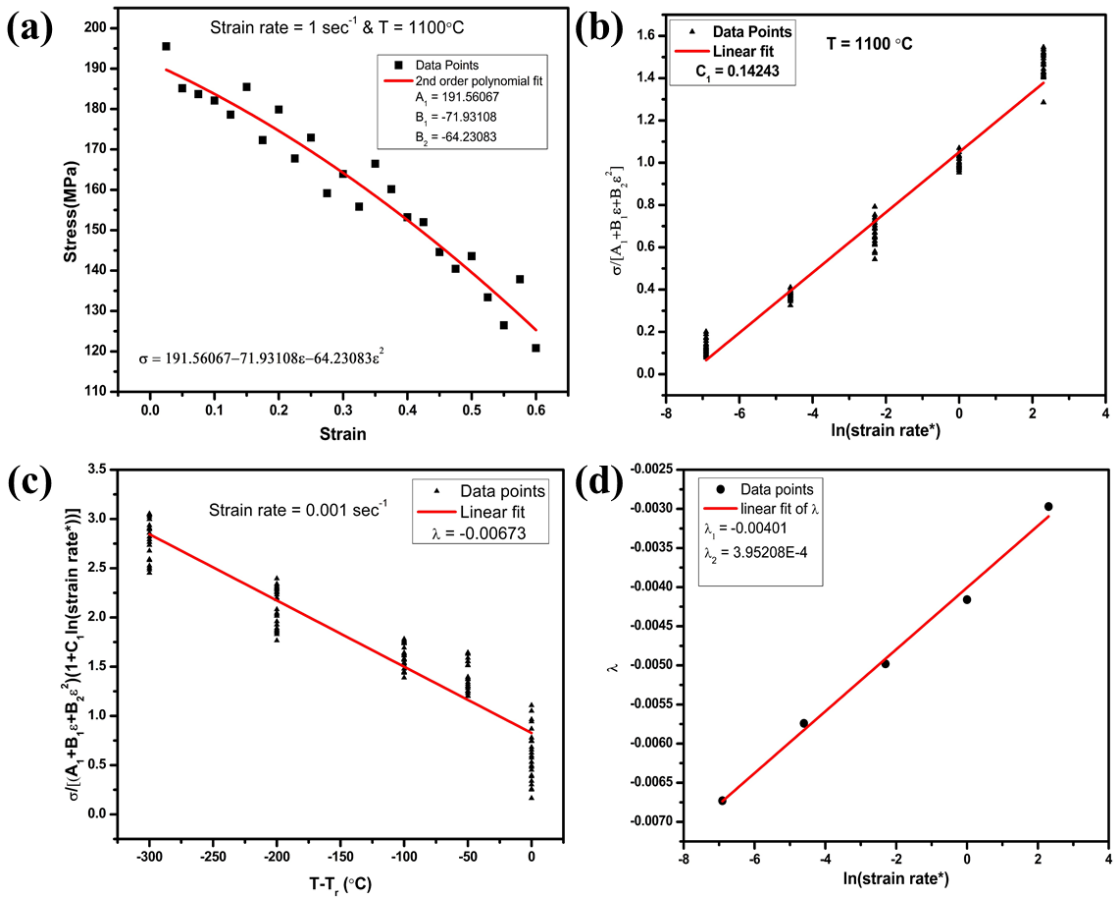

Figure 6.3 Calculation of material constant for modified JC model

The predicted and experimental flow stress at different hot working conditions using modified JC model is given in **Figure 6.4**.

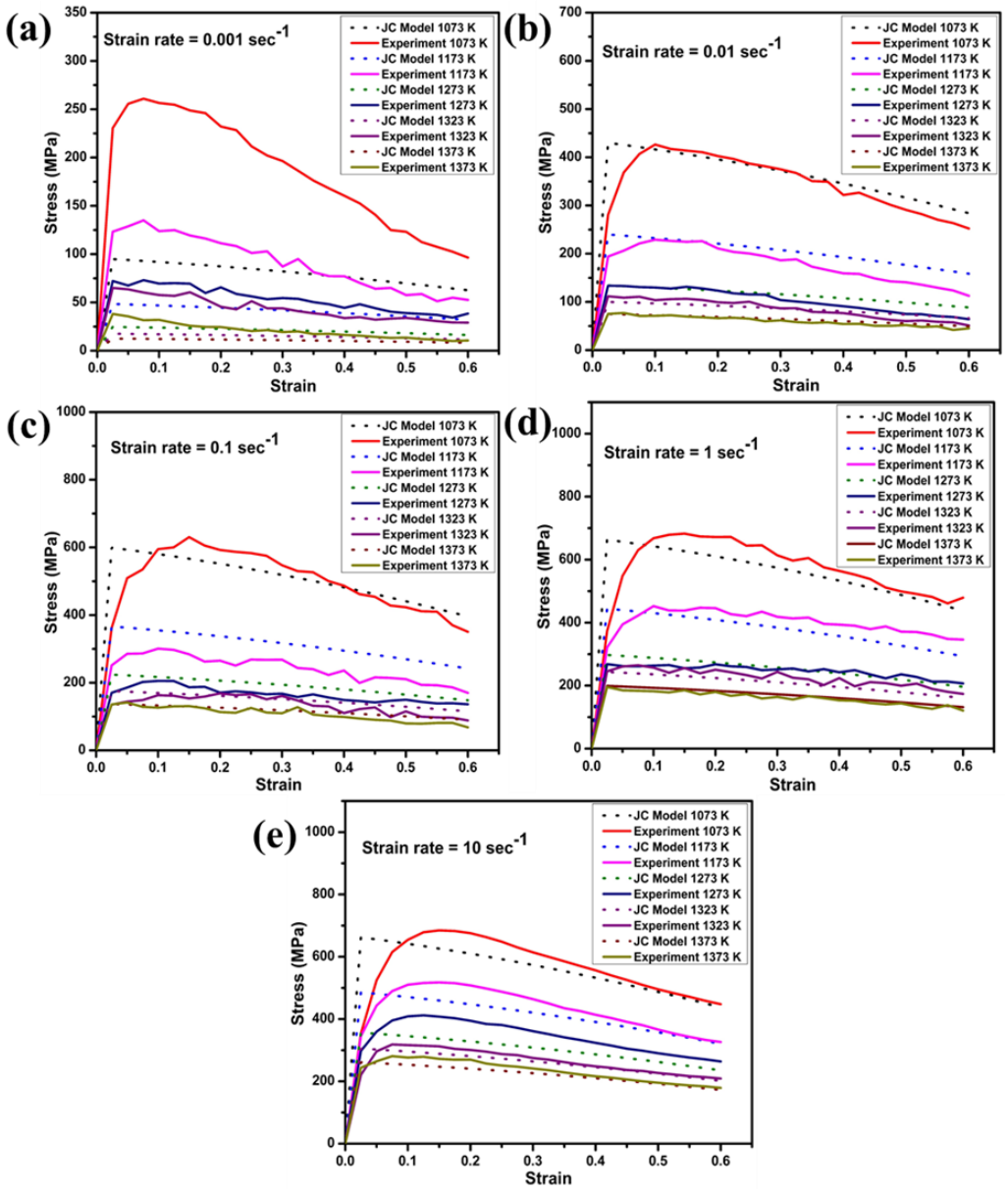

Figure 6.4 Predicted and experimental flow stress at different hot working conditions using modified JC model

6.4.3 Flow curve prediction using Arrhenius model:

In this model, hot deformation flow behavior during hot working of materials can be predicted by using the constitutive equation. In the equation, flow stress is the function of different hot working variables such as temperature, strain, and strain rate. The equation used for that model is already given in chapter 1[169][170].

In the above equation, $\dot{\varepsilon}$ is strain rate (s^{-1}), Q is the activation energy (J/mol), R is the universal gas constant 8.314 J/mol-K, T is deformation temperature in K, σ is hot deformation stress (MPa), and A, α (α= β/N), and n are materials constant. The value of different material constant is calculated by linear fitting of different plots mentioned in **Figure 6.5**. The value β and N are the slopes of the lnσ *Vs.* ln$\dot{\varepsilon}$ and σ *Vs.* ln$\dot{\varepsilon}$ plot with a linear fit (**Figure 6.5a** and **6.5b**). Linear fitting of ln$\dot{\varepsilon}$ *Vs.* ln[sinh(ασ)] plot yields the value of n (given in **Figure 6.5c**).

The value of s is the slope after linear fitting the plot between 10,000/T *Vs.* ln[sinh(ασ)] (given in **Figure 6.5d**) and intercept of plot between the ln[sinh(ασ)] *Vs.* lnZ determines the value of A, which is represented in **Figure 6.5e**.

Here, n is dependent on temperature and strain rate, so the value of n is the average slope of plot $\{(\partial \ln \dot{\varepsilon}) / \partial \ln[\sinh(\alpha\sigma)]\}$ at various hot working temperatures. The value of different parameters for strain 0.5 is represented in **Figure 6.5**. The parameter Z, $\dot{\varepsilon}$, and σ at strain 0.5 can be expressed by the following equations:

$$Z_{0.5} = \dot{\varepsilon}.\exp\left(\frac{254865}{RT}\right) \qquad (6.19)$$

$$\dot{\varepsilon} = 9.26 \times 10^9 \times [\sinh(0.005563.\sigma_{0.5})]^5 \times \dot{\varepsilon}.\exp\left(\frac{254865}{RT}\right) \qquad (6.20)$$

$$\sigma_{0.5} = \frac{1}{0.005563} \times \ln\left\{\left(\frac{Z_{0.5}}{9.26\times10^9}\right)^{\frac{1}{3.43}} + \left[\left(\frac{Z_{0.5}}{9.26\times10^9}\right)^{\frac{2}{3.43}} + 1\right]^{\frac{1}{2}}\right\} \qquad (6.21)$$

Similarly, flow stress is calculated for all strains by putting the α, Z, A, and n in the above equation. The obtained predicted flow curve using the Arrhenius model and experimental flow curve at different thermomechanical conditions are represented in **Figure 6.6**.

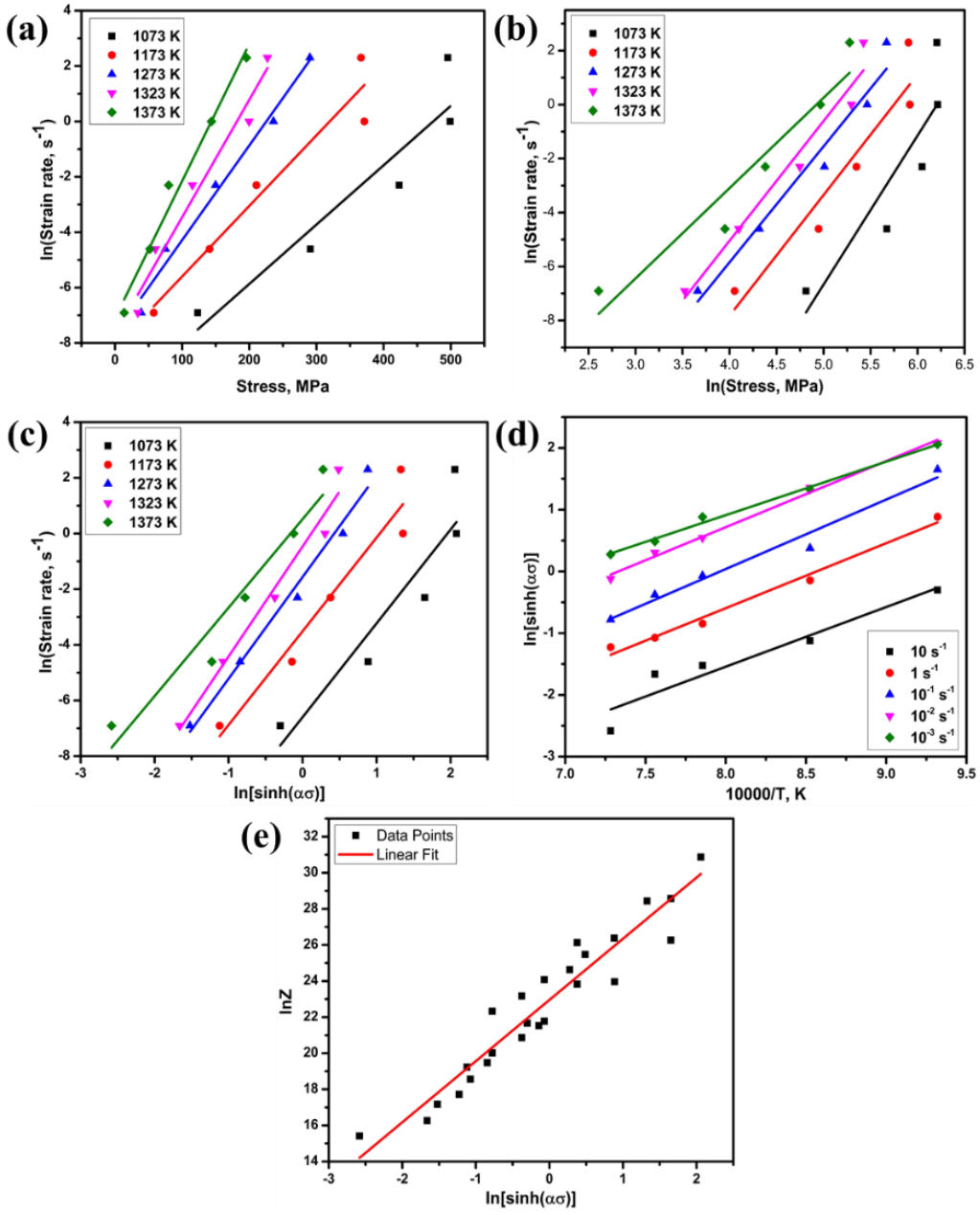

Figure 6.5 Calculation of material constant for Arrhenius model

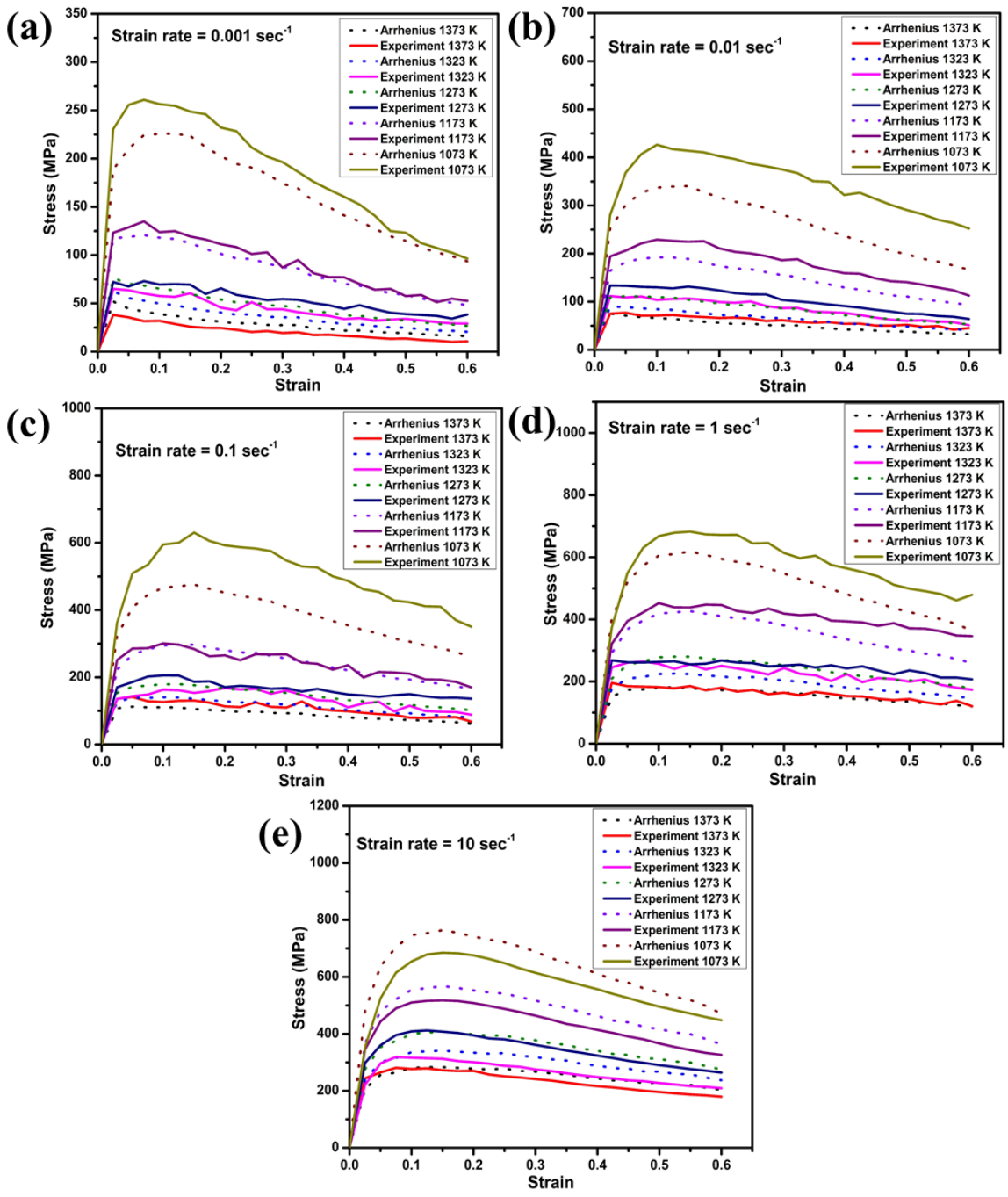

Figure 6.6 Predicted and experimental flow stress at different hot working conditions using Arrhenius model

6.4.4 Artificial neural network (ANN) modeling approach for flow stress prediction:

ANN modelling approach is based on the human brain that collects the data by adoptive self-learning [171], which solves the simple as well as a complex problem by adaptive learning.

Recently this approach is extensively used in the materials community to design novel material for specific applications. In this approach, there is different layers which can solve the problem with a proper database. The input layer first receives the input data and then transfers it to hidden layer, after training in hidden layer by activation function, the data is transferred into an output layer. Before training, the data scaling should be performed to convert the data between 0-1. In this study, data scalling is done by two approaches which are mentioned in **Table 4.3**; as designated as ANN model-1 and ANN model-2. Both the ANN models have been used a feed-forward backpropagation approach with the L-M algorithm. In present study, a total of 2400 input-target (temperature, strain, strain rate, and flow stress) data is used. The model trains the data to get the output, and then that compares with the targeted value. The output after several iterations for both the ANN models is presented in **Table 7.1**. The mean square error (MSE) plot and coefficient of correlation (R) during training, validation, testing, and overall data for ANN model-1 and ANN model-2 are represented in **Figures 6.7a**, **6.7b** and **Figures 6.9a**, **6.9b**, respectively. The comparison of the flow curves for ANN model-1 and ANN model-2 at different temperatures and strain rates is given in **Figure 6.8** and **Figure 6.10**, which shows that the prediction of flow stress at a higher strain rate is better than at a lower strain rate.

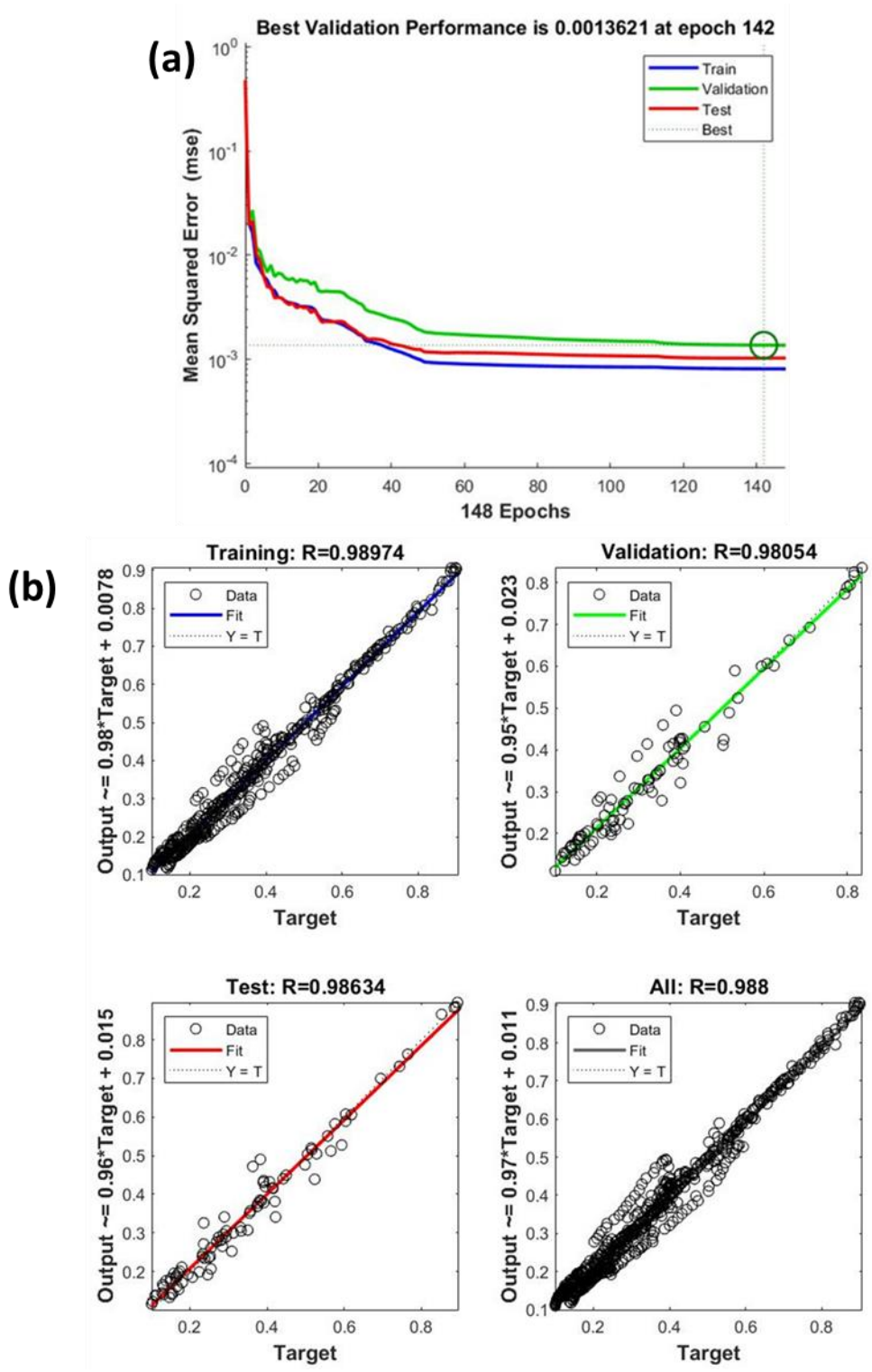

Figure 6.7 (a) MSE (mean square error) and (b) coefficient of correlation at different stages of ANN model 1

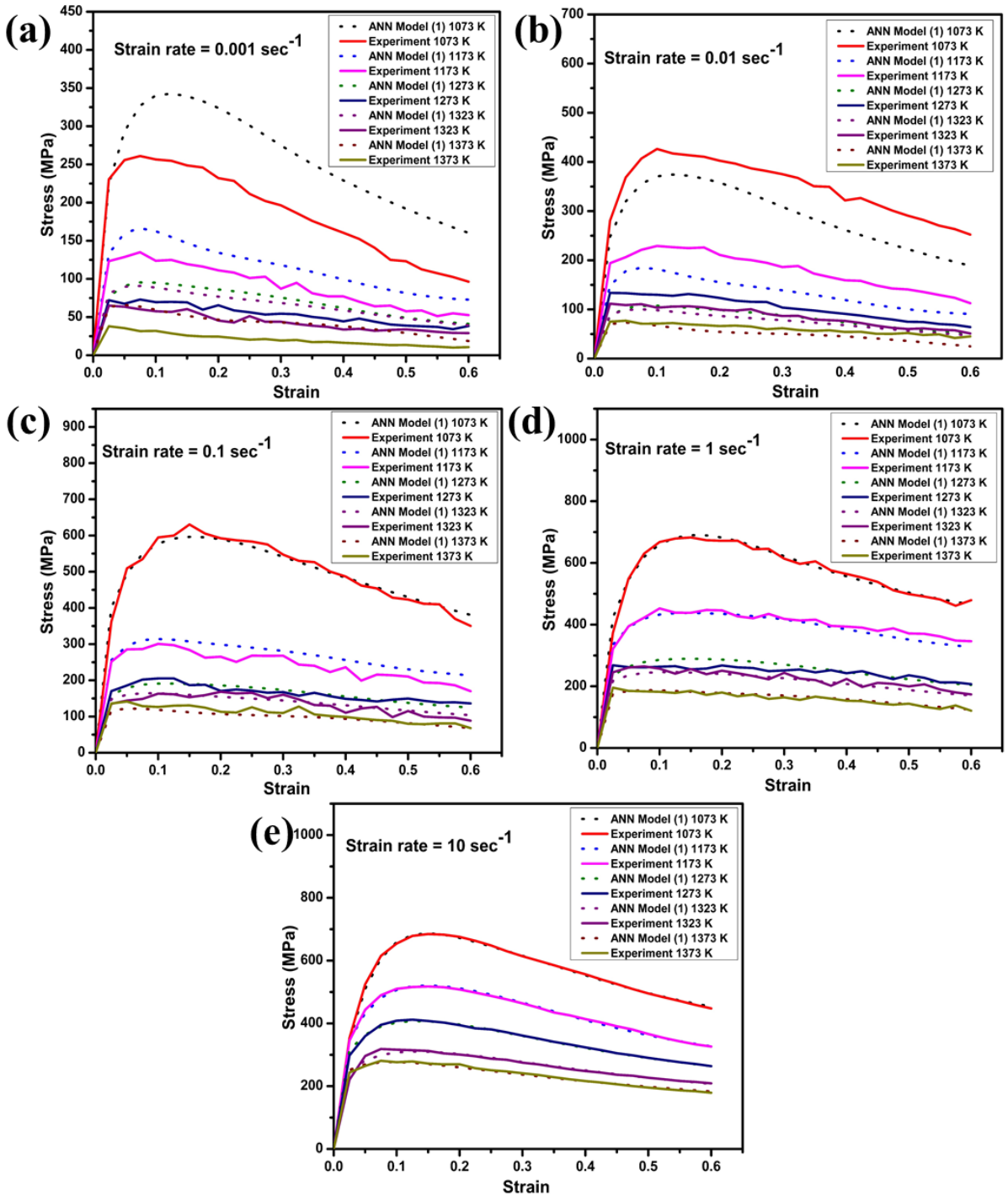

Figure 6.8 Predicted and experimental flow stress at different hot working conditions using ANN model 1

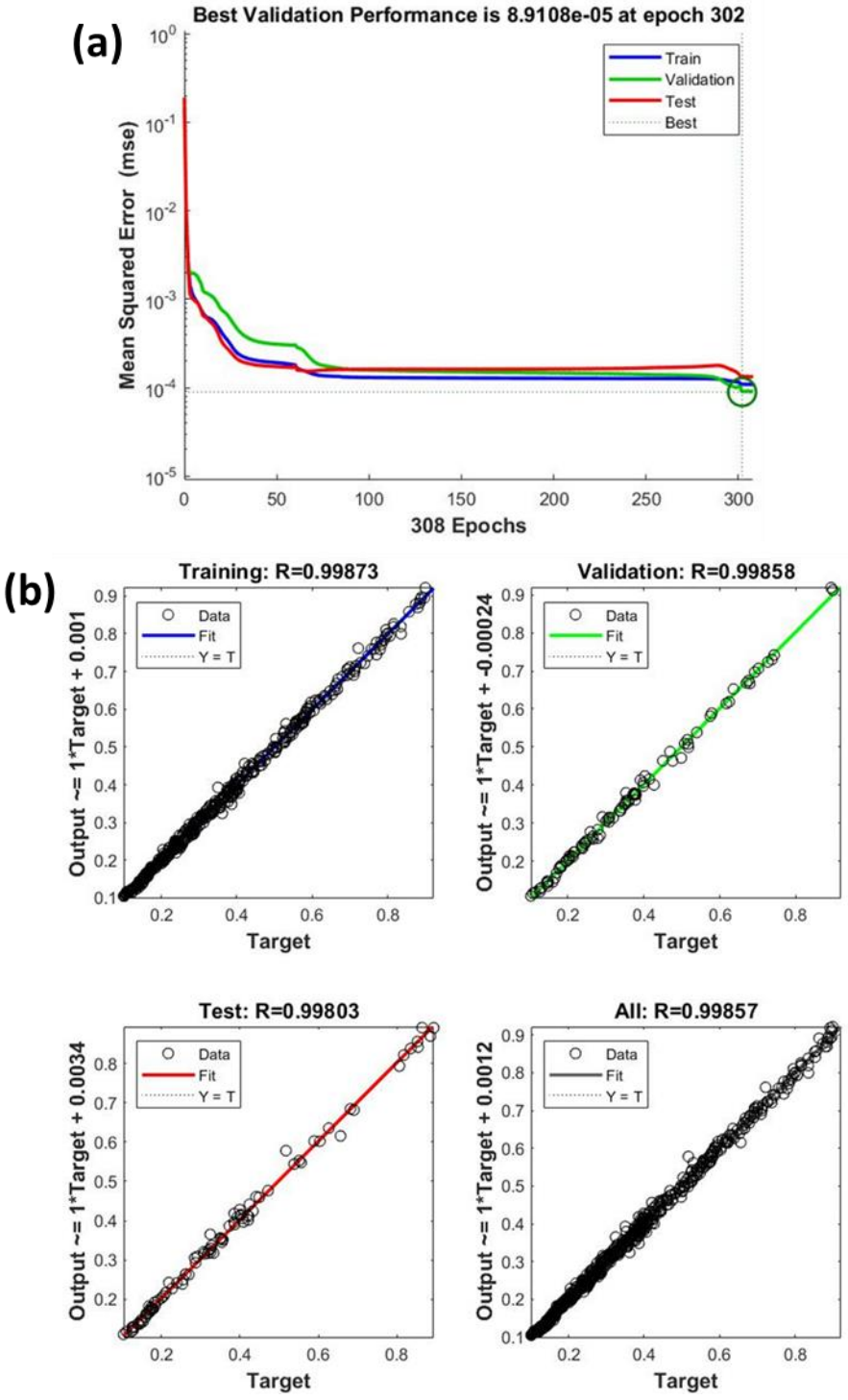

Figure 6.9 MSE (mean square error) and coefficient of correlation at different stages of ANN model 2

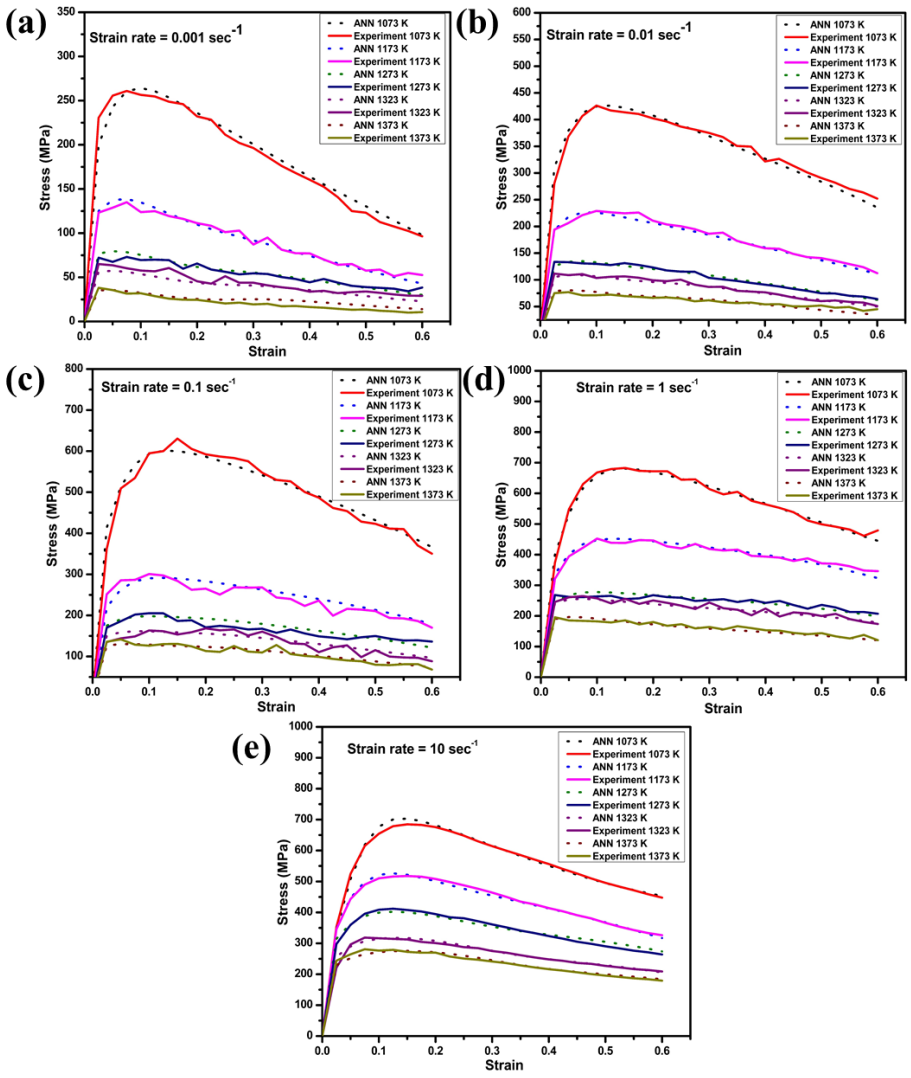

Figure 6.10 Predicted and experimental flow stress at different hot working conditions using ANN model 2

6.4.5 Performance of the models:

The performance of all the above-discussed models are evaluated by the coefficient of correlation (R) and average absolute relative error (AARE) (formula given in chapter 1) [21][153]. The performance of all models are represented in **Figure 6.11**. From the result, it is observed that the ANN model-2 predicts flow behavior more accurately as compared to all other models.

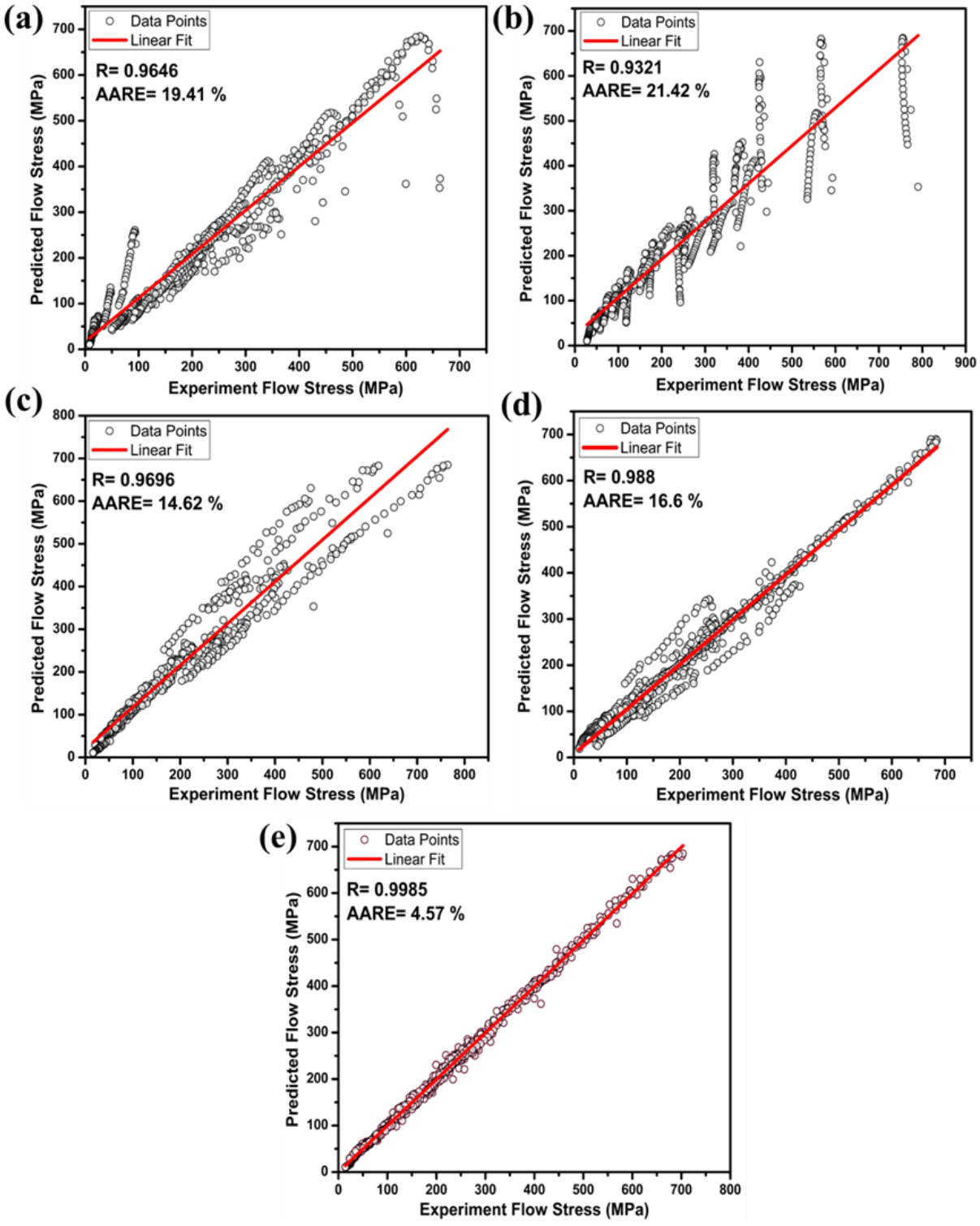

Figure 6.11 Performance of models (a) Modified JC, (b) modified ZA, (c) Arrhenius model, (d) ANN model 1, and (e) ANN model 2

6.5 Summary:

In the present work, two phenomenological, one physical-based, and two ANN-based models have been used to predict the flow behavior (at temperature range 800-1100°C and strain rates range 10^{-3}-10 s^{-1} of $AlCoCrFeNi_{2.1}$ eutectic EHEA. The followings conclusions are drawn based on the above-presented result and discussion.

- The flow curve prediction is done by a physics-based modified ZA model with R=0.9321 and AARE = 21.42 %. This model does not predict the flow behavior accurately which is attributed to dependence of some variables which require precision equipment to be measured.
- The phenomenological model such as modified JC model does not also provide accurate tracking of flow stress at a higher strain rate and lower temperature which is due to the lack of information available of various phenomena during deformation. The observed value of R and AARE for the modified JC model are 0.9646 and 19.41 %.
- Another phenomenological model such as Arrhenius model (R=0.9696 and AARE= 14.62%) shows the improvement in the predictability of flow curve as compared to modified ZA model and the modified JC model.
- It is observed that the ANN model-2 ANN model with backpropagation training algorithm predict accurately the flow behavior at a wide range of temperature and strain rates with obtained R = 0.9985, MSE= $8.91*10^{-5}$ and AARE= 4.57 %) as compared to ANN model-1 (R = 0.988, MSE = 0.0013621, and AARE = 16.42 %) and conventional models. The predicted flow curve is good agreement with the experimental results which is due to the dependence of input data with proper scaling.

Chapter 7

Design and development of CoFeMnNiTi QHEA

7.1 Introduction:

This chapter describes the phase evolution and hot workability of Co-Fe-Mn-Ni-Ti QHEA and prediction of hot deformation behavior using constitutive and ANN modeling. Multicomponent $Co_{25}Fe_{25}Mn_5Ni_{25}Ti_{20}$ QHEA, synthesized by vacuum arc melting followed by suction casting method, resulted in two types of solid solution phases (FCC CoFeNi-rich (α) and BCC Ti-rich (β)) and Ti_2(Ni, Co) type Laves phase. The pseudo-quasiperitectic four-phases reaction, i.e., L + bcc (β) ⟶ fcc(α) + Ti_2(Ni, Co) is proposed based upon the microstructural features observed in the novel $Co_{25}Fe_{25}Mn_5Ni_{25}Ti_{20}$ quasi-peritectic HEA (QHEA). The hot deformation behaviors have been investigated at temperatures ranging from 1073 to 1273 K and different strain rates (10^{-3}, 10^{-2}, $10^{-1,}$ and 1 s^{-1}). The constitutive relation is established to understand the plastic deformability at high temperature. The average activation energy (Q) for hot deformation of studied QEHEA is 311 kJ/mol, and stress exponent n is 3.5. The constitutive relation for the investigated QHEA is described by the equation as $\dot{\varepsilon} \sim \sigma^{3.5} \exp\left(\frac{311000}{RT}\right)$*. The optimum hot workability conditions of QHEA lies in the temperature range 1073-1273 K and strain rate range 10^{-3} s^{-1} -$10^{-1.6}$ s^{-1} as well as temperature 1130-1225K and strain rate $10^{-0.5}$ s^{-1} - 1 s^{-1}. FEM simulation is used to understand the effective plastic strain distribution during deformation of studied QHEA at different temperatures and strain rate 1 s^{-1}.*

An artificial neural network (ANN) approach-based computational model has been established to predict the hot deformation behavior of CoFeMnNiTi QHEA. A constitutive equation also evaluates the flow stress during hot deformation based on the hyperbolic-sinusoidal Arrhenius type model. The performance of both models are assessed by using the coefficient of correlation (R) and average absolute relative error (AARE). The ANN model with R=0.9994 and AARE=1.52 provides better prediction than the Arrhenius type model with R=0.9769 and AARE=11.52. The compressive flow behavior of QHEA is also studied and understood by the

softening and hardening phenomenon during deformation. A schematic representation of the detailed study on QHEA is given in ***Figure 7.1***.

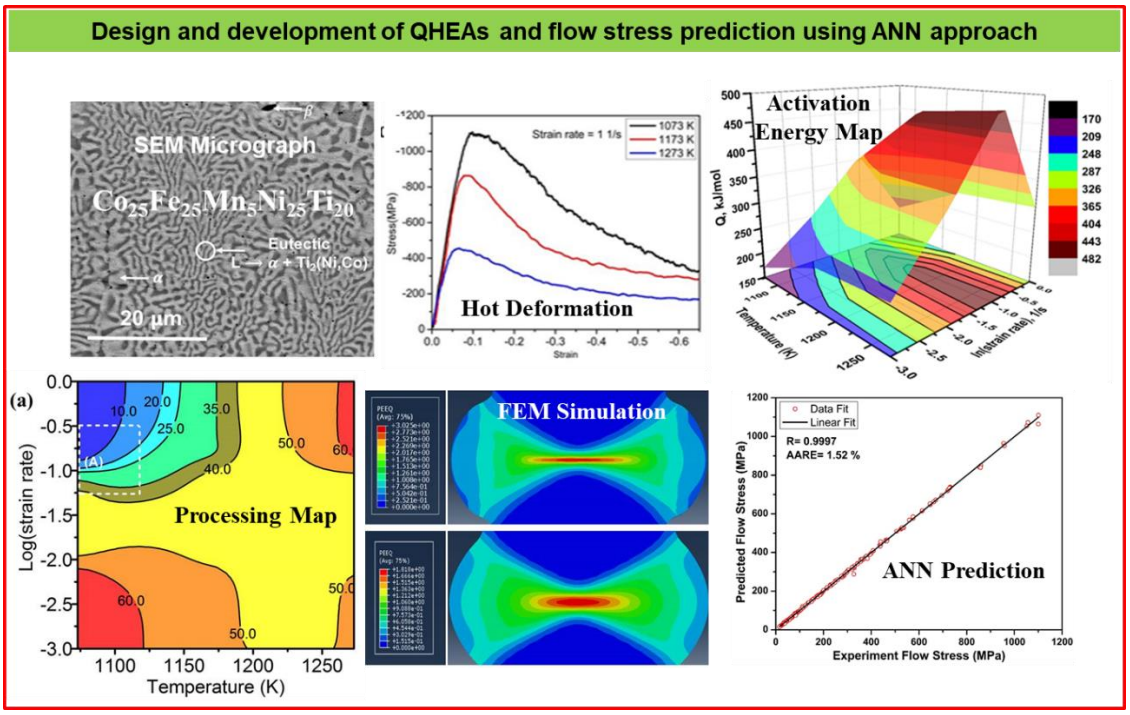

Figure 7.1 A schematic representation of the work for CoFeMnNiTi QHEA

7.2 Objective:

(i) To develop a novel of CoFeMnNiTi QHEA consisting of both peritectic and eutectic by an integrated approach of combining thermodynamic simulation and experimental solidification techniques and establishing new quasi-peritectic four-phase equilibria during solidification based upon the presence of peritectic and eutectic microstructure in the present studied HEA.

(ii) To identify the hot workability regimes of high temperature deformation of $Co_{25}Fe_{25}Mn_5Ni_{25}Ti_{20}$ QHEA at different temperatures and strain rates as well as to determine the activation energy through kinetics analysis.

(iii) To predict the flow curve at different temperatures and strain rates of QHEA using Arrhenius-type constitutive equation and ANN approach.

(iv) To generate the processing maps using multiple models to identify hot workability regimes and understand the plausible deformation mechanism of novel QHEA.

(v) To carry out Finite element method (FEM) simulation to identify the plastic strain variation.

7.3 Experimental and simulation details:

High purity elemental forms of Co, Fe, Mn, Ni, and Ti (purity level ≥ 99.7) were used as starting material. The multicomponent $Co_{20}Fe_{20}Mn_{20}Ni_{20}Ti_{20}$ and $Co_{25}Fe_{25}Mn_{5}Ni_{25}Ti_{20}$ QHEAs were prepared by arc melting cum casting machine from highly pure (C 99.7%) Co, Fe, Mn, Ni and Ti elements in a Ti-gettered ultra high-purity argon atmosphere to get arc melted alloy button. The alloy button was remelted 5–6 times to make sure that the alloy was chemically homogenized in liquid state. To understand the hot deformation behaviours of EHEA at high temperature and different strain rates Gleeble@3800, thermo-mechanical simulator with hydrawege module was used to perform isothermal hot compression tests. The cylindrical specimens (Ø=6 mm and an aspect ratio of 1.5:1) were used for isothermal hot compression tests. The uni-axial hot compression tests were performed at the temperatures, i.e. 800^{o}C (1073 K), 900^{o}C (1173 K) and 1000°C (1273 K) nominal strain rates of 0.001, 0.01, 0.1 and 1 s^{-1}. Graphite sheet, along with Ni paste, was used between sample ends and anvil to reduce friction during hot compression. Before compression test, all the specimens were heated at a heating rate of 5 K/s from room temperature to the desired hot-working temperature and held there for 5 minutes to reach homogeneous temperature distribution throughout the entire specimen. It is to be noted that all the hot compression tests were carried out under an argon atmosphere. The samples were subjected to a 50 % reduction in the height and then immediately water quenched to room temperature to maintain its deformed microstructure. The flow curve (true stress-strain) information was recorded for all strain rates and deformation temperatures during the process of hot compression. Subsequently, Microstructural analysis of the deformed samples was carried out along the compression axis.

The simulation of the hot deformation process was done using ABAQUS software at different deformation temperatures and strain rates conditions. By governing the loading velocity and time, the average strain rate is achieved for hot deformation. The simulation was performed using a quadrilateral element with mesh size 0.25 mm and assumed the 3D model. The meshing of the model of hot deformed EHEA cylinder was done in ABAQUS FE tool with C3D8R elements. Adaptive mesh control manager in ABAQUS/Explicit method was performed due to

the substantial deformation expected during the process, maintaining the high quality of the mesh and hence reduces the chances of mesh distortion during the analysis. The mechanical properties of materials different temperature from flow curves are obtained from the Gleeble®. The other properties which are not available from flow curves are calculated using the rule of mixture. The properties of EHEA such as density, Young's modulus, Poisson's ratio, thermal conductivity, shear modulus and coefficient of thermal expansion are calculated as 7.6954 gm/cm^3, 188.1 GPa, 0.225, 72.285 W/m-K, 107.755 GPa and 1.2355x10^{-5} K^{-1} respectively. The finite element method (FEM) simulation of a hot compression test of EHEA was carried out using an interface friction factor of 0.5 between the die and the workpiece interface. The effective plastic strain field during plastic deformation is established.

7.4 Result and discussion

7.4.1 Thermodynamic simulation

The thermodynamic simulation is done for the prediction of phases which are developed in HEAs during solidification by thermodynamic simulation approach. **Figure 7.2a and 7.2b** shows phase fraction Vs. temperature plot for $Co_{20}Fe_{20}Mn_{20}Ni_{20}Ti_{20}$ and $Co_{25}Fe_{25}Mn_5Ni_{25}Ti_{20}$ QHEA, respectively. **Figure 7.2c** temperature *Vs.* mole fraction of solid, indicting the solidification pathways of $Co_{25}Fe_{25}Mn_5Ni_{25}Ti_{20}$ QHEA. It is important to note that FCC_L12, FCC_L12#2, FCC_L12#3, BCC_B2, C14_laves are observed to form directly from the liquid phase. While SIGMA, BCC_B2, Ni_3Ti_D024, C15_laves phases are formed during solid state transformation.

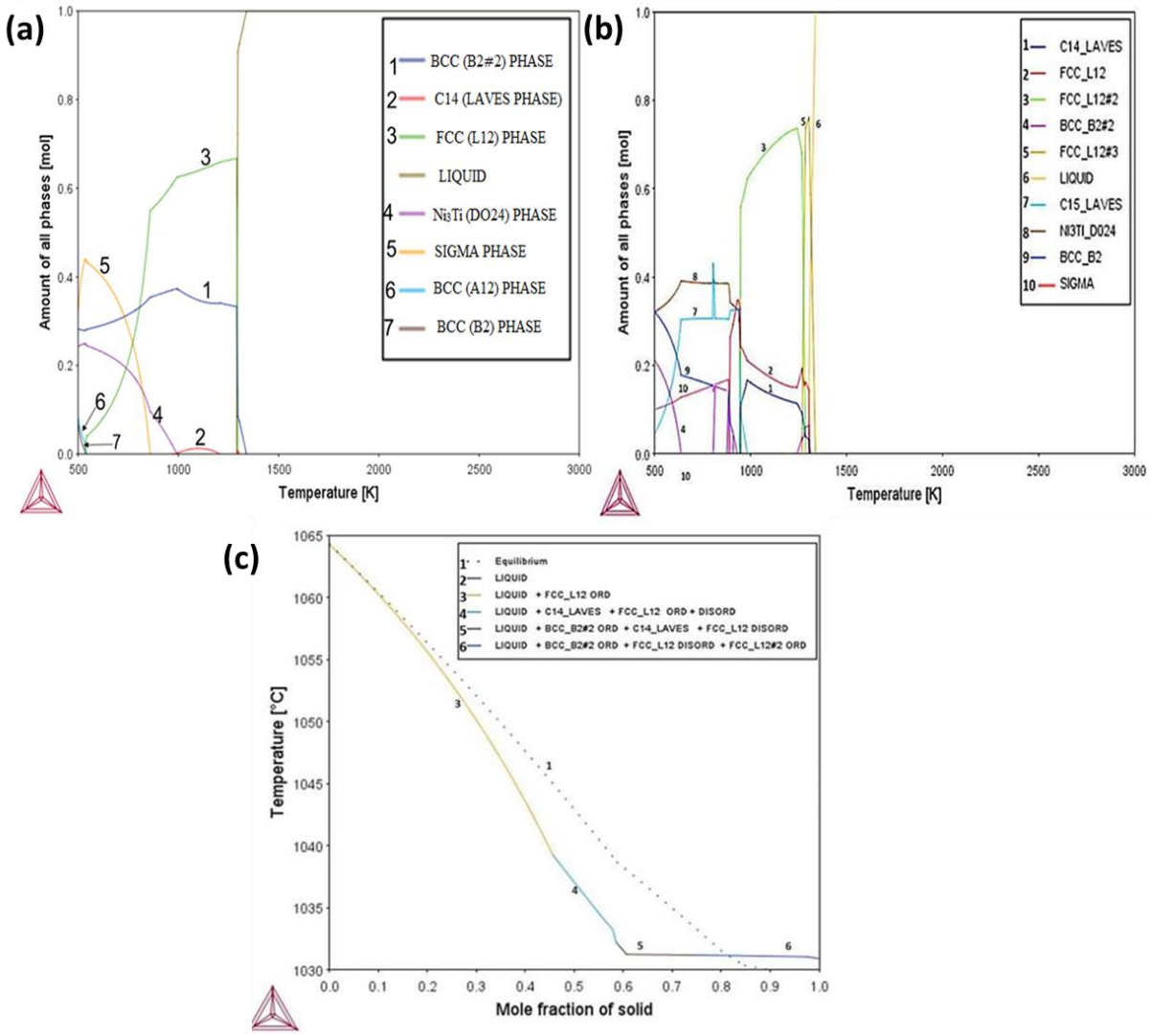

Figure 7.2 Amount of phases with temperature plot (a) $Co_{20}Fe_{20}Mn_{20}Ni_{20}Ti_{20}$ QHEA, (b) $Co_{25}Fe_{25}Mn_{5}Ni_{25}Ti_{20}$ QHEA

7.4.2 Structural and Microstructural characterization

7.4.2.1 XRD analysis

The XRD pattern of Fe-Co-Ni-MnTi multicomponent eutectic high entropy alloys is shown in **Figure 7.3**. The XRD plot indicates the presence of BCC phase (β), FCC phase (α) and Ti_2(Co, Ni) type laves phase. It is to be noted here that all predicted equilibrium phases are not observed in studied EHEA which is attributed to the high cooling rate achieved during the non-equilibrium solidification processing of QHEA.

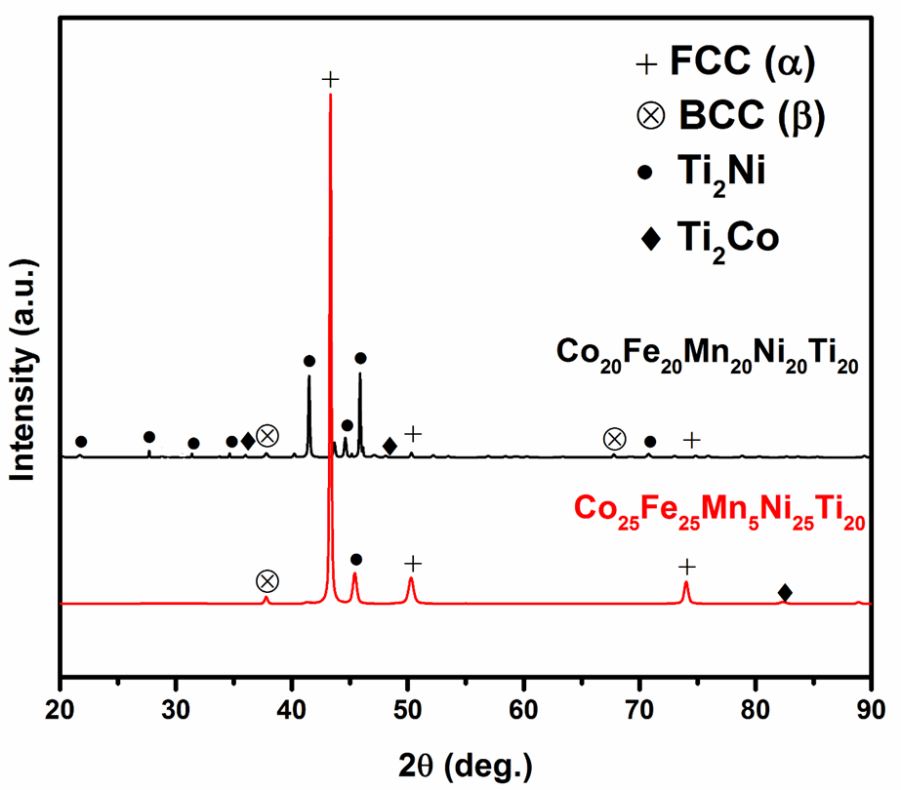

Figure 7.3 XRD pattern for $Co_{20}Fe_{20}Mn_{20}Ni_{20}Ti_{20}$ and $Co_{25}Fe_{25}Mn_5Ni_{25}Ti_{20}$ QHEAs

7.4.4.2 Scanning electron microscopy (SEM) results

The microstructural characterization of QHEAs is carried out by FESEM with backscattered electron mode (as given in **Figure 7.4**). The different phases present in studied QHEAs are marked based on the elemental analysis using EDS attached with FESEM. The microstructure shows solid solution phase having Ti-rich with black contrast (β), Fe-Co-Ni-rich with bright contrast (α) and Ti_2(Co, Ni) type Laves phase with grey contrast. It is to be noted that Ti-rich phase (β) is bounded by Ti_2(Co, Ni) type Laves phase, signifying peritectic reaction. It is found that peritectic reaction occurs between bcc Ti-rich (β) and liquid phase to yield secondary fcc CoFeNi-rich (α) phase. While the eutectic reaction occurs between FCC CoFeNi-rich (α) phase and Ti_2(Ni, Co) type Laves phase.

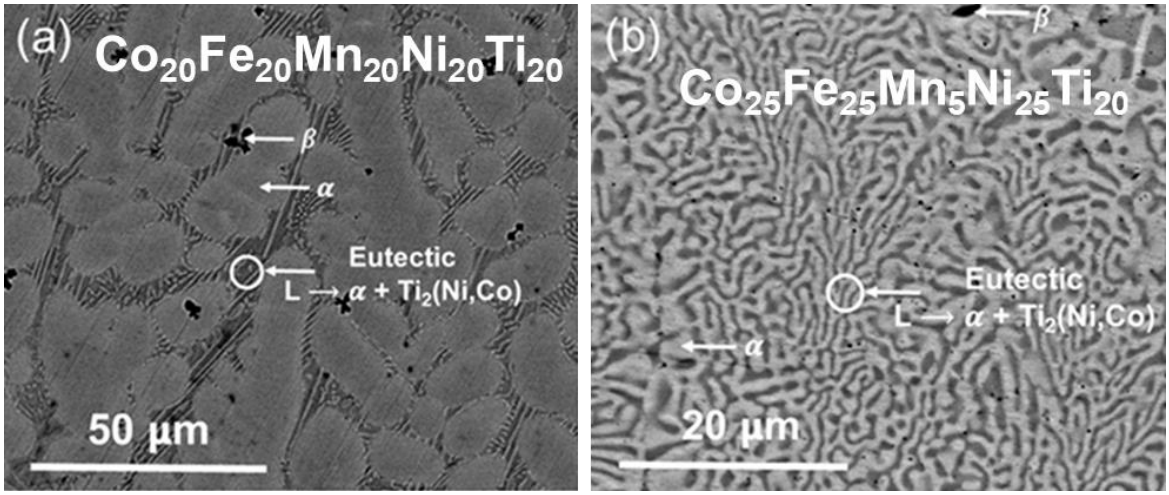

Figure 7.4 SEM micrograph of multicomponent (a) $Co_{20}Fe_{20}Mn_{20}Ni_{20}Ti_{20}$ and (b) $Co_{25}Fe_{25}Mn_5Ni_{25}Ti_{20}$ HEAs.

7.4.3 Flow behaviour of hot compressed materials:

During hot-compression tests, the stress *Vs*. strain plots at different temperature and strain rate are given in **Figure 7.5**. Furthermore, it is observed that the tress increases with increase in the strain rate and decreases with increase in temperature [172]. During the hot deformation, mainly two mechanisms such as strain hardening and softening plays a vital role. Before the maximum stress is reached, the dislocation density increases multiplies significantly and hence the flow stress increased rapidly with increase in strain at particular temperature and attains the maximum. Furthermore, after peak stress, the softening process becomes dominant and hence the stress falls with increase in strain at fixed temperature [173][174][175]

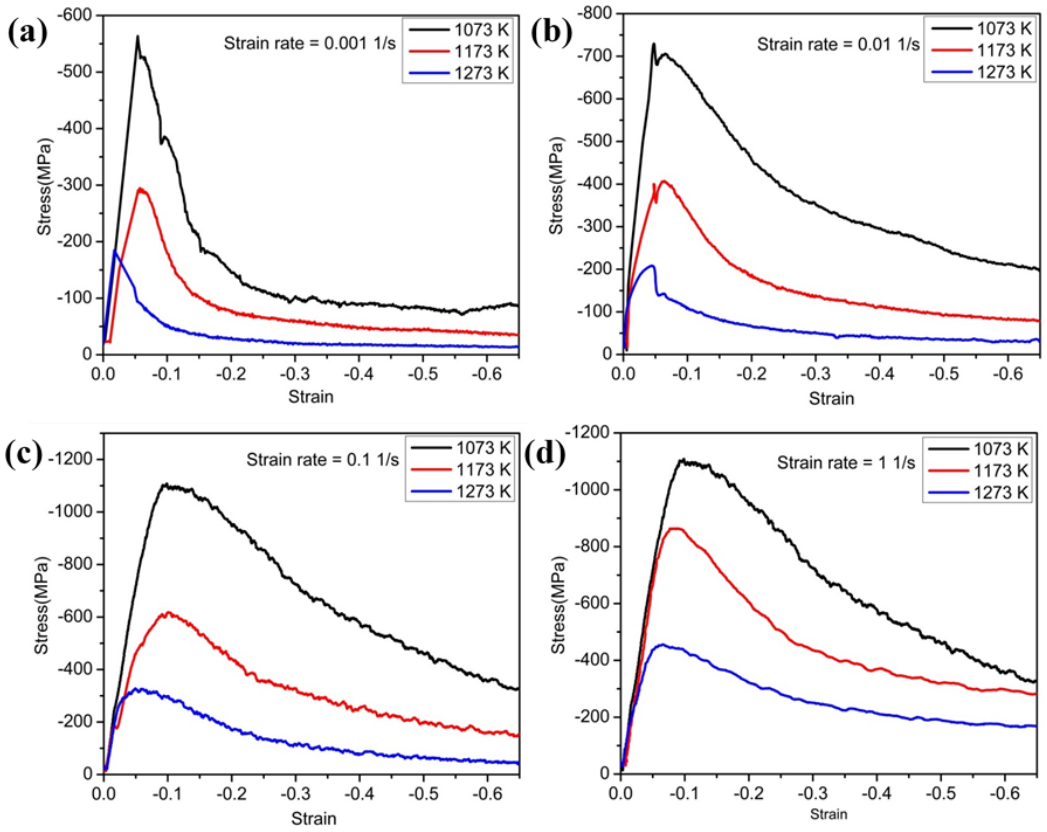

Figure 7.5 True stress-strain plot for $Co_{25}Fe_{25}Mn_5Ni_{25}Ti_{20}$ EHEA at different temperature (K) and strain rate (1/s), (a) 0.001, (b) 0.01, (c) 0.1. and (d) 1

7.4.3.1 Compressive behavior of QHEA:

The flow curve behavior is attributed to either dynamic recrystallization (DRX) or globularization of the laves phase. The volume fraction of β-phase is very low compared to α-phase and laves phases. At the large strain, a saturation of flow curve occurs due to the DRX mechanism. In **Figure 7.5** experimental flow curve indicates a continuous drop in stress values with an increase in strain values except at 0.001 s^{-1} and 0.01 s^{-1} at 1273 K, suggesting that the globularization of laves phase during hot deformation. The strength of materials can be improved by an interaction between dislocations or solute atoms/second phase particles, which can be captured by plotting the rate of softening curves with stress values. The highest value of stress is deducted to eliminate the effect of temperature on the microstructure and plotted in **Figure 7.6,** which shows the rate of softening values with stress values. Each sample shows two softening values after the peak stress. The values of rate of softening are documented in **Table 7.1.**

Table 7.1 Rate of softening values at different hot working condition

Strain rate (s^{-1})	Temperature (^{o}C)	θ_1	θ_2	θ_2 / θ_1
0.001	800	-8.32	-14.92	1.79
	900	-12.38	-26.05	2.1
	1000	-10.94	-20.68	1.89
0.01	800	-2.67	-5.65	2.11
	900	-6.31	-9.37	1.48
	1000	-5.2	-8.15	1.56
0.1	800	-1.17	-3.23	2.76
	900	-3.85	-6.61	1.71
	1000	-3.85	-7.04	1.82
1	800	-1.14	-3.7	3.24
	900	-4.2	-8.51	2.02
	1000	-3.49	-5.99	1.71

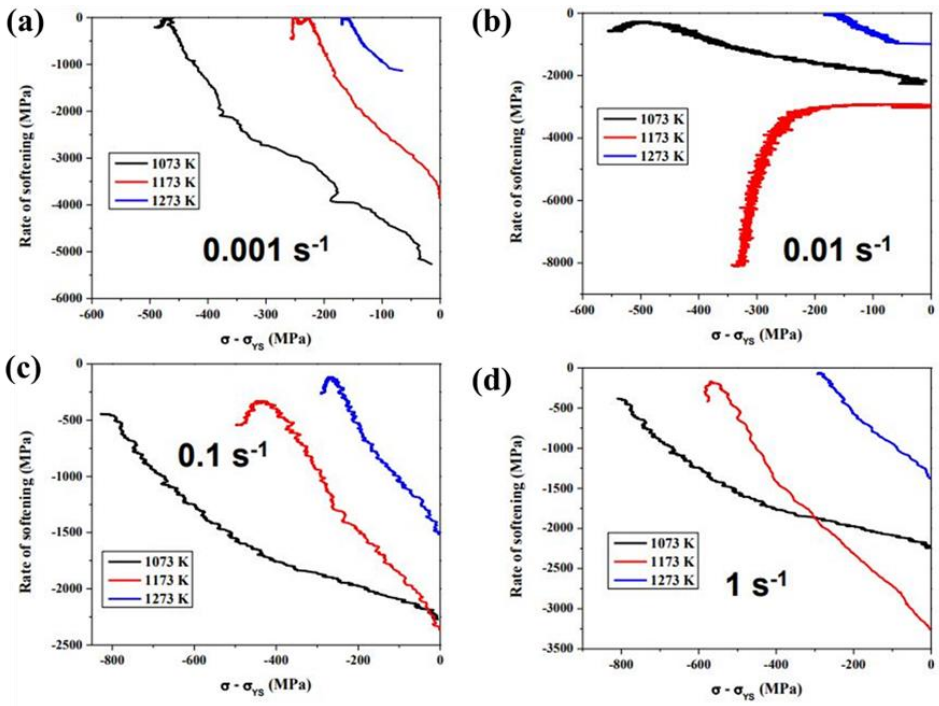

Figure 7.6 Plot between rate of softening and stress

It is remarked that the initial rate of softening is low compared to the rate of softening values at later stage. The rate of softening depends on the initial orientation of the grains with respect to the compression direction resulting in the variation in softening rate either with increase in temperature at a fixed strain rate or with increase in strain rate at a fixed temperature. However, no regular trend in the values of softening rate is observed because of the variation in initial grain orientation with respect to the loading axis.

The plot between mean free path and stress represents in **Figure 7.7**. The mean free path of dislocation indicates a continuous increase in the value with strain which can be attributed to the breakdown of laves phases during deformation which facilitates the cross slip of dislocations in addition to the climb of dislocations. The climb and cross slip of dislocations increase the mean free path of dislocations with increase in strain value. The increase in mean free path of dislocations results in a decrease in the stress value of the sample. The decrease in the mean free path to zero value indicates that the completeness of globularization phenomenon during deformation, which is observed for the samples deformed at 1273 K in the strain rate range of 0.001to 1 s^{-1}.

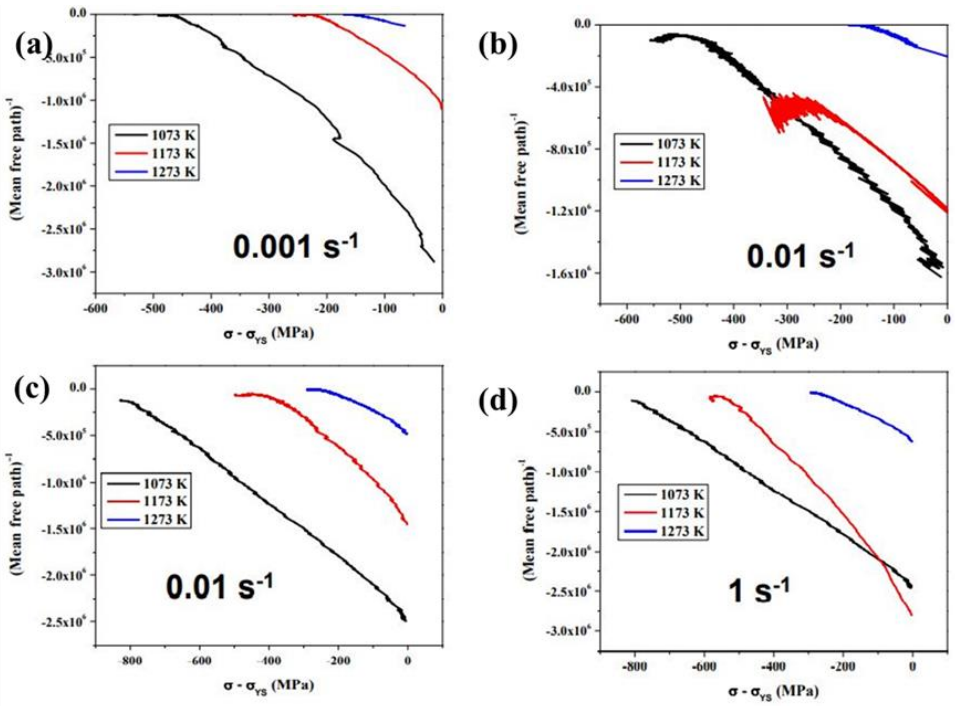

Figure 7.7 Plot between mean free path and stress

The starting microstructure contains the mixture of α-phase (white space present between the purple colors) and laves phase (purple color) as an alternate lamellae in the grain (**Figure 7.8a**). The orientation of lamellae varies from one grain to next grain. Further, the microstructure contains the β-phase (see black color marks in **Figure 7.8a**) which is randomly distributed in the grains. During deformation at high temperature, laves phase bend within the grains and the extent of bending depends on the orientation of laves phase with respect to the loading axis. The bended laves phase of a grain (**Figure 7.8d**) is shown in the magnified form in **Figure 7.8e** where it is clearly observed that dislocations are piled up at the nose of the bend region. It is well known that atomic potential of laves phase is the maximum in the tip of the bend region and decreases towards its lateral sides. Since, the deformation was done at high temperature, the high atomic potential of the tip of the bend region along with the enhanced pipe diffusion by the presence of dislocation breaks the single lamellae of laves phase into two lamellae (see **Figure 7.8f**). This procedure is observed in the other grains of the microstructure during deformation. This breaking of laves phase lamellae facilitates the movement of dislocation further in the α-phase and enhances the dislocation-dislocation interaction. This breaking of laves phase at high temperature during deformation reflects in the decrease in the value of stress with increase in the

strain of the material. However, the breaking of laves phase is incomplete in all the grains when deformation was carried out at high strain rate or low temperature and the above observation is consistent with the microstructure obtained after deformation (see **Figure 7.7**).

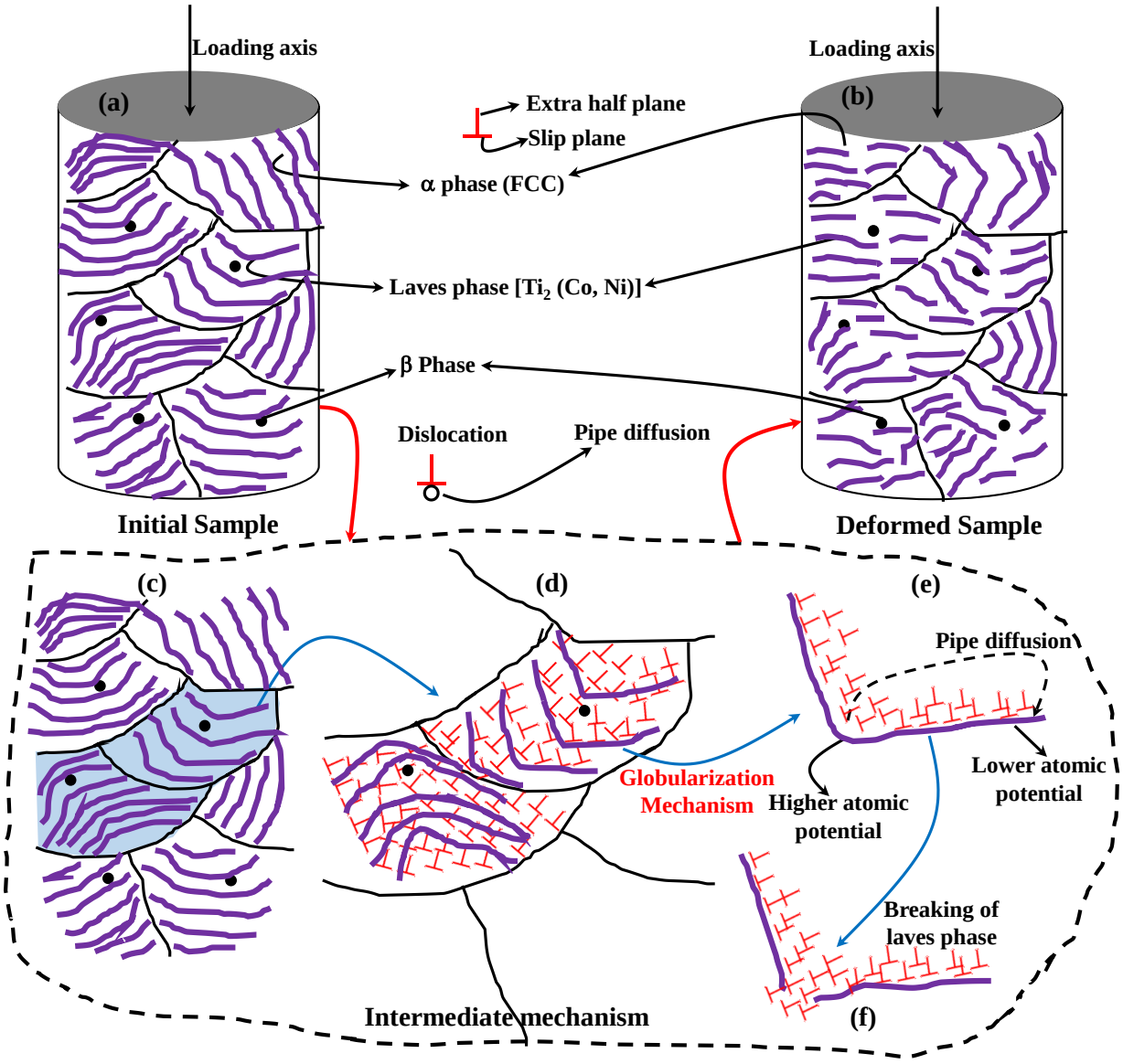

Figure 7.8 Mechanism of eutectic HEA during high temperature deformation; (a) Initial microstructure of the material before deformation, (b) microstructure after deformation. The intermediate mechanism of microstructure evolution during deformation is shown in (c - f).

7.4.3.2 Simple Arrehenius equation (for Q and n calculation):

The constitutive equation is the correlation of true stress, deformation temperature and strain rate. The stress-strain value obtained from the experimentally via a hot compression test can be used to calculate the activation energy and material constant. It is reported [176][169][177] that the simple power-law correlates the flow stress, deformation temperature and strain rate. It is important to note here that the activation energy gives the information about the deformation mechanism which is correlated with the microstructural evolution, mainly dislocation movement, dynamic recovery (DRV), dynamic recrystallization (DRX) and grain boundary movement [109].

According to the constitutive equation, the activation energy is supposed to be a constant physical parameter which can be determined using power law :

$$\dot{\varepsilon} = A_1 \sigma^n \exp[\frac{Q}{RT}] \quad (7.1)$$

After taking the logarithm of both sides and differentiating the equation. Finally, the activation energy is expressed as

$$Q = 2.303R\{\frac{\partial log\dot{\varepsilon}}{\partial log\sigma}\}_T \{\frac{\partial log\sigma}{\partial(\frac{1}{T})}\}_{\dot{\varepsilon}} \quad (7.2)$$

Where, $\frac{\partial \log\dot{\varepsilon}}{\partial \log\sigma}$ is the slope of the log$\dot{\varepsilon}$ *Vs*. log σ and $\frac{\partial \log\sigma}{\partial(\frac{1}{T})}$ is a slope of the logσ *Vs*. 1/T and R= universal gas constant (8.314 J mol $^{-1}$K).

The activation energy (Q) at a strain 0.65 for studied EHEA has been calculated by drawing a plot between log$\dot{\varepsilon}$ *Vs.* log σ at different temperature and between logσ vs 1/T at different strain rate which are given in **Figure 7.9a** and **Figure 7.9b**, respectively. The typical value of activation energy (Q) for studied EHEA at strain 0.65 is found to be 311 kJ/mol, and stress exponent (n) value is 3.5. Further, the activation energy (Q) is estimated as 362 kJ/mol, 293 kJ/mol, 273 kJ/mol, 284 kJ/mol, 287 kJ/mol and 293 kJ/mol at true strain 0.1, 0.2, 0.3, 0.4, 0.5 and 0.6 respectively. Therefore, the constitutive equation at true stain 0.65 as a function of strain rate ($\dot{\varepsilon}$) and temperature (T) for studied EHEA can be described as follows:

$$\dot{\varepsilon} \sim \sigma^{3.52} \exp(\frac{311000}{RT}) \quad (7.3)$$

Though, it is essential to observe that this constitutive equation for studied EHEA defines the stress and strain rate relation in the temperature between 800°C to 1050°C. Rahul et al. [89] found that n and Q values are 5.6 and 306 kJ/mol, respectively for $AlCoCrFeNi_{2.1}$ EHEA in the

deformation temperature range of 800°C-1100°C. It is also reported for $Co_{20}Cu_{20}Fe_{20}Ni_{20}Ti_{20}$ EHEA [86] that n and Q values are obtained as 3.1 and 316 kJ/mol at strain 0.7, respectively.

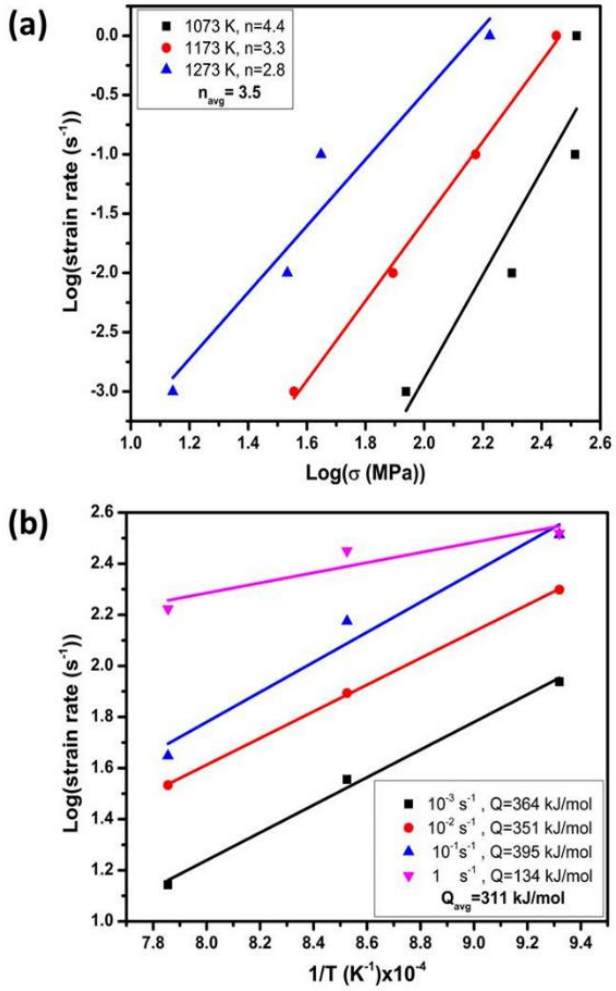

Figure 7.9 Plot between (a) Log Ɛ̇ and Log σ (b) Log σ and 1/T; used for calculating the activation energy (Q) and stress exponent (n) at true strain 0.65.

The calculated activation energy (Q ~ 311 kJ/mol) of investigated EHEA at the last stage of the hot deformation (i.e. at true strain 0.65) is comparable to the commercial Ti-6Al-4V alloys (i.e. Q ~ 265-370 kJ/mol)[178]. Usually, higher is the activation energy, better is the workability of material at elevated temperature. The calculated activation energy at a different stage of hot deformation is shown in the **Figure 7.10**. It is important to note that all alloying element in EHEAs consider as substitutional solutes, the activation energy for the interaction of the solute atoms with dislocation consist of a combination of both energies for the vacancy formation as well as energy for solute motion [86].

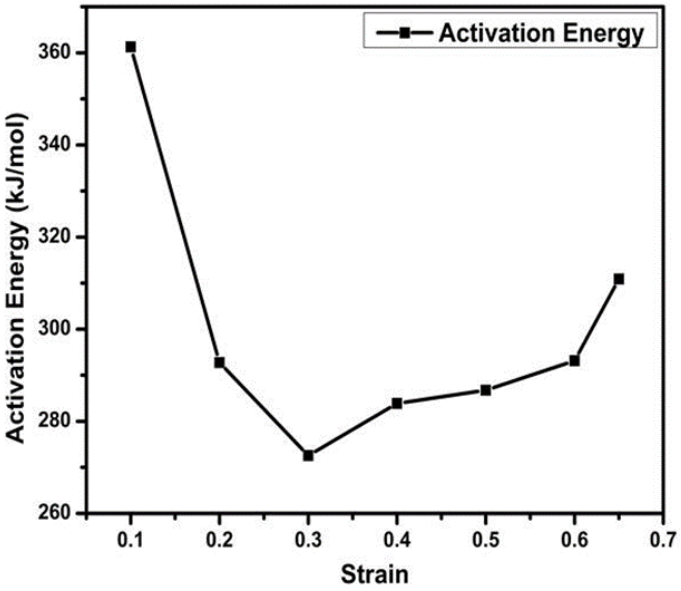

Figure 7.10 Activation energy *Vs* true strain

7.4.4 Deformation windows and processing maps:

It is to be noted that the processing maps of studied EHEA are constructed based on the dynamic material modelling (DMM) and the combination of two contour maps, i.e. iso-efficiency (η) and instability factor $\xi(\overline{\dot{\varepsilon}})$. **Figure 7.11a** shows the processing efficiency contour and instability maps for studied EHEA at strain at 0.65. The maximum efficiency shows the optimal processing conditions. However, the condition with peak efficiency may exhibit a negative instability parameter. It is found that the instability during the deformation occurs mainly due to cracks, localised plastic flow in the microstructure. It is reported [179] that different DMM stability factors are unable to predict the geometrical instability, i.e. excessive bulging during compression testing, necking during tensile testing and uneven deformation in axial and radial loading during torsion testing.

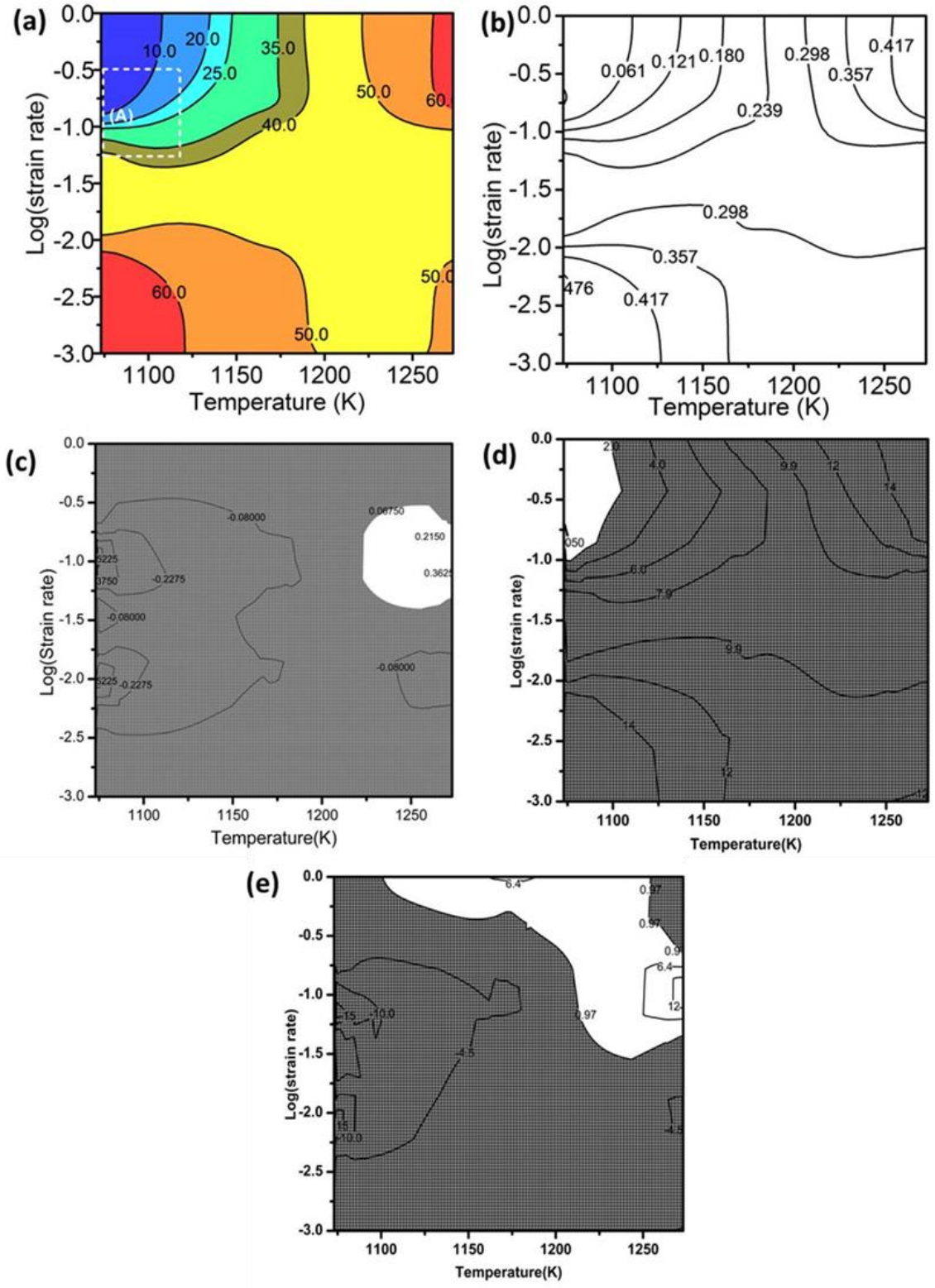

Figure 7.11 Processing map at strain 0.65 (a) Efficiency of power dissipation (b) Strain rate sensitivity m (c) Rate of change of strain rate sensitivity w.r.t. strain rate $\dot{\mathbf{m}}$ (d) s (e) $\dot{\mathbf{s}}$

Moreover, a region of dense contour lines with high power dissipation efficiency and a nearby unstable region are considered metastable regions [180]. It is clear from **Figure 7.11a** that higher value of efficiency (50-60 %) is observed in the two domains. The first one lies in the temperature between 1073 K to 1200 K and the strain rate between 10^{-3} s^{-1} to 10^{-2} s^{-1} and in the temperature range 1225-1273 K and strain rate 10^{-1} s^{-1} - 1 s^{-1}. As per the instability processing map, the processing Instability factor $\xi(\overline{\dot{\varepsilon}})$ shows negative value at a temperature range between 1073 K to 1130 K and strain rate between $10^{-1.25}$ s^{-1} to $10^{-0.5}$ s^{-1}, presented by region A in **Figure 7.11a**. The sensitivity factor related to strain rate m (as shown in **Figure 7.11b**) shows that the stability in all ranges of temperature and strain rate in processing maps. The stability regimes during hot deformation are also predicted by a parameter ($\dot{m}$) (hatched areas as shown in **Figure 7.11c**) and also the stability region predicted by two other parameters s and $\dot{s}$ are indicated in **Figure 7.11d** and **Figure 7.11e,** respectively as hatched areas. The prediction by parameter s and $\dot{s}$ shows the stable region in the temperature ranges 1073-1273K, 1105-1273 K and strain rate ranges 10^{-3}-10^{-1} s^{-1}, 10^{-1}-1 s^{-1}. The workability regimes with different parameters of DMM model provided in **Table 7.2**. Finally, DMM predicts the stable hot workability regimes in the temperature between 1073 K to 1273 K and strain rate between 10^{-3} s^{-1} $10^{-1.55}$ s^{-1} as well as 1130 K to 1225 K and strain rate$10^{-0.5}$ s^{-1} to 1 s^{-1}.

Table 7.2 Stable and unstable region with a different parameter of DMM model

Criteria for stability	Unstable region		Stable region	
	Temperature (K)	**Strain rate (s^{-1})**	**Temperature (K)**	**Strain rate (s^{-1})**
$\xi(\dot{\bar{\varepsilon}})$	1073-1120	$10^{-1.25}$-$10^{-0.5}$	1120-1273, 1073-1273	$10^{-0.5}$-1,10^{-3}-$10^{-1.25}$, $10^{-1.25}$-$10^{-0.5}$
0<m<1	No	No	All	All
$\dot{m} < 0$	1220-1273	$10^{-1.40}$-$10^{-0.5}$	1073-1273, 1073-1220,	10^{-3}-$10^{-1.40}$, $10^{-1.40}$-$10^{0.5}$, $10^{-0.5}$ - 1
$S \geq 1$	1073-1105	10^{-1}-1	1073-1273, 1105-1273	10^{-3}-10^{-1},10^{-1}-1
$\dot{S} \leq 0$	1100-1255 1200-1273	$10^{-0.35}$-1, $10^{-1.5}$-$10^{-0.4}$	1073-1273, 1073-1200, 1073-1100, 1250-1273	10^{-3}-$10^{-1.55}$, $10^{-1.55}$-$10^{-0.65}$, $10^{-0.65}$ - 1

7.4.4.1 Activation energy maps (AEM):

The activation of energy during the hot deformation indicates the level of complexity. It provides useful information regarding the optimization of hot working processing of materials, microstructural features, and flow-stress behavior during the processing. The activation energy (Q_h) at different conditions evaluated for developing the AEM. The AEM for the present alloy at strain 0.5 is given in **Figure 7.12**. At a constant strain rate, the value Q_h increases with increasing the temperature while, at a constant temperature, Q_h increases up to the strain rate of 0.1 and then decreases at a lower strain rate (from 10^{-1} to 10^{-3} s^{-1}). The average activation energy at strain 0.5

was found 308 kJ/mol, however maximum and minimum activation energy at stain 0.5 are 443 kJ/mol (at temperature range 1160-1273 K and strain rate range $10^{-1.4}$-$10^{-0.75}$ s^{-1}) and 209 kJ/mol, respectively. The mechanical properties of CoFeMnNiTi EHEA is correlated with a microstructural feature, which is influenced by activation energy. Finally, it can be concluded that activation energy is sensitive to hot working processing parameters and helps understand the effect of that parameter on the microstructure and mechanical properties of materials.

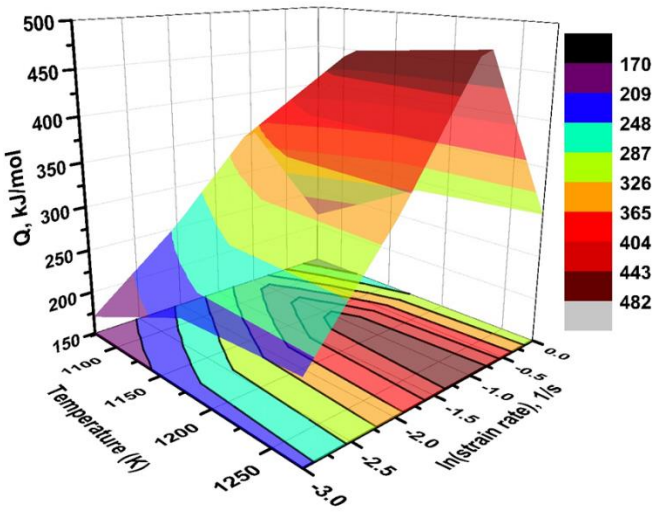

Figure 7.12 Variation in activation energy at different hot working conditions

7.4.5 Microstructural analysis of deformed samples:

The detailed microstructural characterization of the deformed EHEA at different hot working conditions was carried out to correlate with the observation drawn from the developed contour plots using various parameters**.** However, The representative SEM micrograph of deformed sample is shown in Fig. 5. It is found that the cracks are observed in the deformed specimen at temperature of 800°C and strain rate of 1 s^{-1} (as shown in **Figure 7.13a**) and this instability is matched with the region in the contour plot developed using the parameter s. In **Figure 7.13b**, **Figure 7.13c**, **Figure 7.13d** and **Figure 7.13f**, it is found that a uniform distribution of phases as well as cracks and pores free microstructure at different temperatures and strain rates. It is to be noted that the contour plots generated using various parameters show a stable zone at 800°C (strain rate=0.01 s^{-1}), 900°C (strain rate=0.1 s^{-1}) as well as 1000°C (strain rate=0.01 s^{-1}), but the unstable zone is observed at 800°C (strain rate=0.1 s^{-1}). Further, the porosity is found in a

deformed specimen at 1000°C (strain rate=0.1 s^{-1}) (shown in **Figure 7.13e**), which corroborates with the instability regimes in the generated contour plots using parameters such as $\dot{m}$ and $\dot{s}$.

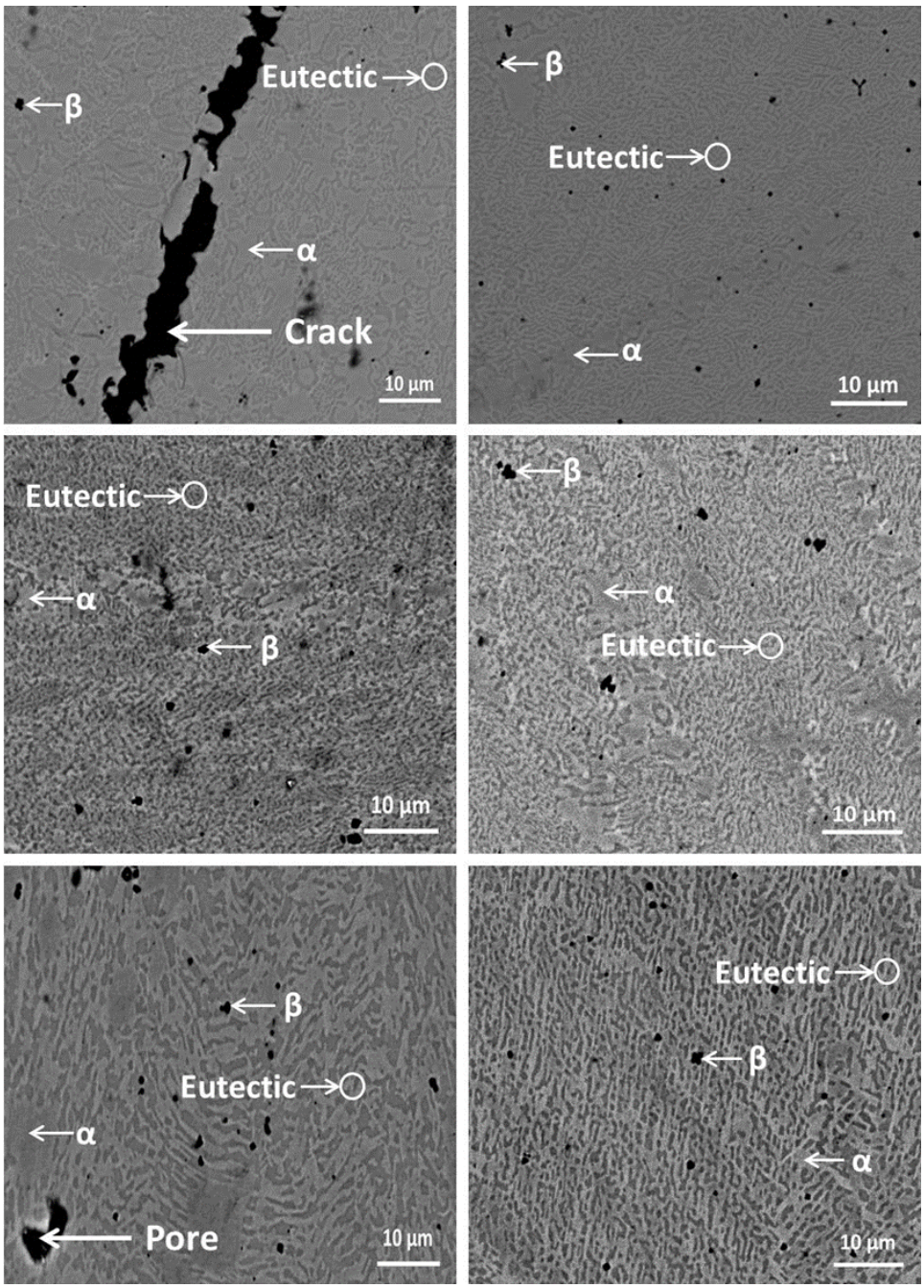

Figure 7.13 SEM BSE images of hot deformed samples at (a) 800°C@SR 1, (b) 800°C@SR 0.1, (c) 800°C@SR 0.01, (d) 900°C@SR 0.1, (e) 1000°C@SR 0.1and (f) 1000°C@SR 0.01

It is evident in the stable regime that microstructural constituents are uniformly distributed throughout the whole specimen and elongated grains are observed in the direction of the compression axis. While in the unstable regime, the localised plastic deformation, cracks and

pores are observed in the microstructure of the deformed sample. It is important to note that the deformation temperature and strain rate play an essential role in the microstructural evolution of deformed EHEAs. The microstructural features at different strain rate (s^{-1}) and Temperature (K) are provided in **Table 7.3**. Therefore, uniform distribution of phases and crack-free microstructure of EHEA are necessary for processing of materials at high-temperature and hence can be considered as potential candidate materials for high-temperature structural applications.

Table 7.3 Microstructural features at different strain rate and Temperature

Domain	Strain rate Range (s^{-1})	Temperature range (K)	Efficiency (η)	Microstructural features
Stable regime	$10^{-1.55}$-$10^{-0.65}$	1073-1200	30-40	Uniform distribution of phases
	10^{-3}-$10^{-1.55}$	1073-1273	40-60	Uniform distribution of phases
	$10^{-1.40}$-$10^{-0.5}$	1073-1220	40-50	Uniform distribution of phases
Unstable regime	10^{-1}-1	1073-1105	10-20	Large cracks
	$10^{-1.5}$-$10^{-0.4}$	1200-1273	40-50	Pores, Localized flow

7.4.6 FEM simulation:

The FEM simulation can be used to identify the bulk deformation characteristics by identifying the strain, stress and strain rate fields in the material. By utilising this capability, the more sensitive zones in material flow regions with complex geometries can be identified in actual industrial production conditions. The stress-strain flow curves obtained in Gleeble 3800® thermo-mechanical simulator at different sets of temperatures and strain rates were imported into ABAQUS ® FEM software to simulate the hot deformation behaviour. The constitutive equation can also be used for developing the material database. Effective plastic strain at a temperature of 1173 K and 1273 K and at strain rate 1 s^{-1} shown in **Figure 7.14a** and **7.14b**. The strain field distribution confirms the inhomogeneous flow behaviour inside the material, resulting in the

microstructural variation at different zones. The results obtained by simulation shows the higher value of effective plastic strain at the center of the deformed sample for both temperatures and the maximum strain values depend on the temperature. It is important to note here that this inhomogeneity needs to take into consideration while characterizing material for high-temperature applications.

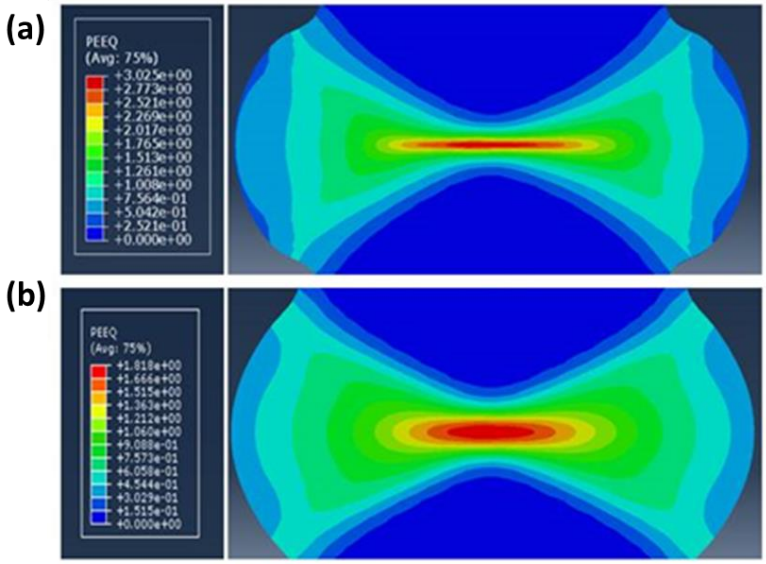

Figure 7. 14 Simulated Effective plastic strain distribution at strain rate 1 and temperature (a) 1173 K, and (b) 1273 K

7.4.7 Flow curve prediction:

For assessing the flow stress by an and Arrhenius type model and ANN model, experimental flow stress data of hot compression tested samples of studied QHEAs with different hot working conditions (temperature range 1073 K-1273 K and strain rate range 10^{-3}-1 s^{-1}) were used.

Flow stress prediction using constitution model (Arrhenius equation):

Many researchers currently use the constitutive equation based on the hyperbolic sinusoidal Arrhenius-type model to estimate the flow stress during hot working [150], but accuracy usually is limited. Further, the improvement in the model by considering the Zener-Holloman parameter (Z) [151] is also known as temperature compensated-strain rate. The detailed procedure (equations and calculation of different parameters) for flow stress prediction using the Arrhenius model is given in chapter 4 (section 4.4.4.3). **Figure 7.15a**, **7.15b**, **7.15c**, and **7.15d** show the

plots for calculation of constant β, N, n, and s, respectively. The linear plot between the ln[sinh(ασ)] vs. lnZ gives the value of lnA (intercept of the plot) as given in **Figure 7.15e**.

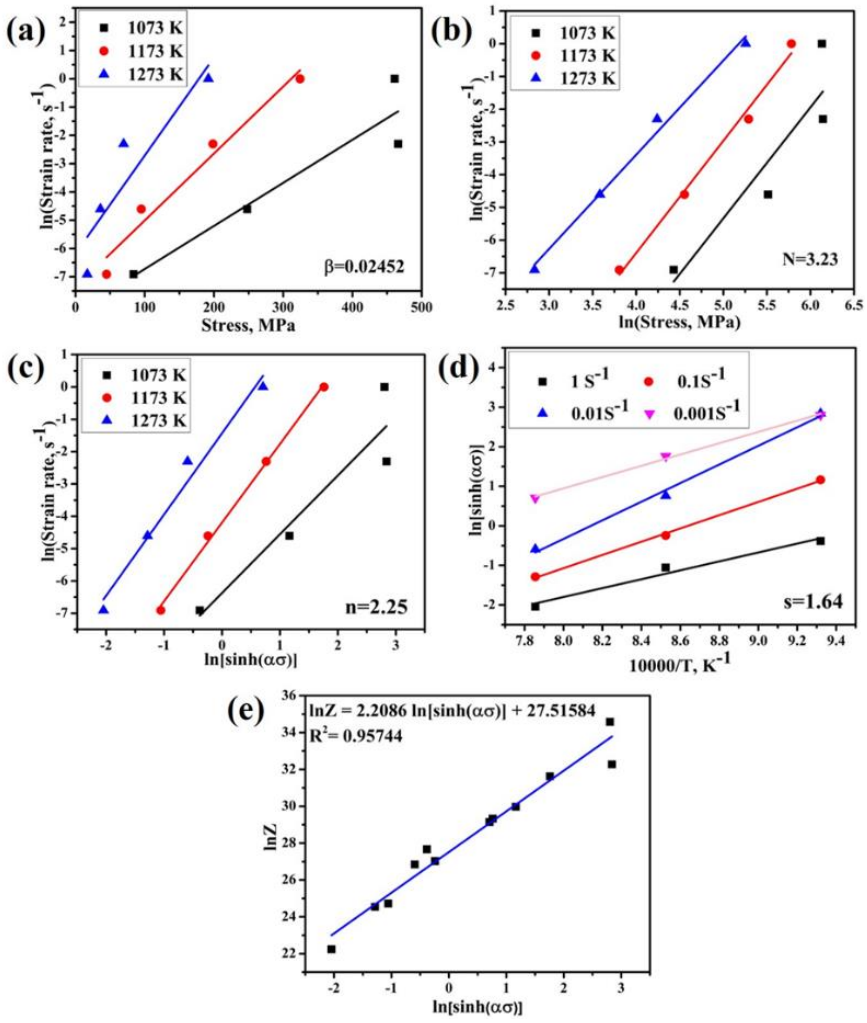

Figure 7.15 Plots for different material constant (a) β, (b) N, (c) n, (d) s, and (e) **lnA**

The n is determined as an average of the slopes of $\{(\partial \ln \dot{\varepsilon})/\partial \ln[\sinh(\alpha\sigma)]\}$ at different temperatures because the n is dependent on temperature and strain rate. Q_h is calculated by putting the value of R, n, and s in equation 3 at strain 0.5 (at strain 0.5 value of β=0.02452, α=0.007585, N=3.23, n=2.25, and s=1.64), which is approximately 308468 J/mol. The parameter Z, ε̇ and σ at strain 0.5 can be expressed as the following equation:

$$Z_{0.5} = \dot{\varepsilon}.\exp\left(\frac{308468}{RT}\right) \qquad (7.4)$$

$$\dot{\varepsilon} = 8.91 \times 10^{11} \times [\sinh(0.007585.\sigma_{0.5})]^{2.2541} \times \dot{\varepsilon}.\exp\left(\frac{308468}{RT}\right) \qquad (7.5)$$

$$\sigma_{0.5} = \frac{1}{0.007582} \times \ln\left\{\left(\frac{Z_{0.5}}{8.11\times10^{11}}\right)^{\frac{1}{2.2541}} + \left[\left(\frac{Z_{0.5}}{8.11\times10^{11}}\right)^{\frac{2}{2.2541}} + 1\right]^{\frac{1}{2}}\right\} \qquad (7.6)$$

Figure 7.16 shows the effect of strain on material constant (α, Q, n, and A_0). For calculating the flow stress at different strain, the material constant (α, Q, n, and A_0) is calculated by the polynomial fitting and is fitted by sixth-order, which is found to be good correlation with strain and can be expressed as:

$$\ln A_0 = -1398.168\varepsilon + 10936.386\varepsilon^2 - 42533.268\varepsilon^3 + 87846.688\varepsilon^4 - 92303.215\varepsilon^5 + 38800.137\varepsilon^6 + 98.276 \qquad (7.7)$$

$$Q = -13773.473\varepsilon + 107945.454\varepsilon^2 - 42.663.603\varepsilon^3 + 870539.300\varepsilon^4 - 916452.012\varepsilon^5 + 385959.408\varepsilon^6 + 994.608 \qquad (7.8)$$

$$\alpha = -0.03011\varepsilon + 0.42851\varepsilon^2 - 1.6888\varepsilon^3 + 3.0726\varepsilon^4 - 2.5599\varepsilon^5 + 0.74712\varepsilon^6 + 0.00282 \qquad (7.9)$$

$$n = -305.584\varepsilon + 2385.786\varepsilon^2 - 9362.457\varepsilon^3 + 19592.326\varepsilon^4 - 20831.632\varepsilon^5 + 8823.861\varepsilon^6 + 17.339 \qquad (7.10)$$

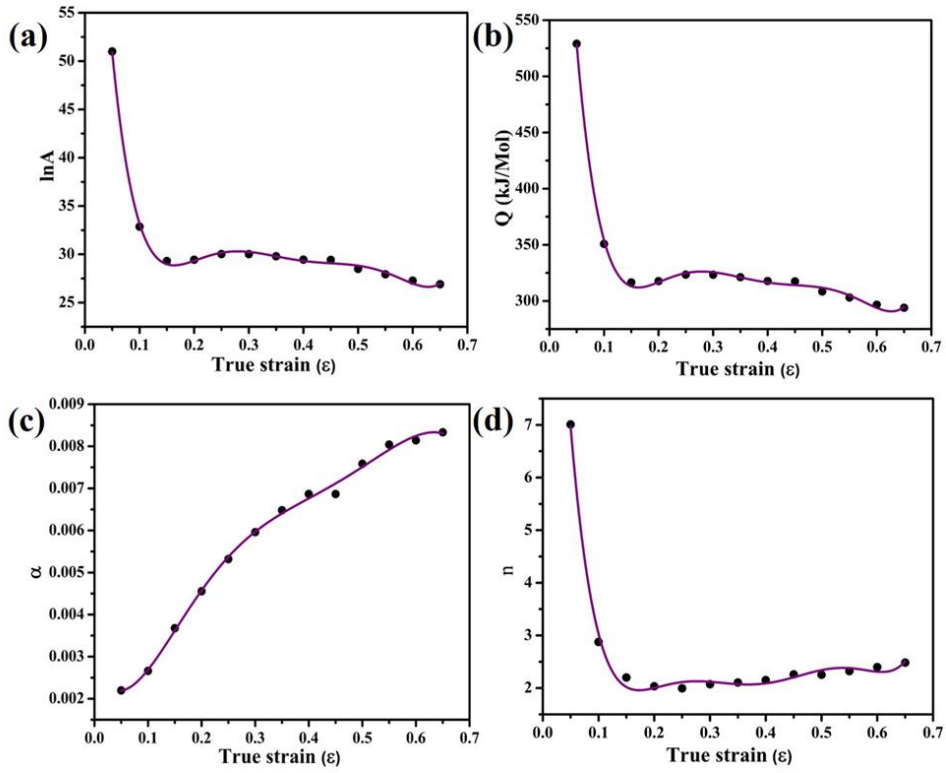

Figure 7.16 Variation on material constant (α, Q, n, and A) with strain

The flow stress at different temperature and strain rate calculated by putting the value of $\dot{\varepsilon}$, Z and T in the equations mentioned above (Equations 6 and 8). **Figure 7.17** indicates the predicted flow stress (dotted line) with experimental flow stress (solid line) at different temperatures and strain rates using the Arrhenius equation.

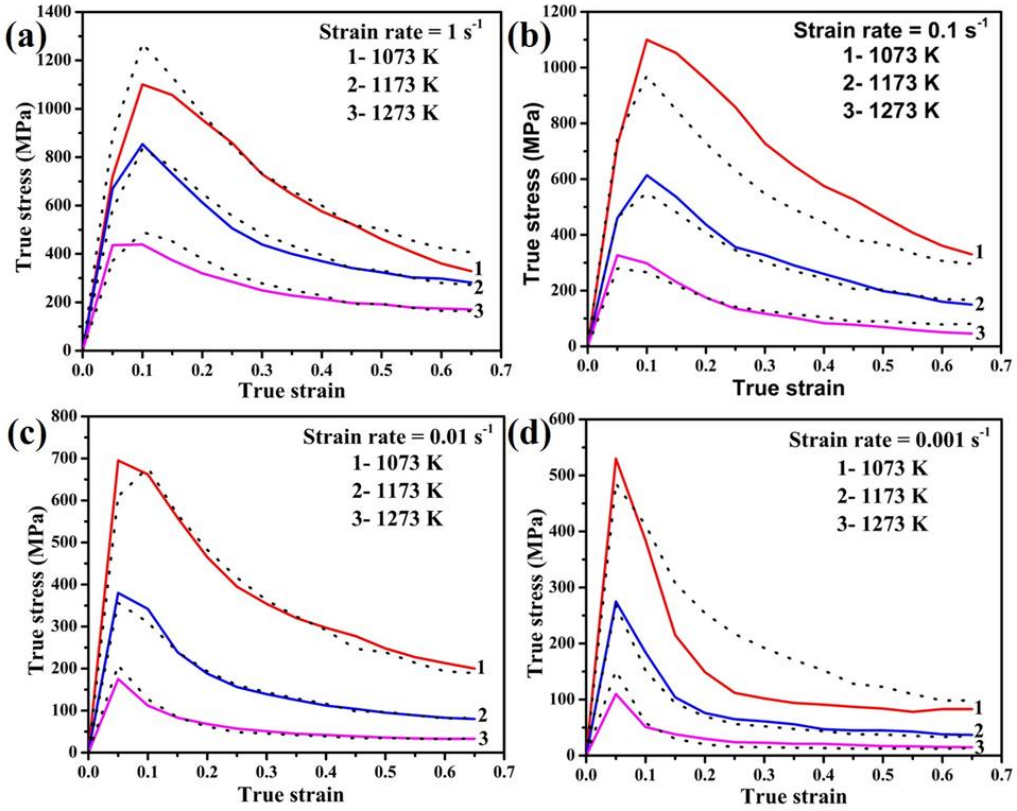

Figure 7.17 Representation of predicted flow stress (dotted line) and experimental flow stress (solid line) using the Arrhenius equation

Flow stress prediction using ANN model:

For the flow stress prediction in the present study, MATLAB 9.6 (R2019b) version has been used. Before performing the training, the data is first normalized in a range of 0 to1 for accurate predictions. But the deviation in strain rate is found to be large and after normalization, the amount of strain rate is minimal, which is not appropriately learned by ANN in the present study. Further, the logarithm equation is used to normalize the strain rate. The details of the normalization of data are given in **Table 4.2** (in chapter 4). The ANN model is established to examine the flow stress by using the neural network using the L-M training algorithm. The input of that model is the strain, temperature, and strain rate, and the output of the model is flow stress. A total of 624 data points were employed for the ANN model. The 3-15-1 network system of ANN model predicts flow stress with optimum accuracy after several trains, where the 15 shows neurons in the hidden layer. The network with 15 neurons in the hidden layer gives the best possible result (mean square error and coefficient of correlation). For ANN modeling, 156

datasets are used; among these, 110 datasets (70 %) are used in training, 23 datasets (15%) are used for validation, and 23 datasets (15%) are used in testing. Finally, **Figure 7.18** and **Figure 7.19** show the predicted flow stress (dotted line) with experimental flow stress (solid line) at different temperatures and strain rates using the ANN model 1 and ANN model 2.

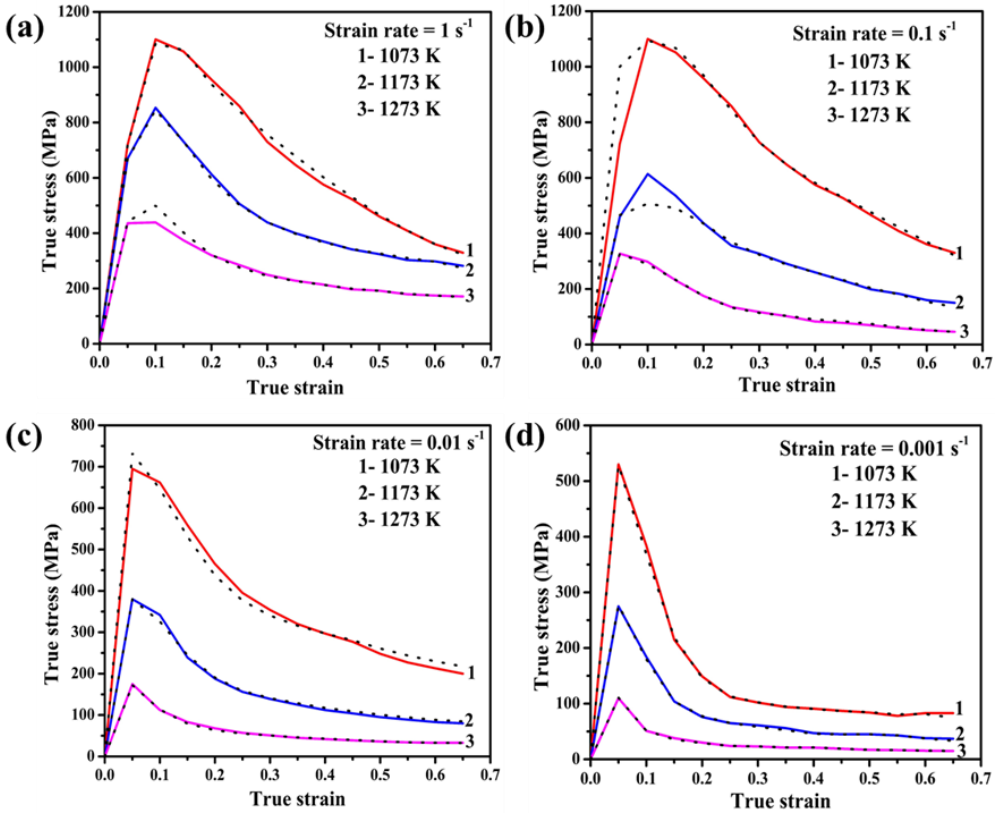

Figure 7.18 Representation of predicted flow stress (dotted line) and experimental flow stress (solid line) using the ANN model 1

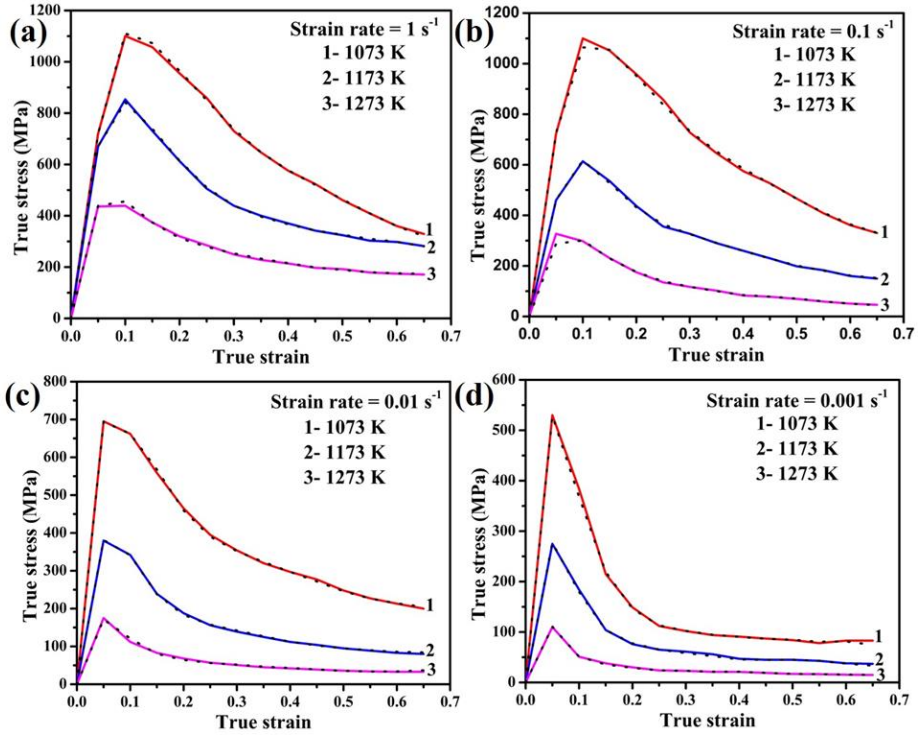

Figure 7.19 Representation of predicted flow stress (dotted line) and experimental flow stress (solid line) using the ANN model 2

Figure 7.20a and Figure 7.20b shows MSE convergence during the training of the model for ANN model 1 and model 2, respectively**.** Convergence to mean square error is 0.0027 saturated at epoch 29 for model 1, and 1.6062 x 10^{-4} is saturated at epoch 113 for model 2.

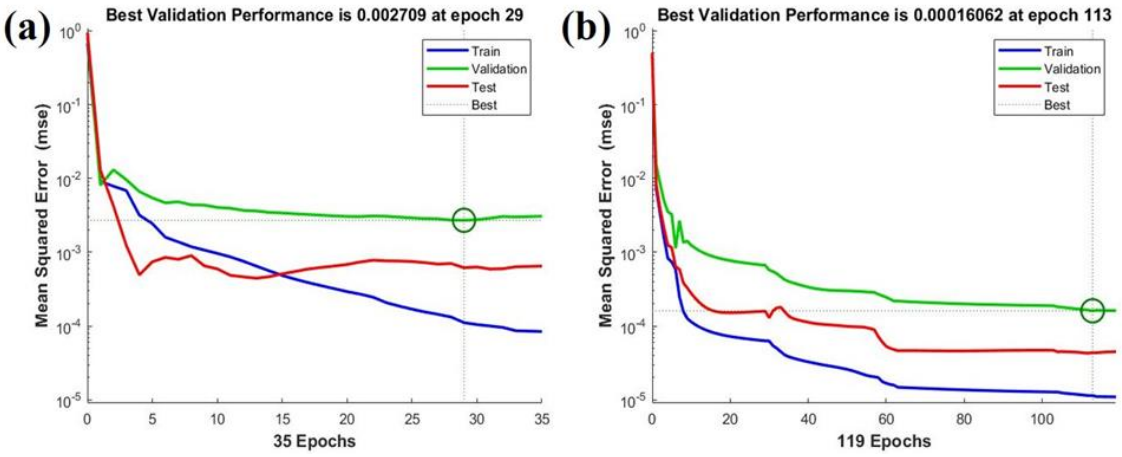

Figure 7.20 Mean square error during the training of the model (a) ANN model 1, and (b) ANN model 2.

Performance of the models:

The predictability of models is assessed by R and AARE (formula given in chapter 4, section 4.4.4.5). In the present study, performance (R and AARE) obtained from different models are represented in **Figure 7.21. Figures 7.21a**, **7.21b)**, and **7.21c** represent the variation between the targeted (experimental) and predicted flow stress for CoFeMnNiTi EHEA developed by the Arrhenius type model, ANN model 1, and ANN model 2, respectively.

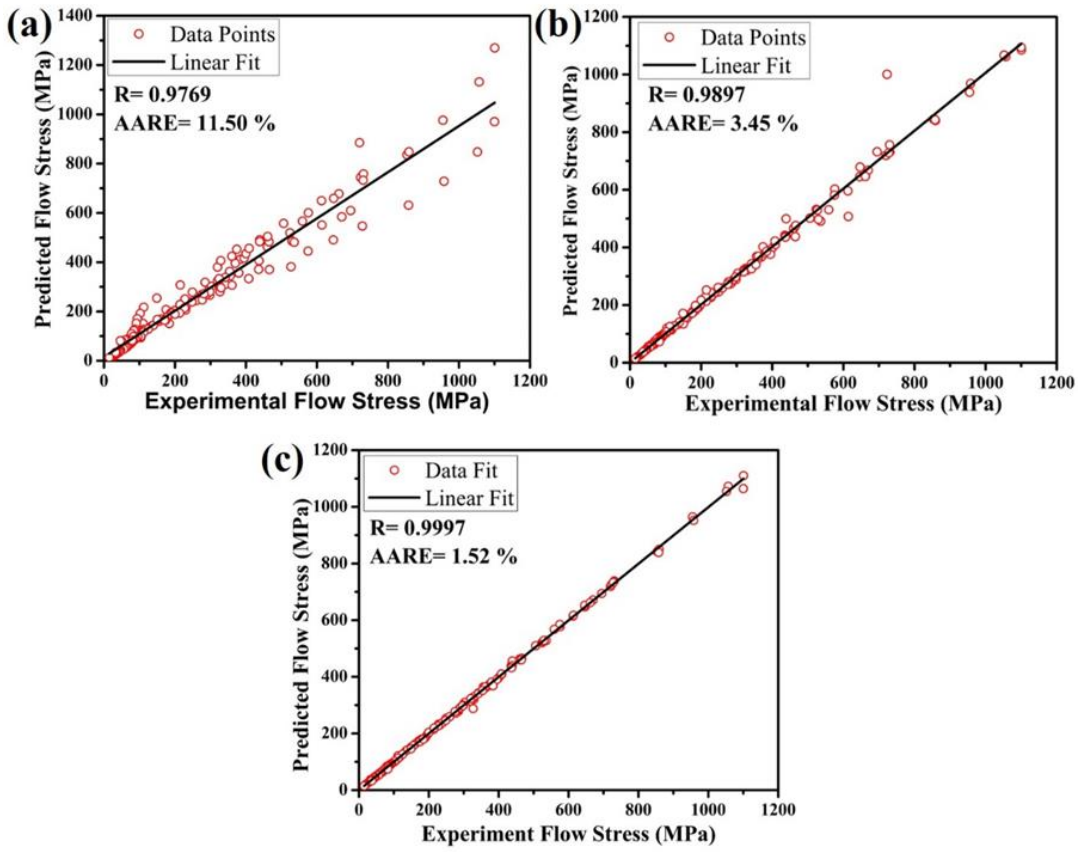

Figure 7.21 Performance of models, (a) sine hyperbolic Arrhenius model (b) ANN model 1, and (c) ANN model 2.

8.1 Summary

The hot deformation behaviour of the studied $Co_{25}Fe_{25}Mn_5Ni_{25}Ti_{20}$ HEA was examined by conducting the compressive test in Gleeble thermo-mechanical simulator in the temperature

between 1073 K to 1273 K and strain rate between 10^{-3} s^{-1} to 1 s^{-1}. Based on the above results and discussions, the following outcomes can be summarized for studied HEA.

- The studied $Co_{25}Fe_{25}Mn_5Ni_{25}Ti_{20}$ HEA shows the peritectic reaction between bcc (β) and liquid phase (L) to form fcc (α) (i.e., bcc (β) + L⟶ fcc (α) as well as eutectic reaction between fcc (α) and Ti_2(Ni, Co) (i.e. (i.e., L⟶fcc (α)+Ti_2(Ni, Co)). The present study explores the understanding of new pseudo-quasiperitectic four-phases reaction, i.e., L + bcc (β) ⟶ fcc(α) + Ti_2(Ni, Co) in the novel $Co_{25}Fe_{25}Mn_5Ni_{25}Ti_{20}$ quasi-peritectic HEA (QHEA).
- The average activation energy (Q) for hot deformation of studied EHEA is 311 kJ/mol, and stress exponent (n) is 3.5. The constitutive relation for the investigated EHEA is described by the equation as $\dot{\varepsilon} \sim \sigma^{3.5} \exp(\frac{311000}{RT})$
- The optimal hot workability regimes are identified by generating contour plots using dynamic materials modelling, and the thermomechanical processing parameters lie in temperature range 1073-1273 K and strain rate range 10^{-3} - $10^{-1.6}$ s^{-1} as well as 1130-1225 K and strain rate $10^{-0.5}$-1 s^{-1}.
- FEM simulation is used to understand the effective plastic strain distribution during deformation of studied EHEA at different temperature and strain rate 1 s^{-1}.
- It is observed that the ANN model with proper normalization of datasets can be utilized to predict the flow behavior accurately at a broader range of temperatures and strain rates during hot deformation as compared to the Arrhenius type model. Finally, the current study provides future opportunities to design new HEA materials using ANN approach for high-temperature applications.

Chapter 8

Design and development of CoCrFeNiZr QHEA

8.2 Introduction

This chapter present the development of ultrahigh strength novel Co-Cr-Fe-Ni-Zr quasi-peritectic high entropy alloy by an integrated approach using experiment and simulation approach. For the first time, we report here that $(CoCrFeNi)_{90}Zr_{10}$ *bimodal eutectics HEA consisting of both globular eutectics (i.e.,* $L \longrightarrow FCC\ (\alpha) + Ni_2Zr$*-type Laves phases) and lamellar eutectics (i.e.,* $L \longrightarrow FCC\ (\alpha) + Ni_7Zr_2$*) is designed and developed by an integrated approach of using thermodynamic simulation and experimental techniques. The present study explores the understanding of new pseudo-quasiperitectic four-phases equilibrium reaction, i.e.,* $L + Ni_2Zr \longrightarrow FCC\ (\alpha) + Ni_7Zr_2$ *in the novel* $(CoCrFeNi)_{90}Zr_{10}$ *quasi-peritectic HEA (QHEA). The hot deformation behavior of QHEA has been investigated in the temperature range 1073-1323 K and different strain rates (*10^{-3}*,*10^{-1}*,1and 10* s^{-1}*). Arrhenius-type constitutive equation and artificial neural network (ANN) model have been used to predict the flow stress of QHEA during thermomechanical processing. Also, the constitutive relation of novel QHEA is described as* $\dot{\varepsilon} = 4.8 \times 10^{12} \times [sinh(0.0065.\sigma_{0.65})]^{3.4} \times exp\left(\frac{329000}{RT}\right)$ *at strain 0.65, signifying plastic deformability of material during the hot working process and the predicted flow curve of QHEA using ANN modeling is in good agreement with the experimental data over a broad range of temperatures and strain rates. The hot workability regimes of QHEA has been identified using multiple model parameters, indicating stable regimes in temperature range 1073-1323 K and strain rate range* 10^{-3}-$10^{-1.3}s^{-1}$ *as well as temperature range 1073-1125 K and strain rate range*10^{-3}-$10^{-0.75}$ s^{-1}*. Furthermore, FEM simulation is used to predict the effective plastic strain distribution during thermomechanical processing of studied QHEA at different temperatures and a particular strain rate of 10* s^{-1} *as well as to understand material flow behavior at T = 1073 K and* $\dot{\varepsilon}$ *= 10* s^{-1}*. The detailed sequence of phase evolution of investigating multicomponent HEAs is monitored, revealing a transition from single FCC HEA (x = 0 at. %) to eutectic HEA (x=2.5, 5, 7.5 at. %) and finally, to bimodal eutectic HEA (x=10 at. %). A schematic representation of the detailed study on QHEA is given in* ***Figure 8.1****.*

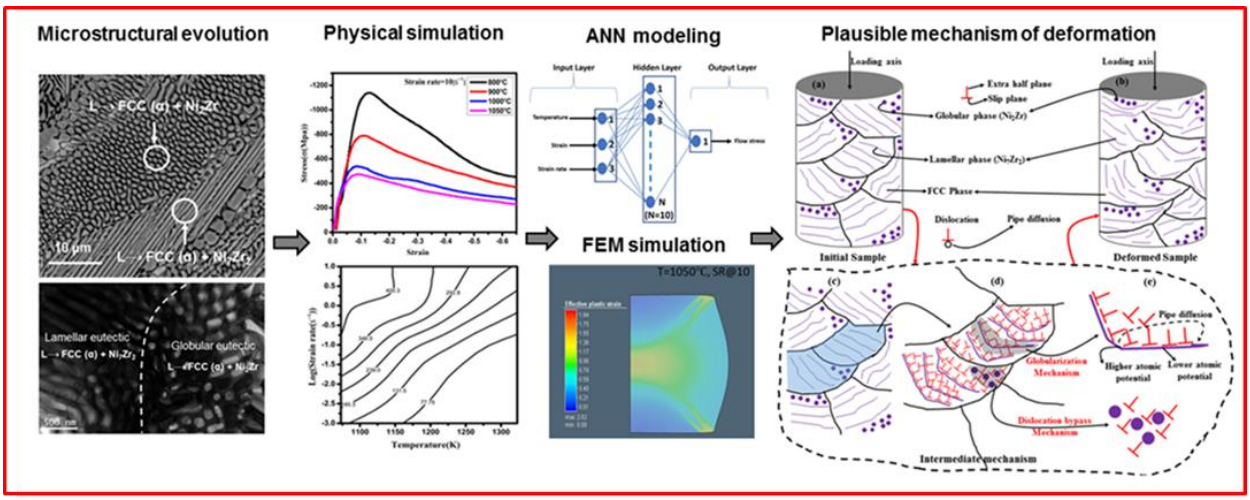

Figure 8.1 A schematic representation of the work.

8.3 Objective

The primary objectives of the present investigation are listed as follows:

(i) To develop a novel of $(CoCrFeNi)_{90}Zr_{10}$ QHEA consisting of two different eutectics by an integrated approach of combining thermodynamic simulation and experimental solidification techniques and establishing new quasi-peritectic four-phase equilibria during solidification based upon the presence of bimodal eutectics in the present studied HEA.

(ii) To generate the contour plots using multiple models to identify hot workability regimes and understand the plausible deformation mechanism of novel QHEA.

(iii) To predict the flow curve at different temperatures and strain rates of QHEA using hyperbolic sinusoidal Arrhenius-type constitutive equation and ANN approach as well as to study the material flow behaviour and strain distribution using finite element method (FEM) simulation during thermomechanical processing of QHEA.

8.4 Experimental and simulation details

High purity commercial Fe, Co, Ni, Cr, and Zr (≥ 99.9 %) were used as the starting materials to prepare by arc melting technique under ultra-high purity argon gas to obtain arc melted alloy button. The structural characterization of studied $(CoCrFeNi)_{100-x}Zr_x$ HEA was carried out by X-ray diffraction (XRD) (Panalytical X-pert pro instrument) with Cu-K_α (λ = 0.154056 nm) radiation, operating at 45 kV and 30 mA, with step size of 2θ = 0.017 deg. The peaks in the XRD pattern were identified using the International Committee for Diffraction Data (ICDD) database

in PCPDFWIN software. The microstructural characterization of the samples was examined using the scanning electron microscopy (SEM, model: Inspect F) equipped with an energy-dispersive spectroscopy (EDS). Isothermal hot compression tests of the cylindrical samples (ϕ = 6 mm and aspect ratio of 1.5:1) were carried out using Gleeble 3800® thermomechanical simulator at different deformation temperatures of 800^{o}C (1073 K), 900^{o}C (1173 K), 1000^{o}C (1273 K) and 1050^{o}C (1323 K) with the different strain rates 0.001, 0.1, 1 and 10 s^{-1}. The cylindrical specimen was deformed to approximately 50 % reduction in the height and was quenched with distilled water to freeze the microstructure at the testing temperature. The microstructural analysis of the deformed specimen was done along the compression axis using SEM.

8.5 Results and Discussion

8.5.1 Thermodynamic simulation for the design of high entropy alloys

It is worthy of mentioning that the HEA with unique phase equilibria is designed by a thermodynamic simulation approach using Thermo-Calc® software with the help of the TCHEA2® database. **Figure 8.2** shows the property diagram and Scheil's solidification plots, which indicates the detailed phase formation prediction in the multi-component $(CoCrFeNi)_{100-x}Zr_x$ HEAs. **Figure 8.2a** shows the amount of phases with temperature plot for equiatomic FeCoNiCr HEA, which indicates that the composition range of FCC solid solution single-phase very wide and also is stable at high temperature. **Figure 8.2b** shows the Scheil's solidification plot of FeCoNiCr HEA, indicating the formation of only the FCC solid solution phase from the liquid. While **Figure 8.2c** shows the amount of phases *Vs.* Temperature plot of $(CoCrFeNi)_{90}Zr_{10}$ HEA, indicating the possibility of formation of two phases mixture and three phases mixture. The Scheil's solidification plot (**Figure 8.2d**) of $(CoCrFeNi)_{90}Zr_{10}$ HEA predicts that firstly, FCC solid solution single phase is formed from the liquid, followed by the evolution of two-phase mixture (FCC + C15_Laves phase), then the evolution of three-phase mixture (FCC + C15_Laves phase + Ni_7Zr_2 intermetallics). Finally, a minute fraction of four-phase mixtures (FCC + C15_Laves phase + HF8NI21 Sigma phase + Ni_7Zr_2 intermetallics and FCC + C15_Laves phase + HF8NI21 Sigma phase + $Ni_{10}Zr_7$ intermetallics) are developed from the remaining liquid during solidification.

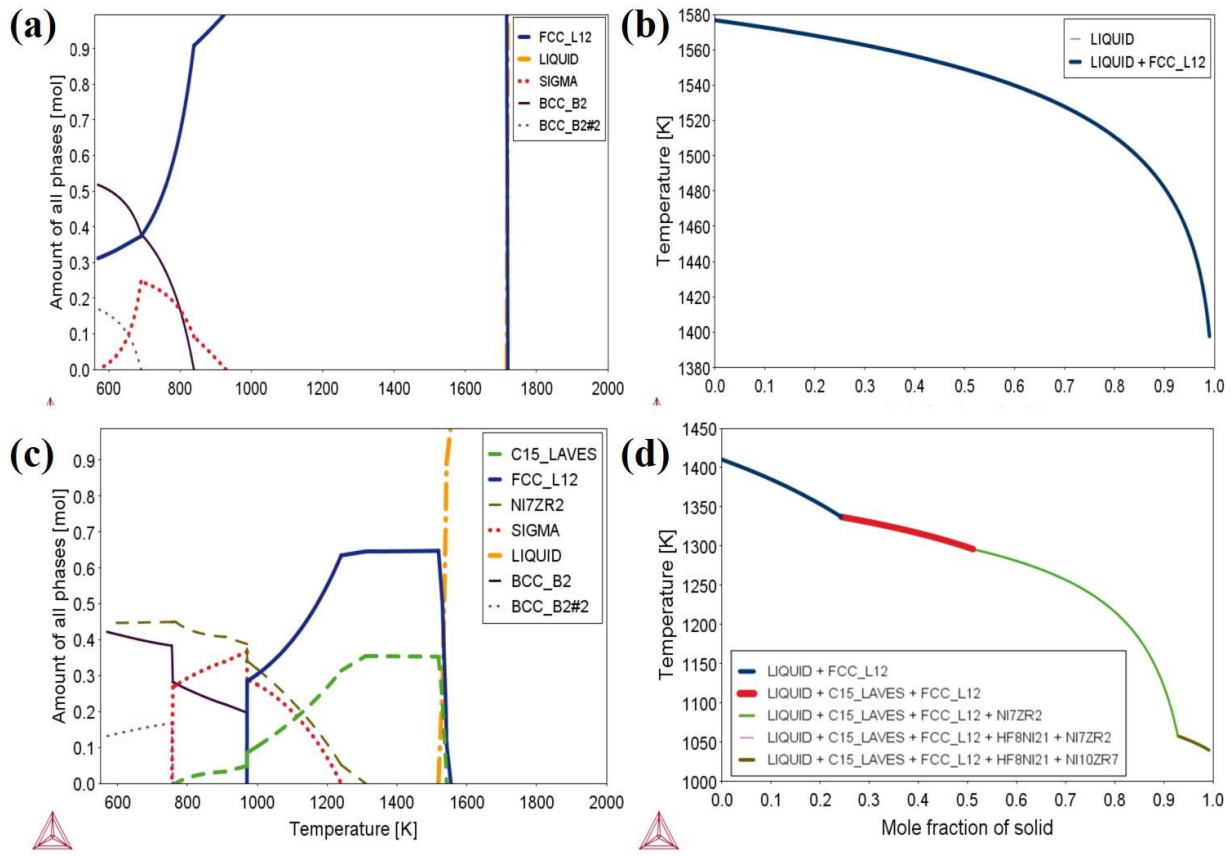

Figure 8.2 Phase fraction *Vs.* T and Scheil solidification plot of multicomponent $(CoCrFeNi)_{100-x}Zr_x$ HEAs; x = 0 at. % (a and b) and x = 10 at. % (c and d) respectively.

8.5.2 Structural and Microstructural characterization

8.5.2.1 XRD analysis

The XRD pattern of multicomponent $(CoCrFeNi)_{100-x}Zr_x$ (x=0, 2.5, 5, 7.5, 10 at. %) HEAs is shown in **Fig. 8.3(a)**. The XRD pattern shows the intense diffraction peaks corresponding to the FCC solid solution phase (α) and two types of intermetallics, i.e., Ni_2Zr-type Laves phases and σ-phase (Ni_7Zr_2-type).

8.5.2.2 Scanning electron microscopy (SEM) results

The detailed microstructural characterization of multi-component $(CoCrFeNi)_{100-x}Zr_x$ (x=0, 2.5, 5, 7.5, 10 at. %) HEA was carried out using backscattered electron (BSE) imaging mode in SEM. However, the representative SEM micrograph of the studied HEA is given in **Figure 8.3(b-e)** to decipher the different phases in the microstructure. The different phases in the microstructure of the studied HEA are marked based on the compositional analysis using EDS coupled with SEM. The microstructure of FeCoNiCr alloy reveals the presence of single-phase with the nearly

equiatomic ratio is showing in **Figure 8.3a**. In contrast, $(CoCrFeNi)_{100-x}Zr_x$ (x=0, 2.5, 5, 7.5 at. %) shows the presence of primary dendritic phase and eutectic region in microstructure after the addition zirconium. The eutectic region consists of the FeCoNiCr-rich phase and Ni_2Zr type Laves phase. It is important to note that $(CoCrFeNi)_{90}Zr_{10}$ shows the presence of primary dendritic phase and bimodal eutectics demonstrated in **Figure 8.3e**. The microstructure of bimodal eutecticHEA reveals the presence of primary FeCoNiCr-rich solid solution phase (α) with dark grey contrast, globular eutectic between FeCoNiCr-rich solid solution phase (α) and Ni_2Zr phases (i.e., $L \rightarrow \alpha + Ni_2Zr$) and lamellar eutectic between FeCoNiCr-rich solid solution phase (α) andNi_7Zr_2 phases (i.e., $L \rightarrow \alpha + Ni_7Zr_2$).

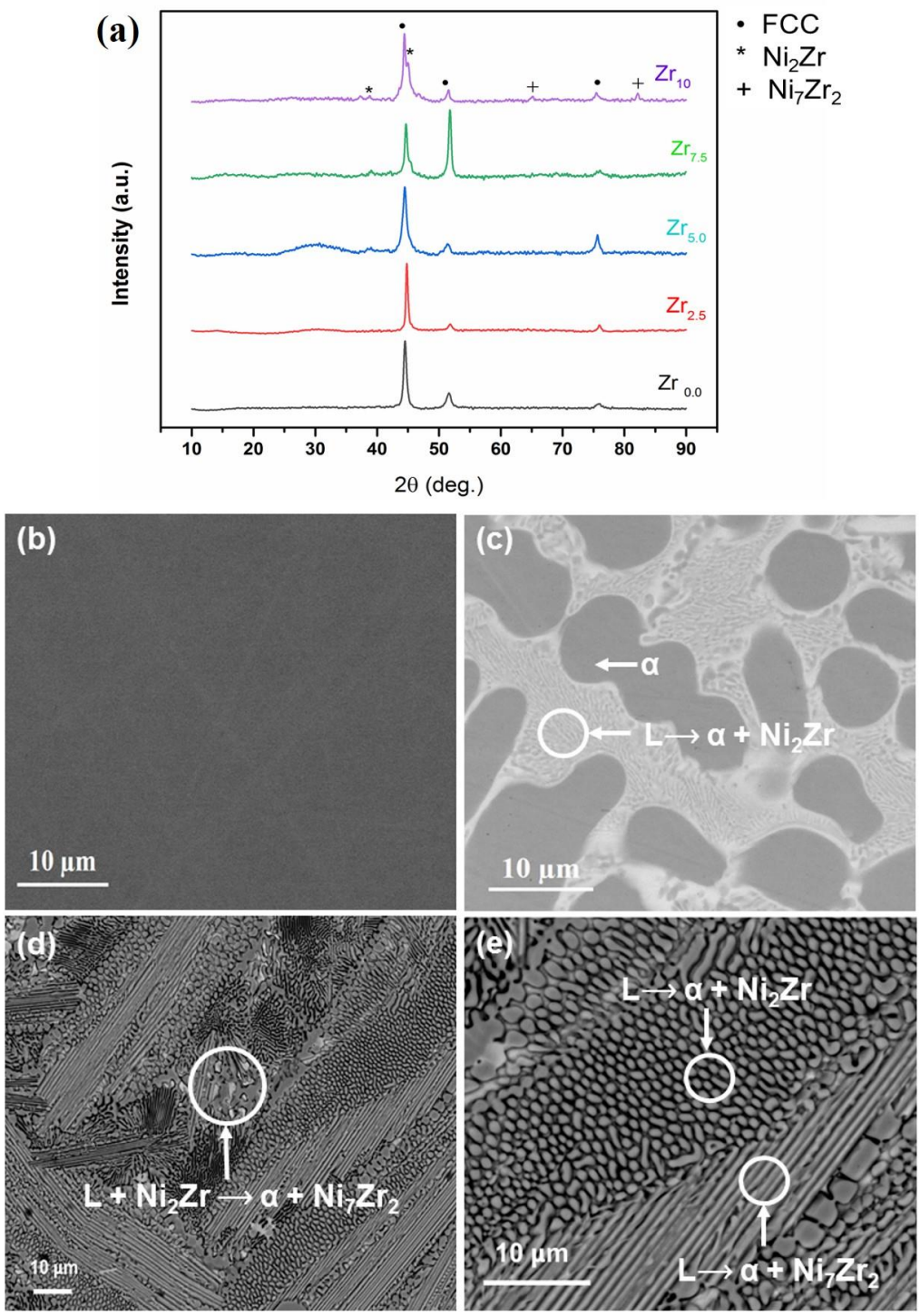

Figure 8. 3 (a) XRD pattern of as-cast multicomponent $(CoCrFeNi)_{100-x}Zr_x$ (x=0, 2.5, 5, 7.5, 10 at. %) HEAs and BSE-SEM micrograph of multicomponent $(CoCrFeNi)_{100-x}Zr_x$ HEAs; (b) x = 0, (c) x = 7.5 and (d), (e) x =10 at. %.

8.5.2.3 Transmission electron microscopy (TEM) results

The fine-scale microstructural feature of studied $(CoCrFeNi)_{90}Zr_{10}$ HEA is carried out using TEM, and the constituent phases in the microstructure are identified using obtained selected area electron diffraction (SAED) patterns and EDS measurements. The phases in the microstructure are also quantitatively analyzed using EDS analysis. **Figure 8.4** shows the representative TEM micrograph, indicating the presence of both lamellar and globular eutectics. It is to be noted that the microstructure shows globular eutectic between FCC (α) and Ni_2Zr phases (i.e., L→FCC (α) + Ni_2Zr) and lamellar eutectic between FCC (α) and Ni_7Zr_2 phases (i.e., L→FCC (α) + Ni_7Zr_2).

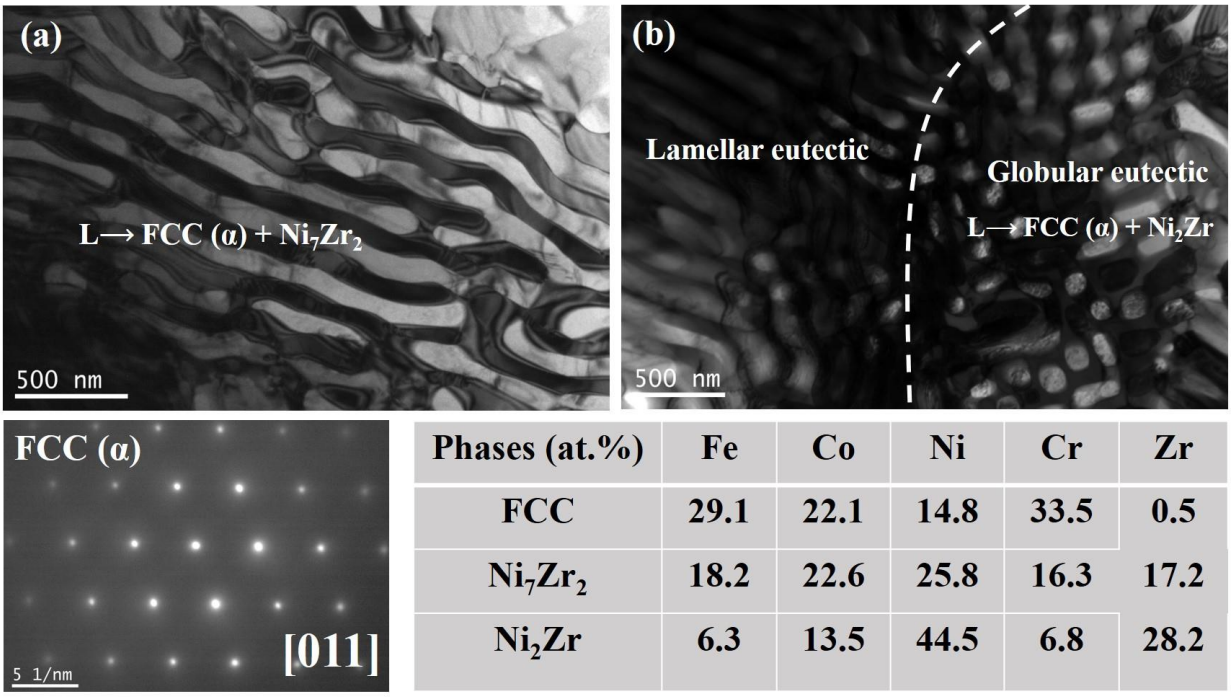

Phases (at.%)	Fe	Co	Ni	Cr	Zr
FCC	29.1	22.1	14.8	33.5	0.5
Ni_7Zr_2	18.2	22.6	25.8	16.3	17.2
Ni_2Zr	6.3	13.5	44.5	6.8	28.2

Figure 8.4 TEM micrograph and EDS analysis from constituent phases of the multicomponent $(CoCrFeNi)_{90}Zr_{10}$ QHEA.

8.5.3 Phase equilibria of multi-component Co-Cr-Fe-Ni-Zr HEA:

It is important to note that the microstructure of $(CoCrFeNi)_{90}Zr_{10}$ shows the presence of two types of eutectics and four-phases reaction (as shown in **Figure 8.3d** and **8.3e**). Therefore, the solidification pathways for the investigated multi-component $(CoCrFeNi)_{90}Zr_{10}$ HEA has been described using XRD and electron microscopy results in the following;

(i) At first, the FCC (α) solid solution phase is evolved from the liquid during solidification, followed by

(ii) The eutectic reaction to form between FCC (α) solid solution phase and Ni_2Zr-type Laves phase, i.e., globular eutectic: $L \rightarrow FCC(\alpha) + Ni_2Zr$ and then

(iii) Precipitation of Ni_7Zr_2 intermetallic phase from remaining liquid and equilibrium with a globular eutectic.

(iv) The remaining liquid undergoes eutectic reaction to form FCC (α) solid solution phase and Ni_7Zr_2 intermetallic phase, i.e., lamellar eutectic: $L \rightarrow FCC(\alpha) + Ni_7Zr_2$.

Based upon the microstructural features observed in the studied multi-component $(CoCrFeNi)_{90}Zr_{10}$ HEA, the four-phase reaction, i.e., $L + Ni_2Zr \rightarrow FCC\ (\alpha) + Ni_7Zr_2$, has been proposed for this alloy. It is evident that this four-phase reaction is known as a quasi-peritectic reaction, which is cooperated by two eutectic reactions, i.e., $L \rightarrow FCC + Ni_2Zr$ and $L \rightarrow FCC + Ni_7Zr_2$ above and below the quasi-peritectic reaction, respectively. Furthermore, the observation of four-phases reactions in experimental results corroborate well with the thermodynamic simulation result (as shown in **Figure 8.2d**). This unique microstructural feature consisting of two different kinds of eutectics and solid solution phases in multi-component QHEA can be considered a potential candidate for high-temperature structural applications.

8.5.4 Flow stress behaviour of QHEA during hot deformation

The true uniaxial stress (σ) and strain (ε) curves of multi-component QHEA is obtained at different temperatures (T) 800℃ (1073 K), 900℃ (1173 K), 1000℃ (1273 K), and 1050℃ (1323 K) and different strain rates (0.001, 0.1, 1 and 10 s^{-1} by isothermal compression testing using cylindrical specimen (aspect ratio = 1.5:1 and diameter (∅) = 6 mm) to understand the flow behaviour during thermomechanical processing.

8.5.5 Compressive mechanical behaviour of QHEA

The obtained flow stress curves of studied QHEA at different deformation temperature (T) and strain rates ($\dot{\varepsilon}$) are shown in **Figure 8.5**. It is observed that the flow stress (σ) of the material decreases continuously at a given fixed strain rate on increasing the temperature. In contrast, for a given temperature (T), flow stress (σ) of the material increases with an increase in the strain rate. It is clear from **Figure 8.5** that the flow stress of the material increases with strain and reaches a maximum value, and then the stress value decreases with further increase in strain. At

strain 0.65, the variation of flow stress concerning strain rates and temperatures is shown in **Figure 8.5e**. It is also observed from the flow curve that after reaching the peak stress, the studied bimodal eutectic HEA deforms plastically up to 70 % of true strain value with no fracture of the specimen. The true stress vs. strain curve in **Figure 8.5** shows a peak value in strength, followed by a continuous decrease in stress values. The decrease in stress values after the peak stress is attributed to either dynamic recrystallization (DRX) or globularization of the second phase. It is reported in the literature that dynamic recrystallization leads to the saturation of stress values at large strain values. However, the present mechanical testing data shows a continuous decrease in stress values with an increase in strain values suggesting that the globularization of the second phase during high-temperature deformation. It is well known that the strength of the material comes either by the interaction of dislocations with other dislocations or solute atoms/second phase particles.

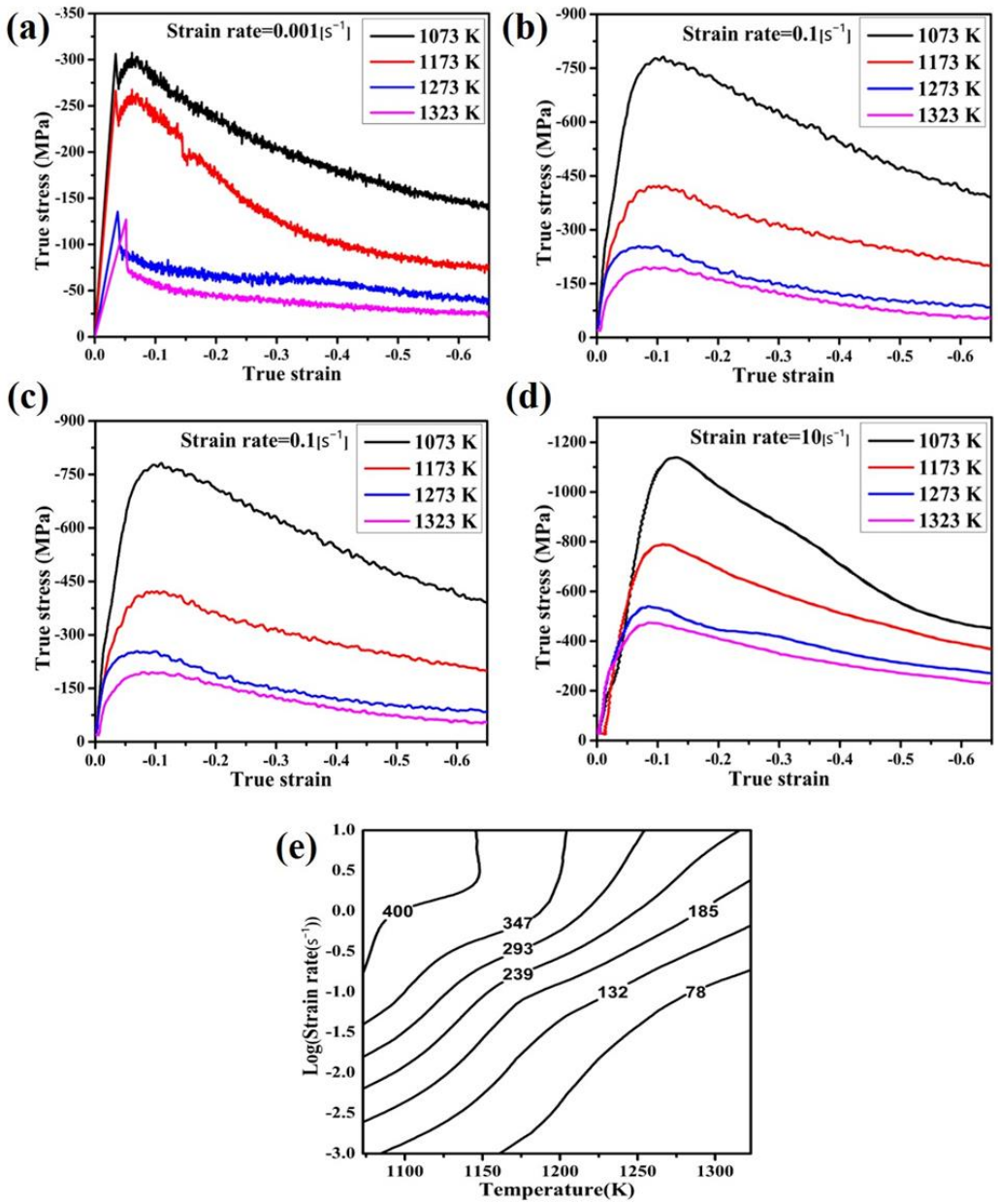

Figure 8.5 True stress Vs. true strain plot of as-cast multicomponent $(CoCrFeNi)_{90}Zr_{10}$ QHEA.; at (a) $\dot{\varepsilon} = 0.001\ s^{-1}$, (b) $\dot{\varepsilon} = 0.1\ s^{-1}$ (c) $\dot{\varepsilon} = 1\ s^{-1}$ and (d) $\dot{\varepsilon} = 10\ s^{-1}$, and (e) effect of temperatures and strain rates on flow stress

In the present QHEA, all the samples during deformation show softening after the peak stress values. However, the rate of softening is different for the samples deformed at different temperatures and strain rates. The softening rate of all the samples is captured by plotting the rate of softening with stress values. It is well known that the rate of softening is effected both by temperature and strain rate of deformation. Hence, to remove the effect of temperature on the microstructure evolution, the peak stress value is subtracted and plotted in **Figure 8.6**. Values of

the rate of softening at different temperatures and strain rates for multi-component $(CoCrFeNi)_{90}Zr_{10}$ QHEA mentioned in **Table 1**.

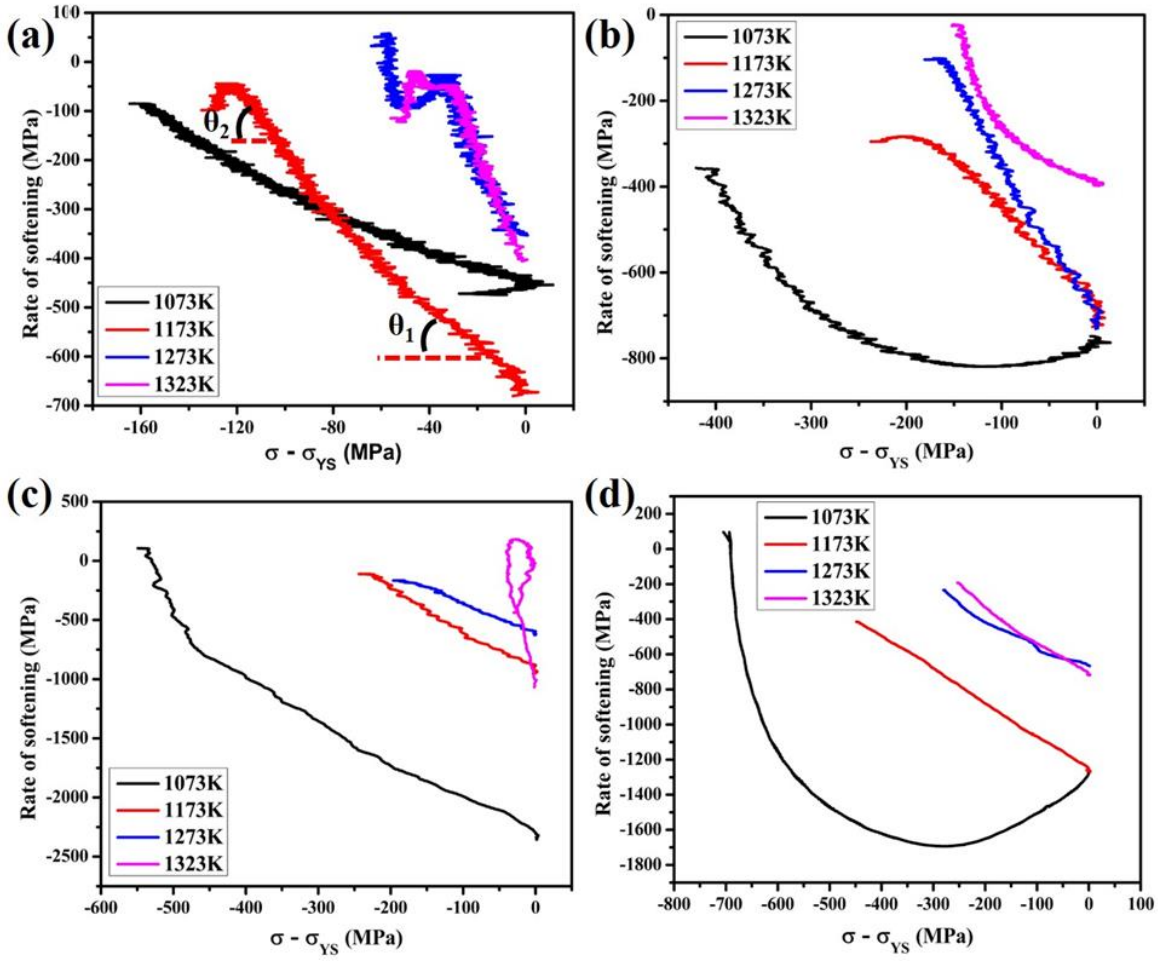

Figure 8.6 Rate of softening *Vs.* stress plot of multicomponent $(CoCrFeNi)_{90}Zr_{10}$ QHEA.

Table 8.1 Values of the rate of softening at different temperatures and strain rates for multicomponent $(CoCrFeNi)_{90}Zr_{10}$ QHEA

Temperature (K)	Θ_1	Θ_2	Θ_3	Θ_4
$\dot{\varepsilon}$ = 0.001 s^{-1}				
1073	-1.348	-2.43		
1173	-3.46	-6.01		
1273	-3.16	-4.8	-1.32	-4.73
1323	-11.18	0	7.87	
$\dot{\varepsilon}$ = 0.1 s^{-1}				
1073	-0.89	-3.49		
1173	-2.31	0.49		
1273	-2.98	-3.93		
1323	-0.88	-4.81		
$\dot{\varepsilon}$ = 1 s^{-1}				
1073	-3.57	-12.31		
1173	-2.70	-3.91		
1273	-2.61	-1.72		
1323	-22.50	-8.04	14.46	
$\dot{\varepsilon}$ = 10 s^{-1}				
1073	1.69	-1.13	-3.64	-27.79
1173	-2.0			
1273	-0.779	-2.3178	-1.063	-2.796
1323	-1.64	-2.59		

It is observed that the initial rate of softening is low, and later on, it increases for the sample deformed at a strain rate of $0.001s^{-1}$ till 1173K. However, at high temperatures (1273K and 1323K), more than two different slopes are observed at $0.001s^{-1}$, suggesting microstructure evolution is abrupt at high temperatures. The sample deformed at 1323K shows a maximum softening rate at $0.001s^{-1}$, followed by hardening. Similarly, two stages of softening rate are observed for the sample deformed at 0.1 s^{-1} in the temperature range of 1073K-1323K. Except

for the sample deformed at 1173K, where hardening is observed after the initial stage of softening, all the samples show an increase in the softening rate with the increase in the amount of deformation.

Similarly, the sample deformed at a strain rate of 1 s^{-1} shows two different stages of softening rate from 1073K-1273K except for the sample deformed at 1323K, suggesting abrupt evolution of microstructure. Samples deformed at 1073K and 1173K show an increase in softening rate with an increase in the amount of deformation, whereas samples deformed at 1273K and 1323K show a decrease in softening rate with an increase in the amount of deformation. Sample deformed at a strain rate of 10 s^{-1}, all the samples show a four-stage of the rate of softening at 1073K and 1273K. Samples deformed at 1173K and 1323K shows two stages of hardening. The rate of softening values gives an idea about the dislocation content in the material at a given temperature, strain, and strain rate. Softening occurs in a material because of dislocation annihilation during deformation.

The rate of dislocation accumulation in a material during deformation is given by [Eq. 1, Eq. 2],

$$\frac{d\rho}{d\gamma} = \frac{dL}{bda} = \frac{1}{b\lambda} \qquad (8.1)$$

Where λ, dL, da, ρ and b represent the mean free path of the dislocation, length of the dislocation, dislocation stored per unit area, the dislocation density and burgers vector, and γ is the shear strain of the material.

The relationship between accumulated dislocations with flow stress is given by,

$$\tau = \alpha\mu b\rho^{1/2} \qquad (8.2)$$

; where τ, α and μ represent the shear stress, obstacle strength, and shear modulus, respectively. The rate of dislocation accumulation in the material can be estimated through differentiating Eqn. (8.2), i.e.

$$2\tau\frac{d\tau}{d\gamma} = (\alpha\mu b)^2\frac{d\rho}{d\gamma} \qquad (8.3)$$

Using Eq. (8.1) and value of $\theta = \frac{d\tau}{d\gamma}$ in Eq. (8.3) gives.

$$\tau\theta = \frac{(\alpha\mu)^2}{2} \cdot \frac{b}{\lambda} \qquad (8.4)$$

Using Eq. (8.3) in Eq. (8.44) give

$$s\frac{\theta}{\mu} = \frac{\alpha}{2} \cdot \frac{l}{\lambda} \quad \text{where } l = \rho^{-1/2} \qquad (8.5)$$

Firstly, if it is assumed that the mean free path of dislocations is constant, then there is no dislocation accumulation inside the grain, which makes the value of τθ is constant (see Eq. 4), and the value of λ depends on the grain size of the material. Secondly, if the principle of similitude (mean free path of dislocation is proportional to dislocation spacing), then the value of θ is constant, according to Eq. (5), which means the value of τθ is proportional to τ. In real materials, dislocation accumulation effects both mean free path of dislocation and dislocation spacing. Hence, the mean free path of dislocation is plotted against the plastic flow stress and is shown in **Figure 8.7**.

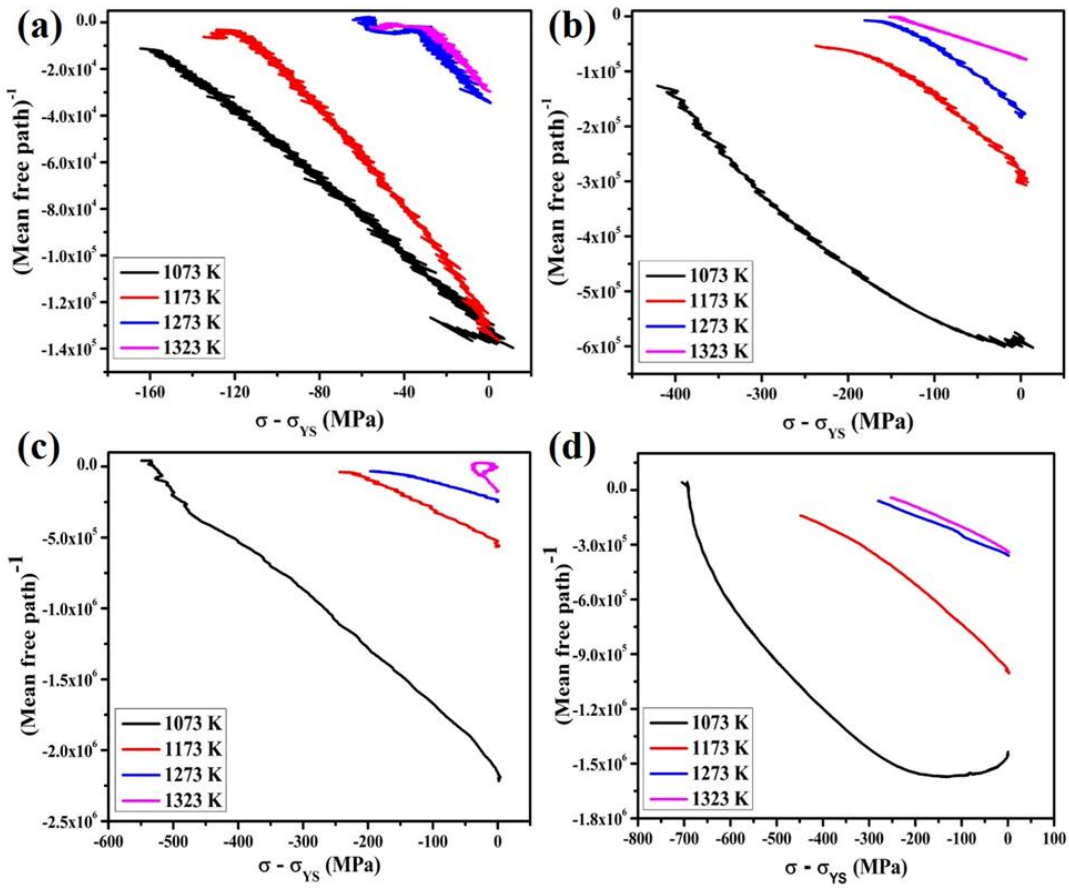

Figure 8.7 Mean free path *Vs.* Stress plot of multicomponent $(CoCrFeNi)_{90}Zr_{10}$ QHEA.

It has been noted that the plastic flow stress means the value of yield stress is subtracted from the total value of the flow stress. A continuous increase in the mean free path of dislocations is observed for the samples with an increase in stress values suggesting that globularization of the second phase occurs continuously with an increase in the amount of deformation. However, for the samples deformed at a low strain rate of 0.001 s^{-1} and 1273 K, 1323K shows a constant mean

free path of dislocations, which suggests that the globularization phenomenon is completed at high true strain values of greater than 0.5 (**Table 8.1**). Hence, the processing map is generated for the samples deformed at a strain of 0.65 for all the samples. It is important to note that the high strength of the studied bimodal HEA at high temperature is attributed to the presence of two eutectics at different length scales, solid solution strengthening and intermetallic, i.e., A_2B type Laves phases. It is known that all the principal elements in the multi-component HEAs are assumed to be substitutional solute elements. It is to be noted from the stress vs. strain curve that the bimodal eutectic HEA consisting of FCC and two intermetallic shows better high strength as compared to the eutectic HEA consisting of FCC and one intermetallic. The microstructural stability during deformation at high temperatures is observed for the studied bimodal eutectic HEA.

8.5.6 Modeling of flow curves: Constitutive relation

The flow stress (σ) is a function of temperature (T), strain (ε), and strain rate ($\dot{\varepsilon}$) for the particular material through constitutive relation, which can be written in the functional form as $\sigma = f(T, \varepsilon, \dot{\varepsilon})$. The activation energy (Q) and stress exponent (n) parameters are derived by using experimental data [86][89][104].

8.5.6.1 Determination of activation energy for hot deformation

The activation energy (Q) is a strain rate and a temperature-dependent physical parameter that is typically used to understand the thermomechanical process such as rolling, extrusion, forming, and forging for any type of materials [105][106][107]. It also provides important information about dislocation movement, dynamic recovery (DRV), DRX, movement of the grain boundary, and deformation mechanism, which is associated with the microstructural evolution during the hot forming process [108][109]. Zener-Holloman parameter (Z), which is also known as temperature compensated-strain rate [20].

In this study, the hot deformation activation energy (Q) of multi-component QHEA is calculated by using the hyperbolic sinusoidal Arrhenius type constitutive equation (given in Eq. 8) after plotting curves between the σ vs. $\ln\dot{\varepsilon}$ and $\ln\sigma$ vs. $\ln\dot{\varepsilon}$ at various deformation temperature (T) as well as the plot between $\ln\dot{\varepsilon}$ vs. $\ln[\sinh(\alpha\sigma)]$ at different strain rate ($\dot{\varepsilon}$), indicating straight line Eq.in term of Y=mx+c; where m is the slope and c is the intercept, slopes of these curves give the constant β, N, n, and s as shown in **Figure 8.8**.

The average activation energy (Q) value of the studied multi-component QHEA at strain 0.65 is estimated as 329 kJ/mol using constant values (β=0.0315, N= 4.9, α=0.0065, n=3.4, and s=1.16). The high value of activation energy at the last stage of the hot deformation process signifies the retention of work-strength, which is essential for hot workability at high temperatures. Further, the intercept of the linear plot between the ln[sinh(ασ)] vs. lnZ gives the value of lnA, as shown in **Figure 8.8e**.

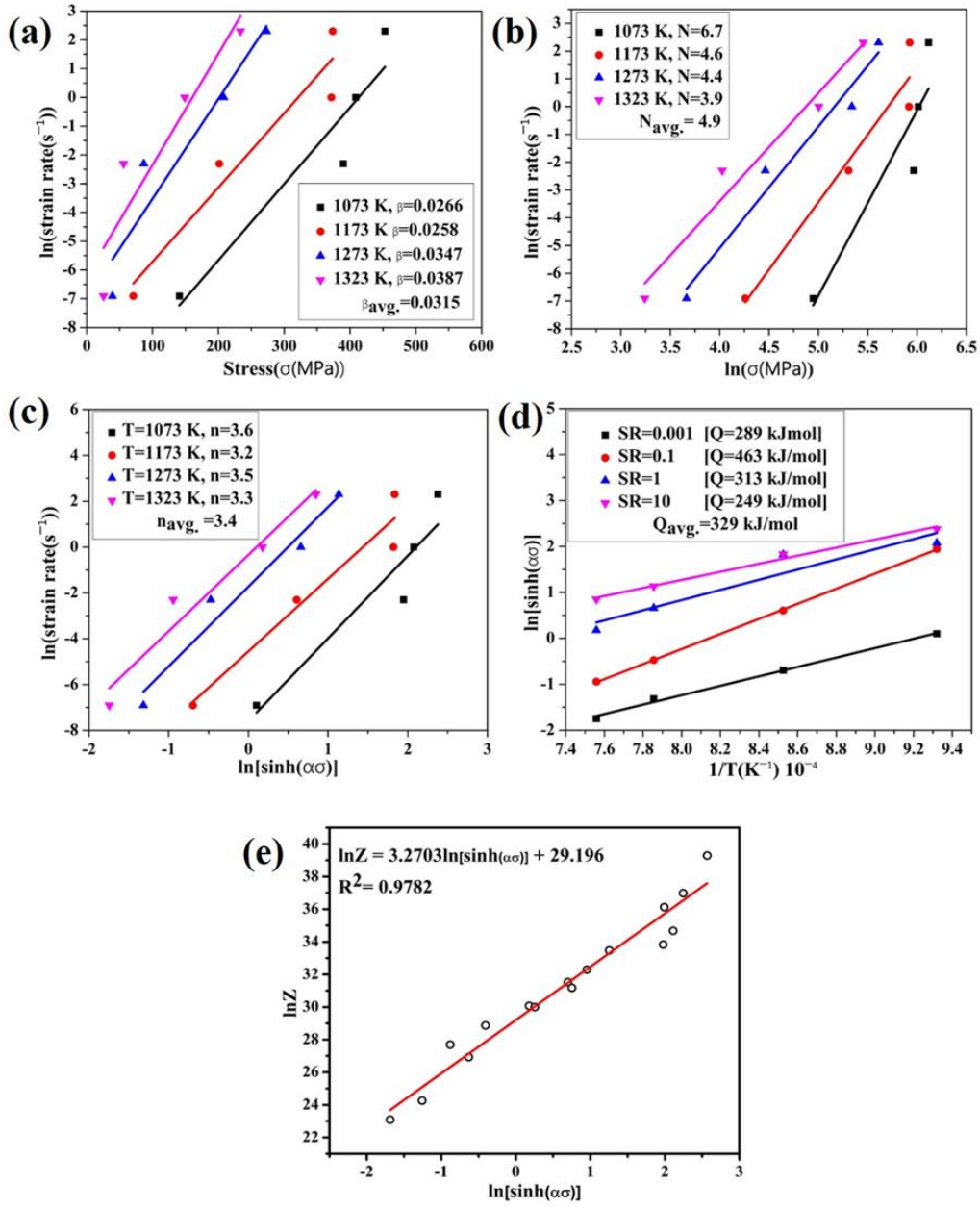

Figure 8.8 Calculation for (a) β, (b) N, (c) n, (d) s, and (e) lnA

8.5.6.2 Constitutive relation of flow stress during hot deformation

The constitutive Eq. describes the flow stress behaviour of the multi-component QHEA, The true stress and true strain curves obtained under the different temperatures and different strain rates can be employed to determine the stress exponent (n) and activation energy (Q) at last stage of hot deformation, i.e., strain 0.65 and the parameter Z, $\dot{\varepsilon}$ and σ can be expressed as the following Equation:

$$Z_{0.65} = \dot{\varepsilon}.\exp\left(\frac{329000}{RT}\right) \qquad (8.6)$$

$$\dot{\varepsilon} = 4.8 \times 10^{12} \times [\sinh(0.0065.\sigma_{0.65})]^{3.4} \times \dot{\varepsilon}.\exp\left(\frac{329000}{RT}\right) \qquad (8.7)$$

$$\sigma_{0.5} = \frac{1}{0.0065} \times \ln\left\{\left(\frac{Z_{0.65}}{4.8\times10^{12}}\right)^{\frac{1}{3.4}} + \left[\left(\frac{Z_{0.65}}{4.8\times10^{12}}\right)^{\frac{2}{3.4}} + 1\right]^{\frac{1}{2}}\right\} \qquad (8.8)$$

The constitutive relation for the studied multi-component QHEA describe the correlation between the flow stress (σ), temperature (T) and strain rate ($\dot{\varepsilon}$), especially at high-temperature range1073K-1323K. Similarly, the hot deformation activation energy (Q) is evaluated at different true strains, which vary in the range 0.1–0.65. The value of Q varies between 329 kJ/mol at strain 0.65 to 377 kJ/mol at strain 0.1. The predictions of flow stress at different temperatures and strain rates are made using the above-mentioned equation, for a given true strain in the range of 0.1 to 0.65. **Figure 8.9** shows the experimental (solid line) comparison and predicted (dotted line) flow stress at different hot working conditions using the hyperbolic sinusoidal Arrhenius type constitutive equation. The developed hyperbolic sinusoidal Arrhenius type constitutive model has been successfully applied for the prediction flow behaviour of the multi-component QHEA at elevated temperatures.

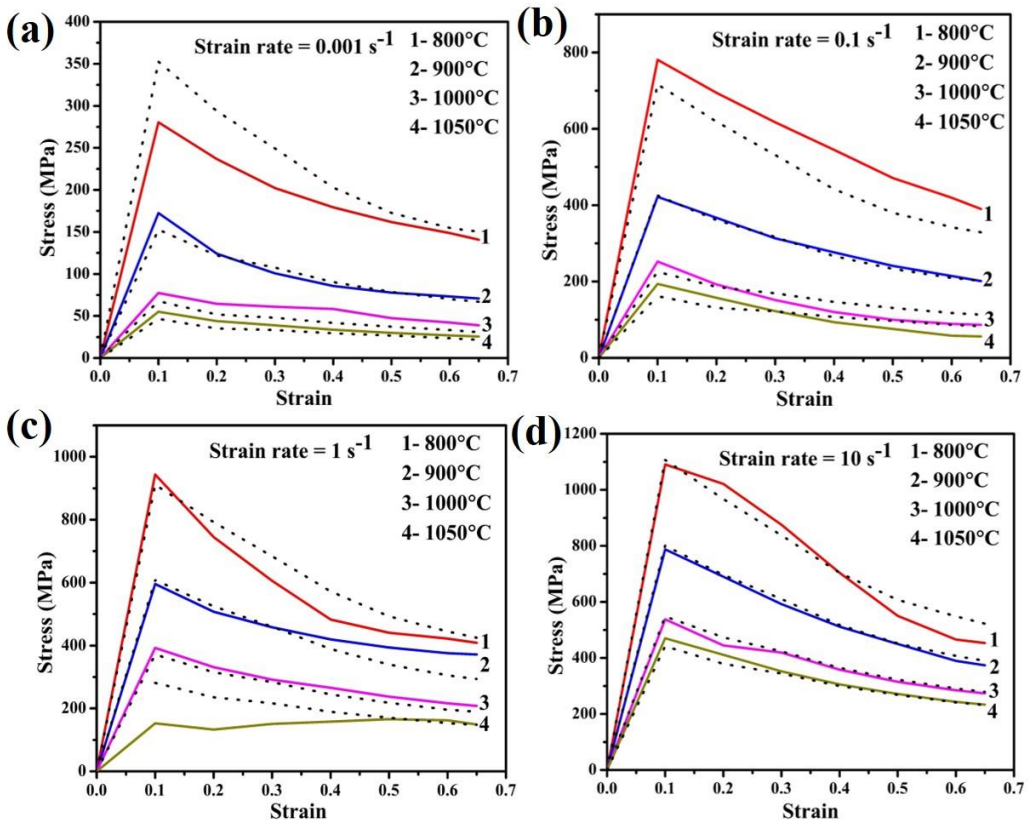

Figure 8.9 Comparisons between the experimental (solid lines) and predicted (dotted lines) flow curve using the hyperbolic sinusoidal Arrhenius type model at various temperatures for strain rates (a)10 s^{-1}, (b)1 s^{-1}, (c) 0.1 $s^{-1}$and (d) 0.001 s^{-1}, of multicomponent $(CoCrFeNi)_{90}Zr_{10}$ QHEA.

8.5.7 Modelling of flow curves: Artificial neural network

An ANN is a computational approach that collects the information by adaptive learning from the external source and is available for use to predict the properties of materials. A neural network consists of an interconnected layer, and that layers contain the small unit known as neurons with the parallel weighted connection. The network has three kinds of layers that are input layers, hidden layers, and output layers. It is reported [20] that the hot deformation behaviour of aermet 100 steel is predicted using the ANN model in the temperature from 800°C -1200°C and the strain rate from 0.01 s^{-1} to 50 s^{-1}. The ANN model is used to predict the flow behaviour at different hot deformation working conditions by training the experimental data obtained from the isothermal hot compression test to obtain the minimum mean squares error between experimental output and targeted output during network training. In the current study, the hot deformation behaviour of $(CoCrFeNi)_{90}Zr_{10}$ HEA has been carried out in the temperature range 1073K-1323K and strain rate of 0.001, 0.1, 1, 10 s^{-1}. It is to be noted that temperature, strain rate, and strain are

taken as input data, and flow stress as output data and a total of 448 experimental input-output data points are used to develop the ANN model. The data set could be reduced to the value between 0 - 1 before applying for the training, and the feature scaling could be achieved [124] (details are given in chapter 1).

The 3-10-1 (3, 10, and 1 are neurons in the input layer, hidden layer, and output layer, respectively) neuron system was found to be the optimal structure for the ANN model after several trains. The schematic representation of the ANN model for flow stress prediction at different hot-working conditions is given in **Figure 8.10a**. For ANN modeling, a total of 112 datasets are used; among these, 70 % dataset is used in training, 15% dataset is used for validation, and 15% dataset is used in testing. It is observed that a network with ten neurons in the hidden layer gives a minimum mean square error (MSE) and the correlation coefficient (R).

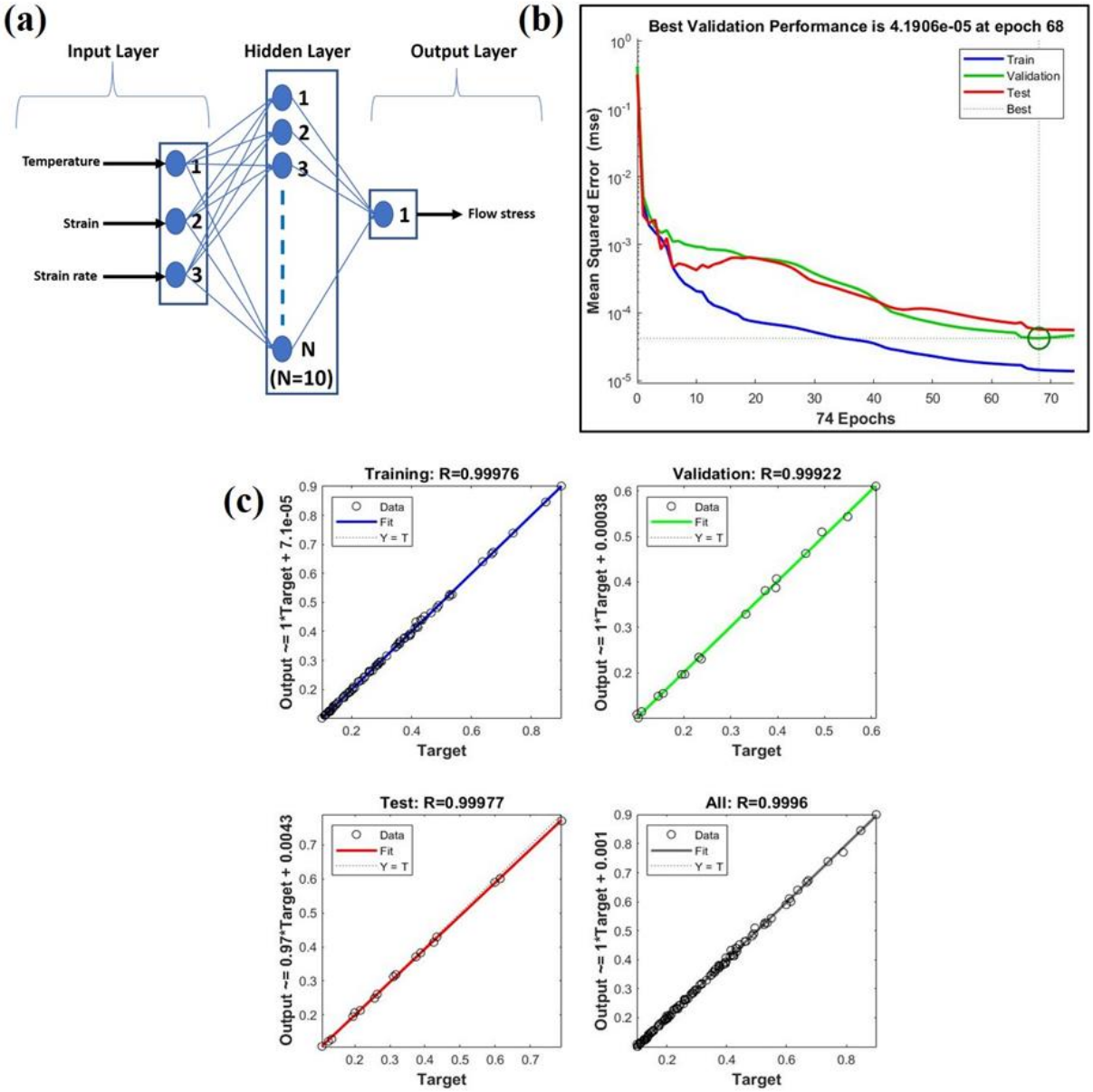

Figure 8.10 (a) Schematic representation of the ANN model for flow stress prediction, (b) MSE convergence during the training of the ANN model, (c) Correlation between the experimental and ANN predicted flow stress data of multicomponent $(CoCrFeNi)_{90}Zr_{10}$ QHEA for the training data, validation data, testing data, and overall data.

The MSE convergence during the training of the ANN model and correlation between the experimental flow stress and predicted flow stress for the training, validation, testing, and comprehensive data are shown in **Figure 8.10b and 8.10c**, respectively. The observed MSE value of the model is 1.4906×10^{-5} at epoch 68. The variation of the experimental and predicted value of flow stress of multi-component studied QHEA for different temperatures (1073K -

1323K), and strain rate (0.001,0.1,1 and 10 s^{-1}) is shown in **Figure 8.11**. It is worth mentioning that the predicted flow curve of studied HEA using the ANN model can track the experimental data over a wider range of temperatures and strain rates.

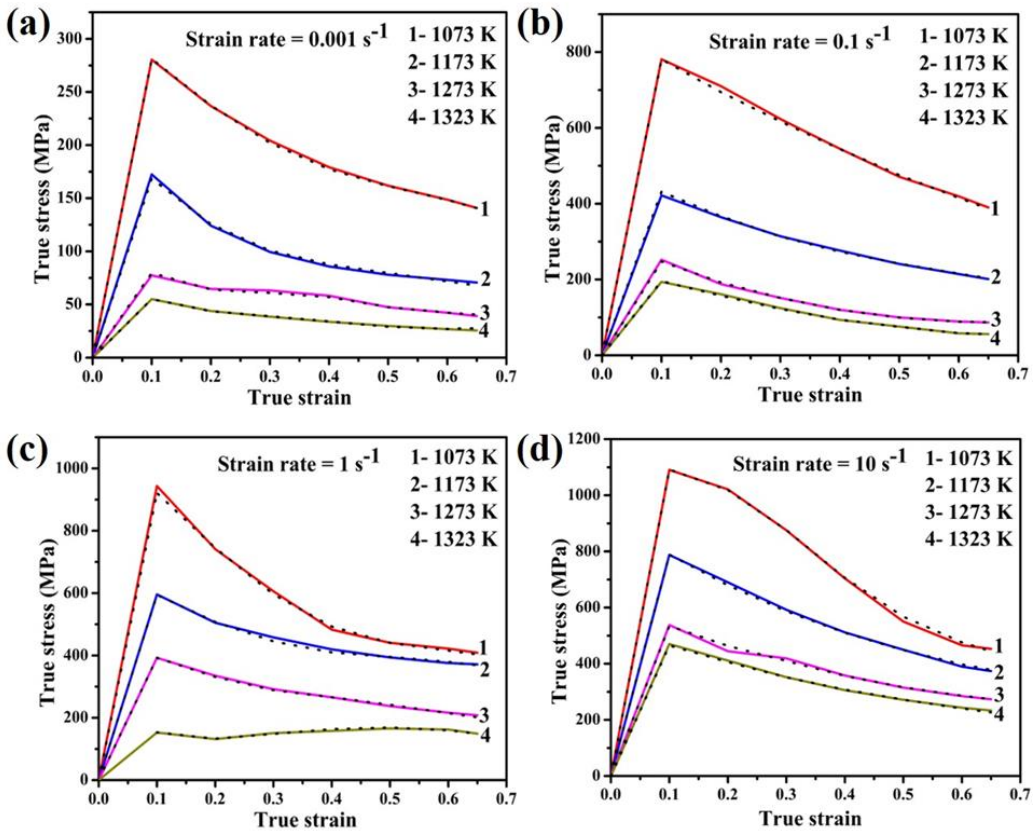

Figure 8.11 Comparisons between the experimental (solid lines) and predicted (dotted lines) flow curves with the help of ANN model at various temperatures for strain rates (a) 10 s^{-1}, (b) 1 s^{-1}, (c) 0.1 $s^{-1}$and (d) 0.001 s^{-1}, of multicomponent $(CoCrFeNi)_{90}Zr_{10}$ QHEA.

Finally, the predictability of flow stress by the Arrhenius type model and the ANN model is evaluated by parameter R and average absolute relative error (AARE) [20]. The performance of the hyperbolic sinusoidal Arrhenius type model and ANN model are given in **Figure 8.12a and Figure 8.12b**, respectively. The number of neurons in the hidden layer influences the accuracy of the predicted values. Hence, several trains were carried out to decide the optimum number of neurons. In the present study, the 3-10-1 model has been utilized to predict the hot deformation behaviour of QHEA. The R and AARE value for the ANN model found to be 0.998 and 1.22, respectively. It is observed that the ANN model can be used to predict the flow stress accurately at different hot working conditions as compared to the strain compensated Arrhenius type model.

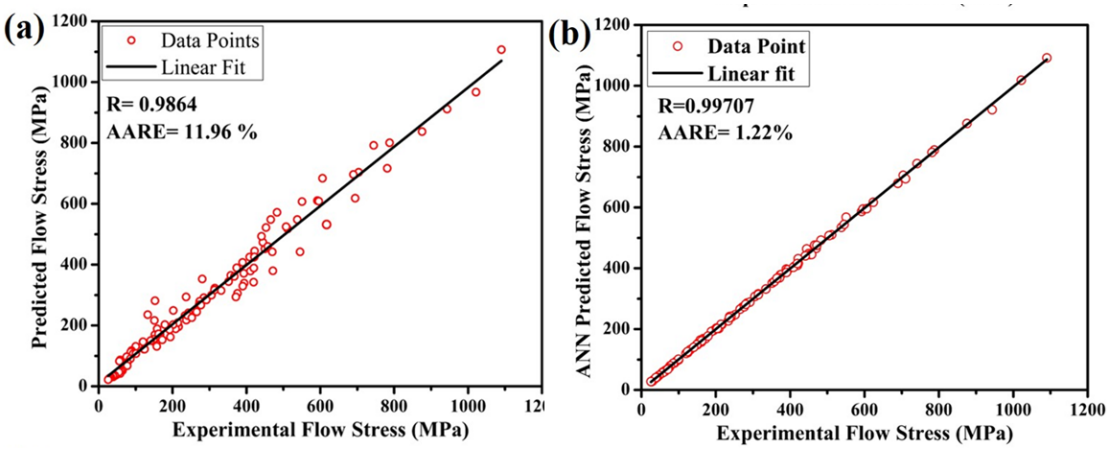

Figure 8.12 Performance (a) Arrhenius type model, (b) ANN model.

8.5.8 Generation of processing map

The processing map provides information about optimum deformation conditions for identifying the hot working domains [86][89][102]. The dynamic material model (DMM) methodology has been utilized to develop the processing map of the investigated multi-component QHEA during the thermomechanical processing [181][102], which helps in understanding the flow behaviour at high temperature. It is important to note here that the constitutive relation is obtained from the thermomechanical processing data of studied multi-component QHEA. The efficiency map (η) is superimposed on the instability parameter $\xi(\bar{\dot{\varepsilon}})$ to identify the safe region (i.e., homogeneous deformation) of studied QHEA. In the DMM, strain rate, and cylindrical work-piece act as the energy input and energy dissipater [102][181][113]. During the hot deformation, DMM assumed that dissipation of energy occurs in two complementary parts. These energies are (i) dissipated through the plastic deformation due to the adiabatic heating, and (ii) energy dissipater through the metallurgical process such as DRV, DRX, and superplasticity [106][154].

8.5.8.1 Strain rate sensitivity (m)

The strain rate sensitivity index m is an essential parameter of flow stress, especially for the deformation mechanism of material, which can also affect the hot workability of the material [89]. Therefore, m is obtained by the partial derivative of $\left[\frac{\partial \log \sigma}{\partial \log \dot{\varepsilon}}\right]_{T,\varepsilon}$ at constant absolute temperature (T) and strain (ε), This is an equivalent to the partial derivative of power attributed to metallurgical changes w.r.t. total plastic deformation [89]. The value of m is found as 0.149,

0.206, 0.229, and 0.257 at temperature1073K, 1173K, 1273K, and 1323K, respectively, indicating that the estimated m-value (i.e., calculated by the relation m=1/n) continuously increases with the increase of hot deformation temperature.

8.5.8.2 Power dissipation efficiency

The contour map of power dissipation efficiency is plotted using non-linear power dissipater condition, which refers to the variation of power efficiency with temperature (T) and strain rate ($\dot{\varepsilon}$). While the power dissipation is initiated through the DRX, DRV, and superplasticity [89][102] at high temperatures. The strain rate sensitivity (m) is assumed to be an identity for the linear power dissipation condition.

8.5.8.3 Instability parameters

The instability parameter $\xi(\bar{\dot{\varepsilon}})$ describes the flow behaviour of the material which changes with the strain rate ($\dot{\varepsilon}$) and temperature (T) [102]. The plotted $\xi(\bar{\dot{\varepsilon}})$ the curve is used to identify the flow instability region by the condition of stability ($0 < (\eta) \leq 2m$) and instability ($2m < (\eta) \leq 0$). It is to be noted that both conditions are applicable for any type of stress and strain curves under the isothermal hot deformation process [89][181][154]. The negative values in the contour map represent flow instability region for the $\xi(\bar{\dot{\varepsilon}})$. The parameter $\dot{m}$ and $\dot{s}$ describes the partial derivative of strain rate sensitivity and temperature sensitivity with respect to strain rate, while s is the temperature sensitivity parameter. The variation of parameters such as $\xi(\bar{\dot{\varepsilon}})$, $\dot{m}$ and $\dot{s}$ as a function of strain rate and temperature (T) provide the safe region (homogeneous deformation/stable plastic flow) and unsafe region (inhomogeneous deformation/unstable plastic flow) for thermomechanical processing of material [86][102].

The processing maps are constructed with the variation of the third parameter in the z-axis at various temperature and strain rates (as shown in **Figure 8.13**). The obtained homogeneous deformation/ stable plastic flow and inhomogeneous deformation/ unstable plastic flow from the maps are correlated with the hot deformed SEM micrograph. It is found that the obtained crack-free microstructure shows the stable plastic flow or homogeneous deformation condition. While during inhomogeneous deformation of unstable plastic flow conditions, the hot deformed sample shows the crack in the microstructure.

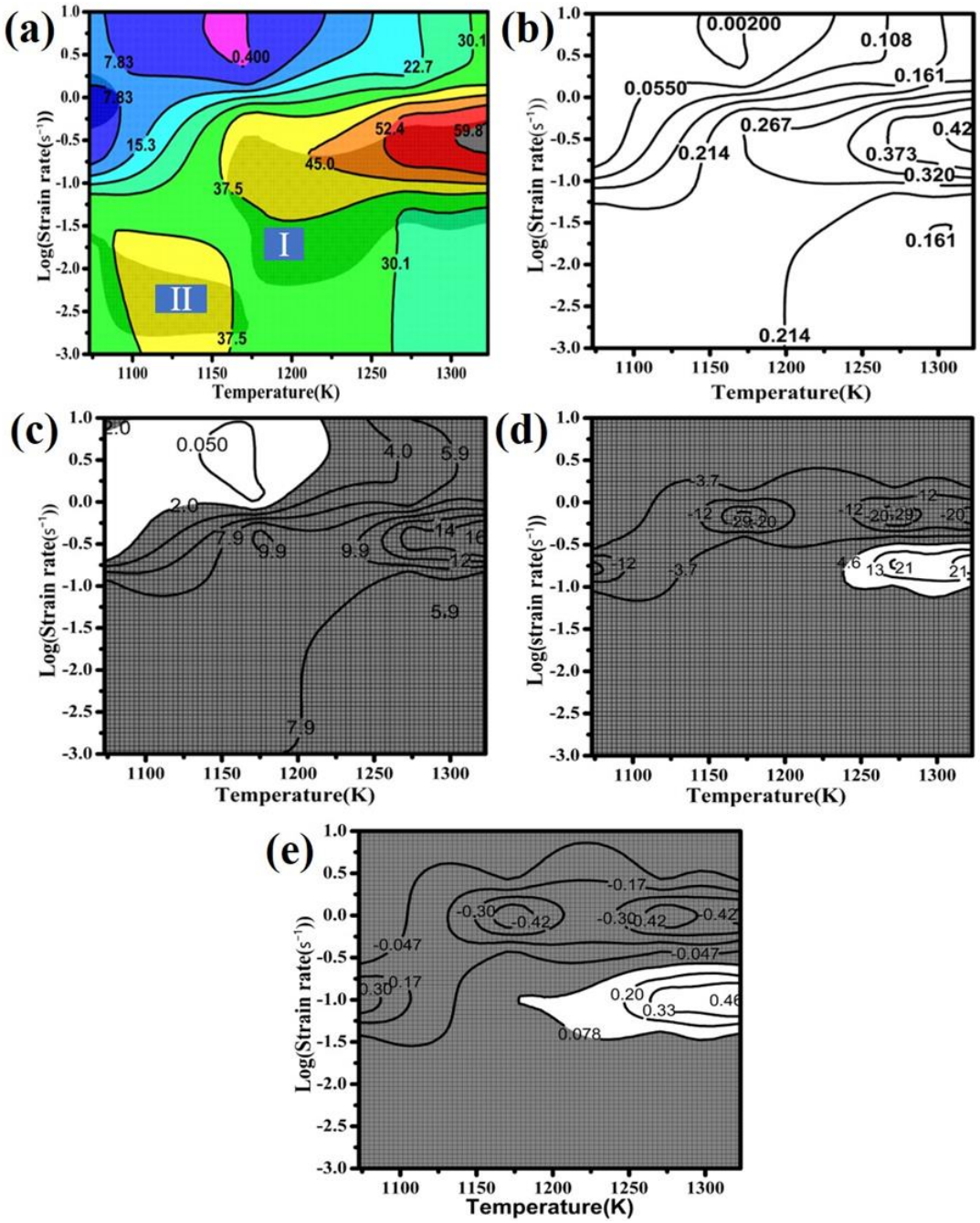

Figure 8.13 (a) Processing map at 0.65 strain, (b) m, (c) s, (d) $\dot{s}$ and (e) $\dot{m}$ of multicomponent $(CoCrFeNi)_{90}Zr_{10}$ QHEA.

It is essential to understand that the DMM technique fails to predict some macroscopically geometry-related instability parameters [155][156] such as excessive bulging in compressive loading, which was observed in the deformed samples under the thermomechanical deformation

condition. Therefore, Semiatin and Jonas [155][156] proposed the criteria of flow localization for estimating the above geometry-related instabilities. **Figure 8.13a** shows the processing map that is obtained by superimposing the power efficiency over the instability parameter at true strain 0.65 and found the two major stable regions1 and 11 (hatched line stain) in $\xi(\bar{\dot{\varepsilon}})$. The remaining part represents the instability region. While the iso-efficiency contour plots (black lines) represent the variation of efficiency (η) with temperature and strain rate. Comparing the variation of the efficiency (η) with $\xi(\bar{\dot{\varepsilon}})$; it is observed that stable region shows greater than 30 % efficiency, and it has also been observed that the efficiency increases with the increase of temperature in both regions I and II at fixed strain rate regime. The maximum efficiency of approx. 60 % is attained at temperature range 1300K-1323K between $10^{-0.8}$ to $10^{-0.5}$strain rate. The remaining part represents the instability region that has less than 30 % efficiency.

The DMM stability parameter, such as strain rate sensitivity (m) contour plots, is generated and observed that there is no instability region for the entire range of temperature with the strain rate. The strain rate sensitivity range (0.002 to 0.426) represents that there is no variation of m with the increased temperature and strain rate. The stability parameter s, $\dot{s}$ and $\dot{m}$ are also used to determine the safe zone (as indicated in **Figure 8.13c, Figure 8.13d, and Figure 8.13e**). **Figure 8.13c** shows one large, unsafe zone or instability region (as marked by the white region in the contour plot) that shows greater than 90% in the superimposed map. The remaining part of the processing map indicates the safe region (as shown by hatched area), where two other parameters$\dot{s}$ and$\dot{m}$shows small regions of instabilities (as marked by white regions) and large regions of stabilities (hatched area), respectively. It is observed that the parameter "s" is strongly dependent on the strain rate and found that the flow instability area increases continuously with the increasing strain rate. It is also noted that the instability area (unsafe region) of $\dot{s}$ and $\dot{m}$ increases with the rise of temperature. The stable and unstable regions with different parameters using the DMM model are given in **Table 8.2**.

Table 8.2 Stable and unstable regions with different parameters using DMM model.

DMM Parameters	Stable region	Unstable region
m	All	No
η	T=1073-1323K, 1150-1323K $\dot{\varepsilon}=10^{-3}$-$10^{-1.5}$, $10^{-1.5}$-$10^{-0.3}$	T=1073-1150K, 1073-1300K $\dot{\varepsilon}=10^{-1}$-1, 1-10 S^{-1}
$\xi(\dot{\varepsilon}) \leq 0$	T=1100-1175K, 1175-1323K $\dot{\varepsilon}=10^{-3}$-$10^{-1.7}$, 10^{-2}-$10^{-0.5}$	T= 1073-1175, 1175-1323K, 1073-1323K $\dot{\varepsilon}=10^{-1.5}$-$10^{-0.5}$, 10^{-3}-10^{-2}, $10^{-0.5}$-10
$\dot{m} < 0$	T=1073-1323K, 1073-1175K, $\dot{\varepsilon}=10^{-3}$-$10^{-1.5}$, $10^{-0.5}$-10, $10^{-1.5}$-$10^{-0.5}$	T=1175-1323K $\dot{\varepsilon}=10^{-1.5}$-$10^{-0.8}$
$S \geq 0$	T=1073-1323K, 1100-1323K, 1225-1323K $\dot{\varepsilon}=10^{-3}$-$10^{-0.75}$, $10^{-0,75}$-$10^{-0.1}$, $10^{-0.1}$-10	T=1073-1175K, 1073-1225K $\dot{\varepsilon}=10^{-0.75}$-1, 1-10
$\dot{S} \leq 0$	T=1073-1323K, 1073-1225K $\dot{\varepsilon}=10^{-3}$-$10^{-1}$, $10^{-0.5}$-10, 10^{-1}-$10^{-0.5}$	T=1225-1323K $\dot{\varepsilon}=10^{-1}$-$10^{-0.5}$

8.5.8.4 Microstructural analysis of the deformed sample

It is to be noted that the microstructural features of the hot deformed QHEA sample at different strain rates and temperatures are taken into consideration for identifying homogeneous and inhomogeneous deformation and then correlated with the processing maps. The microstructures of the multi-component QHEA, deformed at various combinations of temperatures and strain rate, are shown in **Figure 8.14**. It is observed that the microstructure shows the homogeneous distribution under the hot deformation of the sample and hence identified as a stable regime. In contrast, the unstable regime is characterized by localized plastic flow, pores, and adiabatic shear banding. **Figure 8.14a** shows microscopic cracks and porosity in the hot deformed sample regions at temperature 1073 K and strain rate 10 s-1, while **Figure 8.14b** shows the uniform

distribution of constituents temperatures1273 K and strain rate 0.1 s^{-1} for the hot deformed samples. It is also observed that superimposed processing maps showing less than 30% efficiency for the unstable region and greater than 30% for the stable region [86][89]. The microstructural features, efficiency, temperature range, and strain rate range are highlighted in **Table 8.3** to better understand stable and unstable regimes.

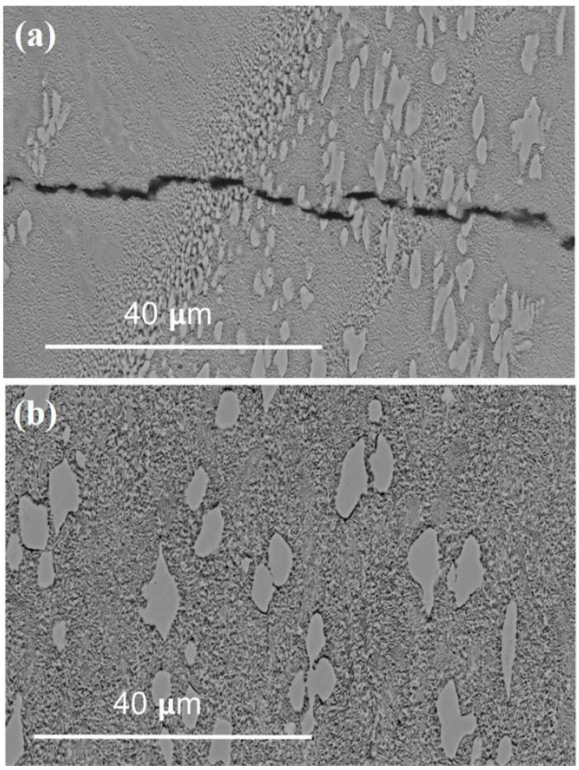

Figure 8.14 SEM micrograph of hot deformed $(CoCrFeNi)_{90}Zr_{10}$ QHEA samples (a) 1073K and $\dot{\varepsilon}$=10 s^{-1}, (b) 1273K and $\dot{\varepsilon}$=0.1 s^{-1}.

Table 8.3 Microstructural features at different strain rates and temperatures.

Domain	$\dot{\varepsilon}$ (s^{-1})	Temperature (K)	η (%)	Microstructural feature
Stable regimes	10^{-3}-$10^{-1.3}$	1073-1323	30- 50	Uniform distribution of phases in microstructure
	10^{-3}-$10^{-0.75}$	1073-1125	30-40	Uniform distribution of phases in microstructure
Unstable regimes	10^{0}-10^{1}	1073-1225	5-10	Crack observation
	10^{0}-10^{1}	1073-1225	5-10	Pores in the deformed microstructure
	$10^{-0.2}$-10^{1}	1173-1125	7-15	Crack observation

The schematic (**Figure 8.15**) shows the mechanism of breaking down of lamellar phase (Ni_7Zr_2) during deformation. The breakage of the lamellar phase requires the peak stress value, which is a function of stress and temperature during deformation. The peak stress corresponds to the pile-up of the critical amount of dislocations against the lamellar phase. The value of the critical amount of dislocation depends on the temperature of deformation. This piling up of dislocations causes the lamellar phase to bend during deformation. The atoms at the tip of the bend are having higher atomic potential than the atoms away from the tip of the bend region resulting in the diffusion of atoms from the higher atomic potential to lower atomic potential. The pile-up of dislocations against the lamellar phase facilitates the process by the mechanism of pipe diffusion resulting in the breaking down of one lamella into two lamellae. As the deformation process continues further, more lamellae break down and convert into globules of Ni_7Zr_2. The stress value decreases with an increase in deformation, which is attributed to the bypass of dislocations by the breaking of the lamellar phase. The above bypass mechanism occurring mechanically at high temperatures causes the annihilation of dislocations pointing towards the saturation of stress value. The saturation of stress value at higher strain corresponds to the complete conversion of the lamellar phase of Ni_7Zr_2 to the globular phase of Ni_7Zr_2.

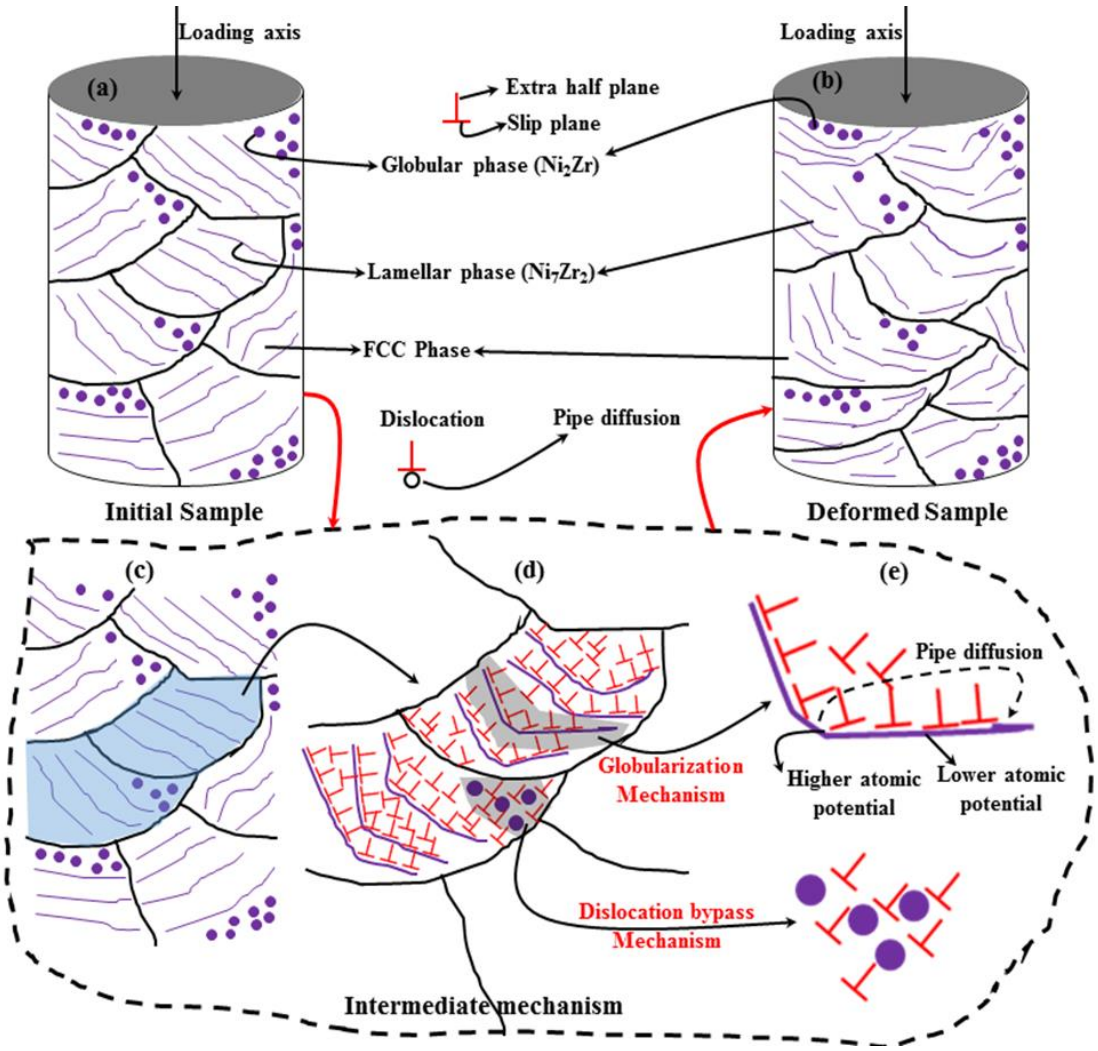

Figure 8.15 Schematic diagram for the plausible mechanism of deformation of $(CoCrFeNi)_{90}Zr_{10}$ QHEA.

8.5.9 FEM simulation during hot deformation of the material

The FEM simulation was carried out to better understanding the hot deformation behaviour, plastic strain field distribution, material flow behaviour during thermomechanical processing of the material. The hot deformation simulation of multi-component QHEA was simulated at different deformation temperatures and constant strain rate using stress-strain experiment data. The contour maps were obtained with the different strain field distribution after 70% deformation during hot deformation on the created geometry in the FEM package (as shown in **Figure 8.16a**) and observed that strain filed distribution of the studied QHEA changes on increasing the deformation temperature at constant strain rate 10 s^{-1}. The strain field distribution decreases on increasing the deformation temperature at a given strain rate and observed after

compression all processing conditions in FEM simulation. It is also found that the maximum flowability occurs at the center of the deformed sample. The maximum strain field distribution is obtained at deformation temperature 1073Kand at strain rate 10 s^{-1}. The flowability of the material decreases on the moving from the left side to the right side and also found that very less amount of flowability occurs near the contact area, which is attributed to friction as expected. The (instability/inhomogeneity) and (stability/homogeneity) within the sample can also be verified with the help of FEM simulation. The material flowability during hot deformation is also understood by FEM simulation. **Figure 8.16b** show the different deformation modes of the deformed sample at different deformation percentage 0%, 5%, 25% 50%, 75%, 95% and 100%. The FEM simulation was done to understand the material flow behaviour, direction of flow, and flow magnitude. The FEM simulation was done at a strain rate of 10 s^{-1} and at temperature 1073 K, which provides information about material flow vectors during the compression test. The compression simulation was carried out in the FEM package at 1073 K on the sample between the upper moving die and lower stationary die.

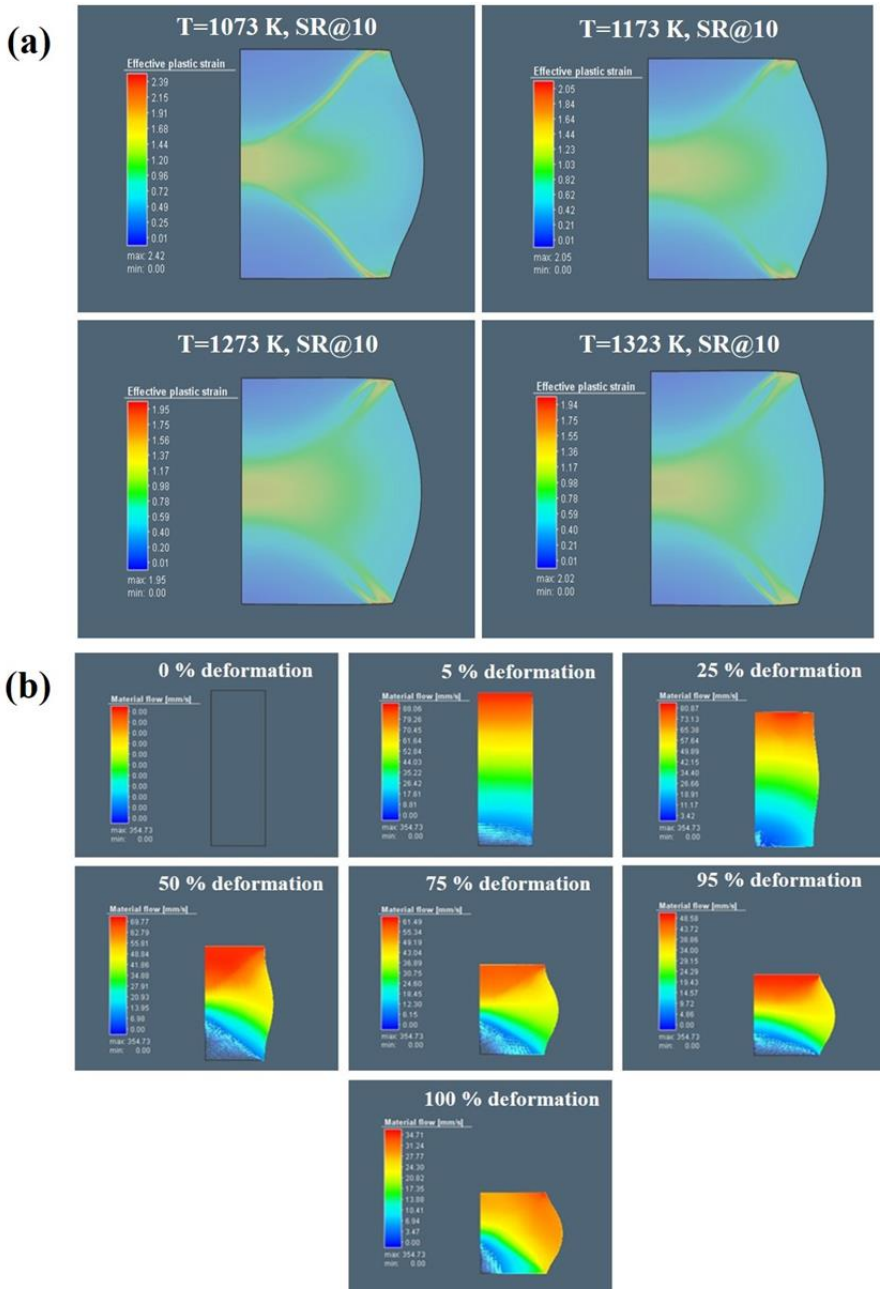

Figure 8.16 FEM simulation of plastic strain field distribution at different temperatures (a) 1073 K, 1173 K, 1273 K, 1323 K at constant strain rate 10 s^{-1} (b) Material flow behavior during high temperature compression at (1073K, SR=10) of $(CoCrFeNi)_{90}Zr_{10}$ QHEA.

After the deformation process, it was observed from the results that the material flows perpendicular to the ram movement and was also found that the maximum magnitude of the material flow vector occurs on the moving die side and minimum magnitude on the stationary die side. The sample changes its shape, showing the maximum barrelling at 100% deformation. Here the material flow behaviour can be used to understand the final shape of the deformed

material. Therefore, it is important to note that the development of novel QHEA with unique phase equilibria having bimodal eutectics at different length scales opens up new pathways in the field of designing novel high entropy structural materials for high-temperature applications. In order to accelerate the induction of newly developed EHEAs into the application, it is important to not only characterize the deformation behaviour of as-solidified material but also provide data that integrates with the FEM simulations. The flow curve data from thermomechanical simulations help in this process via deformation maps. The ANN models expand this possibility by application to a wider range of alloys if the datasets are expanded accordingly.

8.6 Summary

- The detailed sequence of phase evolution of investigating multi-component HEAs is monitored, revealing a transition from single FCC HEA (x = 0 at. %) to eutectic HEA (x=2.5, 5, 7.5 at. %) and finally, to bimodal eutectic HEA (x=10 at. %). The phase formation in the studied HEAs is understood by using different thermodynamic parameters and thermodynamic simulations.
- $(CoCrFeNi)_{90}Zr_{10}$ HEA shows bimodal eutectic microstructure having globular eutectic (i.e., L $\rightarrow$ FCC+ Ni_2Zr) and lamellar eutectic (i.e., L $\rightarrow$ FCC+ Ni_7Zr_2). The Pseudo-quasiperitectic reaction, i.e., L + Ni_2Zr $\rightarrow$ FCC (α) + Ni_7Zr_2, has been proposed for $(CoCrFeNi)_{90}Zr_{10}$ HEA, which is coupled with two eutectic reactions.
- Also, the constitutive relation of novel QHEA is described as $\dot{\varepsilon} = 4.8 \times 10^{12} \times [\sinh(0.0065.\sigma_{0.65})]^{3.4} \times \exp\left(\frac{329000}{RT}\right)$, signifying plastic deformability of material during the hot working process and the predicted flow curve of QHEA using ANN modeling is in good agreement with the experimental data over a broad range of temperatures and strain rates.
- The optimum thermomechanical processing parameters are identified in the stable regimes, i.e., T = 1073-1323 K and $\dot{\varepsilon}$ = 10^{-3}-$10^{-1.3}$ s^{-1} as well as T = 1073-1125 K and $\dot{\varepsilon}$ = 10^{-3}-$10^{-0.75}$ s^{-1}.
- Furthermore, FEM simulation is used to predict the effective plastic strain distribution during thermomechanical processing of studied QHEA at different temperatures and a particular strain rate of 10 s^{-1} as well as to understand material flow behaviour at T = 1073 K and $\dot{\varepsilon}$ = 10 s^{-1}.

Chapter 9

Conclusions and Scope for Future Work

9.1 Conclusions

The following conclusions may be summarized based on present research work:

(i) The single-phase $Fe_{25}Co_{25}Ni_{25}Cr_{20}V_5$ FCC HEA is successfully developed using the ICME approach.

(ii) Seven component $Fe_{35-x}Co_{10}Ni_{25}Cr_{15}Mn_5V_{10}Nbx$ (x =2.5, 5, 7.5, and 10 at. %) and higher-order $Fe_{32.5-x}Co_{10}Ni_{25}Cr_{15}Mn_5V_{10}Al_{2.5}Nbx$ (x= 5, 7.5, 10, and 12.5 at. %) EHEAs are developed using integrated approach of combining thermodynamic simulation and experimental method. It is found that the studied EHEAs consist of FCC solid solution phase and intermetallics phase.

(iii) $Co_{25}Fe_{25}Mn_5Ni_{25}Ti_{20}$ QHEAs is developed consisting of peritectic and eutectic microstructure and having two types of solid solution phases (FCC CoFeNi-rich (α) and BCC Ti-rich (β)) and Ti_2(Ni, Co) type Laves phase. Based on structural and microstructural characterization, a new pseudo-quasi-peritectic four-phase reaction, i.e., L + BCC (β) ⟶ FCC (α) + Ti_2(Ni, Co) is established for CoFeMnNiTi QHEA.

(iv) $(CoCrFeNi)_{90}Zr_{10}$ QHEA consisting of both globular eutectics (i.e., L ⟶ FCC ($\boldsymbol{\alpha}$) + Ni_2Zr-type Laves phases) and lamellar eutectics (i.e., L ⟶FCC ($\boldsymbol{\alpha}$) + Ni_7Zr_2) is designed and developed by an integrated approach of using thermodynamic simulation and experimental techniques. Based on structural and microstructural characterization, a new pseudo-quasi-peritectic four-phase reaction, i.e., L + Ni_2Zr → FCC (α) + Ni_7Zr_2 is proposed for $(CoCrFeNi)_{90}Zr_{10}$ QHEA.

(v) The hot deformation behavior of studied HEAs is understood using the experimental modeling, and simulation (FEM) approaches.

(vi) The optimum thermomechanical processing conditions during hot deformation of HEAs are identified using processing maps.

(vi) Mechanical properties and flow curve (at different temperatures and strain rate) are predicted using ANN model for studied HEAs and are in good agreement with the predicted results.

(viii) Finally, QHEA having peritectic and eutectic microstructure or two eutectics microstructure shows balanced mechanical properties in terms of strength and ductility at elevated temperature as compared to others studied HEAs (as given in **Figure 9.1**).

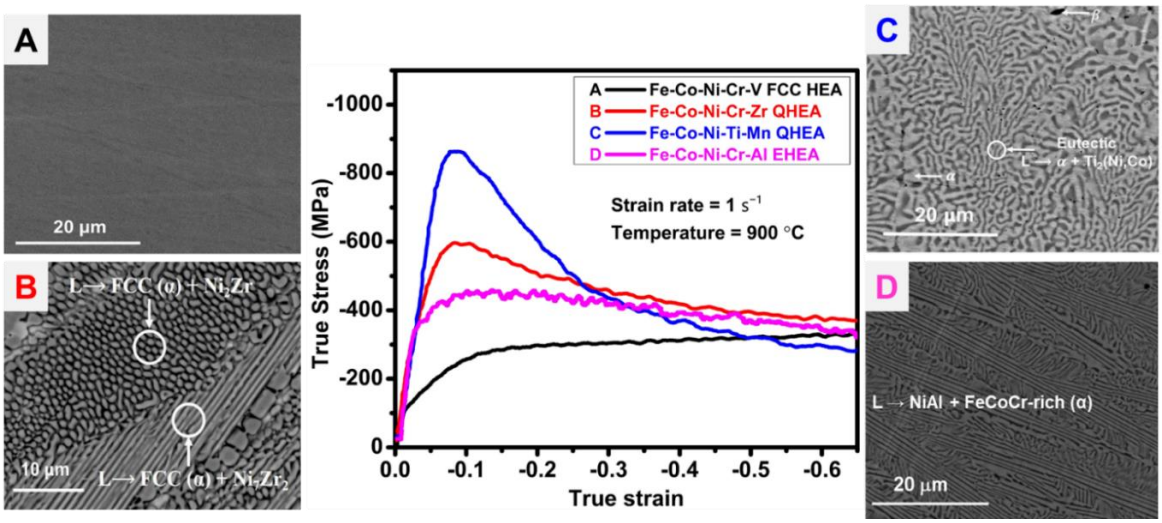

Figure 9.1 Comparison of mechanical properties at strain rate 1 s^{-1} and temperature 900 °C

9.2 Scope for Future Work

Based upon the studies carried out, related to the subject of different types of high entropy alloys (HEAs) in the present dissertation, a number of research problems could be foreseen.

- Hot deformation behaviour and processing maps of higher-order EHEAs having nanoscale microstructural features are to be carried out at different temperatures and strain rates to understand plausible deformation mechanisms and to identify the thermomechanical processing conditions for applicability at high temperature.
- The in-depth analysis of the deformed samples is to be done using TEM characterization to understand the deformation mechanism during thermomechanical processing of HEAs.

- New types of HEAs in-situ composite consisting of eutectic dendrites of two-phase microstructure embedded in the ternary eutectic matrix having three phase mixture are to be designed and developed by integrated approach and subsequently, the phase equilibria of developed HEAs are to be understood, which will open up new avenues in engineering the microstructure for design of high temperature materials.
- Isothermal and non-isothermal oxidation studies of developed HEAs are to be carried out to understand the oxidation kinetics.
- Corrosion study of developed HEAs at different electrolyte media is to be investigated to understand the corrosive resistance of developed HEAs.
- The tribological behaviour of developed HEAs is to be done to understand the environmental effect on the mechanical behavior of HEAs.

APPENDIX

Appendix 1 The experimental and ANN microhardness calculated values for high entropy alloys.

Alloys	Fe	Co	Ni	Cr	V	Mn	Al	Nb	Experimental (HV)	ANN (HV)	Error %
1	24.95	9.99	24.89	13.23	8.64	4.66	0	13.65	415	485.07	16.89
2	24.03	9.94	24.76	13.16	8.59	4.63	0	14.89	469	529.02	12.80
3	23.81	9.93	24.27	13.14	8.58	4.63	0	15.18	494	550.60	11.46
4	23.77	9.93	24.72	13.14	8.58	4.63	0	15.23	547	538.00	6.44
5	23.7	9.92	24.71	13.13	8.58	4.63	0	15.33	512	544.98	1.23
6	21.34	22.52	22.42	19.87	0	0	10.31	3.55	569	531.09	1.30
7	20.26	21.38	21.29	18.86	0	0	9.79	8.43	668	631.30	0.63
8	18.68	19.72	19.64	17.4	0	0	9.03	15.54	747	746.96	0.77
9	19.05	19.05	19.05	19.05	4.76	19.05	0	0	151	152.85	4.36
10	18.18	18.18	18.18	18.18	9.09	18.18	0	0	186	157.84	4.22
11	17.4	17.4	17.4	17.39	13.04	17.4	0	0	342	346.45	2.19
12	16.67	16.67	16.67	16.67	16.67	16.67	0	0	650	654.10	14.09
13	19.61	19.61	19.61	19.61	0	19.61	1.96	0	180	181.39	1.78
14	19.23	19.23	19.23	19.23	0	19.23	3.84	0	171	178.46	0.27
15	18.58	18.58	18.58	18.58	0	18.58	7.06	0	182	177.80	0.49
16	18.41	18.41	18.41	18.41	0	18.41	7.92	0	183	190.73	1.62
17	18.21	18.21	18.21	18.21	0	18.21	8.92	0	220	224.81	2.13
18	17.98	17.98	17.98	17.98	0	17.98	10.07	0	278	317.17	0.91
19	17.79	17.79	17.79	17.79	0	17.79	11.03	0	405	412.22	1.67
20	17.6	17.6	17.6	17.6	0	17.6	11.97	0	486	487.31	5.54
21	17.39	17.39	17.39	17.39	0	17.39	13.04	0	530	528.71	0.59
22	17.21	17.21	17.21	17.21	0	17.21	13.94	0	539	541.65	6.50
23	17.07	17.07	17.07	17.07	0	17.07	14.96	0	533	541.64	21.05
24	16.8	16.8	16.8	16.8	0	16.8	15.96	0	535	546.39	20.20
25	15.96	15.96	15.96	15.96	0	15.96	20.17	0	539	543.91	12.19
26	24.05	25.41	25.28	22.39	0	0	2.87	0	110	111.83	1.81
27	23.87	25.22	24.39	22.22	0	0	4.26	0	131	138.26	3.46
28	21.72	25.22	25.09	22.23	0	0	5.65	0	159	159.95	0.52
29	22.73	24.01	23.89	21.16	0	0	7.99	0	388	413.24	1.07
30	22.42	23.69	23.57	20.88	0	0	9.15	0	538	452.19	0.22
31	22.12	23.37	23.25	20.6	0	0	10.28	0	484	470.93	0.34
32	22.12	23.37	23.25	20.6	0	0	10.28	0	395	478.14	0.32
33	22.12	23.37	23.25	20.6	0	0	10.28	0	520	468.76	0.65
34	21.55	22.77	22.65	20.06	0	0	12.41	0	487	475.05	4.42
35	21	22.19	22.07	19.55	0	0	14.41	0	484	476.59	1.64
36	21	22.19	22.07	19.55	0	0	14.41	0	402	483.19	6.66
37	19.98	21.12	21	18.61	0	0	19.32	0	509	479.18	5.49

38	19.98	21.12	21	18.61	0	0	19.32	0	432	484.67	0.01
39	19.06	20.15	20.04	17.75	0	0	23.03	0	487	495.80	15.14
40	18.22	19.26	19.15	16.97	0	0	26.42	0	506	504.35	2.31
41	22.3	23.56	23.44	20.76	0	9.96	0	0	176	119.66	0.24
42	22.3	23.56	23.44	20.76	0	9.96	0	0	144	125.47	15.95
43	19.36	20.43	20.34	18.02	0	19.04	2.81	0	125	129.32	2.70
44	23.2	20.03	24.38	21.6	0	5.19	5.6	0	198	199.02	9.85
45	19.54	19.99	16.8	20.4	0	5.82	17.45	0	522	527.61	2.45
46	7.28	7.69	6.38	39.56	0	21.5	17.6	0	605	606.36	1.53
47	11.78	11.19	6.19	38.38	0	17.96	14.51	0	628	630.12	5.86
48	11.58	22	6.7	37.74	0	8.55	13.43	0	650	652.11	0.33
49	22.48	0	23.62	20.93	0	22.11	10.86	0	552	555.56	0.65
50	32.02	10.4	25.89	13.76	8.99	4.85	0	4.1	277	275.75	0.45
51	29.08	10.23	25.47	13.54	8.84	4.77	0	8.06	315	328.93	4.42
52	26.24	10.07	25.07	13.32	8.7	4.69	0	11.9	449	420.29	6.40
53	23.48	9.91	24.68	13.12	8.57	4.62	0	15.63	607	551.87	9.08
*** Present Work**									**Average error**		**4.82**

Appendix 2 Comparison of the microhardness of the ANN model and experimental microhardness for different HEAs.											
Alloys	**Fe**	**Co**	**Ni**	**Cr**	**V**	**Mn**	**Al**	**Nb**	**Experimental (HV)**	**ANN Prediction (HV)**	**Absolute error%**
1	24.95	9.99	24.89	13.23	8.64	4.66	0	13.65	415.00	449.80	8.39
2	24.03	9.94	24.76	13.16	8.59	4.63	0	14.89	469.00	500.35	6.68
3	23.81	9.93	24.27	13.14	8.58	4.63	0	15.18	494.00	516.04	4.46
4	23.77	9.93	24.72	13.14	8.58	4.63	0	15.23	547.00	511.88	6.42
5	23.70	9.92	24.71	13.13	8.58	4.63	0	15.33	512.00	515.00	0.59
6	21.34	22.52	22.42	19.87	0	0	10.31	3.55	569.00	560.63	1.47
7	20.26	21.38	21.29	18.86	0	0	9.79	8.43	668.00	646.01	3.29
8	18.68	19.72	19.64	17.40	0	0	9.03	15.54	747.00	748.89	0.25
9	19.05	19.05	19.05	19.05	4.76	19.05	0	0	151.00	161.67	7.07
10	18.18	18.18	18.18	18.18	9.09	18.18	0	0	186.00	183.26	1.48
11	17.40	17.40	17.40	17.39	13.04	17.40	0	0	342.00	350.29	2.43
12	16.67	16.67	16.67	16.67	16.67	16.67	0	0	650.00	650.56	0.09
13	19.61	19.61	19.61	19.61	0	19.61	1.96	0	180.00	175.88	2.29
14	19.23	19.23	19.23	19.23	0	19.23	3.84	0	171.00	157.56	7.86
15	18.58	18.58	18.58	18.58	0	18.58	7.06	0	182.00	155.48	14.57
16	18.41	18.41	18.41	18.41	0	18.41	7.92	0	183.00	181.02	1.08
17	18.21	18.21	18.21	18.21	0	18.21	8.92	0	220.00	233.75	6.25
18	17.98	17.98	17.98	17.98	0	17.98	10.07	0	278.00	319.39	14.89
19	17.79	17.79	17.79	17.79	0	17.79	11.03	0	405.00	395.34	2.39
20	17.60	17.60	17.60	17.60	0	17.60	11.97	0	486.00	458.42	5.67
21	17.39	17.39	17.39	17.39	0	17.39	13.04	0	530.00	507.51	4.24
22	17.21	17.21	17.21	17.21	0	17.21	13.94	0	539.00	531.65	1.36
23	17.07	17.07	17.07	17.07	0	17.07	14.96	0	533.00	546.40	2.51
24	16.80	16.80	16.80	16.80	0	16.80	15.96	0	535.00	551.11	3.01
25	15.96	15.96	15.96	15.96	0	15.96	20.17	0	539.00	550.84	2.20
26	24.05	25.41	25.28	22.39	0	0	2.87	0	110.00	133.03	20.93
27	23.87	25.22	24.39	22.22	0	0	4.26	0	131.00	148.53	13.38
28	21.72	25.22	25.09	22.23	0	0	5.65	0	159.00	157.44	0.98
29	22.73	24.01	23.89	21.16	0	0	7.99	0	388.00	358.28	7.66
30	22.42	23.69	23.57	20.88	0	0	9.15	0	538.00	425.32	20.94
31	22.12	23.37	23.25	20.60	0	0	10.28	0	484.00	463.10	4.32
32	22.12	23.37	23.25	20.60	0	0	10.28	0	395.00	463.10	17.24
33	22.12	23.37	23.25	20.60	0	0	10.28	0	520.00	463.10	10.94
34	21.55	22.77	22.65	20.06	0	0	12.41	0	487.00	478.95	1.65
35	21.00	22.19	22.07	19.55	0	0	14.41	0	484.00	469.94	2.90
36	21.00	22.19	22.07	19.55	0	0	14.41	0	402.00	469.94	16.90
37	19.98	21.12	21.00	18.61	0	0	19.32	0	509.00	465.73	8.50

38	19.98	21.12	21.00	18.61	0	0	19.32	0	432.00	465.73	7.81
39	19.06	20.15	20.04	17.75	0	0	23.03	0	487.00	480.82	1.27
40	18.22	19.26	19.15	16.97	0	0	26.42	0	506.00	501.81	0.83
41	22.30	23.56	23.44	20.76	0	9.96	0.00	0	176.00	149.53	15.04
42	22.30	23.56	23.44	20.76	0	9.96	0.00	0	144.00	149.53	3.84
43	18.72	9.88	24.59	13.07	8.54	4.60	1.13	19.46	614.00	621.53	1.23
44	27.00	10.36	25.79	13.71	8.96	4.83	1.19	8.17	318.00	311.03	2.19
45	19.36	20.43	20.34	18.02	0	19.04	2.81	0	125.00	153.66	22.93
46	23.20	20.03	24.38	21.60	0	5.19	5.60	0	198.00	264.53	33.60
47	19.54	19.99	16.80	20.40	0	5.82	17.45	0	522.00	507.95	2.69
48	7.28	7.69	6.38	39.56	0	21.50	17.60	0	605.00	607.30	0.38
49	11.78	11.19	6.19	38.38	0	17.96	14.51	0	628.00	645.94	2.86
50	11.58	22.00	6.70	37.74	0	8.55	13.43	0	650.00	629.73	3.12
51	22.48	0.00	23.62	20.93	0	22.11	10.86	0	552.00	552.55	0.10
*** Present Work Error %**										**Average**	**6.57**

REFERENCES:

1. Yeh JW, Chen SK, Lin SJ, Gan JY, Chin TS, Shun TT, Tsau CH, Chang SY (2004) Nanostructured high-entropy alloys with multiple principal elements: Novel alloy design concepts and outcomes. Adv Eng Mater 6:299–303 (DOI:10.1002/adem.200300567)

2. Cantor B, Chang ITH, Knight P, Vincent AJB (2004) Microstructural development in equiatomic multicomponent alloys. Mater Sci Eng A 375–377:213–218 (DOI:10.1016/j.msea.2003.10.257)

3. Praveen S, Murty BS, Kottada RS (2012) Alloying behavior in multi-component AlCoCrCuFe and NiCoCrCuFe high entropy alloys. Mater Sci Eng A 534:83–89 (DOI:10.1016/j.msea.2011.11.044)

4. Jien Wei Yeh, Su Jien Lin, Tsung Shune Chin, Jon Yiew Gan, Swe Kai Chen, Tao Tsung Shun, Chung Huei Tsau SC (2010) Formation of simple crystal structures in Cu-Co-Ni-Cr-Al-Fe-Ti-V alloys with multiprincipal metallic elements. 35:2533–2536 (DOI:https://doi.org/10.1007/s11661-006-0234-4)

5. Murty BS, Yeh JW, Ranganathan S (2014) High Entropy Alloys, 1st ed. Elsevier

6. Zhang Y, Zuo TT, Tang Z, Gao MC, Dahmen KA, Liaw PK, Lu ZP (2014) Microstructures and properties of high-entropy alloys. Prog Mater Sci 61:1–93 (DOI:10.1016/j.pmatsci.2013.10.001)

7. Tsai K, Tsai M, Yeh J (2013) Sluggish diffusion in Co – Cr – Fe – Mn – Ni high-entropy alloys. Acta Mater 61:4887–4897 (DOI:10.1016/j.actamat.2013.04.058)

8. Zhang C, Gao MC (2016) CALPHAD modeling of high-entropy alloys. Springer, Cham

9. Lu Y, Dong Y, Guo S, Jiang L, Kang H, Wang T, Wen B, Wang Z, Jie J, Cao Z, Ruan H, Li T (2014) A promising new class of high-temperature alloys: Eutectic high-entropy alloys. Sci Rep 4:1–5 (DOI:10.1038/srep06200)

10. Guo Y, Liu L, Zhang Y, Qi J, Wang B, Zhao Z, Shang J, Xiang J (2018) A superfine eutectic microstructure and the mechanical properties of CoCrFeNiMox high-entropy

alloys. J Mater Res 33:3258–3265 (DOI:10.1557/jmr.2018.177)

11. Jiang H, Han K, Gao X, Lu Y, Cao Z, Gao MC, Hawk JA, Li T (2018) A new strategy to design eutectic high-entropy alloys using simple mixture method. Mater Des 142:101–105 (DOI:10.1016/j.matdes.2018.01.025)

12. Wu M, Wang S, Huang H, Shu D, Sun B (2019) CALPHAD aided eutectic high-entropy. Mater Lett 127175 (DOI:10.1016/j.matlet.2019.127175)

13. Lu Y, Jiang H, Guo S, Wang T, Cao Z, Li T (2017) A new strategy to design eutectic high-entropy alloys using mixing enthalpy. Intermetallics 91:124–128 (DOI:10.1016/j.intermet.2017.09.001)

14. Chanda B, Das J (2019) An assessment on the stability of the eutectic phases in high entropy alloys. J Alloys Compd 798:167–173 (DOI:10.1016/j.jallcom.2019.05.241)

15. Kim MJ, Kang GC, Hong SH, Park HJ, Mun SC, Song G, Kim KB (2020) Understanding microstructure and mechanical properties of (AlTa0.76)xCoCrFeNi2.1 eutectic high entropy alloys via thermo-physical parameters. J Mater Sci Technol 57:131–137 (DOI:10.1016/j.jmst.2020.03.045)

16. Rahul MR, Phanikumar G (2019) Design of a Seven-Component Eutectic High-Entropy Alloy. Metall Mater Trans A 50:2594–2598 (DOI:10.1007/s11661-019-05210-3)

17. He F, Wang Z, Shang X, Leng C, Li J, Wang J (2016) Stability of lamellar structures in CoCrFeNiNbx eutectic high entropy alloys at elevated temperatures. Mater Des 104:259–264 (DOI:10.1016/j.matdes.2016.05.044)

18. Wu Q, Wang Z, Zheng T, Chen D, Yang Z, Li J, Kai J jung, Wang J (2019) A casting eutectic high entropy alloy with superior strength-ductility combination. Mater Lett 253:268–271 (DOI:10.1016/j.matlet.2019.06.067)

19. Wani IS, Bhattacharjee T, Sheikh S, Clark IT, Park MH, Okawa T, Guo S, Bhattacharjee PP, Tsuji N (2017) Cold-rolling and recrystallization textures of a nano-lamellar AlCoCrFeNi2.1 eutectic high entropy alloy. Intermetallics 84:42–51 (DOI:10.1016/j.intermet.2016.12.018)

20. Guoliang Ji, Fuguo Li ,Qinghua Li ,Huiqu Li ZL (2011) A comparative study on Arrhenius-type constitutive model and artificial neural network model to predict high-temperature deformation behaviour in Aermet100 steel. Mater Sci Eng A 528:4774–4782 (DOI:10.1016/j.msea.2011.03.017)

21. Sabokpa O, Zarei-Hanzaki A, Abedi HR, Haghdadi N (2012) Artificial neural network modeling to predict the high temperature flow behavior of an AZ81 magnesium alloy. Mater Des 39:390–396 (DOI:10.1016/j.matdes.2012.03.002)

22. Singh K, Rajput SK, Soota T, Verma V, Singh D (2018) Prediction of hot deformation behavior of high phosphorus steel using artificial neural network. IOP Conf Ser Mater Sci Eng 330: (DOI:10.1088/1757-899X/330/1/012038)

23. Chen J, Zhou X, Wang W, Liu B, Lv Y, Yang W, Xu D, Liu Y (2018) A review on fundamental of high entropy alloys with promising high–temperature properties. J Alloys Compd 760:15–30 (DOI:10.1016/j.jallcom.2018.05.067)

24. Bhattacharjee T, Zheng R, Chong Y, Sheikh S, Guo S, Clark IT, Okawa T, Wani IS, Bhattacharjee PP, Shibata A, Tsuji N (2018) Effect of low temperature on tensile properties of AlCoCrFeNi2.1 eutectic high entropy alloy. Mater Chem Phys 210:207–212 (DOI:10.1016/j.matchemphys.2017.06.023)

25. Ye YF, Wang Q, Lu J, Liu CT, Yang Y (2016) High-entropy alloy: challenges and prospects. Mater Today 19:349–362 (DOI:10.1016/j.mattod.2015.11.026)

26. Cropper MD (2018) Thin films of AlCrFeCoNiCu high-entropy alloy by pulsed laser deposition. Appl. Surf. Sci. 455:153–159

27. Mohanty S, Maity TN, Mukhopadhyay S, Sarkar S, Gurao NP, Bhowmick S, Biswas K (2017) Powder metallurgical processing of equiatomic AlCoCrFeNi high entropy alloy: Microstructure and mechanical properties. Mater Sci Eng A 679:299–313 (DOI:10.1016/j.msea.2016.09.062)

28. Jin G, Cai Z, Guan Y, Cui X, Liu Z, Li Y, Dong M, zhang D (2018) High temperature wear performance of laser-cladded FeNiCoAlCu high-entropy alloy coating

29. Shang C, Axinte E, Ge W, Zhang Z, Wang Y (2017) High-entropy alloy coatings with excellent mechanical, corrosion resistance and magnetic properties prepared by mechanical alloying and hot pressing sintering. Surfaces and Interfaces 9:36–43 (DOI:10.1016/j.surfin.2017.06.012)

30. Yu PF, Zhang LJ, Cheng H, Zhang H, Ma MZ, Li YC, Li G, Liaw PK, Liu RP (2016) The high-entropy alloys with high hardness and soft magnetic property prepared by mechanical alloying and high-pressure sintering. Intermetallics 70:82–87 (DOI:10.1016/j.intermet.2015.11.005)

31. Chen YY, Duval T, Hung UD, Yeh JW, Shih HC (2005) Microstructure and electrochemical properties of high entropy alloys-a comparison with type-304 stainless steel. Corros Sci 47:2257–2279 (DOI:10.1016/j.corsci.2004.11.008)

32. Zhang LJ, Fan JT, Liu DJ, Zhang MD, Yu PF, Jing Q, Ma MZ, Liaw PK, Li G, Liu RP (2018) The microstructural evolution and hardness of the equiatomic CoCrCuFeNi high-entropy alloy in the semi-solid state. J Alloys Compd 745:75–83 (DOI:10.1016/j.jallcom.2018.02.170)

33. Huo W, Liu X, Tan S, Fang F, Xie Z, Shang J, Jiang J (2018) Ultrahigh hardness and high electrical resistivity in nano-twinned, nanocrystalline high-entropy alloy films. Appl Surf Sci 439:222–225 (DOI:10.1016/j.apsusc.2018.01.050)

34. Yusenko K V., Riva S, Crichton WA, Spektor K, Bykova E, Pakhomova A, Tudball A, Kupenko I, Rohrbach A, Klemme S, Mazzali F, Margadonna S, Lavery NP, Brown SGR (2018) High-pressure high-temperature tailoring of High Entropy Alloys for extreme environments. J Alloys Compd 738:491–500 (DOI:10.1016/j.jallcom.2017.12.216)

35. Wang R, Chen W, Zhong J, Zhang L (2018) Experimental and numerical studies on the sluggish diffusion in face centered cubic Co-Cr-Cu-Fe-Ni high-entropy alloys. J Mater Sci Technol 34:1791–1798 (DOI:10.1016/j.jmst.2018.02.003)

36. Guo S, Ng C, Lu J, Liu CT (2011) Effect of valence electron concentration on stability of fcc or bcc phase in high entropy alloys. J Appl Phys 109:1–5 (DOI:10.1063/1.3587228)

37. Wang F, Zhang Y, Chen G, Davies HA (2009) Tensile and compressive mechanical behavior of a CoCrCuFeNiAl0.5 high entropy alloy. Int J Mod Phys B 23:1254–1259 (DOI:10.1142/s0217979209060774)

38. Otto F, Dlouhý A, Somsen C, Bei H, Eggeler G, George EP (2013) The influences of temperature and microstructure on the tensile properties of a CoCrFeMnNi high-entropy alloy. Acta Mater 61:5743–5755 (DOI:10.1016/j.actamat.2013.06.018)

39. Senkov ON, Wilks GB, Miracle DB, Chuang CP, Liaw PK (2010) Refractory high-entropy alloys. Intermetallics 18:1758–1765 (DOI:10.1016/j.intermet.2010.05.014)

40. Kuznetsov A V., Shaysultanov DG, Stepanov ND, Salishchev GA, Senkov ON (2012) Tensile properties of an AlCrCuNiFeCo high-entropy alloy in as-cast and wrought conditions. Mater Sci Eng A 533:107–118 (DOI:10.1016/j.msea.2011.11.045)

41. Hemphill MA, Yuan T, Wang GY, Yeh JW, Tsai CW, Chuang A, Liaw PK (2012) Fatigue behavior of Al 0.5CoCrCuFeNi high entropy alloys. Acta Mater 60:5723–5734 (DOI:10.1016/j.actamat.2012.06.046)

42. Tong CJ, Chen MR, Chen SK, Yeh JW, Shun TT, Lin SJ, Chang SY (2005) Mechanical performance of the AlxCoCrCuFeNi high-entropy alloy system with multiprincipal elements. Metall Mater Trans A Phys Metall Mater Sci 36:1263–1271 (DOI:10.1007/s11661-005-0218-9)

43. Martin Eden Glicksman (2011) Principals of solidification An Introduction to Modern Casting and Crystal Growth Concepts. Springer

44. Zhang Y, Zhou YJ (2007) Solid Solution Formation Criteria for High Entropy Alloys. Mater Sci Forum 561–565:1337–1339 (DOI:10.4028/www.scientific.net/msf.561-565.1337)

45. Zhang Y, Zhou YJ, Lin JP, Chen GL, Liaw PK (2008) Solid-solution phase formation rules for multi-component alloys. Adv Eng Mater 10:534–538 (DOI:10.1002/adem.200700240)

46. Yang X, Zhang Y (2012) Prediction of high-entropy stabilized solid-solution in multi-

component alloys. Mater Chem Phys 132:233–238 (DOI:10.1016/j.matchemphys.2011.11.021)

47. Kumar A, Kumar N, Dwivedi A, Subramaniam A (2014) A geometrical parameter for the formation of disordered solid solutions in multi-component alloys. Intermetallics 53:112–119 (DOI:10.1016/j.intermet.2014.04.019)

48. Saal JE, Berglund IS, Sebastian JT, Liaw PK, Olson GB (2018) Equilibrium high entropy alloy phase stability from experiments and thermodynamic modeling. Scr Mater 146:5–8 (DOI:10.1016/j.scriptamat.2017.10.027)

49. Muggianu YM, Gambino M, Bros JP (1975) Enthalpies of formation of liquid bismuth-tin-gallium alloys at 723 k. Choice of an analytical representation of the integral and partial excess quantities of mixing. J Chim Phys 72:83–88 (DOI:10.1051/jcp/1975720083)

50. F. Kohler (1960) To calculate the thermodynamic data of a ternary system from the associated binary systems. Mon Journals Chem Relat parts other Sci 91:738–740 (DOI:10.1007 / BF00899814)

51. Toop GW, Somis CS (2016) Some New Ionic Concepts of Silicate Slags SOME NEW IONIC CONCEPTS

52. Kattner UR (1997) The thermodynamic modeling of multicomponent phase equilibria. JOM 49:14–19 (DOI:https://doi.org/10.1007/s11837-997-0024-5)

53. Gorr B, Azim M, Christ H, Mueller T, Schliephake D, Heilmaier M (2014) Phase equilibria, microstructure, and high temperature oxidation resistance of novel refractory high-entropy alloys. Elsevier B.V.

54. Zhang C, Zhang FAN, Chen S (2012) Computational Thermodynamics Aided High-Entropy Alloy Design

55. Tazuddin, Gurao NP, Biswas K (2016) In the quest of single phase multi-component multiprincipal high entropy alloys. J Alloys Compd. https://doi.org/10.1016/j.jallcom.2016.11.383

56. Dantzig JA (2009) Solidification / J.A. Dantzig and M. Rappaz. Lausanne : EPFL Press ; London : Taylor & Francis [distributor], c2009.

57. Samal S, Biswas K, Phanikumar G Solidification Behavior in Newly Designed Ni-Rich Ni-Ti-Based Alloys. Springer US

58. Alshataif YA, Sivasankaran S, Al-Mufadi FA, Alaboodi AS, Ammar HR (2020) Manufacturing Methods, Microstructural and Mechanical Properties Evolutions of High-Entropy Alloys: A Review

59. Lee CF, Shun TT (2014) Age hardening of the Al0.5CoCrNiTi0.5 high-entropy alloy. Metall Mater Trans A Phys Metall Mater Sci 45:191–195 (DOI:10.1007/s11661-013-1931-4)

60. Zhang A, Han J, Meng J, Su B, Li P (2016) Rapid preparation of AlCoCrFeNi high entropy alloy by spark plasma sintering from elemental powder mixture. Mater Lett 181:82–85 (DOI:10.1016/J.MATLET.2016.06.014)

61. Tang Z, Senkov ON, Parish CM, Zhang C, Zhang F, Santodonato LJ, Wang G, Zhao G, Yang F, Liaw PK (2015) Tensile ductility of an AlCoCrFeNi multi-phase high-entropy alloy through hot isostatic pressing (HIP) and homogenization. Mater Sci Eng A 647:229–240 (DOI:10.1016/j.msea.2015.08.078)

62. Dewangan SK, Samal S, Kumar V (2020) Microstructure exploration and an artificial neural network approach for hardness prediction in AlCrFeMnNiWx High-Entropy Alloys. J Alloys Compd 153766 (DOI:10.1016/j.jallcom.2020.153766)

63. Dewangan SK, Kumar D, Samal S, Kumar V (2021) Microstructure and Mechanical Properties of Nanocrystalline AlCrFeMnNiWx (x = 0, 0.05, 0.1, 0.5) High-Entropy Alloys Prepared by Powder Metallurgy Route. J Mater Eng Perform 2021 306 30:4421–4431 (DOI:10.1007/S11665-021-05552-3)

64. Tsao LC, Chen CS, Chu CP (2012) Age hardening reaction of the Al0.3CrFe1.5MnNi0.5 high entropy alloy. Mater Des 36:854–858 (DOI:10.1016/j.matdes.2011.04.067)

65. Li R, Shi Y, Wang Z, Wang L, Liu J, Jiang W (2010) Densification behavior of gas and

water atomized 316L stainless steel powder during selective laser melting. Appl Surf Sci 256:4350–4356 (DOI:10.1016/j.apsusc.2010.02.030)

66. Zhang KB, Fu ZY, Zhang JY, Shi J, Wang WM, Wang H, Wang YC, Zhang QJ (2009) Nanocrystalline CoCrFeNiCuAl high-entropy solid solution synthesized by mechanical alloying. J Alloys Compd 485:34–37 (DOI:10.1016/j.jallcom.2009.05.144)

67. Zhang KB, Fu ZY, Zhang JY, Wang WM, Lee SW, Niihara K (2010) Characterization of nanocrystalline CoCrFeNiTiAl high-entropy solid solution processed by mechanical alloying. J Alloys Compd 495:33–38 (DOI:10.1016/j.jallcom.2009.12.010)

68. Du Y, Lu Y, Wang T, Li T, Zhang G (2012) Effect of electromagnetic stirring on microstructure and properties of Al0.5CoCrCuFeNi alloy. Procedia Eng 27:1129–1134 (DOI:10.1016/j.proeng.2011.12.562)

69. Luo H, Li Z, Mingers AM, Raabe D (2018) Corrosion behavior of an equiatomic CoCrFeMnNi high-entropy alloy compared with 304 stainless steel in sulfuric acid solution. Corros Sci 134:131–139 (DOI:10.1016/j.corsci.2018.02.031)

70. Gali A, George EP (2013) Tensile properties of high- and medium-entropy alloys. Intermetallics 39:74–78 (DOI:10.1016/j.intermet.2013.03.018)

71. Samal S, Biswas K (2013) Novel high-strength NiCuCoTiTa alloy with plasticity. J Nanoparticle Res 15: (DOI:10.1007/s11051-013-1783-2)

72. Mishra AK, Samal S, Biswas K (2012) Solidification behaviour of Ti-Cu-Fe-Co-Ni high entropy alloys. Trans Indian Inst Met 65:725–730 (DOI:10.1007/s12666-012-0206-x)

73. Dong Y, Jiang L, Tang Z, Lu Y, Li T (2015) Effect of Electromagnetic Field on Microstructure and Properties of Bulk AlCrFeNiMo0.2 High-Entropy Alloy. J Mater Eng Perform 24:4475–4481 (DOI:10.1007/s11665-015-1727-3)

74. Jiang H, Zhang H, Huang T, Lu Y, Wang T, Li T (2016) Microstructures and mechanical properties of Co2MoxNi2VWx eutectic high entropy alloys. Mater Des 109:539–546 (DOI:10.1016/j.matdes.2016.07.113)

75. He F, Wang Z, Cheng P, Wang Q, Li J, Dang Y, Wang J, Liu CT (2016) Designing eutectic high entropy alloys of CoCrFeNiNbx. J Alloys Compd 656:284–289 (DOI:10.1016/j.jallcom.2015.09.153)

76. Huo W, Zhou H, Fang F, Xie Z, Jiang J (2017) Microstructure and mechanical properties of CoCrFeNiZrx eutectic high-entropy alloys. Mater Des 134:226–233 (DOI:10.1016/j.matdes.2017.08.030)

77. Jiang H, Jiang L, Qiao D, Lu Y, Wang T, Cao Z, Li T (2017) Effect of Niobium on Microstructure and Properties of the CoCrFeNbxNi High Entropy Alloys. J Mater Sci Technol 33:712–717 (DOI:10.1016/j.jmst.2016.09.016)

78. Jiang L, Lu Y, Wu W, Cao Z, Li T (2016) Microstructure and Mechanical Properties of a CoFeNi2V0.5Nb0.75 Eutectic High Entropy Alloy in As-cast and Heat-treated Conditions. J Mater Sci Technol 32:245–250 (DOI:10.1016/j.jmst.2015.08.006)

79. Zhang M, Zhang L, Liaw PK, Li G, Liu R (2018) Effect of Nb content on thermal stability, mechanical and corrosion behaviors of hypoeutectic CoCrFeNiNbχ high-entropy alloys. J Mater Res 33:3276–3286 (DOI:10.1557/jmr.2018.103)

80. Chanda B, Das J (2017) Composition Dependence on the Evolution of Nanoeutectic in CoCrFeNiNb x ($0.45 \leq x \leq 0.65$) High Entropy Alloys . Adv Eng Mater 1700908:1700908 (DOI:10.1002/adem.201700908)

81. Zhang L, Zhou Y, Jin X, Du X, Li B (2018) Precipitation-hardened high entropy alloys with excellent tensile properties. Mater Sci Eng A 732:186–191 (DOI:10.1016/j.msea.2018.06.102)

82. Jiang H, Han K, Qiao D, Lu Y, Cao Z, Li T (2018) Effects of Ta addition on the microstructures and mechanical properties of CoCrFeNi high entropy alloy. Mater Chem Phys 210:43–48 (DOI:10.1016/j.matchemphys.2017.05.056)

83. Huo W, Zhou H, Fang F, Zhou X, Xie Z, Jiang J (2018) Microstructure and properties of novel CoCrFeNiTax eutectic high-entropy alloys. J Alloys Compd 735:897–904 (DOI:10.1016/j.jallcom.2017.11.075)

84. Han L, Xu X, Li Z, Liu B, Liu CT, Liu Y (2020) A novel equiaxed eutectic high-entropy alloy with excellent mechanical properties at elevated temperatures. Mater Res Lett 8:373–382 (DOI:10.1080/21663831.2020.1772395)

85. Ma SG ZY (2012) Effect of Nb addition on the microstructure and properties of AlCoCrFeNi high-entropy alloy. Mater Sci Eng A 480–486 (DOI:https://doi.org/10.1016/j.msea.2011.10.110)

86. Samal S, Rahul MR, Kottada RS, Phanikumar G (2016) Hot deformation behaviour and processing map of Co-Cu-Fe-Ni-Ti eutectic high entropy alloy. Mater Sci Eng A 664:227–235 (DOI:10.1016/j.msea.2016.04.006)

87. Dong Y, Lu Y, Kong J, Zhang J, Li T (2013) Microstructure and mechanical properties of multi-component AlCrFeNiMo x high-entropy alloys. J Alloys Compd 573:96–101 (DOI:10.1016/j.jallcom.2013.03.253)

88. Li A, Ma D, Zheng Q (2014) Effect of Cr on microstructure and properties of a series of AlTiCr x FeCoNiCu high-entropy alloys. J Mater Eng Perform 23:1197–1203 (DOI:10.1007/s11665-014-0871-5)

89. Rahul MR, Samal S, Venugopal S, Phanikumar G (2018) Experimental and finite element simulation studies on hot deformation behaviour of AlCoCrFeNi2.1 eutectic high entropy alloy. J Alloys Compd 749:1115–1127 (DOI:10.1016/j.jallcom.2018.03.262)

90. Dong Y, Gao X, Lu Y, Wang T, Li T (2016) A multi-component AlCrFe2Ni2 alloy with excellent mechanical properties. Mater Lett 169:62–64 (DOI:10.1016/j.matlet.2016.01.096)

91. Wani IS, Bhattacharjee T, Sheikh S, Bhattacharjee PP, Guo S, Tsuji N (2016) Tailoring nanostructures and mechanical properties of AlCoCrFeNi2.1 eutectic high entropy alloy using thermo-mechanical processing. Mater Sci Eng A 675:99–109 (DOI:10.1016/j.msea.2016.08.048)

92. Lee CF, Shun TT (2016) Effect of Fe content on microstructure and mechanical properties of Al0·5CoCrFexNiTi0.5 high-entropy alloys. Mater Charact 114:179–184

(DOI:10.1016/j.matchar.2016.02.018)

93. Ma SG, Jiao ZM, Qiao JW, Yang HJ, Zhang Y, Wang ZH (2016) Strain rate effects on the dynamic mechanical properties of the AlCrCuFeNi2 high-entropy alloy. Mater Sci Eng A 649:35–38 (DOI:10.1016/j.msea.2015.09.089)

94. Shukla S, Wang T, Cotton S, Mishra RS (2018) Hierarchical microstructure for improved fatigue properties in a eutectic high entropy alloy. Scr Mater 156:105–109 (DOI:10.1016/j.scriptamat.2018.07.022)

95. Wang T, Komarasamy M, Shukla S, Mishra RS (2018) Simultaneous enhancement of strength and ductility in an AlCoCrFeNi2.1 eutectic high-entropy alloy via friction stir processing. J Alloys Compd 766:312–317 (DOI:10.1016/j.jallcom.2018.06.337)

96. Hu X, Chen D (2018) Effect of Ceramic Rolling and Annealing on Mechanical Properties of AlCoCrFeNi2.1 Eutectic High-Entropy Alloys. J Mater Eng Perform 27:3566–3573 (DOI:10.1007/s11665-018-3430-7)

97. Lu Y, Gao X, Jiang L, Chen Z, Wang T, Jie J, Kang H, Zhang Y, Guo S, Ruan H, Zhao Y, Cao Z, Li T (2017) Directly cast bulk eutectic and near-eutectic high entropy alloys with balanced strength and ductility in a wide temperature range. Acta Mater 124:143–150 (DOI:10.1016/j.actamat.2016.11.016)

98. Rogal L, Morgiel J, Świątek Z, Czerwiński F (2016) Microstructure and mechanical properties of the new Nb25Sc25Ti25Zr25 eutectic high entropy alloy. Mater Sci Eng A 651:590–597 (DOI:10.1016/j.msea.2015.10.071)

99. Rogal L, Ikeda Y, Lai M, Körmann F, Kalinowska A, Grabowski B (2020) Design of a dual-phase hcp-bcc high entropy alloy strengthened by ω nanoprecipitates in the Sc-Ti-Zr-Hf-Re system. Mater Des 192:108716 (DOI:10.1016/j.matdes.2020.108716)

100. Tiwary CS, Pandey P, Sarkar S, Das R, Samal S, Biswas K, Chattopadhyay K (2021) Five decades of research on the development of eutectic as engineering materials. Prog Mater Sci 100793 (DOI:10.1016/j.pmatsci.2021.100793)

101. Chanda B, Potnis G, Jana PP, Das J (2020) A review on nano- / ultra fi ne advanced

eutectic alloys. J Alloys Compd 827:154226 (DOI:10.1016/j.jallcom.2020.154226)

102. Prasad YVRK, Rao KP, Sasidhara S (2015) Hot Working Guide A Compendium of processing maps. ASM Int 636 (DOI:10.1016/B978-0-08-033454-7.50019-X)

103. Kutumbarao V V., Rajagopalachary T (1996) Recent developments in modeling the hot working behavior of metallic materials. Bull Mater Sci 19:677–698 (DOI:10.1007/bf02745160)

104. Patnamsetty M, Saastamoinen A, Somani MC, Peura P (2020) Constitutive modelling of hot deformation behaviour of a CoCrFeMnNi high-entropy alloy. Sci Technol Adv Mater 21:43–55 (DOI:10.1080/14686996.2020.1714476)

105. Deschamps A, Bréchet Y (2002) Influence of quench and heating rates on the ageing response of an Al–Zn–Mg–(Zr) alloy. Mater Sci Eng A 251:200–207 (DOI:10.1016/s0921-5093(98)00615-7)

106. McQueen HJ, Spigarelli S, Kassner ME, Evangelista E (2011) Hot Deformation and Processing of Aluminum Alloys, 1st ed. CRC Press

107. Zhang MJ, Li FG, Wang SY, Liu CY (2011) Effect of powder preparation technology on the hot deformation behavior of HIPed P/M nickel-base superalloy FGH96. Mater Sci Eng A 528:4030–4039 (DOI:10.1016/j.msea.2011.01.118)

108. Sellars CM, McTegart WJ (1966) On the mechanism of hot deformation. Acta Metall 14:1136–1138 (DOI:10.1016/0001-6160(66)90207-0)

109. Sang D, Fu R, Li Y (2016) The Hot Deformation Activation Energy of 7050 Aluminum Alloy under Three Different Deformation Modes. Metals (Basel) 6:49 (DOI:10.3390/met6030049)

110. Pan QL, Li B, Wang Y, Zhang YW, Yin ZM (2013) Characterization of hot deformation behavior of Ni-base superalloy Rene'41 using processing map. Mater Sci Eng A 585:371–378 (DOI:10.1016/j.msea.2013.07.066)

111. Reyes-Calderón F, Mejía I, Cabrera JM (2013) Hot deformation activation energy (QHW)

of austenitic Fe-22Mn-1.5Al-1.5Si-0.4C TWIP steels microalloyed with Nb, V, and Ti. Mater Sci Eng A 562:46–52 (DOI:10.1016/j.msea.2012.10.091)

112. Raj R (1981) Development of a Processing Map for Use in Warm-Forming and Hot-Forming Processes. Metall Trans A, Phys Metall Mater Sci 12 A:1089–1097 (DOI:10.1007/BF02643490)

113. Prasad YVRK, Gegel HL, Doraivelu SM, Malas JC, Morgan JT, Lark KA, Barker DR (1984) Modeling of dynamic material behavior in hot deformation: Forging of Ti-6242. Metall Trans A 15:1883–1892 (DOI:10.1007/BF02664902)

114. Malas James Christopher III, Malas III JC, Gunasekera JS (1991) Methodology for design and control of thermomechanical processes. 9211849:205-205 p.

115. Huang K, Logé RE (2016) A review of dynamic recrystallization phenomena in metallic materials. Mater Des 111:548–574 (DOI:10.1016/j.matdes.2016.09.012)

116. Alaneme KK, Okotete EA (2019) Recrystallization mechanisms and microstructure development in emerging metallic materials: A review. J Sci Adv Mater Devices 4:19–33 (DOI:10.1016/j.jsamd.2018.12.007)

117. Shi C, Lai J, Chen XG (2014) Microstructural evolution and dynamic softening mechanisms of Al-Zn-Mg-Cu alloy during hot compressive deformation. Materials (Basel) 7:244–264 (DOI:10.3390/ma7010244)

118. Huang SH, Shu DY, Hu CK, Zhu SF (2016) Effect of strain rate and deformation temperature on strain hardening and softening behavior of pure copper. Trans Nonferrous Met Soc China (English Ed 26:1044–1054 (DOI:10.1016/S1003-6326(16)64201-2)

119. Bert Verlinden, Julian Driver, Indradev Samajdar, Roger Doherty (2007) Thermo-Mechanical Processing of Metallic Materials. Elsevier Science

120. Luton MJ, Sellars CM (1969) Dynamic recrystallization in nickel and nickel-iron alloys during high temperature deformation. Acta Metall 17:1033–1043 (DOI:10.1016/0001-6160(69)90049-2)

121. Gopala Krishna V, Prasad YVRK, Birla NC, Sambasiva Rao G (1996) Hot-deformation mechanisms in near-alpha titanium alloy 685. Jom 48:56–59 (DOI:10.1007/bf03223106)

122. Li Y, Ji H, Cai Z, Tang X, Li Y, Liu J (2019) Comparative study on constitutive models for 21-4N heat resistant steel during high temperature deformation. Materials (Basel) 12: (DOI:10.3390/ma12121893)

123. Waszczyszyn Z (1999) Fundamentals of Artificial Neural Networks. Springer, Vienna, pp 1–51

124. Liu J, Chang H, Hsu TY, Ruan X (2000) Prediction of the flow stress of high-speed steel during hot deformation using a BP artificial neural network. J Mater Process Technol 103:200–205 (DOI:10.1016/S0924-0136(99)00444-6)

125. Du KL, Swamy MNS (2006) Neural networks in a softcomputing framework. Neural Networks a Softcomputing Framew 1–566 (DOI:10.1007/1-84628-303-5)

126. Sun Y, Zeng WD, Zhang XM, Zhao YQ, Ma X, Han YF (2011) Prediction of tensile property of hydrogenated Ti600 titanium alloy using artificial neural network. J Mater Eng Perform 20:335–340 (DOI:10.1007/s11665-010-9695-0)

127. Martin T. Hagan,Howard B. Demuth, Mark Hudson Beale ODJ Neural Network Design

128. Huang W, Martin P, Zhuang HL (2019) Machine-learning phase prediction of high-entropy alloys. Acta Mater 169:225–236 (DOI:10.1016/j.actamat.2019.03.012)

129. Agarwal A, Prasada Rao AK (2019) Artificial Intelligence Predicts Body-Centered-Cubic and Face-Centered-Cubic Phases in High-Entropy Alloys. Jom 71:3424–3432 (DOI:10.1007/s11837-019-03712-4)

130. Islam N, Huang W, Zhuang HL (2018) Machine learning for phase selection in multi-principal element alloys. Comput Mater Sci 150:230–235 (DOI:10.1016/j.commatsci.2018.04.003)

131. Dixit S, Singhal V, Agarwal A, Prasada Rao AK (2020) Multi-label phase-prediction in high-entropy-alloys using Artificial-Neural-Network. Mater Lett 268:127606

(DOI:10.1016/j.matlet.2020.127606)

132. Raj RE, Daniel BSS (2008) Prediction of compressive properties of closed-cell aluminum foam using artificial neural network. Comput Mater Sci 43:767–773 (DOI:10.1016/j.commatsci.2008.01.041)

133. Paliwal M, Kumar UA (2009) Neural networks and statistical techniques : A review of applications. Expert Syst Appl 36:2–17 (DOI:10.1016/j.eswa.2007.10.005)

134. Hassan AM, Alrashdan A, Hayajneh MT, Mayyas AT (2009) Prediction of density, porosity and hardness in aluminum-copper-based composite materials using artificial neural network. J Mater Process Technol 209:894–899 (DOI:10.1016/j.jmatprotec.2008.02.066)

135. Altinkok N (2006) Use of artificial neural network for prediction of mechanical properties of α-Al2O3 particulate-reinforced al-si10mg alloy composites prepared by using stir casting process. J Compos Mater 40:779–796 (DOI:10.1177/0021998305055547)

136. Malinov S, Sha W (2004) Application of artificial neural networks for modelling correlations in titanium alloys. Mater Sci Eng A 365:202–211 (DOI:10.1016/j.msea.2003.09.029)

137. Perzyk M, Kochański AW (2001) Prediction of ductile cast iron quality by artificial neural networks. J Mater Process Technol 109:305–307 (DOI:10.1016/S0924-0136(00)00822-0)

138. Zhang Z, Klein P, Friedrich K (2002) Dynamic mechanical properties of PTFE based short carbon fibre reinforced composites: Experiment and artificial neural network prediction. Compos Sci Technol 62:1001–1009 (DOI:10.1016/S0266-3538(02)00036-2)

139. Lin CM, Tsai HL (2011) Evolution of microstructure, hardness, and corrosion properties of high-entropy Al0.5CoCrFeNi alloy. Intermetallics 19:288–294 (DOI:10.1016/j.intermet.2010.10.008)

140. Chuang MH, Tsai MH, Wang WR, Lin SJ, Yeh JW (2011) Microstructure and wear behavior of AlxCo 1.5CrFeNi1.5Tiy high-entropy alloys. Acta Mater 59:6308–6317 (DOI:10.1016/j.actamat.2011.06.041)

141. Chen ST, Tang WY, Kuo YF, Chen SY, Tsau CH, Shun TT, Yeh JW (2010) Microstructure and properties of age-hardenable AlxCrFe1.5MnNi0.5 alloys. Mater Sci Eng A 527:5818–5825 (DOI:10.1016/j.msea.2010.05.052)

142. Chou HP, Chang YS, Chen SK, Yeh JW (2009) Microstructure, thermophysical and electrical properties in AlxCoCrFeNi ($0 \leq x \leq 2$) high-entropy alloys. Mater Sci Eng B Solid-State Mater Adv Technol 163:184–189 (DOI:10.1016/j.mseb.2009.05.024)

143. Kao YF, Chen SK, Sheu JH, Lin JT, Lin WE, Yeh JW, Lin SJ, Liou TH, Wang CW (2010) Hydrogen storage properties of multi-principal-component CoFeMnTi xVyZrz alloys. Int J Hydrogen Energy 35:9046–9059 (DOI:10.1016/j.ijhydene.2010.06.012)

144. Sahlberg M, Karlsson D, Zlotea C, Jansson U (2016) Superior hydrogen storage in high entropy alloys. Sci Rep 6:1–6 (DOI:10.1038/srep36770)

145. Yao Y, Huang Z, Xie P, Lacey SD, Jacob RJ, Xie H, Chen F, Nie A, Pu T, Rehwoldt M, Yu D, Zachariah MR, Wang C, Shahbazian-Yassar R, Li J, Hu L (2018) Carbothermal shock synthesis of high-entropy-alloy nanoparticles. Science (80-) 359:1489–1494 (DOI:10.1126/science.aan5412)

146. Lee JI, Tsuchiya K, Tasaki W, Oh HS, Sawaguchi T, Murakami H, Hiroto T, Matsushita Y, Park ES (2019) A strategy of designing high-entropy alloys with high-temperature shape memory effect. Sci Rep 9: (DOI:10.1038/s41598-019-49529-8)

147. Piorunek D, Frenzel J, Jöns N, Somsen C, Eggeler G (2020) Chemical complexity, microstructure and martensitic transformation in high entropy shape memory alloys. Intermetallics 122:106792 (DOI:10.1016/j.intermet.2020.106792)

148. Murugesan M, Jung DW (2019) Two flow stress models for describing hot deformation behavior of AISI-1045 medium carbon steel at elevated temperatures. Heliyon 5:e01347 (DOI:10.1016/j.heliyon.2019.e01347)

149. Lin YC, Chen XM (2011) A critical review of experimental results and constitutive descriptions for metals and alloys in hot working. Mater Des 32:1733–1759 (DOI:10.1016/j.matdes.2010.11.048)

150. Liu J, Wang X, Liu J, Liu Y, Li H, Wang C (2019) Hot deformation and dynamic recrystallization behavior of Cu-3Ti-3Ni-0.5Si alloy. J Alloys Compd 782:224–234 (DOI:10.1016/j.jallcom.2018.12.212)

151. Zener C, Hollomon JH (1944) Effect of strain rate upon plastic flow of steel. J Appl Phys 15:22–32 (DOI:10.1063/1.1707363)

152. Jain R, Dewangan SK, Kumar V, Samal S (2020) Artificial neural network approach for microhardness prediction of eight component FeCoNiCrMnVAlNb eutectic high entropy alloys. Mater Sci Eng A 797:140059 (DOI:10.1016/j.msea.2020.140059)

153. Jain R, Jain A, Rahul MR, Kumar A, Dubey M, Sabat RK, Samal S, Phanikumar G (2020) Development of ultrahigh strength novel Co–Cr–Fe–Ni–Zr quasi-peritectic high entropy alloy by an integrated approach using experiment and simulation. Materialia 14: (DOI:10.1016/j.mtla.2020.100896)

154. Venugopal S, Mannan SL, Prasad YVRK (1993) Criteria for prediction of flow instabilities and microstructural manifestations during warm working of AISI 304L stainless steel. Mater Sci Technol (United Kingdom) 9:1021–1030 (DOI:10.1179/mst.1993.9.11.1021)

155. S L Semiatin, J J Jonas (1984) Formability and Workability of Metals: Plastic Instability and Flow Localisation. ASM International

156. Semiatin SL, Lahoti GD (1981) Deformation and unstable flow in hot forging of Ti-6Ai-2Sn-4Zr-2Mo-0.1Si. Metall Trans A 12:1705–1717 (DOI:https://doi.org/10.1007/BF02643753)

157. Guo S, Liu CT (2011) Phase stability in high entropy alloys: Formation of solid-solution phase or amorphous phase. Prog Nat Sci Mater Int 21:433–446 (DOI:10.1016/S1002-0071(12)60080-X)

158. Senkov ON, Zhang C, Pilchak AL, Payton EJ, Woodward C, Zhang F (2019) CALPHAD-aided development of quaternary multi-principal element refractory alloys based on NbTiZr. J Alloys Compd 783:729–742 (DOI:10.1016/j.jallcom.2018.12.325)

159. Chen H, Ab TS, Ab TS, Chen H, Mao H, Chen Q (2018) Database development and Calphad calculations for high entropy alloys : Challenges , strategies , and tips Database development and Calphad calculations for high entropy alloys : Challenges , strategies , and tips. Mater Chem Phys. https://doi.org/10.1016/j.matchemphys.2017.07.082

160. Stein F, Palm M, Sauthoff G (2004) Structure and stability of Laves phases. Part I. Critical assessment of factors controlling Laves phase stability. Intermetallics 12:713–720 (DOI:10.1016/j.intermet.2004.02.010)

161. Machon L, Sauthoff G (1996) Deformation behaviour of Al-containing C14 Laves phase alloys. Intermetallics 4:469–481 (DOI:10.1016/0966-9795(96)00023-4)

162. Thoma D., Chu F, Peralta P, Kotula P., Chen K., Mitchell T. (1997) Elastic and mechanical properties of Nb(Cr,V)2 C15 Laves phases. Mater Sci Eng A 239–240:251–259 (DOI:10.1016/S0921-5093(97)00589-3)

163. Trivedi R, Magnin P, Kurz W (1987) Theory of eutectic growth under rapid solidification conditions. Acta Metall 35:971–980 (DOI:https://doi.org/10.1016/0001-6160(87)90176-3)

164. Gorsse S, Nguyen MH, Senkov ON, Miracle DB (2018) Database on the mechanical properties of high entropy alloys and complex concentrated alloys. Data Br 21:2664–2678 (DOI:10.1016/j.dib.2018.11.111)

165. Chang YJ, Jui CY, Lee WJ, Yeh AC (2019) Prediction of the Composition and Hardness of High-Entropy Alloys by Machine Learning. Jom 71:3433–3442 (DOI:10.1007/s11837-019-03704-4)

166. Safari A, Imran M, Weiss S (2021) A Comparative Study on Modified Johnson–Cook and Arrhenius-Type Constitutive Models to Predict the Hot Deformation Behaviour of Molybdenum-Hafnium-Carbide Alloy. J Mater Eng Perform 2021 303 30:1945–1956 (DOI:10.1007/S11665-021-05464-2)

167. Motlagh ZS, Tolaminejad B, Momeni A (2020) Prediction of Hot Deformation Flow Curves of 1.4542 Stainless Steel. Met Mater Int. https://doi.org/10.1007/s12540-020-00627-7

168. Zhang Y ben, Yao S, Hong X, Wang Z gang (2017) A modified Johnson–Cook model for 7N01 aluminum alloy under dynamic condition. J Cent South Univ 24:2550–2555 (DOI:10.1007/s11771-017-3668-5)

169. Saravanan L, Senthilvelan T (2016) Constitutive equation and microstructure evaluation of an extruded aluminum alloy. J Mater Res Technol 5:21–28 (DOI:10.1016/j.jmrt.2015.04.002)

170. Gao X, Li HX, Han L, Santillana B, Ruvalcaba D, Zhuang LZ (2018) Constitutive Modeling and Activation Energy Maps for a Continuously Cast Hyperperitectic Steel. Metall Mater Trans A Phys Metall Mater Sci 49:4633–4648 (DOI:10.1007/s11661-018-4801-2)

171. Hosseini SMK, Zarei-Hanzaki A, Yazdan Panah MJ, Yue S (2004) ANN model for prediction of the effects of composition and process parameters on tensile strength and percent elongation of Si - Mn TRIP steels. Mater Sci Eng A 374:122–128 (DOI:10.1016/j.msea.2004.01.007)

172. Dieter GE (1961) Yielding Criteria for Ductile Metals. Mech. Metall. 646

173. McQueen HJ, Ryan ND (2002) Constitutive analysis in hot working. Mater Sci Eng A 322:43–63 (DOI:10.1016/S0921-5093(01)01117-0)

174. Medina SF, Hernandez CA (1996) General expression of the Zener-Hollomon parameter as a function of the chemical composition of low alloy and microalloyed steels. Acta Mater 44:137–148 (DOI:10.1016/1359-6454(95)00151-0)

175. Kingkam W, Li N, Zhang HX, Zhao CZ (2017) Hot Deformation Behavior of High Strength Low Alloy Steel by Thermo Mechanical Simulator and Finite Element Method. IOP Conf Ser Mater Sci Eng 205: (DOI:10.1088/1757-899X/205/1/012001)

176. Zener C and Hollomon JH (1944) Effect of strain rate upon plastic flow of steel. J Appl Phys 15:22–32 (DOI:10.1063/1.1707363)

177. Lin YC, Chen MS, Zhong J (2008) Effect of temperature and strain rate on the compressive deformation behavior of 42CrMo steel. J Mater Process Technol 205:308–

315 (DOI:10.1016/j.jmatprotec.2007.11.113)

178. Roy S, Suwas S (2013) The influence of temperature and strain rate on the deformation response and microstructural evolution during hot compression of a titanium alloy Ti-6Al-4V-0.1B. J Alloys Compd 548:110–125 (DOI:10.1016/j.jallcom.2012.08.123)

179. Semiatin S., Seetharaman V, Weiss I (1999) Flow behavior and globularization kinetics during hot working of Ti–6Al–4V with a colony alpha microstructure. Mater Sci Eng A 263:257–271 (DOI:10.1016/s0921-5093(98)01156-3)

180. Wang H, Wang C, Mo Y, Wang H, Xu J (2019) Hot deformation and processing maps of Al-Zn-Mg-Cu alloy under coupling-stirring casting. J Mater Res Technol 8:1224–1234 (DOI:10.1016/j.jmrt.2018.08.009)

181. Malas JC, Seetharaman V (1992) Using material behavior models to develop process control strategies. Jom 44:8–13 (DOI:10.1007/BF03222246)